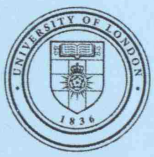

UNIVERSITY OF LONDON THESIS

Degree PhD Year 2007 Name of Author SHIRAL, Masae

Experimental Investigations of Frustrated Antiferromagnets

Masae Shirai

University College London / DFRL

Supervisor: Prof. S T Bramwell

ProQuest LLC
789 East Eisenhower Parkway
P.O. Box 1346
Ann Arbor, MI 48106-1346

Abstract

This thesis describes the investigation of frustrated magnetic systems, focusing on the pyro -chlore antiferromagnets (AFM). The rare-earth pyrochlore oxides $R_2B_2O_7$ (R^{3+} = rare earth, B^{4+} = transition metal), crystallizes in the $Fd\bar{3}m$ space group, with the magnetic ions (R) and the non-magnetic transition metal (B) ions situated on the 16*c* and on the 16*d* sites, respectively. As a result, the magnetic ions form lattices of corner-sharing tetrahedra -a stage in which frustration is manifested.

Erbium titanate $Er_2Ti_2O_7$ and stannate $Er_2Sn_2O_7$ are both frustrated pyrochlore antiferr -omagnets which are expected to have very similar magnetic properties. However, $Er_2Ti_2O_7$ magnetically orders at $T_N \sim 1.1$ K but $Er_2Sn_2O_7$ remains disordered down to $T \sim 150$ mK. The main aim of this thesis is therefore to investigate the origin of this difference. The magnetic properties of the series $Er_2Ti_{2-x}Sn_xO_7$ were studied as a function of x ($x = 0 \sim 2$).

Firstly, from the powder neutron diffraction patterns obtained, it was shown that the detected order diminishes as $x \rightarrow 2$. However, in contrast to the previously reported result, a long-ranged ordering transition was detected for $Er_2Ti_2O_7$ (at ~ 80 mK) as well as for $Er_2Ti_2O_7$ (at ~ 1.2 K). The ordered magnetic structure was determined; while $Er_2Ti_2O_7$ orders into the Champion state (one of the ground state of the pyrochlore ⟨111⟩-XY AFM), $Er_2Sn_2O_7$ orders into a ground state of a Heisenberg pyrochlore AFM with dipolar interaction (Palmer-Chalker state).

Secondly, the existence of the quantum critical point (QCP) in the composition range $1.5 \leq x \leq 2$ was investigated by means of low temperature magnetization measurements. The critical composition $x_{critical} \sim 1.55$ was determined.

Thirdly, the single ion anisotropy of the series $Er_2Ti_{2-x}Sn_xO_7$ ($x = 0 \sim 2$) was studied by analyzing the crystal electric field (CEF) measured by the inelastic neutron scattering. As a result, the single-ion moments were shown to retain a constant size (~ 3 μ_B) throughout the series. In contrast, the nature of the single ion anisotropy changed from being XY-like for $x = 0$ into being Ising-like for $x = 2$ (with respect to the ⟨111⟩- axes).

Finally, the temperature-field phase diagram of the experimental realization of the Heisenberg pyrochlore AFM –$Gd_2Ti_2O_7$, was investigated by means of powder neutron diffraction.

Acknowledgements

I would like to thank my supervisor Professor Steven Bramwell for his incredible patience and understanding during my long Ph.D. years. An enormous appreciation for Andrew Wills for teaching me the ABCs of Representational Analysis method, Jason Gardner, Georg Ehlers, Ross Stewart for the scientific helps regarding the neutron work at the ILL; Clemens Ritter, Paul Henry and the Cryogenics team at the ILL for technical support; Rob Bewley and D.T.Adroja for instrumental support at ISIS.

I need to give my word of appreciation to Prof. Richard Catlow, the UCL graduate school and EPSRC for the financial support that allowed me survive through the hard days and gave me chance to attend interesting schools/training courses and conferences; also to Mark Green for being my secondary supervisor.

A warm appreciation goes to Fiona Coomer and Prof. Andrew Harrison for making me feel at home during the otherwise rather lonely experiments in a foreign environment!; to Prof. Andrew Boothroyd for the inspiring lectures at the Oxford neutron summer school and Prof. Stephen Blundell for the beautiful textbook of magnetism that supported almost every moment of my Ph.D. I would like to send my best regards to all the friendly people I met during the muon and neutron training courses (Enrique Gimenez Melero, Tom Weller, Pui, Chu-Hong, Mark.....).

Dickon Champion, Tom Fennell, Simon Banks and Andrea Taroni have always been my admiring group-mates. My views towards the world of frustrated magnetism wouldn't have been so exciting without their existence!

I do also have to send my thanks to the other side of the world; to Prof. Sakakibara and his group at ISSP, Japan (specially to Watanuki-san, Tayama-san); also to K.Matsuhira. It was a totally new exotic world they introduced me to.

Last, but not least, I would like to thank all the intimate friends and families who stood by me throughout the difficult times, happy days and cold nights; Judy my definitely longest coffee-pal, for me London would have been a very different and difficult place to live without you. Misbah and Saira for their positive attitudes and

happy company. Yumiko for baring a flatmate like me for 2 years!

Mom, Dad, Ryo, Tia Sanae and Batian – my closest families who always cheered me up and provided safety and love from home Barcelona, Kyoto, and Sao-Paulo. I promised you I will one day reach 'the moon' and I hope I have – reached my own star. And Ryuji, a very special person, who coincidentally talks the language of 'spin ice'.

Again, there is no measure one can give to the size of my thanks that is dedicated to you, Steve. *Science, became the pillow for me to dream*. And it is you who gave me that gift, at the first lecture you gave – it is now 8 years since. I will not ever forget the fascinating tales you told me under those beautiful stars, by the Isère.

Thank you !

Contents

Chapter 1. Introduction to Magnetism

Chapter 2. Frustrated Magnetism

Chapter 3. Neutron Scattering

Chapter 4. Solid State Synthesis

Chapter 5. Magnetic Diffraction of $Er_2Ti_{2-x}Sn_xO_7$

Chapter 6. Low Temperature Magnetization of $Er_2Ti_{2-x}Sn_xO_7$

Chapter 7. Crystal Field Measurement of $Er_2Ti_{2-x}Sn_xO_7$

Chapter 8. Neutron Diffraction work on $Gd_2Ti_2O_7$ in Applied Fields

Chapter 9. Discussion and Future Work

List of Figures

List of Tables

Chapter 1

Introduction to Magnetism

This first chapter is devoted to introduce the reader the basic concepts that will be needed in order to read the rest of the thesis. These are mainly the knowledge in solid state magnetism. Among the many textbooks [1-6] that were employed during the write up of this chapter, the main ones that were heavily consulted were Blundell [2], Crangle [1], Stanley [3] and Kittel [4].

Magnetism is an enormous field of study which has been studied for nearly three thousand years commencing from the Lodestone, an iron ore, which attracted the attention of Greek scholars and philosophers. During the last two centuries magnetism became associated with electricity as the two components of light and subsequently with the theory of relativity. Today, magnetism in condensed matter is a phenomenon that attracts much interest.

Macroscopic systems exhibit magnetic properties which are fundamentally different from their basic constituents, the atoms and the molecules. This is because magnetism is a collective phenomenon, involving the mutual cooperation of enormous numbers of particles. In this sense, we can say that magnetism is similar to the phenomenon of the solid state itself. Likewise, many states of matter have magnetic analogs. For example, a simple paramagnet is thermodynamically equivalent to an ideal gas since a magnetic equation of state is also obeyed by the non-interacting spins, similar to the familiar P, V, T relationship obeyed by the ideal gas. This equivalence is schematically shown in Fig.1.9. Hence, collective phenomena in nature can be

approached by studying magnetic systems. There are two major advantages of using magnetic systems to study the generic concepts. These are the availability of a large variety of diverse magnetic materials that could approximate simple theoretical toy models, and their ease of study by a variety of well-developed experimental techniques. [7]

In this section we briefly review the basic knowledge that one might find useful in discussing general magnetism.

1.1 Paramagnetism

1.1.1 What is a *magnetic moment*?

The magnetic moment, μ, is the fundamental object in magnetism. In classical electromagnetism this can be thought in terms of a current loop. An elementary current loop of area |dS| carrying a current I gives rise to a magnetic moment $d\mu$ given by

$$d\mu = I\,dS. \tag{1.1}$$

Then the magnetic moment for a finite size loop becomes $\mu = \int d\mu = I \int dS$.

The magnetic moment is always associated with an angular momentum since all the moving charges giving rise to magnetism have mass. If we consider the orbital motion of an electron in an atom, the (orbital) angular momentum $\mathbf{L}$ of that electron and the associated magnetic moment μ take the form $\mu = \gamma \mathbf{L}$, where γ is a constant called the gyromagnetic ratio. The magnitude of the magnetic moment of an electron (charge $-e$, mass m_e) circularly orbiting in a hydrogen atom can be estimated to be

$$|\mu_e| = \pi r^2 I = -\, e\hbar / 2m_e \equiv -\mu_B, \tag{1.2}$$

where the current I around the atom is $I = -e/\tau$ with the orbital period $\tau = 2\pi r/v$, speed $v = |\mathbf{v}|$ and radius r. Here the angular momentum of the electron, $m_e v r$, is taken to be $\hbar$ as it should be in its ground state in the language of quantum mechanics. This unit magnetic moment size ($\mu_B = 9.274 \times 10^{-24}$ Am^2) is called the Bohr magneton and is widely employed as the unit for describing the size of atomic magnetic moments. The

gyromagnetic ratio for the electron is $\gamma_e = -e/2m_e$.

Keeping in mind the quantized nature of the angular momentum, let us expand the scale of the system in question from a single electron into an atom containing many electrons. The magnetic moment of a free atom/ion $\boldsymbol{\mu}_J$ is associated with its total angular momentum vector **J** by

$$\boldsymbol{\mu}_J = \gamma \mathbf{J} = -g_J \mu_B \mathbf{J} = -g_J \mu_B \hbar \sqrt{J(J+1)}. \qquad (1.3)$$

This relation arises from the expression of the magnetic moment operator $\hat{\mu} = \mu_B g_J \hat{J}$. **J** is the sum

$$\mathbf{J} = \mathbf{L} + \mathbf{S}, \qquad (1.4)$$

where **L** and **S** are *atomic* orbital and spin angular momentum vectors; i.e. angular moments summed over all the electrons in the atom. These quantities are all measured in units of $\hbar$. This comes from representation of the eigenvalues of the angular moment operators; $\mathbf{S}^2 = S(S+1)\hbar^2$, $\mathbf{L}^2 = L(L+1)\hbar^2$ and $\mathbf{J}^2 = J(J+1)\hbar^2$, where S, L and J are *atomic* quantum numbers for the spin, orbital and total angular moment. The constant g_J is called the Landé g-factor. For an electron this becomes the spectroscopic splitting factor $g = 2.0023$, usually taken as 2.00. For ions where ground state quantum numbers can be estimated sufficiently well by Hund's rule (e.g. 4*f* ions with spin-orbit coupling having larger effect on energy than the crystal field) this g-factor is given by

$$g_J = 1 + \frac{J(J+1) + S(S+1) - L(L+1)}{2J(J+1)}. \qquad (1.5)$$

Hund's rule is stated as follows. If the Russell-Saunders spin-orbit coupling (the L-S coupling) is a weak perturbation compared to the electrostatic interactions that control the values of L and S, the orbital and spin angular moments of the electrons are first separately combined to give $S = \Sigma_i s_i$ and $L = \Sigma_i l_i$. The spin-orbit interaction is then applied as a weak perturbation to give a range of J values; $J = |L+S|, |L+S-1|, \ldots, |L-S+1|, |L-S|$. (For atoms with high atomic number Z, the spin-orbit interaction is the dominant energy and hence the *j-j* coupling scheme is employed instead.) 4*f* ions obey Hund's rule particularly well because the partially filled outer shell electrons (4*f*

electrons) are well contracted in space, lying deep within the ion beneath the 5*s* and 5*p* shells. Hence, they can be treated as localized free ions. On the other hand, the effective magnetic moments of the 3*d* ions calculated using the Hund's rule give much poorer agreement with the experimentally determined values since the ions are much more affected by the local crystal environment. Implied by the use of Hund's rule, the Russell-Saunders coupling scheme is employed for the 4*f* ions in this thesis.

1.1.2 Susceptibility of a paramagnet

When a magnetic field is applied to a system containing magnetic moments, the magnetic moments respond to the applied field in various ways, depending on the nature of the system, to induce a magnetization **M** within the system. For a linear material this induced magnetization is proportional to the applied field **H**;

$$\mathbf{M} = \chi \mathbf{H}, \tag{1.6}$$

where χ is the magnetic susceptibility. The magnetization is defined as the magnetic moment induced per unit volume, hence, by the above relation χ is defined as the field induced magnetization per volume. This volume susceptibility χ can be easily converted into molar susceptibility χ_m or mass susceptibility χ_g if appropriate. If $\chi>0$, the system is termed paramagnetic, and if $\chi < 0$ the system is diamagnetic. Paramagnetism occurs for systems containing unpaired electrons. The magnetic moments in a perfect paramagnet are 'isolated'; i.e. they do not interact with each other nor with the environment, and when a magnetic field is applied, the induced magnetization is parallel to the applied field.

In a paramagnetic system, the interactions between magnetic moments are very weak, so magnetic moments behave independently, pointing in random directions in the absence an applied field. The application of a magnetic field tends to align the magnetic moments, giving rise to positive magnetization, while an increase in the temperature will disorder them. This *B*/*T* dependence of the magnetization of paramagnetic material, with J = integer or half integer, is expressed by the Brillouin function $B_J(y)$;

$$\frac{M}{M_S} = \frac{\langle m_J \rangle}{J} = \mathrm{B}_J(y), \tag{1.7}$$

where the saturation magnetization $M_S = n g_J \mu_B m_J^{max} = n g_J \mu_B J$. The value of the thermal average $\langle m_J \rangle$ can be expressed using the partition function Z;

$$Z = \sum_{m_J=-J}^{J} \exp\left(m_J g_J \mu_B B / k_B T\right), \tag{1.8}$$

then

$$\langle m_J \rangle = \frac{\sum_{m_J=-J}^{J} m_J \exp(m_J g_J \mu_B B / k_B T)}{Z}. \tag{1.9}$$

This leads to the expression of the Brillouin function;

$$\mathrm{B}_J(y) = \frac{2J+1}{2J} \coth\left(\frac{2J+1}{2J} y\right) - \frac{1}{2J} \coth \frac{y}{2J}, \tag{1.10}$$

where $y = g_J \mu_B JB / k_B T$. The normal experimental situation corresponds to small y, except at extremely high fields or ultra low temperatures. When y is small (and hence $\chi << 1$) $\mathrm{B}_J(y)$ is approximated to $\mathrm{B}_J(y) = \frac{(J+1)y}{3J} + O(y^3)$, using Maclaurin expansion of coth y. So the T^{-1} dependence of the susceptibility χ is derived to be

$$\chi = \frac{M}{H} \approx \frac{\mu_o M}{B} = \frac{n \mu_o \mu_{eff}^2}{3 k_B T} = \frac{C_{Curie}}{T}, \tag{1.11}$$

with

$$\mu_{eff} = g_J \mu_B \sqrt{J(J+1)}. \tag{1.12}$$

The constant C_{Curie} is the Curie constant. Eqn.(1.11) describes the common observation that the inverse of the susceptibility of a paramagnet is proportional to temperature and is called the Curie law. When the susceptibility is evaluated in the limit of vanishing applied field, then from Eqn.(1.11) and Eqn.(1.12), the magnetic moment is given by $\mu_{eff} = g_J \mu_B \sqrt{J(J+1)}$. However, the magnetic moments in high fields tend to align fully with the applied field to give the saturation magnetization M_S, hence, the magnetic moment should be expressed in terms of J in the form $\mu = g_J \mu_B m_J^{max} = g_J \mu_B J$. The two values μ_{eff} and μ ($= M_S / n$) are not equal except for a classical system with $J = \infty$.

1.1.3 Magnetic energy

In absence of a field the energy levels of the ion are degenerate (i.e. all m_J-levels are degenerate). The application of a field will split the levels, depending upon the projection of the moment in the field direction. This is called Zeeman splitting. The energy levels of the ions in the field B are

$$E = g_J m_J \mu_B B, \tag{1.13}$$

where m_J takes values $J, J-1, \cdots -J$.

In the special case of where $m_J = \pm \frac{1}{2}$ and $g_J = 2$, this results in a two level splitting with separation $2\mu_B B$. The two levels correspond to parallel and antiparallel projections of the moment on the field direction. The parallel alignment of the spin with the field is energetically favored over the antiparallel alignment and hence a population difference is created. The populations of the levels depend on the available thermal energy and the strength of the applied field. By application of the Boltzmann distribution the populations are

$$\frac{N_1}{N} = \frac{\exp\left(\frac{\mu B}{k_B T}\right)}{\exp\left(\frac{\mu B}{k_B T}\right) + \exp\left(\frac{-\mu B}{k_B T}\right)}; \quad \frac{N_2}{N} = \frac{\exp\left(\frac{-\mu B}{k_B T}\right)}{\exp\left(\frac{\mu B}{k_B T}\right) + \exp\left(\frac{-\mu B}{k_B T}\right)}; \tag{1.14}$$

where N_1 and N_2 are the populations of the lower and upper levels, and $N = N_1 + N_2$ is the total number of atoms. Since there is a population difference there will also be a net moment. With N atoms per unit volume the net magnetization for this special case for the two-level system can be expressed as

$$M = (N_1 - N_2)\mu = N\mu \frac{\exp(x) - \exp(-x)}{\exp(x) + \exp(-x)} = N\mu \tanh x, \tag{1.15}$$

where $x = \frac{\mu B}{k_B T}$. For a general magnetic atom with total angular moment J, this expression becomes

$$M = N g_J J \mu_B \mathrm{B}_J(y), \quad \left(y = \frac{g_J J \mu_B B}{k_B T}\right) \tag{1.16}$$

where $\mathrm{B}_J(y)$ is the Brillouin function mentioned in section 1.1.2.

1.2 Environments –The Crystal Field

Now let us consider the effect of the local environment due to the crystal on the energy levels of an atom. In crystal field theory the neighboring orbitals surrounding the central magnetic ion are modeled as negative point charges. These neighboring atoms in the crystal exert an electrostatic field on the central ion called the crystal field (or crystal electric field, CEF). The size and nature of the crystal field effect depends crucially on the symmetry of the local environment. The crystal field exerts its greatest influence on the direction of the orbital angular momentum and it does not directly affect the spin. In an atom, orbitals corresponding to different values of L and m_l have different spatial distributions of electronic charge. Only s-orbitals ($L = 0$) are spherically symmetric. The others have significant angle dependence and they spread out in various directions in the form of lobes and other shapes. In the free atom with no applied magnetic field, the directions of these different orbital distributions are not distinguished, hence all energy levels will be degenerate. However, in a solid crystal, those lobes of charge pointing towards neighboring atoms, having higher energies, will be differentiated with respect to those which pointing between atoms with lower energy. Two examples for the energy level splitting caused by the crystal field is illustrated in Fig.1.1 (octahedral CEF) and Fig.1.2 (axial CEF). What in free space would be a degenerate situation (involving different m_Js) is split in the crystal into different (sets of) energy levels. The separations of these crystal field levels are often wide enough to be immune for thermal excitation at modest temperatures.

1.2.1 Kramers v.s. Jahn-Teller theorem

There is an important theorem concerning the energy levels of magnetic ions in a crystalline environment that we will mention here. This is Kramers theorem [8] that states that the energy levels of odd-electron ions under electrostatic interaction of any nature are at least two-fold degenerate in the absence of a magnetic field. The pairs of states are time conjugate of each other and therefore can be split by a magnetic field but not by an electric field. Ions with odd numbers of electrons, such as Gd^{3+} ($4f^7$), Dy^{3+} ($4f^9$) and Er^{3+} ($4f^{11}$), are called Kramers ions.

On the other hand, when Kramers theorem does not apply, the surroundings of a magnetic ion will distort and always tend to give non-degenerate energy levels. This is called the Jahn-Teller [9] distortion and often occurs for even-electron ions. Thus, even-electron ions, such as Tb^{3+} ($4f^8$) or Ho^{3+} ($4f^{10}$), tend to have singlet energy levels in crystals.

1.3 Magnetic Interactions

There are several different pathways by which magnetic moments may interact, potentially producing long range order. Here we introduce the main magnetic interactions.

1.3.1 Magnetic dipole interaction

The dipolar interaction is present in all magnets but is weak when the moments are small; its magnitude is approximately ~1 K in temperature units for two moments of ~1 μ_B. It occurs through space and is anisotropic and long ranged, due to the $1/r^3$ dependence. The dipole energy for two magnetic dipoles $\boldsymbol{\mu}_i$ and $\boldsymbol{\mu}_j$ separated by $\mathbf{r}$ has the form;

$$E_{ij}^{dipole} = \frac{\mu_0}{4\pi r^3}[\boldsymbol{\mu}_i \cdot \boldsymbol{\mu}_j - \frac{3}{r^2}(\boldsymbol{\mu}_i \cdot \mathbf{r})(\boldsymbol{\mu}_j \cdot \mathbf{r})]. \qquad (1.17)$$

Since many materials order at $T >> 1$ K (e.g. 1043 K in Fe), the magnetic dipolar interaction must be too weak to account for the ordering of most materials. However, it becomes more important in rare earth magnets where moments are large, specially for those system that orders at milliKelvin temperatures.

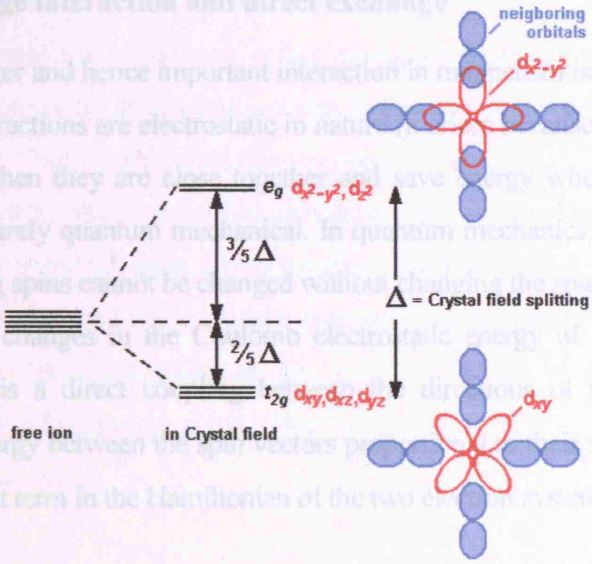

Figure 1.1: The splitting of the free ion term by the crystal field. Here the central atom is a transition metal ion and its *d*-orbitals are subjected to an octahedral crystal field.

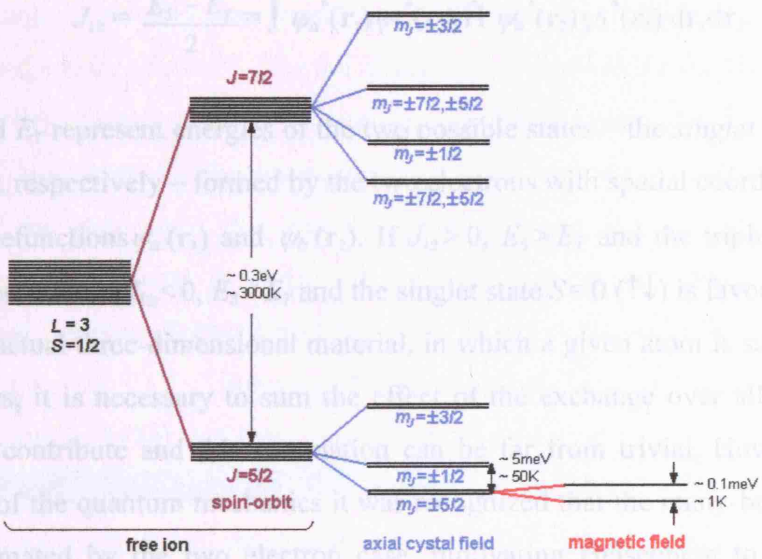

Figure 1.2: The schematic energy levels of Ce^{3+} ion showing the splitting of the free ion term by an axial crystal field. [2]

1.3.2 Exchange interaction and direct exchange

A much stronger and hence important interaction in magnetism is the exchange interaction. Exchange interactions are electrostatic in nature (it arises because charges of the same sign cost energy when they are close together and save energy when they are apart) and its treatment is purely quantum mechanical. In quantum mechanics, the relative directions of two interacting spins cannot be changed without changing the spatial distribution of charge. The resulting changes in the Coulomb electrostatic energy of the whole system act as though there is a direct coupling between the directions of the spins involved, with interaction energy between the spin vectors proportional to their scalar product $\mathbf{S}_1 \cdot \mathbf{S}_2$. The spin-dependent term in the Hamiltonian of the two electron system can be written as

$$\hat{\mathrm{H}}_{\mathrm{spin}} = -2J_{12}\,\mathbf{S}_1 \cdot \mathbf{S}_2, \tag{1.18}$$

where J_{12} is the exchange constant (or *exchange integral*) defined by

$$J_{12} = \frac{E_S - E_T}{2} = \int \psi_a^*(\mathbf{r}_1)\psi_b^*(\mathbf{r}_2)\,\hat{\mathrm{H}}\,\psi_a^*(\mathbf{r}_2)\psi_b^*(\mathbf{r}_1)\,\mathrm{d}\mathbf{r}_1\mathrm{d}\mathbf{r}_2. \tag{1.19}$$

Here E_S and E_T represent energies of the two possible states – the *singlet* state and the *triplet* state, respectively – formed by the two electrons with spatial coordinates $\mathbf{r}_1$ and $\mathbf{r}_2$ and wavefunctions $\psi_a(\mathbf{r}_1)$ and $\psi_b(\mathbf{r}_2)$. If $J_{12} > 0$, $E_S > E_T$ and the triplet state $S = 1$ ($\uparrow\uparrow$) is favored but if $J_{12} < 0$, $E_S < E_T$ and the singlet state $S = 0$ ($\uparrow\downarrow$) is favored.

In an actual three-dimensional material, in which a given atom is surrounded by many others, it is necessary to sum the effect of the exchange over all interactions which can contribute and this summation can be far from trivial. However, in the early days of the quantum mechanics it was recognized that the many-body case will be approximated by the two electron case, motivating Heisenberg to propose his Hamiltonian

$$\hat{\mathrm{H}}_{\mathrm{Heisenberg}} = -2\sum_{\langle i,j\rangle} J_{ij}\,\mathbf{S}_i \cdot \mathbf{S}_j, \tag{1.20}$$

where J_{ij} is now the exchange constant between all i^{th} and j^{th} spins.(The notation $\langle i,j\rangle$

under the summation avoids the double-counting.)

Direct exchange is defined as the exchange interactions between electrons on neighboring magnetic atoms without any intermediary. Orbital overlap between two atoms means that their electrons become correlated. Coulombic repulsion is minimized and the Pauli exclusion principle is satisfied, resulting in a singlet ground state with anti-parallel spins (forming the *bonding* orbital). Though this seems the most obvious route for the exchange interaction to take, this is not a very important mechanism in real materials as the overlap of the magnetic *d* or *f* electron wavefunctions is extremely small. Thus it is necessary to consider indirect exchange mechanisms instead.

1.3.3 Indirect exchange (superexchange, double exchange and RKKY)

Superexchange

Superexchange is usually the most important type of magnetic interaction in insulators and semiconductors. Like the direct exchange mechanism it is mediated by orbital overlap. However, in this case, the exchange interaction occurs via an intermediate non-magnetic ligand or anion placed in between the magnetic ions. An example of an ionic solid that has a magnetic ground state explainable by the superexchange mechanism is MnO (see Fig.1.3). It is an antiferromagnet with no direct overlap between electrons on Mn^{2+} ions but rather the exchange interaction is mediated by the O^{2-} ligands. Usually superexchange interactions are antiferromagnetic (AFM), but ferromagnetic (FM) exchange may occur depending on the orbitals and angles involved. The mechanism by which AFM superexchange interactions are preferred is illustrated in Fig.1.5 and the angle dependence of the superexchange interaction is shown in Fig.1.6. Superexchange pathways are short, usually confined to nearest neighbors, though they may extend to second or third nearest neighbors.

Double exchange

Double exchange is a ferromagnetic exchange interaction which occurs in a system containing magnetic ions that can show mixed valency. Examples of this include compounds containing the Mn ion which can exist in oxidation states Mn^{3+} or Mn^{4+} (e.g. $La_{1-x}Sr_xMnO_3$; $0 \leq x \leq 1$). The mechanism is again explained with reference to Fig.1.4. The e_g electron on Mn^{3+} ion can hop to a neighbouring site only if there is a vacancy there of the same spin (since the hopping is done without spin-flipping). The receiving ion can be the Mn^{4+} ion. From Hund's rule (stated in section 1.1.1) there is a strong exchange interaction between the e_g electron and the three electrons in the t_{2g} level which wants to keep them all aligned. Thus it is energetically more favorable for the e_g electron to hop if the neighbouring ions are ferromagnetically aligned and the system aligns ferromagnetically to save kinetic energy.

RKKY (Ruderman, Kittel, Kasuya and Yoshida) interaction

This is an indirect-exchange mechanism which is mediated by conduction electrons and therefore occurs only in metallic systems. The presence of a localized magnetic moment in a sea of conduction electrons spin-polarizes the conduction electrons and this polarization in turn couples to a neighbouring magnetic moment. This results in coupling of the two moments that are not directly interacting. The RKKY interaction is long range and has an oscillatory dependence on the distance between the magnetic moments. Hence it may be ferromagnetic or antiferromagnetic depending on the separation.

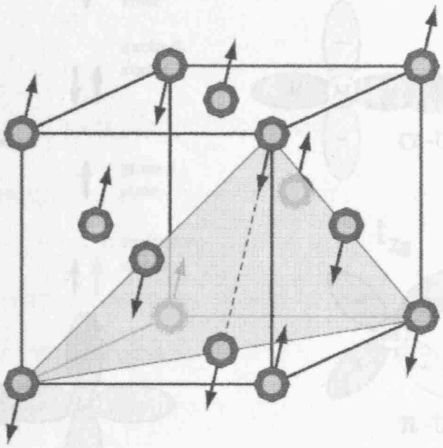

Figure 1.3: The magnetic structure of antiferromagnetic MnO ordered by the superexchange mechanism. The spins are known to lie on the ferromagnetic (111) sheets but their direction within these planes is unknown [10].

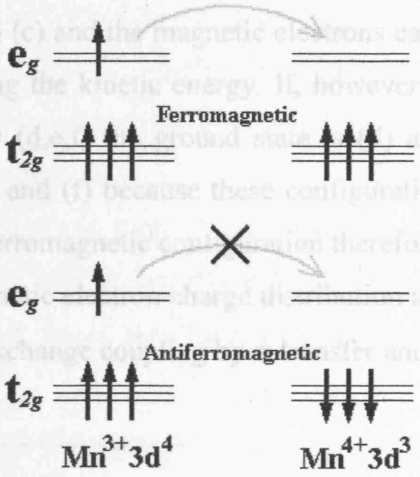

Figure 1.4: Double exchange mechanism giving ferromagnetic coupling between Mn^{3+} and Mn^{4+} ions participating in electron transfer. [2]

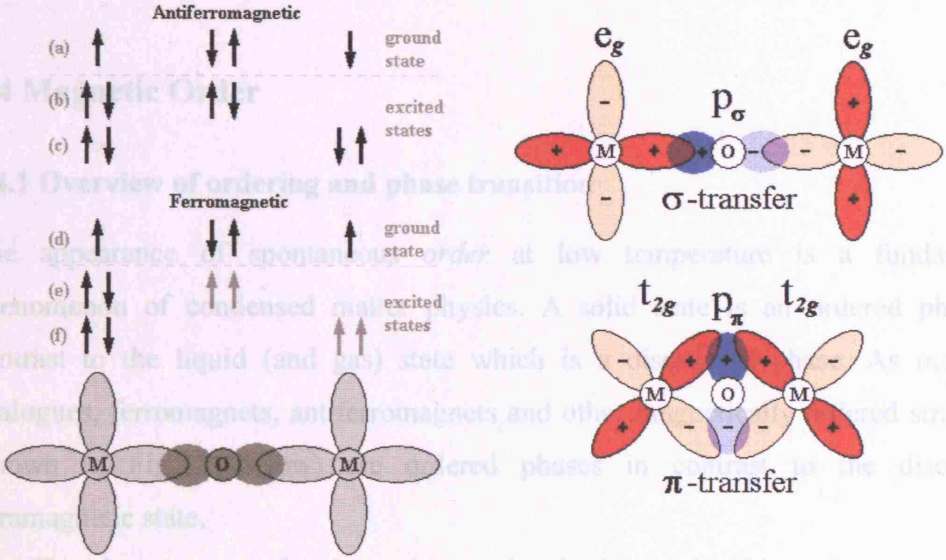

Figure 1.5 (*Left*): Mechanism of superexchange in a magnetic oxide. The magnetic atom M is assumed to have a single unpaired electron. The arrows show spins of the four electrons that are distributed over M and the oxygen atoms. If the moments of Ms are coupled antiferromagnetically (a,b,c) the ground state is (a) and this *can* mix with excited states (b) and (c) and the magnetic electrons can be delocalized over the M-O-M unit, thus lowering the kinetic energy. If, however, the moments of Ms are coupled ferromagnetically (d,e,f) the ground state is (d) and this *cannot* mix with excited configurations (e) and (f) because these configurations are prevented by the exclusion principle. The ferromagnetic configuration therefore costs more energy. [2]

Figure 1.6 (*Right*): Schematic electron charge distribution around interacting cations M and anions O in superexchange coupling by σ-transfer and π-transfer. [1]

1.4 Magnetic Order

1.4.1 Overview of ordering and phase transition

The appearance of spontaneous *order* at low temperature is a fundamental phenomenon of condensed matter physics. A solid state is an ordered phase in contrast to the liquid (and gas) state which is a disordered phase. As magnetic analogues, ferromagnets, antiferromagnets and other magnetically ordered structures (shown in Fig.1.7 below) are ordered phases in contrast to the disordered paramagnetic state.

The phenomenon of *ordering* is associated with the breaking of symmetry. For example, in a liquid-solid transition, the complete translational and rotational symmetries of the liquid is lost upon ordering. This situation is similar in a paramagnet-ferromagnet transition (see Fig.1.9); a paramagnetic state above the Curie temperature T_{Curie} possesses complete rotational symmetry but below T_{Curie} the system 'chooses' a unique direction for all the spins to point. Hence, the higher rotational symmetry (in zero applied field) of the high temperature state is broken. An important point to notice is that it is impossible to change symmetry *gradually*. Either a particular symmetry is present or it is not. Hence, phase transitions that involve symmetry breaking are sharp and there is a clear delineation between ordered and disordered states. (Not all phase transitions involve a change of symmetry. A liquid-gas transition is one example that retains all symmetry after the transition.)

1.4.2 Types of ordered ground states

In this sub-section the common magnetic ground states which result from the magnetic moment interactions will be listed. For an illustrative diagram, see Fig.1.7.

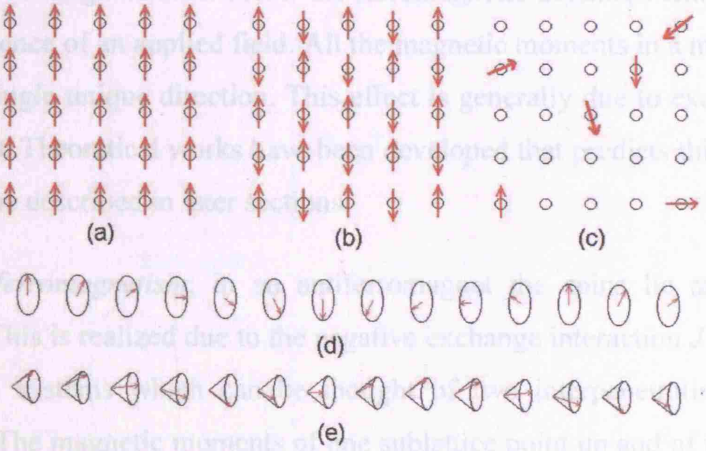

Figure 1.7: Various spin arrangements in ordered systems: (a) ferromagnets, (b) antiferromagnets, (c) spin glasses, (d) spiral and (e) helical structures.

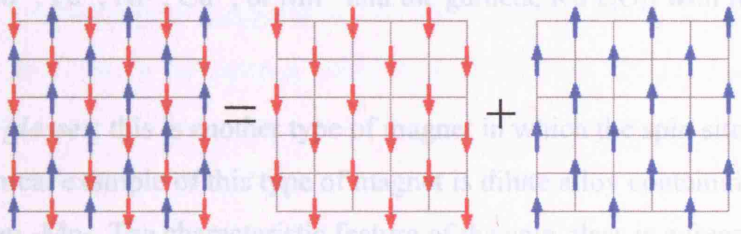

Figure 1.8: Decomposition of an antiferromagnetic lattice into two interpenetrating sublattices with opposite and equivalent magnetizations.

Ferromagnetism: a ferromagnet is characterized by the appearance of a spontaneous magnetization below the ferromagnetic transition temperature (T_C), even in the absence of an applied field. All the magnetic moments in a magnetic domain lie along a single unique direction. This effect is generally due to exchange interactions with $J > 0$. Theoretical works have been developed that predicts this phenomenon and this will be described in later sections.

Antiferromagnetism: in an antiferromagnet the spins lie anti-parallel to one another. This is realized due to the negative exchange interaction $J < 0$. Very often this occurs in systems which can be thought of two interpenetrating sublattices (see Fig.1.8). The magnetic moments of one sublattice point up and of the other sublattice point down.

Ferrimagnetism: when the magnetizations of the two sublattices in the antiferromagnet are not of the same order they will not cancel out and the material will have a net magnetization. This phenomenon is called ferrimagnetism. Important example of ferrimagnets are the ferrites; $MO \cdot Fe_2O_3$ where M is a divalent cation such as Zn^{2+}, Co^{2+}, Fe^{2+}, Ni^{2+}, Cu^{2+}, or Mn^{2+} and the garnets; $R_3Fe_5O_{12}$ with R = trivalent rare earth ion.

Spin glasses: this is another type of magnet in which the spin sites are disordered. The canonical example of this type of magnet is dilute alloy containing magnetic ions such as $Au_{1-x}Mn_x$. The characteristic feature of the spin glass is a freezing transition at T_f in which the system changes from a paramagnet to a history dependent frozen state. The reason for this is the random distribution of the magnetic ions. Locally, clusters of spins can minimize their energies but between clusters are spins which cannot simultaneously minimize their interaction energies with all their neighbors. The frozen state has lead to the name spin glass for these materials.

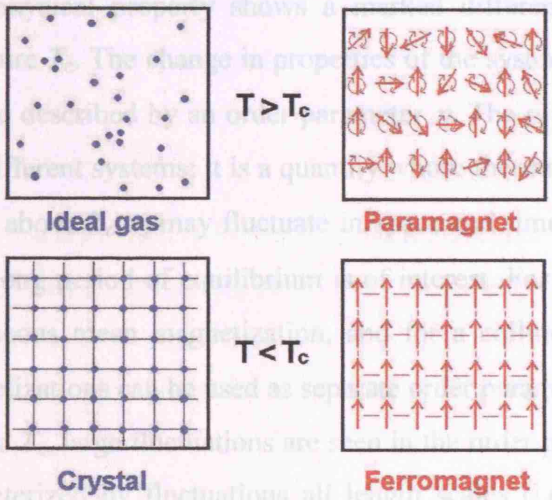

Figure 1.9: Comparison of analogous phase transitions in two systems; (Left) Liquid-solid phase transition, and (Right) Paramagnet-ferromagnet phase transition. The high temperature state (statistically averaged) has complete translational (gas only) and rotational (gas and paramagnet) symmetry, whereas, these symmetries are broken as the system becomes a solid (crystal) or ferromagnet below the critical temperature T_c.

1.4.3 Critical temperature and order parameter

The phenomena of ordering are characterized by a temperature dependence in which some relevant physical property shows a marked difference above and below a critical temperature T_c. The change in properties of the system as the phase boundary is crossed can be described by an order parameter η. The order parameter is defined differently for different systems; it is a quantity whose thermal average is finite below T_c and vanishes above T_c. η may fluctuate in space and time; in general the thermal average over a long period of equilibrium is of interest. For a ferromagnet, η would be the instantaneous mean magnetization, and for a collinear antiferromagnet two sublattice magnetizations can be used as separate order parameters, $\eta_\uparrow$ and $\eta_\downarrow$.

Very near to T_c, large fluctuations are seen in the order parameter and the critical region is characterized by fluctuations all length scales (i.e. the correlation length becomes infinite at T_c).

1.4.4 Correlation function

Another useful parameter that characterizes the ordered phase is a correlation function. For a ordered magnetic system a general correlation function takes the form $\langle \mathbf{S}_i \cdot \mathbf{S}_j \rangle$, where $\langle ... \rangle$ denotes the thermal average. The correlation function shows how closely correlated different parts of an interacting system are. If the spins are non-interacting the correlation function is simply a product of individual spin contributions, i.e. $\langle \mathbf{S}_i \mathbf{S}_j \rangle = \langle \mathbf{S}_i \rangle \langle \mathbf{S}_j \rangle$, with $i \neq j$. For two interacting spins i and j, the two-point (connected) correlation function is written as

$$G_c^{(2)}(i,j) = \langle \mathbf{S}_i \mathbf{S}_j \rangle - \langle \mathbf{S}_i \rangle \langle \mathbf{S}_j \rangle, \tag{1.21}$$

where subtraction term is the contribution due only to correlation of individual spins with themselves.

As the temperature is decreased, thermal fluctuations become less effective at randomizing the spins and correlation due to interactions between spins increases. As T_c is approached from above, firstly, short-range correlations evolve, and on reaching

T_c the correlation length diverges and phase transition occurs. Once $T < T_c$ the system has long range order and the order parameter is finite. Even below T_c the moments continue to fluctuate due to thermal energy. The ordered structure is the time average of the moment distribution. These thermal fluctuations continue to drop as the sample is cooled further towards $T = 0$ and so the order parameter continues to rise.

1.4.5 Order of phase transition

The order of a phase transition (whether it is a structural or magnetic phase transition) is the order of the lowest differential of the free energy which shows a discontinuity at the transition. A first-order phase transition would have a discontinuous jump in the first derivative of the free energy, i.e. in quantities like the volume, entropy and the magnetization;

$$V = \left(\frac{\partial E}{\partial P}\right)_S = \left(\frac{\partial G}{\partial P}\right)_T, S = -\left(\frac{\partial G}{\partial T}\right)_{P,B} = -\left(\frac{\partial A}{\partial T}\right)_{V,M}, M = -\left(\frac{\partial E}{\partial B}\right)_S = -\left(\frac{\partial G}{\partial H}\right)_T. \quad (1.22)$$

A second-order phase transition has a discontinuity in the second derivative of the free energy, i.e. in quantities like the compressibility, susceptibility or the heat capacity.

$$K_S = -\frac{1}{V}\left(\frac{\partial^2 E}{\partial P^2}\right)_S, K_T = -\frac{1}{V}\left(\frac{\partial^2 G}{\partial P^2}\right)_T, \quad C_P = -T\left(\frac{\partial^2 G}{\partial T^2}\right)_P, C_V = -T\left(\frac{\partial^2 A}{\partial T^2}\right)_V \quad (1.23)$$

$$\chi_S = -\left(\frac{\partial^2 E}{\partial B^2}\right)_S, \chi_T = -\left(\frac{\partial^2 G}{\partial H^2}\right)_T, \quad C_B = -T\left(\frac{\partial^2 G}{\partial T^2}\right)_B, C_M = -T\left(\frac{\partial^2 A}{\partial T^2}\right)_M. \quad (1.24)$$

Another way of classifying the order of phase transition is of following Landau; when the order parameter has a discontinuity at the transition it is said to be first-order transition, otherwise it is second-order.

1.4.6 Quantum Phase Transition

The phase transitions we have been considering so far are all driven by temperature. In such phase transitions, it is the thermal fluctuations (whose energy scale is controlled by $k_B T$) which destroy the order as the sample is warmed through its

transition. As a contrast to this thermal phase transition, there is the *quantum phase transition*; another type of phase transition that can occur at $T = 0$. Here, instead of the temperature, other factors (such as pressure, magnetic field or doping level) control the transition. Hence, at some critical value of this variable the quantum phase transition may occur; this is the *quantum critical point*. The relevant fluctuations are no longer thermal but the quantum mechanical fluctuations determined by the Heisenberg's uncertainty principle.

1.5 Magnetic Models

To describe the magnetism of a compound, including the selection of a particular ground state, it is necessary to consider a spin Hamiltonian to determine the energies of microstates of the system. Application of statistical thermodynamics then allows the calculation of properties such as the susceptibility or specific heat, as it was shown for the paramagnetic case in section 1.1.2. In general the energy of a state is determined by the size and type of the moments and exchange interactions with neighbors (and further neighbors). Using this basic form of the spin Hamiltonian, terms may be added to formulate the effects of single ion anisotropy, application of magnetic field or the effect of the dipole-dipole interaction.

The first important choice in constructing a spin Hamiltonian is the nature of the moment. An atomic magnetic moment is an object which is best described by quantum mechanics, allowing contributions from spin and orbital angular momentum (or using g_J to adjust the contributions). However, it is often easier to solve classical problems and in such case quantum spins are replaced by classical vector spins.

Once the energy levels and the anisotropy which determine the behavior of an isolated spin are decided, interactions with other spins are considered to see how they behave collectively. There are different approximations to model this collective behavior and we will introduce some of them below.

1.5.1 Mean field theory

The first approximation available is Mean Field Theory (MFT). The basic assumption of MFT is that the spins interact by an effective molecular or mean field. The strength of the mean field is proportional to the magnetization. MFTs are the simplest type of theory that can be constructed to describe many different types of phase transition and give similar results in each case.

Although the theory is fairly straightforward to solve, it has its weakness. Because MFT ignores correlations and fluctuations which become near T_c it fails to explain the critical region accurately. The assumption that all regions of the sample are the same becomes too crude in this situation. Below we briefly introduce two important models that are constructed using MFT.

Weiss model of ferromagnet/antiferromagnet

This is a mean field theoretical derivation of the Curie law (Eqn.1.11). Here the applied field is augmented by a molecular field $\mathbf{B}_m$ to give an effective field; $\mathbf{B}_{eff}=\mathbf{B}_{app}+\mathbf{B}_m$. The molecular field for a ferromagnet with $J = ½$ and $T_{Curie} \sim 10^3$K is of the order $B_m \sim 1500$ Tesla. This is an enormous effective magnetic field and reflects the strength of the exchange interaction. Because it is assumed that $\mathbf{B}_m$ is proportional to magnetization ($\mathbf{B}_m = \lambda \mathbf{M}$, where λ is the molecular field parameter), the effective field becomes

$$\mathbf{B}_{eff} = \mathbf{B}_{app} + \lambda \mathbf{M}. \qquad (1.25)$$

The problem is treated as if the system were a simple paramagnet placed in a magnetic field $\mathbf{B}_{eff}$. When the model is solved, it predicts a spontaneous magnetization of the ferromagnet that occurs below T_{Curie}. It also predicts the nature of the phase transition between the non-magnetic and ferromagnetic phases to be second-order. The same argument can be applied to model the antiferromagnet by using two separate molecular fields $\mathbf{B}_m^+$ and $\mathbf{B}_m^-$ for each sublattice (magnetic moments pointing up or down). Ultimately this leads to the derivation of the Curie-Weiss Law

$$\chi = \frac{C_{\text{Curie}}}{T - \theta_{\text{CW}}} \tag{1.26}$$

where χ is the susceptibility, C_{Curie} is the Curie constant (defined in section 1.1.2) and θ_{CW} is the correction term called the Curie-Weiss temperature. If $\theta_{\text{CW}} = 0$, the equation simplifies into Curie law and the material is paramagnet. If $\theta_{\text{CW}} > 0$ the material is ferromagnetic and we expect $\theta_{\text{CW}} = T_{\text{Curie}}$. If $\theta_{\text{CW}} < 0$ the material is antiferromagnetic and we expect $\theta_{\text{CW}} = -T_{\text{N}}$, where T_{N} is the Néel temperature.

Landau theory of phase transition

Landau's model that produces a phase transitions is also based on MFT which again assumes that all spins feel an identical average exchange field produced by all their neighbors. In Landau theory, the basic assumption is that near to the critical point the thermodynamic energy functions may be expanded as a Taylor series [11]. For a magnetic system to obtain stability, its Gibbs free energy G should be at its minimum. The thermodynamic function $F(T, M)$ which is the approximation to G is thus expanded in terms of M, the magnetization (or the order parameter) as

$$F(T, M) = F_0 + \alpha_2(T) M^2 + \alpha_4(T) M^4 + \alpha_6(T) M^6 \cdots \tag{1.27}$$

where F_0 is constant and $\alpha_2(T)$, $\alpha_4(T)$, $\alpha_6(T)$.. are temperature dependent factors. Here, depending on how we define the prefactors α_2, α_4, α_6 ... the model changes its behavior as to predict whether the second order or the first order phase transition.

When α_4 and α_6 is set to be constant ($\alpha_4 > 0$ and $\alpha_6 = 0$), and additionally, if $\alpha_2(T)$ is allowed to change sign at the transition temperature T_C, then the model yields an appropriate *second order* phase transition. Near the transition, this $\alpha_2(T)$ takes the form $\alpha_2(T) = \alpha_0(T - T_C)$ where α_0 is a positive constant. When the solution is looked for $\partial F / \partial M = 0$, there emerges two solutions

$$M = 0 \quad \text{or} \quad M = \pm\left[\frac{\alpha_0(T_C - T)}{2\alpha_4}\right]^{1/2}. \tag{1.28}$$

The free energy function $F(T, M)$ for different T and the magnetization curve are

shown in Fig.1.10 and Fig.1.11, respectively. The F - F_0 plots (Fig.1.11 (a) to (c)) clearly show the continuous nature of the transition. Starting from a single minumum at $T > T_C$, as the temperature is lowered the curve flattens ($T = T_C$), gradually producing two minima around the $M = 0$ that moves away from $M = 0$ as the temperature is lowered further ($T < T_C$). The corresponding magnetization (Fig.1.10) is zero for $T \geq T_C$ and is finite and increases proportional to $(T_C - T)^{1/2}$ for $T < T_C$.

On the other hand, Landau theory can also predict the first order phase transition behavior. This is done by considering the free energy as a function of other (non-ordering) fields g (such as anisotropy or a staggered field) and allowing α_4 to depend on g. It is also needed to include the sixth order term $\alpha_6(T)\, M^6$ in the expansion (Eqn.1.27). When $\alpha_4 > 0$ and $\alpha_6 > 0$, the solutions will be the same for case in the second order phase transition (Eqn.1.28). As g is varied α_4 changes, and at a particular point it becomes zero. This point is called the *tricritical* point. This is where the order of the transition changes from second order into first order. Then, when $\alpha_4 < 0$, five new sets of solutions corresponding to three minima and two maxima of the free energy emerges

$$M = 0 \quad \text{or} \quad M^2 = \frac{-\alpha_4}{3\alpha_6}\left[1 \pm \left(1 - \frac{3\alpha_2\alpha_6}{\alpha_4^2}\right)^{1/2}\right]. \tag{1.29}$$

This is again plotted as three isotherms in Fig.1.11 (d) to (f) at different T. At $T > T_C$, the system is paramagnetic and the system is settled at the lowest minimum $M = 0$. At $T = T_C$, the three minima are degenerate and thus represents the coexistance of the paramagnetic state ($M = 0$) and the ordered state ($M \neq 0$). When $T < T_C$ the ordered states gain stability over the paramagnetic state. In this sense the transition is said to be first order with temperature; the order parameter M changes discontinuously at T_C.

This Landau model of first order phase transition also predicts the common characteristic often associated with the first order transition, the existence of hysteresis. This occurs due to the existence of the metastable states at $T > T_C$ that can remain stable for a while above T_C. As a result, the transition is observed at a higher T for heating than for the cooling process.

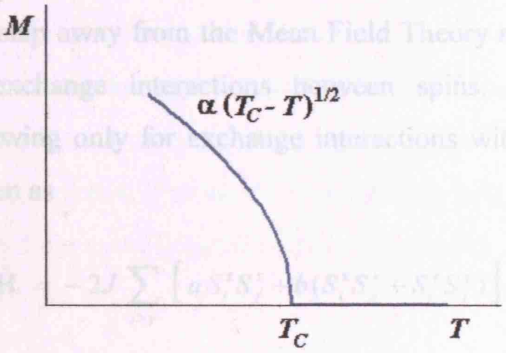

Figure 1.10: Magnetization curve calculated by Landau theory. The 6th order term is neglected in the Taylor expansion and the solution M is found out of $F - F_0 = a(T)\, M^2 + b\, M^4$. It predicts the nature of second order phase transition.

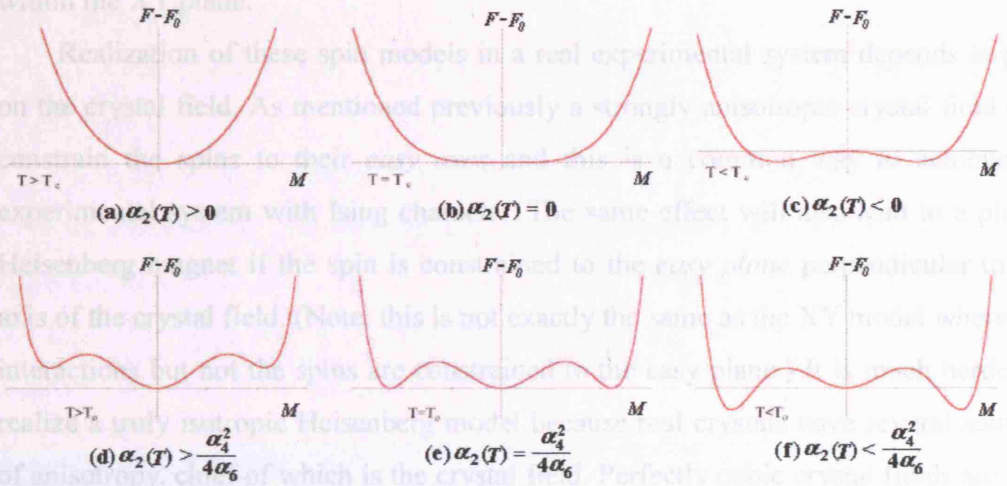

Figure 1.11: Free energy F-F_0 plotted for two separate models that show second order, (a to c), and first order (d to f) phase transition [12]. The transition in the position of the minimum (minima) is continuous in the (a) to (c), whereas is discontinuous in (d) to (f) at T_C.

1.5.2 Heisenberg, XY and Ising models

To take a further step away from the Mean Field Theory requires some microscopic model for the exchange interactions between spins. The simplest interaction Hamiltonians allowing only for exchange interactions with the nearest neighboring spins can be written as

$$\hat{H} = -2J \sum_{i>j} \left[a S_i^z S_j^z + b(S_i^x S_j^x + S_i^y S_j^y) \right] \tag{1.30}$$

where summation is over nearest neighbors only and J is the exchange constant. If $a = b = 1$ the interactions are wholly isotropic, this is known as the *Heisenberg model.* If $a = 1$ and $b = 0$ the *Ising model* is obtained. In this case the spins are one dimensional vectors and are constrained to lie on an axis. They can point only "up" or "down". Exchange is considered only between the z-components of the spins. The third common case is the *XY model* in which $a = 0$ and $b = 1$. XY spins only interact within the XY plane.

Realization of these spin models in a real experimental system depends largely on the crystal field. As mentioned previously a strongly anisotropic crystal field will constrain the spins to their *easy axes* and this is a common way to achieve an experimental system with Ising character. The same effect will also lead to a planar Heisenberg magnet if the spin is constrained to the *easy plane* perpendicular to the axis of the crystal field. (Note: this is not exactly the same as the XY model where the interactions but not the spins are constrained to the easy plane.) It is much harder to realize a truly isotropic Heisenberg model because real crystals have several sources of anisotropy, chief of which is the crystal field. Perfectly cubic crystal fields are rare because a Jahn-Teller distortion is usually favored. The best way to avoid this is to use a "spin-only" ion such as Gd^{3+} ($S = 7/2$, $L = 0$).

These three models have been extensively investigated with the effects of lattice (d) and spin (D) dimensionality being the central themes of investigation. (In general D is known as the dimensionality of the order parameter.) The spins in the Hamiltonian can be represented by both classical or quantum spins for the $D = 2$ (XY

model) and $D = 3$ (Heisenberg model) but for $D = 1$ (Ising model) it should be only classical due to its violation of the uncertainty principle if applied to a quantum spin. As generalizations it can be stated that the $d = 3$ models are all expected to order at finite temperatures and to show quasi-classical behavior. As the lattice dimensionality is decreased and the spin dimensionality is increased the transition to order occurs at lower and lower temperature. For all $d = 1$ models no long range order occurs at any temperature greater than zero (because entropy always favors the formation of defects in $d = 1$ lattice at $T > 0$).

References for Chapter 1

[1] J. Crangle, *Solid State Magnetism*, Van Nostrand Reinford, N.Y. 1991.

[2] S. Blundell, *Magnetism in Condensed Matter*, Oxford University Press Inc.,N.Y. 2001.

[3] H. E. Stanley, *Introduction to Phase Transitions and Critical Phenomena*, Oxford University Press, Oxford, 1971.

[4] C. Kittel, *Introduction to Solid State Physics*, John Wiley and Sons, Inc., Chichester, 1996.

[5] J. J. Binney, N. J. Dowrick, A. J. Fisher, and M. E. J. Newman, *The Theory of Critical Phenomena: An Introduction to the Renormalization Group*, Clarendon, Oxford, 1992.

[6] L. J. de Jongh and A. R. Miedema, *Experiments on Simple Magnetic Model Systems*, Taylor & Francis, London, 1974.

[7] S. T. Bramwell and M.J.P.Gingras, *Science* **294** (5546), 1495 (2001).

[8] H. A. Kramers, koninki.Ned.Akad.Wetenschap., Proc. **B33**, 959 (1930).

[9] H. A. Jahn and E. Teller, Proc.Roy.Soc.**A161**, 220 (1937).

[10] A. L. Goodwin, M. G. Tucker, M. T. Dove and A. D. Keen, Phys. Rev. Lett. **96**, 047209 (2006).

[11] L. D. Landau, Phys. Z. Sowjet. **11**, 26 (1937).

[12] J. D. M. Champion, *Ph.D. Thesis*, Univ. London, 2001.

Chapter 2

Frustrated Magnetism

In the previous chapter, we introduced the basic field of magnetism in order to follow the rest of the thesis. In this chapter, we will be more specific and will try to give a general introduction to the field of *frustrated magnetism*. Starting from the introduction of what frustration is about, we will cover different theoretical magnetic models that exhibit frustration in the first half of this chapter. Then, in the second half, some experimental realizations of frustrated magnets are specifically introduced; these include the frustrated pyrochlore ferromagnets – the *spin ice* materials, and the frustrated pyrochlore antiferromagnets – $Gd_2Ti_2O_7$ and $Er_2Ti_2O_7$ / $Er_2Sn_2O_7$.

2.1 Third Law of Thermodynamics and Zero Point Entropy

The *third law of thermodynamics* states that

> *'The entropy of a pure condensed substance in internal thermodynamic equilibrium should be zero at absolute zero.' (Planck)* [1-2]

suggesting that at absolute zero any system should order into a non-degenerate and unique ground state configuration. Here, entropy S is defined as:

$$S = k_B \ln (W) \qquad (2.1)$$

where W is the microscopic configuration of the system and k_B is the Boltzmann constant. Therefore, at the temperature of absolute zero the system will have to order into a single configuration, i.e. $W = 1$. However, this is not always the possible case. In some systems it is impossible to satisfy all the interactions in the system simultaneously to find a unique ground state. Instead, this leads to a variety of degenerate low energy states in which the dilemma of non-minimization of energies is shared around as much as possible. These systems are said to be *frustrated.* Now, the ground state configuration is not unique, hence W in Eqn.2.1 is now $W \neq 1$, leading to a finite entropy at absolute zero. This is so called the *residual entropy* or the *zero point entropy.* Frustration often induces complex and hence interesting phenomena in condensed matter. For example, frustration is at the origin of the mechanism of protein folding and of the stripe-like structures in cuprate high-temperature superconductors [3]. This is where our interest initiates – the exploration into the phenomena of frustration [3-5]

2.2 Geometrically Frustrated Magnets

As it was introduced above, the concept of frustration in itself extends over a vast field. In this thesis we focus on the frustration exhibited in magnetic systems. Magnetic systems may often serve as ideal experimental testing grounds of generic concepts of collective phenomena in nature. This is due to the wide availability of both experimental materials that can approximate simple theoretical models and experimenting techniques. The phenomenon on frustration is no exception to this, and magnetic crystals provide the simplest stage in which the influence of frustration is investigated.

When frustration arises purely from the geometry or topology of the lattice (rather than due to disorder) these systems are referred as '*geometrically frustrated magnets* (GFM)' [4,11]. GFM materials have been the focus of intense study over the past several years and a number of reviews exist [3-4,7,11-14]. In addition, four specialist conferences, Highly Frustrated Magnetism (HFM), have been held since 2000 – Waterloo-Canada (2000), Santa Fe (2002), Grenoble (2003) and Osaka

(2006). Today, magnetic frustration continues to attract much attention especially due to their propensity to unusual, even exotic magnetic ground states such as spin glass behavior [4,23], noncollinear and incommensurate order [4,24] or ground states with macroscopic degeneracy [4,15-22].

In the rest of this section we will introduce the scaffold of the stage where frustration acts; starting from the basic building blocks of the system, up to the symmetry of the entire lattice. In the following section general insights will be given to the ground states of the frustrated magnets. Then, finally in sections 2.5 and 2.6, two real experimental materials that are directly relevant to our study, $Gd_2Ti_2O_7$ and $Er_2Ti_2O_7$ / $Er_2Sn_2O_7$ will be reviewed in some detail.

2.2.1 Frustrated simplex unit – the plaquettes

Frustrated sublattices can be constructed by the condensation of a basic 'simplex' unit or *plaquette* of q interacting spins. The two canonical examples of plaquettes that are often associated with the phenomena of frustration is the triangular plaquette (q = 3) and the tetrahedral plaquette (q = 4). We will show how frustration arises in such plaquettes considering the Hamiltonian

$$\hat{H} = -J \sum_{<i,j>} \mathbf{S}_i \cdot \mathbf{S}_j \qquad (2.2)$$

where J is the exchange interaction, $\mathbf{S}_i$ and $\mathbf{S}_j$ are spin vectors for spin i and j respectively, and $\langle i,j \rangle$ denotes a sum over all neighbour spins in the lattice. Taking the canonical example of an equilateral triangular plaquette (q = 3), if the nearest neighbour exchange interaction, J_{nn}, is *antiferromagnetic* (i.e. $J_{nn} < 0$) then the energy is minimized for collinear (parallel or antiparallel) spin alignments. This is illustrated in Fig.2.1 (a). Only two of the three spin constraints can be satisfied simultaneously, hence, the system is geometrically frustrated. Frustration is not confined to two dimensions but can also arise for the three dimensional system – this is the case of the tetrahedron, see Fig.2.1 (b). Here the same principle applies for the frustration with $J_{nn} < 0$. Frustration can also be introduced to certain system by considering the next-nearest neighbour exchange, J_{nnn}, in addition to the nearest-neighbour exchange, J_{nn}. This is illustrated for the case in the square lattice

(q = 4) , see Fig.2.1 (c) ~ (e). For the cases where $J_{nn} >> J_{nnn}$ (Fig.2.1 (c)) and $J_{nn} << J_{nnn}$ (Fig.2.1 (d)) the plaquettes are not frustrated. However, for the special case where $J_{nn} = J_{nnn}$ (Fig.2.1 (e)) frustration occurs.

2.2.2 Geometrically frustrated lattices

Lattices formed by the plaquettes (triangles, tetrahedra or others) connected by sharing of corners, edges or faces (in the case of tetrahedra) constitute many real materials. Some examples of frustrated lattices are shown in Fig.2.2.

There are many systems wherein frustrations are observed, both in two dimensional lattice materials as well as in the three dimensional ones. The anhydrous alums, $A^{I}M^{III}(SO_4)_2$ (A^{I} = group I element, M^{III} = trivalent transition metal ion) [25] with perfect edge-sharing equilateral triangle M^{III} lattices and jarosites, $AB_3(SO_4)_2(OH)_6$ (A = Na^+, K^+, Ag^+, Tl^+, NH_4^+, H_3O^+, $^1/_2Pb^{2+}$, or $^1/_2Hg^{2+}$. B = Fe^{3+},Cr^{3+},In^{3+},Al^{3+} or Ga^{3+}) [26] with kagome lattice structure are the two most studied two dimensional frustrated materials.

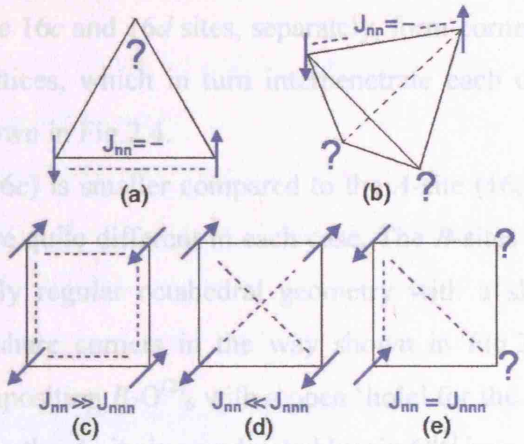

Figure 2.1: Plaquettes with both nearest neighbour and next nearest neighbour exchange interaction, J_{nn} and J_{nnn}, being antiferromagnetic [4]. (a) an equilateral triangle, (b) a tetrahedron, (c) the square plane with $J_{nn} >> J_{nnn}$, (d) square plane with $J_{nn}<<J_{nnn}$, (e) square plane with $J_{nn} = J_{nnn}$. (a), (b) and (e) are frustrated plaquettes, while (c) and (e) are not frustrated.

In this thesis we choose the three dimensional pyrochlore framework as the magnetic system to be investigated. The pyrochlore lattice is made up of corner shared tetrahedra, the vertexes of the tetrahedra corresponding to the 16*c* or 16*d* sites in space group $Fd\bar{3}m$. This is also equivalent to the ..ABCABC... stacking of kagome layers as shown in Fig.2.3. Pyrochlore structures occur in both spinel oxides, AB_2O_4, and pyrochlore structure oxides, $A_2B_2O_7$. We will concentrate only on the $A_2B_2O_7$ materials in this thesis.

2.2.3 $A_2B_2O_7$ pyrochlore oxides

Taking the standard case of the pyrochlore oxide, $A_2B_2O_7$, the *A*-site is commonly occupied by the trivalent rare earth ion (R^{3+}) and the *B*-site by a tetravalent transition metal (B^{4+}). The formula can be written in an alternative way, $A_2O^{(1)}{\cdot}B_2O^{(2)}{}_6$, to illustrate that the lattice actually constitute of two independent sublattices $A_2O^{(1)}$ and $B_2O^{(2)}{}_6$.

As it was mentioned in the previous section, the space group of this rare earth oxide $R_2B_2O_7$ is $Fd\bar{3}m$ with R^{3+} in the 16*d*, B^{4+} in the 16*c*, $O^{(1)}$ in 8*b* and $O^{(2)}$ in 48*f* sites [27]. Both the 16*c* and 16*d* sites, separately, form corner-shared tetrahedral (i.e. pyrochlore) sublattices, which in turn interpenetrate each other to form the actual lattice – this is shown in Fig.2.4.

The *B*-site (16*c*) is smaller compared to the *A*-site (16*d*), thus the coordination around the sites are quite different in each case. The *B*-sites are six-fold coordinated by $O^{(2)}$ in a nearly regular octahedral geometry with a slight trigonal distortion. These octahedra share corners in the way shown in Fig.2.5 (a), forming a rigid framework of composition $B_2O^{(2)}{}_6$ with a open 'hole' for the R^{3+} ion to sit in. In turn, the rare earth ion in the *A*-site is coordinated by six $O^{(2)}$ ions that form a puckered six membered ring and two $O^{(1)}$ ions which form the linear $O^{(1)}$-*R*-$O^{(1)}$ units orientated normal to the average plane of the puckered ring. This coordination is illustrated in Fig.2.5 (b) below. The two $O^{(1)}$ lie at a much shorter distance than the six $O^{(2)}$, producing a strong axial interaction around the rare earth ion. In fact, the single ion symmetry around the rare earth in this coordination is the trigonal $D_{3d}(3m)$, and this gives a huge impact on the chemistry of the rare earth pyrochlore oxides influencing

the single ion properties of the rare earth ion and the crystal field around it.

As mentioned above, the geometry around the *A*-site (16*d*) is very different to that of *B*-site (16*c*). Consequently, the chemistry will be very different depending on the choice of the material; i.e. on which site to make magnetic. There are three possibilities, either the *A*-site or *B*-site atoms being magnetic or both site atoms being so. *B*-site magnetic compounds have been extensively studied for the past years, for example $Y_2Mo_2O_7$ which shows phase transition to a spin glass state at 22K [28], and $Y_2Mn_2O_7$ which show no true long range order despite of being a nearly ferromagnetic insulator. [29] Also, compounds with both *A*-site and *B*-site occupied by magnetic ions have been widely studied, represented by the $R_2Mn_2O_7$ and $R_2Mo_2O_7$ materials (*R* = trivalent rare earth ions, except Y^{3+}) [8-9]. $R_2Mo_2O_7$ molybdates show metal-insulator transition as a function of R, the rare earth ion. (*R* = Gd is a correlated ferromagnetic metal and R = Tb is a small activation energy semiconductor) [9-10]. We will mainly focus on the A-site materials, $R_2B_2O_7$ (R^{3+} = magnetic rare earth ion, B^{4+} = non-magnetic transition metal ion) in this thesis.

2.2.4 Measure for magnetic frustration

In a magnetic system without frustration, the susceptibility curve strongly deviates from its Curie-Weiss form (see Eqn 1.1.5.1) around $T \sim |\theta_{cw}|$ and the system goes into a long range ordered (LRO) state near $|\theta_{cw}|$. For a ferromagnetic order this is true and $|\theta_{cw}|/T$ is of the order of ~ 1. For an antiferromagnetic order the situation is not as simple and the ratio depends on the exact magnetic structure. Although in general, for non-frustrated lattices, $|\theta_{cw}|/T$ takes the value between 2 to 5. An arbitrary condition, $|\theta_{cw}|/T > 10$ is proposed to be the indication of the system being frustrated [11]. In the absence of frustration, one can determine whether a magnetic system shows LRO or not by simply considering the spin and lattice dimensionality (refer to previous section 1.1.5.2). The presence of frustration complicates this general scenario, giving rise to many exotic ground states; this will be discussed in the following section.

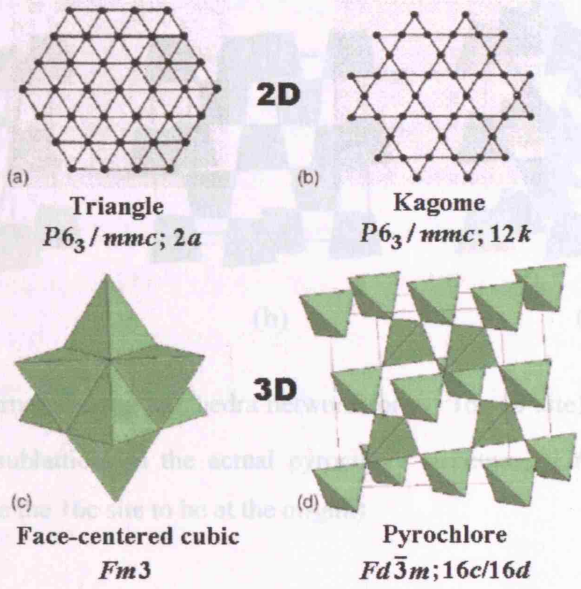

Figure 2.2: Some common geometrically frustrated lattices with their specialized name, their space group and the sites occupied by the magnetic atoms [4,7]. (a) and (c) are lattices formed by edge-sharing plaquettes, and (b) and (d) are lattice formed by corner-sharing plaquettes.

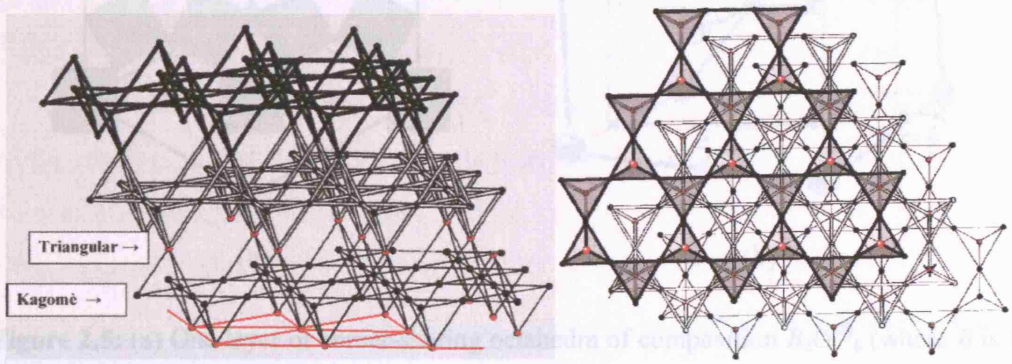

(a) (b)

Figure 2.3: The pyrochlore lattice represented in terms of kagome layers and interstitial atoms. The two different atom sites are distinguished by their colors; the black atoms constitute the kagome layers and the interstitial red atoms lie in between the kagome layers, forming open triangular lattices with triangle edge length doubled compared to that of the kagome layers [4]. (a) View normal to the stacking direction. (b) View along the stacking direction [111] of the cubic pyrochlore cell.

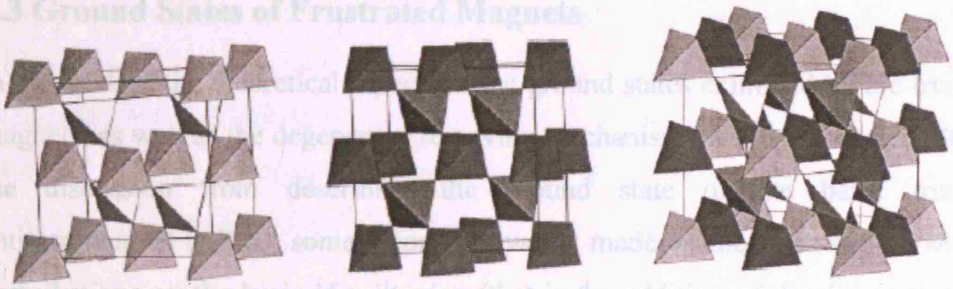

(a) (b) (c)

Figure 2.4: The corner sharing tetrahedra network for (a) 16*c* (*B*-site), (b) 16*d* (*A*-site) and (c) the combined sublattices in the actual pyrochlore structure, $Fd\bar{3}m$ of $A_2B_2O_7$. (It is customary to choose the 16c site to be at the origin.)

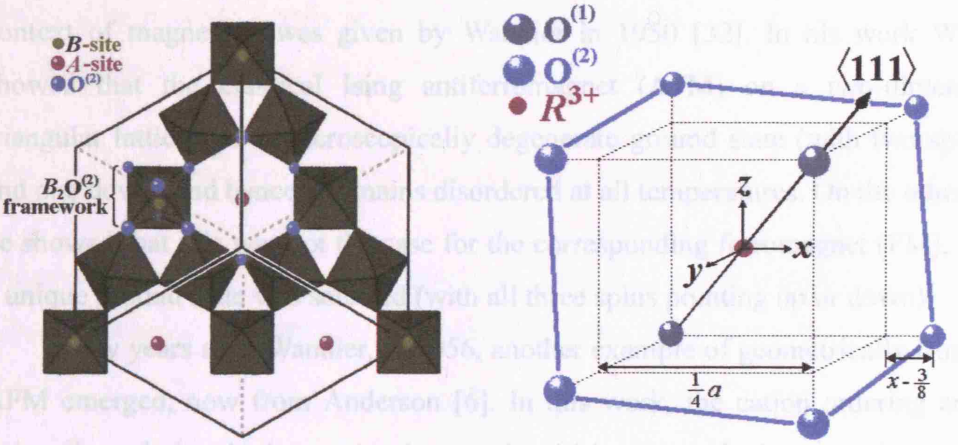

(a) (b)

Figure 2.5: (a) One layer of corner-sharing octahedra of composition $B_2O^{(2)}{}_6$ (where *B* is the *B*-site ion at 16*c* site of $Fd\bar{3}m$) viewed normal to the [111] direction in the $A_2B_2O_7$ pyrochlore structure. The rare earth ions (shown as the A-site ion, in purple) reside in the large hexagonal cavities.[4] (b) Eight-fold coordination around the *A*-site (16*d*) ion (the trivalent rare earth ion, R^{3+}) in $A_2B_2O_7$. The dark blue spheres are the $O^{(1)}$ (8*b*) ions at a short distance of ~2.2Å and the light blue spheres $O^{(2)}$ (48*f*) ions form the puckered six-membered ring at a longer distance of ~2.6Å. The resulting crystal field exerted onto the central R^{3+} ion has a trigonal D_{3d} symmetry [30-31].

2.3 Ground States of Frustrated Magnets

In this section the theoretical aspects of the ground states exhibited by the frustrated magnets, as well as the degeneracy removing mechanisms will be discussed. Starting the discussion from describing the ground state of the basic frustrated antiferromagnet (AFM), some theoretical works made on the frustrated AFMs with perturbations on the basic Hamiltonian (that is the addition of dipolar or single ion anisotropy term) will be introduced in the subsequent subsections. The ground state of the frustrated ferromagnet will be introduced as a separate topic in a following section, section 2.4.

2.3.1 Frustrated antiferromagnet

The first example in which the phenomenon of frustration was considered in the context of magnetism was given by Wannier in 1950 [32]. In his work Wannier showed that the classical Ising antiferromagnet (AFM) on a two-dimensional triangular lattice has a macroscopically degenerate ground state (with two spins up and one down) and hence it remains disordered at all temperatures. On the other hand, he showed that this was not the case for the corresponding ferromagnet (FM), where a unique ground state was selected (with all three spins pointing up or down).

A few years after Wannier, in 1956, another example of geometrically frustrated AFM emerged, now from Anderson [6]. In this work, the cation ordering and the magnetic ordering in inverse and normal spinels, respectively, were investigated. Both of these models map onto the pyrochlore antiferromagnetic Ising model and the ground states are shown to be disordered. One point to note about this model is that it is a rather unphysical model that breaks the cubic symmetry of the pyrochlore lattice and hence there exists no example of real material that realizes it. When dealing with the Ising spins on a pyrochlore lattice one needs to take the $\langle 111 \rangle$ axes as the *local* easy axes in order to be compatible with the local point symmetry of the cubic crystal structure.

The ground state of a more realistic frustrated AFM for a lattice consisting of corner-sharing plaquettes was reviewed by Villain in 1970, 20 years after Anderson

[6]. This became a first detailed study made on the pyrochlore Heisenberg AFM and hence it serves as the starting reference when dealing with this system. According to Villain, the state in which the energy of the individual plaquette (triangle or tetrahedra) is minimized is also a ground state for the whole system. This means that only the local plaquettes are frustrated and there is no increase in the local frustration when this is extended to an entire lattice. This is briefly shown in the subsection below.

Starting with this Villain's argument [15], we will follow how the ground state of the geometrically frustrated AFM is examined. Insight will then be made into theoretical work done on two main specific cases; the Heisenberg kagome and pyrochlore AFMs.

Ground state of a single plaquette [15]

Considering first the energy on a single plaquette of q interacting Heisenberg spins, the Hamiltonian is written as

$$\hat{\mathrm{H}} = \frac{|J|}{2}\sum_{i,j=1}^{q}\mathbf{S}_i\cdot\mathbf{S}_j = \frac{|J|}{2}\left[\left(\sum_{i=1}^{q}S_i\right)^2 - \sum_{i=1}^{q}\mathbf{S}_i\cdot\mathbf{S}_i\right] = \frac{|J|}{2}\left[\left(\sum_{i=1}^{q}\mathbf{S}_i\right)^2 - q\right], \tag{2.3}$$

where the sum is over all bonds twice, and therefore there is a factor of a half [17]. Since the term $-q$ is a constant the condition in order to minimize the energy will be

$$\left(\sum_{i=1}^{q}\mathbf{S}_i\right)^2 = 0. \tag{2.4}$$

Therefore, the q interacting spins on a plaquette should sum up to zero. This argument can be extended to the whole lattice in the similar manner [15, 17]. For a lattice of corner-sharing plaquettes such as the kagomé lattice (corner-sharing triangle) or the pyrochlore lattice (corner-sharing tetrahedra), there are $2N/q$ units and the Hamiltonian for the whole lattice will take the form

$$\hat{\mathrm{H}} = \sum_{\alpha=1}^{2N/q}\frac{|J|}{2}\left[\left(\sum_{i=1}^{q}\mathbf{S}_i^{\alpha}\right)^2 - q\right] \tag{2.5}$$

that is very similar to the Hamiltonian for the single plaquette (Eqn.2.2) and same

conditions are required in order to minimize its energy. Here N is the total numbers of spins in the system.

Constraints and dimensions of ground state manifold

The concept of constraint (that determines the ground state of the individual plaquette) together with the number of degrees of freedom of the system is directly linked to the idea of frustration. If a system is fully constrained, therefore, if no degree of freedom is left in the system, the system will be able to choose a unique ground state. On the other hand, if the number of degrees of freedom exceeds the number of constraints in the system, the system is underconstrained and will be unable to specify a unique ground state. The system is then said to be frustrated.

The degeneracy (or dimension) of the ground states D can be demonstrated using a simple Maxwellian counting argument [16-17]. Taking n-component classical vector spins $\mathbf{S}_i$ with $|\mathbf{S}_i| = 1$ residing at q-sites within a plaquette as the starting point, one should evaluate the degrees of freedom F and the constraint K of the system. The degrees of freedom of the system is expressed as $F = N(n-1)q/B$ where N is the number of units comprising the system and B is the numbers of plaquettes sharing a site. (i.e. $B = 2$ for kagome and pyrochlore lattices formed by corner-sharing plaquettes and $B = 6$ for the triangular lattice formed by edge-sharing plaquettes.) To ensure the antiferromagnetic ground state condition $\Sigma^{q}_{i=1}\mathbf{S}_i = 0$, there should be $K = Nn$ constraints [16]. For example, for Heisenberg AFM ($n = 3$) there are three different constraints per plaquette:

$$\sum_{i=1}^{q} S_i^x = 0, \quad \sum_{i=1}^{q} S_i^y = 0, \quad \sum_{i=1}^{q} S_i^z = 0, \tag{2.6}$$

and hence $K = 3N$ for the entire system. Only when the constraints are independent (which often it turns out not to be the case), the dimension of the ground state manifold can be calculated using the simple equation $D = F - K$. Out of the physically realizable cases ($q \leq 4$, $n \leq 3$), only the Heisenberg pyrochlore AFM system ($q = 4$, $n = 3$, $B = 2$) gives positive and extensive D; $D = N$. This is why the system is interesting to investigate. On the other hand, Heisenberg ($n = 3$) AFM systems with $q = 3$ give rise to $D \leq 0$ when the constraints are all independent. This

should be the case for the non-frustrated Heisenberg AFM on a triangular lattice consisting of *edge-sharing* triangles which has a *unique* ground state ($q = 3$, $n = 3$, $B = 6$, $D = -2N$). This unique ground state spin arrangement is shown in Fig.2.7(a). However, the Heisenberg AFM on a kagome lattice ($q = 3$, $n = 3$, $B = 2$, $D = 0$) which consists of *corner-sharing* triangles has a different scenario. In this system the constraints are *not* all independent and as a result it does not choose a unique ground state. Instead, the degeneracy of the ground state manifold of the kagome Heisenberg AFM is macroscopic [16].

The effect of constraints on Heisenberg AFMs can also be viewed from another angle using a schematic picture (Fig.2.6), where the two continuously varying degrees of freedom α and ϕ remaining for the $q = 4$ case is shown as the origin of extensive ground states [18,21].

Heisenberg spins on the kagome lattice: $q = 3$, $n = 3$, $B = 2$, $D = 0$

The three Heisenberg spins on the triangular plaquette with antiferromagnetic interactions between them are constrained to lie in a plane, mutually oriented at 120° to another (see Fig.2.6) and there are no degrees of freedom left in this unit. However, when this triangular plaquettes are tiled to form a kagomé lattice, many ways of fitting these planar units together arise since not all spins necessarily need to be coplanar. The ground state therefore becomes macroscopically degenerate [19].

Out of these macroscopic ground states (including both coplanar as well as non-coplanar spin arrangements), thermal fluctuation cause the spins to select ground states in which all the spins are coplanar [19]. This coplanar ground state still retains a large number of degeneracies, since there are both *disordered* coplanar states as well as special *long-range ordered* (LRO) coplanar states within it [19]. The two LRO coplanar states of the Heisenberg kagomé AFM ($\mathbf{k} = 000$ and $\sqrt{3} \times \sqrt{3}$ structures) are shown in Fig.2.7 (b)(c). The selection of the coplanar states at finite temperature $T = 0^+$ is an example of the *order by disorder* mechanism – we will refer back to it in section 2.3.2.

A good realization of an experimental kagome system is the jarosite series $AB_3(SO_4)_2(OH)_6$ (where $A = Na^+$, K^+, Rb^+, Ag^+, Tl^+, NH_4^+, $1/2Pb^{2+}$ $1/2Hg^{2+}$, H_3O^+; B

= Fe^{3+}, Cr^{3+}, In^{3+}, Al^{3+}, Ga^{3+},V^{3+})[19-20]. A universality is retained in the ordering of the series; they all show **k** = 000 ordering (when ordered)[20]. Both quantum and classical calculations predict that the **k** = $\sqrt{3}\times\sqrt{3}$ ordering is favored over the **k** = 000 state and hence the spin ordering of the jarosite series contradict the theoretical predictions [18, 20].

Heisenberg spins on the pyrochlore lattice: $q = 4$, $n = 3$, $B = 2$, $D = N$

It is long since the ground state of the AFMs on the pyrochlore lattice was suggested to be macroscopically degenerate [6,15]. Out of this vast ground state, some special submanifolds were picked and investigated. One of this is the four-sublattice state, in which the four spins of each tetrahedron are arranged to be oriented the same way everywhere [15]. In this special set of manifold, any four-spin arrangement that satisfies the ground state condition for the single tetrahedron, $\Sigma^{q}_{i=1}\mathbf{S}_i = 0$, can be repeated periodically through the lattice to yield the ground state for the entire system [21]. One example of this submanifold was investigated by Villain in which the spins of each tetrahedron form two antiparallel pairs [15]. There are infinite ways this configuration can be achieved and hence the ground state degeneracy becomes extensive. Here it originates the name given to the classical Heisenberg pyrochlore AFM; the *cooperative paramagnet* [15]. In 1991-1992, Reimers *et al.* carried out a mean field calculation [17] and Monte Carlo simulations [22] on classical Heisenberg spins residing on a pyrochlore lattice with $J_{nn} < 0$ and demonstrated the absence of long-range order. Following Reimers' work, a fuller investigation of the complete picture of the ground state was carried out by Moessner *et al.* in 1998 [16,21]. They showed that the ground state manifold is 'fully connected', meaning that any ground state can be deformed into any other ground state without an energy cost. Also, their Monte Carlo simulations have shown there to be no order by disorder [16,21]. Thus no ordering or freezing of the spins is observed in any calculation or simulation, and the system is never expected to show static Néel order even at $T = 0$ K [15-16, 21-22]. Calculations on a similar quantum system show no ordering either, and the system is said to be a quantum *spin liquid* [33-34].

$Gd_2Ti_2O_7$ has been proposed as a possible experimental realisation of a classical

spin liquid since Gd^{3+} ions can best approximate the Heisenberg spins having $L = 0$. However, the system shows ordering at a finite temperature [35]. The previous efforts made to find out the nature of this discrepancy will be summarized later in section 2.5. In Chapter 9 we will discuss about the field induced phases of $Gd_2Ti_2O_7$.

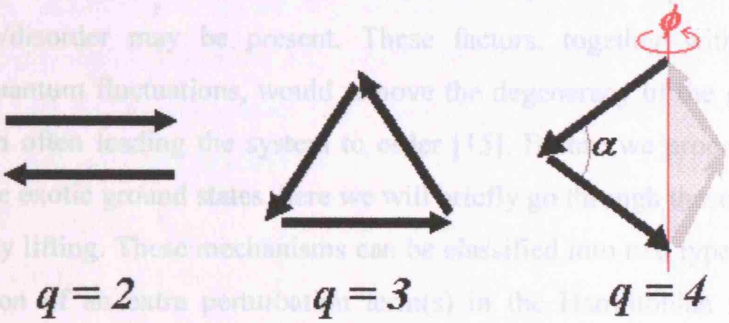

Figure 2.6: Continuous spins on $q = 2$, 3 and 4 spin units satisfying the condition $\Sigma^{q}_{i=1}\mathbf{S}_i = 0$, the antiferromagnetic ground state. The grey pair of spins in the $q = 4$ unit is rotated into the plane by an angle ϕ. The four spins have two continuous degrees of freedom α and ϕ meaning that the ground state of this unit is degenerate. The mutually independent constraints $\Sigma^{q}_{i=1}\mathbf{S}_i = 0$ are not sufficient to specify a unique ground state in this $q = 4$ unit [18, 21].

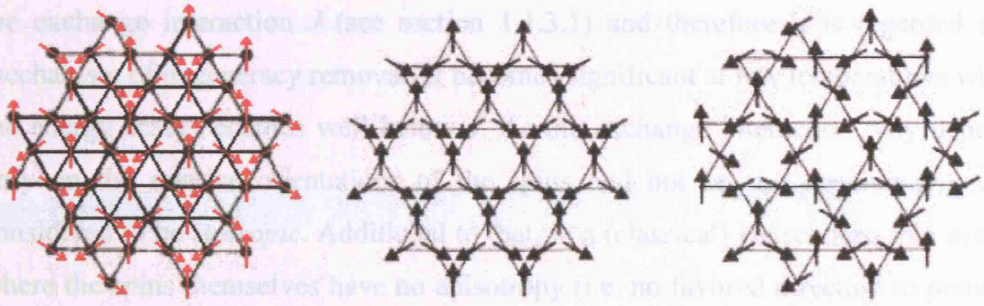

(a) Unique ground state of triangular lattice

(b) One of LRO ground states of kagomé lattice; $\mathbf{q} = 0$

(c) One of LRO ground states of kagomé lattice; $\mathbf{q} = \sqrt{3} \times \sqrt{3}$

Figure 2.7: The ordered antiferromagnetic ground states for (a) the triangular lattice formed by edge-sharing triangle plaquettes, and (b) and (c) for the kagome lattice with propagation vector $\mathbf{q} = 0$ and $\mathbf{q} = \sqrt{3} \times \sqrt{3}$, respectively [4].

2.3.2 Mechanisms of degeneracy removal

Classical models with only nearest-neighbor exchange interaction are often not sufficient to explain all the low-temperature properties of some frustrated magnets. In real materials, several other weak interactions (such as dipole interactions) or impurities/disorder may be present. These factors, together with the effect of thermal/quantum fluctuations, would remove the degeneracy of the ground states of the system often leading the system to order [15]. Before we proceed to introduce some more exotic ground states, here we will briefly go through these mechanisms of degeneracy lifting. These mechanisms can be classified into two types; the first is by the addition of an extra perturbation term(s) in the Hamiltonian and the second mechanism is a fluctuation-induced collective effect called '*order by disorder*'.

Adding extra terms in Hamiltonian

There are many different terms that can be added to the basic Hamiltonian consisting only of nearest-neighbor exchange interaction. These additional terms include; further neighbor exchange, magnetic dipole interaction, external magnetic field or single ion anisotropy.

The magnetic dipole interaction, D_{dd}, is an ordinarily weaker interaction than the exchange interaction J (see section 1.1.3.1) and therefore it is regarded as a mechanism of degeneracy removal. It becomes significant at low temperatures where the energy scale becomes well below J. As the exchange interaction only depends only on the relative orientations of the spins and not on the position ($\mathbf{r}_i$), it is considered to be *isotropic*. Additional to that, in a (classical) Heisenberg spin system where the spins themselves have no anisotropy (i.e. no favored direction to point at) the system is thought to be completely isotropic. The addition of the dipolar interaction thus adds anisotropy to the system, breaking the high symmetry of the system. The long-ranged and anisotropic nature of the dipolar interaction therefore makes it particularly effective in removing degeneracy of the ground state. The specific example of the Heisenberg pyrochlore antiferromagnet with dipole

interaction will be introduced in the following section, section 2.3.3.

Single ion anisotropy is another important perturbation to the Hamiltonian that often leads to the removal of the ground state degeneracy. Refer to section 1.5.2 for how the anisotropy of the spin is defined. There are mainly two types of anisotropy defined in the literature; these are the Ising and XY-type anisotropies. For the Ising system, the anisotropy is effectively infinite and the spins lie along a unique or defined set of *easy-axis*. For the XY system, the anisotropy is finite and the spins are confined to lie on the *easy-plane*. The effect of the finite single ion anisotropy may be incorporated into the Hamiltonian by adding an anisotropy term as follows:

$$\hat{H} = -J\sum_{<i,j>}\mathbf{S}_i\cdot\mathbf{S}_j - D\sum_i(\mathbf{S}_i\cdot\hat{\mathbf{n}}_i)^2 \qquad (2.7)$$

where D is the anisotropy constant and $\hat{\mathbf{n}}_i$ for each spin lie parallel to the four local $\langle 111\rangle$ axes. This is a general form of a Hamiltonian that is employed to define a *local* (i.e. site-dependent) anisotropy and differs from the form

$$\hat{H} = -2J\sum_{i>j}\left[aS_i^zS_j^z + b(S_i^xS_j^x + S_i^yS_j^y)\right] \qquad (2.8)$$

in the sense that the later defines an unique global anisotropy applied to every site. If there is an influence of the crystal electric field (CEF) that confines the spins to lie strictly parallel to the easy axes ($\hat{\mathbf{n}}_i$) then $D = \infty$ and there should not be any canting of spins away from $\hat{\mathbf{n}}_i$. However, when D is finite and positive, $\mathbf{S}_i$ should lie parallel or antiparallel to $\hat{\mathbf{n}}_i$ in order to lower its energy and depending on the strength of D, the spins are allowed to cant away from $\hat{\mathbf{n}}_i$ (in other words this is a system with easy axes with some canting flexibility). On the other hand when D is finite and negative, $\mathbf{S}_i$ is made to lie perpendicular to $\hat{\mathbf{n}}_i$ (this is a system with spins confined to the easy planes with some allowance for the spins to cant away from the easy planes). Therefore, the magnitude of D is a measure for how strongly the spins are related to the local $\hat{\mathbf{n}}_i$ axes, in contrast to J, which is the measure for how strongly the spins are related to each other.

Order by disorder

In Villain's early work [15], thermal fluctuations are cited as a possible degeneracy removing mechanism. This phenomenon is called 'order by disorder (OBD)' and is associated with the existence of the soft (quartic) fluctuations in the system [2,16,19] that cause a selection of a particular ground state at a small but finite temperature $T = 0^+$. We will start with describing what these soft fluctuations are.

In section 2.3.1 we have talked about the constraints imposed on the system. For a AFM with Heisenberg spins on a plaquette with q-sites, these were the three constraints $\Sigma_{i=1}^{q} S_{iv} = 0$ ($v = x,y,z$). The energy of such system as a function of its position in phase space can be considered in terms of the Hamiltonian expanded in a Taylor series

$$H(x) = H_0 + dH/dx\big|_{x=x_0}(x-x_0) + 1/2\, d^2H/dx^2\big|_{x=x_0}(x-x_0)^2 + \ldots.$$

where x is the single phase space variable and the expansion is made around $x = x_0$ where the constraint is satisfied. The minimum in energy H_0 occurs at $x = x_0$ and the constraint give rise to an harmonic restoring force for displacement from $x = x_0$. When the constraints are imposed in a linear way, the first term in the Taylor expansion becomes quadratic, and the low temperature fluctuation of the system may be expressed by a quadratic potential [2,16]. This is shown in Fig.2.8 (a).

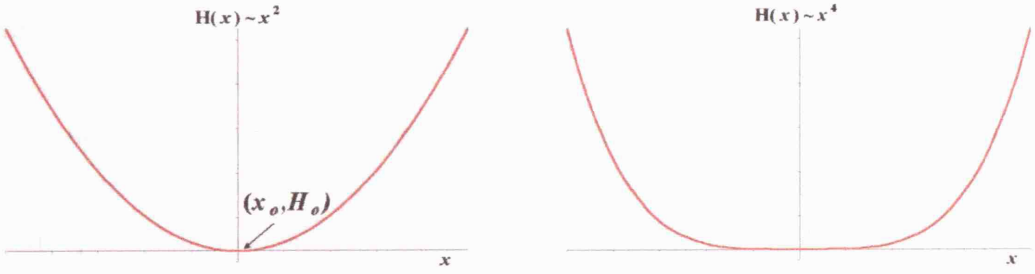

(a) Quadratic potential. (b) Quartic potential.

Figure 2.8: Energy of a system expanded in a Taylor series as a function of position, x, in phase space. The system in a quartic potential can fluctuate further from the ground state for a fixed energy excitation than in the quadratic potential; thus is associated with the soft

fluctuations (*soft modes*).

There exist two types of what we call the 'zero modes'. The first is the true zero mode that arises from the unconstrained degrees of freedom (see section 2.3.1). The second, more generally called the 'soft modes' (since they are not true zero modes), are the soft fluctuations we are more concerned. In some systems, at some *special* points on the energy surface, the constraints are imposed in a non-linear way. The leading term in the Taylor expansion then becomes quartic. This quartic potential is shown in Fig.2.8 (b). In contrast to the quadratic potential, the energy cost for the displacement out of $x = x_0$ is effectively zero for small x in the quartic potential. The existence of these quartic modes in the system can be examined by calculating the normal modes of the system associated with different ground states [2]. From the two potential curves in Fig.2.8, one can see that the system in a quartic potential can fluctuate further from the ground state for a fixed energy excitation. This in turn means that the system in a quartic potential has a higher entropy associated with it.

In a system with a macroscopically degenerate ground state, the ground state manifold contains both ordered and disordered states. Thermal fluctuations allow the system to sample all these ground states. Within this process, anomalous soft fluctuations sometimes occur out of a particular ground state. Remarkably, it is often the case that there are more of the soft and excitable states associated with the ordered ground states than with the disordered states and thus the ordered states have entropic advantage. Eventually, when the entropy gained by making these soft fluctuations dominates the entropy associated with the exploration of the ground states, the system will choose to spend all of its time in these states [2,16]. Because the existence of these soft quartic modes is associated with the collective behavior of all the spins in the system, often this leads to a long-range ordering of the spins. This degeneracy removal by OBD mechanism is observed in the coplanar ordering of the spins in the kagome Heisenberg AFM [19] and in the nematic ordering of spins in the XY pyrochlore AFM [21].

2.3.3 Heisenberg pyrochlore antiferromagnet with dipole interaction

The effect of introducing dipolar interactions to the Hamiltonian of the classical Heisenberg pyrochlore antiferromagnet was considered by Raju *et.al* [35] in 1999. Following the lines of Reimers, Berlinskly and Shi [36], Raju carried out a mean-field analysis for the classical spin model of $Gd_2Ti_2O_7$, a possible realization of Heisenberg pyrochlore antiferromagnet. This involved mean-field calculations expressed as a Landau expression of the free energy and taken to *quadratic* order. The Hamiltonian considered was in the form

$$\hat{H} = \frac{1}{2}\sum_{(i,j)} -J_{ij}\mathbf{S}_i \cdot \mathbf{S}_j + \frac{1}{2}\sum_{(i,j)}\left(\frac{\boldsymbol{\mu}_i \cdot \boldsymbol{\mu}_j}{r_{ij}^3} - 3\frac{\boldsymbol{\mu}_i \cdot \mathbf{r}_{ij}\, \mathbf{r}_{ij} \cdot \boldsymbol{\mu}_j}{r_{ij}^5}\right). \qquad (2.9)$$

First, the effect of the inclusion of further–neighbor exchange (J_2 and J_3) with dipole interaction strength $D_{dd} = 0$ was investigated and as a result, long-range order with various incommensurate and commensurate wave vectors was observed for all cases except for $J_2 \equiv 0$ and $J_3 \leq 0$. Then, from experimental measurements, Raju estimated the nearest-neighbor dipole-dipole interaction of Gd^{3+} ions to be $D_{dd} = \mu_{Gd}^2 \mu_B^2 \mu_0 / (4\pi r_{nn}^3) \approx 0.84$ K (where $\mu_{Gd} = 7.94\ \mu_B$ and μ_0 is the magnetic permeability) and the effective classical nearest-neighbor exchange to be $J_1^{cl} = 3\theta_{CW}/z \sim -4.8$ K ($z = 6$ is the number of nearest neighbor) [2]. This led him to use the ratio $D_{dd}/J_1 = 0.2$, a significant perturbation beyond the nearest-neighbor Heisenberg exchange interaction in his mean-field calculation. In this calculation, the inclusion of dipole interaction did not result in the complete removal of degeneracy but the degeneracy remained in the form of '*degeneration line*' along the $\mathbf{q}^* = [111]$ (See Fig. 2.9) [35]. Often, these kind of degeneracies are known to be removed further by thermal or quantum fluctuations (order-by-disorder) and Raju suggested the operation of this mechanism to induce order in the $Gd_2Ti_2O_7$.

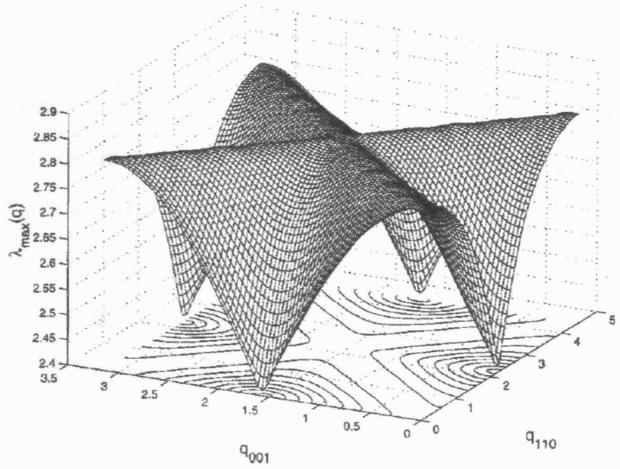

Figure 2.9: A result from a mean-field calculation for the Heisenberg pyrochlore antiferromagnet with $D_{dd}/J_1 = 0.2$ and $J_2 = J_3 = 0$ performed by Raju *et al.* [35].The largest eigenvalue $\lambda_{max}(\mathbf{q})$ is plotted as a function of wave vector **q**. The '*degeneration line*' occurs for **q** in the star of the [111] direction below the mean-field critical temperature, T_c, showing the reduction of degeneracy compared to the '*degeneration zone*' predicted for the $D_{dd} = 0$, $J_1 \leq 0$ ($J_2 = J_3 = 0$) case [35-36].

Following Raju's work, Palmer and Chalker (2000) investigated further into the effect of long-range dipolar interaction on the low temperature state of Heisenberg pyrochlore antiferromagnet [37]. Firstly, the ground states for the spins residing on a single tetrahedron were searched. The results are shown in Fig. 2.10. In these ground state configurations, the spins are coplanar and are parallel to certain edges of the tetrahedron. This set of ground state is a subset of the larger ground state for spins interacting via J_1 only ($D_{dd} = 0$), which is determined by the condition $\Sigma^{q}_{i=1}\mathbf{S}_i = 0$. Therefore, the dipolar interaction acts to fix the internal degrees of freedom of the system. It is however not enough to use the single tetrahedron when considering the dipolar interaction that is long-ranged in nature. The case for the full pyrochlore lattice was then considered using only the nearest-neighbor exchange, J_1, and long-range dipolar interaction, D_{dd}. The authors performed a set of mean-field calculations similar to that of Raju, but in two levels of approximations; considering up to the *quadratic* term or up to the *quartic* term of the free energy expansion. The authors discovered a critical ratio $D_{dd} / J_1 = R_c \sim 5.7$ which separates the behavior of

the system. For the calculations with quadratic term, in the range $D_{dd} / J_1 < R_c$ the 'degeneration line' along $\mathbf{q}^* = [111]$ was recovered but for $D_{dd} / J_1 > R_c$ a non-coplanar incommensurate order emerged below the mean-field critical temperature, T_c. When the quartic term in the free energy expansion is included in the calculation, for the range $D_{dd} / J_1 < R_c$, this lifts the degeneracy of the degeneration line and the system acquires $\mathbf{q} = 0$ long-range order below T_c. This ordering pattern is coplanar and is a four-sublattice Néel state (see Fig. 2.10 (b)), which in turn happens to be a lattice constructed by tiling the ground state configurations derived for the single tetrahedron (Fig. 2.10 (a)). The stability of this ground state was tested against low-temperature fluctuations and it was shown that all distortions have a positive-energy cost, and therefore, the ordering in this model has an energetic origin and is not an example of order-by-disorder. We will call this ordering the 'Palmer-Chalker state' in this thesis.

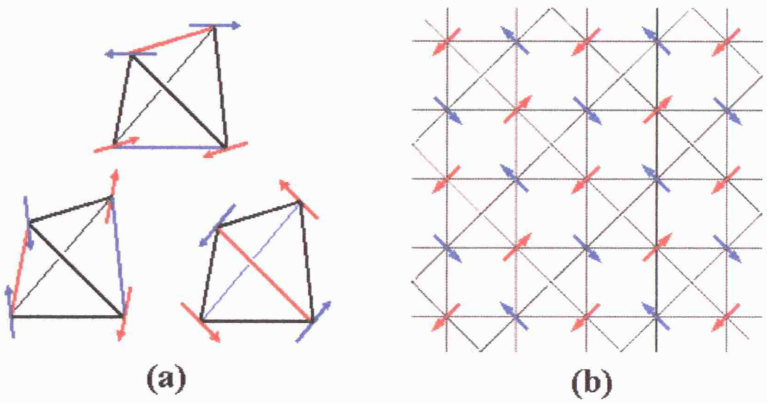

Figure 2.10: (a) Three degenerate ground states for Heisenberg spins on a single tetrahedron with nearest-neighbor dipolar interaction; the Palmer-Chalker states [37]. The four spins are coplanar and are associated into two antiparallel sets, those, in turn, are orthogonal to each set. The antiparallel set of spins lies parallel to one of the tetrahedral edge (this is shown in the figure by different colorings). (b) A projection of the $\mathbf{q} = 0$ ordering pattern found for $D_{dd} / J_1 < R_c \sim 5.7$ onto the xy plane of the cubic lattice. This is a four-sublattice Néel state with all spins being coplanar [37].

2.3.4 Pyrochlore magnets with single ion anisotropy

In this section we summarize the work done on the ground states of the pyrochlore magnets considering the single ion anisotropy. Because the comparison always arises in the pair of ferromagnet ($J > 0$) and antiferromagnet ($J < 0$), we list all the possible combinations of J and Ds explored in the literature [2, 38-39] .

2.3.4.1 Ising anisotropy

The first case considered is the Ising-type spin anisotropy. The effect of introducing Ising-type single ion anisotropies into the pyrochlore system is well summarized in the work of Bramwell and Harris [38]. In their work, two types of Ising-axes are defined. One is a single *global* axis that may be chosen to point anywhere as long as this is kept the same for *all* sites; we will call this the uniaxial Ising system. The second system considered has a set of *local* Ising-axes; an axis is individually assigned for each lattice sites. In the pyrochlore lattice consisting of corner-sharing tetrahedra, these are the four local Ising-axes pointing along the $\langle 111 \rangle$ directions – the lines joining the vertices and the center of the tetrahedron. Therefore, each of the four sites in the tetrahedron has its own $\langle 111 \rangle$ Ising-axis defined locally. We will call this the $\langle 111 \rangle$ Ising system now on.

The ground states of the two systems with $J > 0$ (FM) and $J < 0$ (AFM) are shown in the top row of Fig. 2.13 (note: the axis of the uniaxial Ising system is taken to be the [001] direction as an example). For the uniaxial system, FM is unfrustrated with a unique ground state and hence, it has a phase transition to a long-range ordered (LRO) state at $T \sim |J|$. On the other hand, AFM has a macroscopically degenerate ground state (with two 'up' spins and two 'down' spins) and has no phase transition down to $T \sim 0$ [40]. The results are consistent with the expectations for the conventional FMs and AFMs in the sense that the AFM is more frustrated than the FM.

Although this model is simple and it predicts the general trend of 'FM = unfrustrated' and 'AFM = frustrated', it is a rather inadequate model to use on a

cubic pyrochlore system because the unique symmetry axis does not exist in the cubic symmetry of the lattice. Instead, the ⟨111⟩ Ising model consistent with the lattice symmetry should be considered. Somewhat surprisingly, this choice of Ising-axes reverses the role of the FM and AFM exchange couplings with regards to frustration, making the FM system much more frustrated than the AFM. The degeneracy of the pyrochlore AFM is thus lifted completely by this choice of ⟨111⟩ Ising-axes and the AFM shows a phase transition into a LRO state with a ground state shown in Fig.2.13 (d) that is now unique. This ground state consisting of alternate tetrahedra with four spins 'in' or four spins 'out' is observed in the spin ordering in the pyrochlore compound FeF_3 [41], hence, will be called the *FeF_3 state* in this thesis. The corresponding ⟨111⟩-Ising FM case is the most interesting one out of all combinations. This has a ground state with a tetrahedron with two spins pointing 'in' and two spins 'out' ; Fig.2.11 and Fig.2.13 (c). When these are stacked to form a lattice, the result is a disordered, macroscopically degenerate ground state. This is confirmed by Monte Carlo simulation with the absence of any ordering transition down to all temperatures [38]. Thus, the pyrochlore ⟨111⟩-Ising system with FM coupling is much more strongly frustrated than the corresponding AFM.

Another important point to take notice at this point is the correspondence of the models discussed above to the Pauling's cubic ice model. The two-state AFM model equivalent to model Fig.2.13 (b), previously considered by Anderson [6], maps onto the cubic ice model by associating spin states to the proton positions. However, there is no direct correspondence between spin direction and proton position in this mapping. In this sense, the mapping of the ⟨111⟩-Ising FM model (Fig.2.13 (c)) on to the cubic ice model is more transparent since there is a direct correspondence of spin direction and proton position in this mapping. This mapping is called the *spin ice* mapping, and we will come back to introduce how this was derived in a later section (see section 2.4). Here we will only describe how this mapping works.

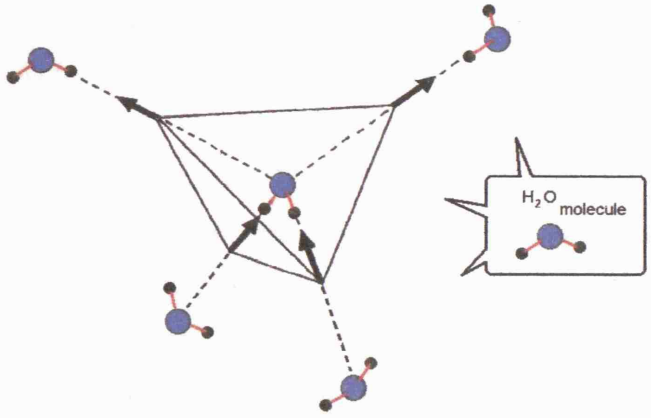

Figure 2.11: Local proton arrangements in ice with displacement of hydrogen atoms from the mid-point (= vertices of tetrahedron) of oxygen-oxygen contact represented in black arrows.

The *spin ice* mapping works as follows; the cubic ice structure is generated by placing an oxygen atom at the centre of every tetrahedron constituting the pyrochlore lattice, then the vertices of the tetrahedra lie at the mid-points of the line connecting the neighbouring two oxygen atoms. If we represent the hydrogen displacements by arrows placed at these mid-points, the two short covalent O-H bonds will be arrows pointing into the centre of the tetrahedron (where the oxygen is), and the two long hydrogen bonds will be arrows pointing out, away form the centre of that tetrahedron. The two-near-two-far configuration of protons around a oxygen atom is controlled by the ice-rules. This is shown in Fig.2.11. When these arrows are replaced by spins, we realize that this is indeed the frustrated ⟨111⟩-Ising FM spin arrangements we had in Fig.2.13 (c).

2.3.4.2 XY anisotropy

Now let us consider the XY-type anisotropies. Again, two types of XY systems have been investigated in the past; (i) the coplanar XY system with *all* the XY planes set

coplanar [21] and (ii) the ⟨111⟩ XY system with *local* XY planes perpendicular to the ⟨111⟩ axes assigned to each of the four lattice sites [2, 42]. These definitions of the XY planes are shown in Fig.2.13 (e) to (h). The different ground states that result from the different combinations of anisotropies and exchange interactions are again shown in this figure.

Moessner *et al.* studied the pyrochlore coplanar XY system with $J < 0$ (AFM) [21]. When the four spins are associated into two pairs of antiparallel spins, these form the ground states of the single tetrahedron in such system. Any of this ground state can be continuously deformed into any other without any energy cost. As it was also the case for the Heisenberg ($D = 0$) pyrochlore AFM, the ground states are therefore said to be 'fully connected'. However, by confining all the spins in the same plane, this XY system has a 'reduced' degeneracy compared to that of the Heisenberg pyrochlore AFM. Moessner *et al.* revealed the reduction in specific heat when the system shows order. This is due to the presence of the soft modes out of the collinear spin states (with two spins 'up', two spins 'down'). [21] Therefore, there is a concentration of statistical weight on this collinear submanifold of ground states and thermal fluctuation selects these states. The order observed here is not a true LRO but is a collinear-nematic order where individual tetrahedra have collinear spin order but the same configuration is not necessarily repeated throughout the lattice. This is the same disorder observed in the spin ice ground state (with two spins 'in', two spins 'out', analogously) that will be discussed later.

Finally, we discuss the pyrochlore ⟨111⟩ XY AFM model. We mainly refer to the works published by Bramwell *et al.*[39] and Champion [2,42]. Bramwell *et al.* studied the Heisenberg pyrochlore AFM with local easy-plane anisotropy using the Hamiltonian

$$\hat{H} = -J\sum_{<i,j>}\mathbf{S}_i \cdot \mathbf{S}_j - D\sum_i (\mathbf{S}_i \cdot \hat{\mathbf{n}}_i)^2 . \qquad (2.10)$$

This form of Hamiltonian allows the anisotropy D to be varied from a small value close to $D = 0$ (the Heisenberg model) up to a large value $D = \infty$ (the XY model) allowing out-of-plane fluctuations. Bramwell *et al.* proposed a $T = 0$ ground state for a single tetrahedron that maximizes the number of AFM bonds. These are the two

coplanar states **I** and **II** shown in Fig.2.14 below. For each state there are three symmetry equivalent spin arrangements, in which the spins lie perpendicular to the three different coordination axes [39]. Allowing all the spins to flip in each configuration, this results in a total of 12 degenerate ground states. When these tetrahedra are tiled to form the pyrochlore lattice, the system will be expressed by two independent 'rods' of AFM spins that are mutually perpendicular to each other. When there are couplings between these spin rods, the system can show long-range $\mathbf{q} = 0$ order (Fig.2.12 - right). However, if all the spins on different rods are flipped, there will be no effective coupling between the rods and the system will be disordered (Fig.2.12 - left). Bramwell and co-workers found a strongly first-order magnetic phase transition to a LRO state in their Monte Carlo simulation (with $J = -1$, $D/J = -5$) around $T/J = 0.1$. They hence concluded that the selection of $\mathbf{q} = 0$ state must be caused by thermally-induced coupling between the spin rods – another example of order by disorder.

Champion elaborated this work looking into the actual ordered structure of the pyrochlore ⟨111⟩ XY AFM with $D = \infty$ [2]. It was discovered that the ground state degeneracy is more extensive than suggested by Bramwell *et al.* The $\mathbf{q} = 0$ ground states can be explicitly described by the linear combination of eight separate pairs of basis vectors and the manifold is fully connected [2]. Apart from the already discussed states **I** and **II**, a non-collinear state **III** and a disordered state **IV** were also found to be the solutions of the ground state manifold. These are shown in Fig.2.14. Champion's Monte Carlo simulation also confirmed the first-order transition into the $\mathbf{q} = 0$ state at $T_N/J = 0.125$. Immediately below T_N there remains a continuous degeneracy in the $\mathbf{q} = 0$ manifold. However, as $T \rightarrow 0$, the spins were found to settle gradually into the non-coplanar state **III** (Fig.2.14 (d)), which turns out to be the true ground state of this model. The author also calculated the normal modes and hence the fluctuations out of these states. This revealed that zero modes only occurred for state **III** and not for the other states. This gives the mechanism for the order by disorder selection of the magnetic ordering structure corresponding to state **III** [2,42]. As a summary, it is found that a manifold of $\mathbf{q} = 0$ states is first selected out of the macroscopically degenerate ground state and then out of this manifold the state **III** is

finally selected. Both of these selection processes are examples of order by disorder.

The ⟨111⟩-XY anisotropy in pyrochlores is found for the AFM material $Er_2Ti_2O_7$ [2,42-43]. From what is stated above, it is clear that ⟨111⟩-XY anisotropy in AFMs causes great complexity in their ground state selection. This will lie at the heart of this thesis; where we will follow the nature of single ion anisotropies of the Er^{3+} ion, by gradually changing its surrounding environment (by substituting Sn for Ti in $Er_2Ti_2O_7$). The more detailed introduction to the materials $Er_2Ti_2O_7$ and $Er_2Sn_2O_7$ will be given in the later section, section 2.6.

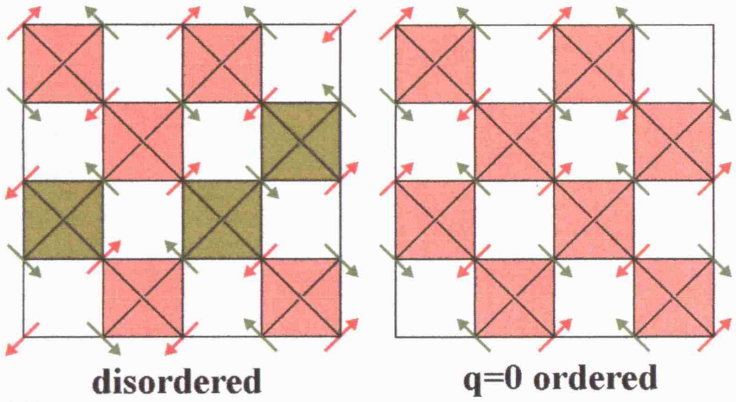

Figure 2.12: The ground states of the pyrochlore ⟨111⟩ XY antiferromagnet expressed by two independent 'rods' of AFM spins that are mutually perpendicular to each other [39]. When there are couplings between these spin rods, the system can show long-range **q** = 0 order (right) but if there is no effective coupling between the rods and the system will be disordered (left).

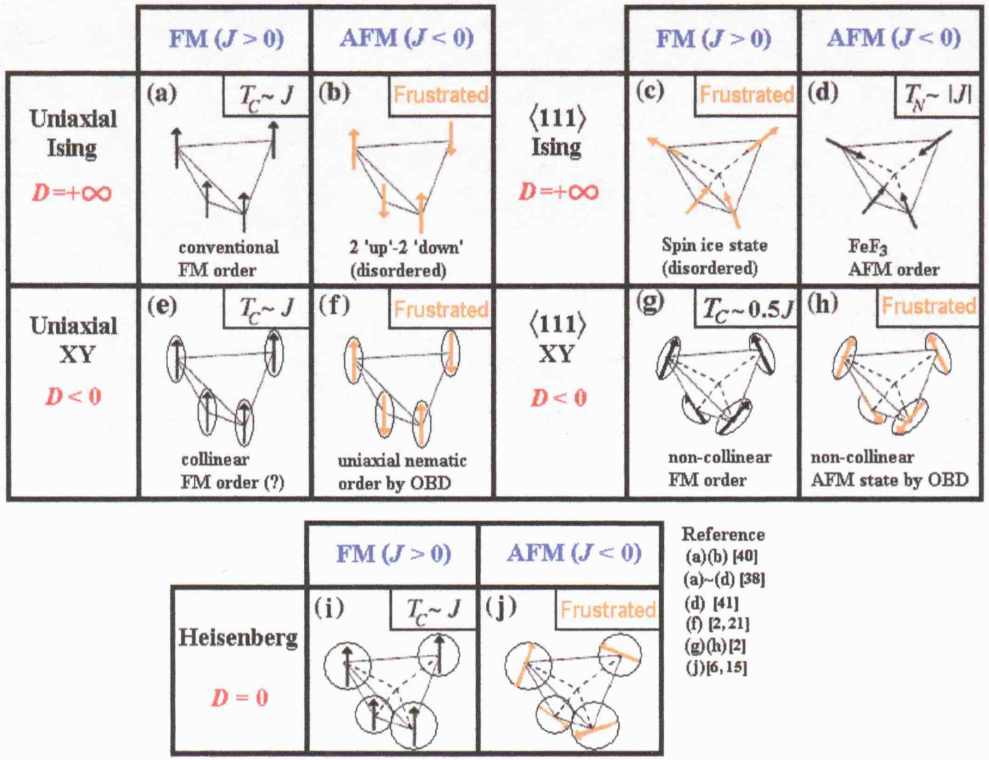

Figure 2.13: The ground states of a single tetrahedron of spins with various combinations of exchange coupling (FM = ferromagnetic, AFM = antiferromagnetic) and single ion anisotropies (both uniaxial and ⟨111⟩ type defined for each of the Ising, XY and Heisenberg anisotropy). The ordering temperatures for each are shown in the inset boxes. Note that the FM is more frustrated than the corresponding AFM only for the case where the anisotropy is of the ⟨111⟩-Ising type [38].

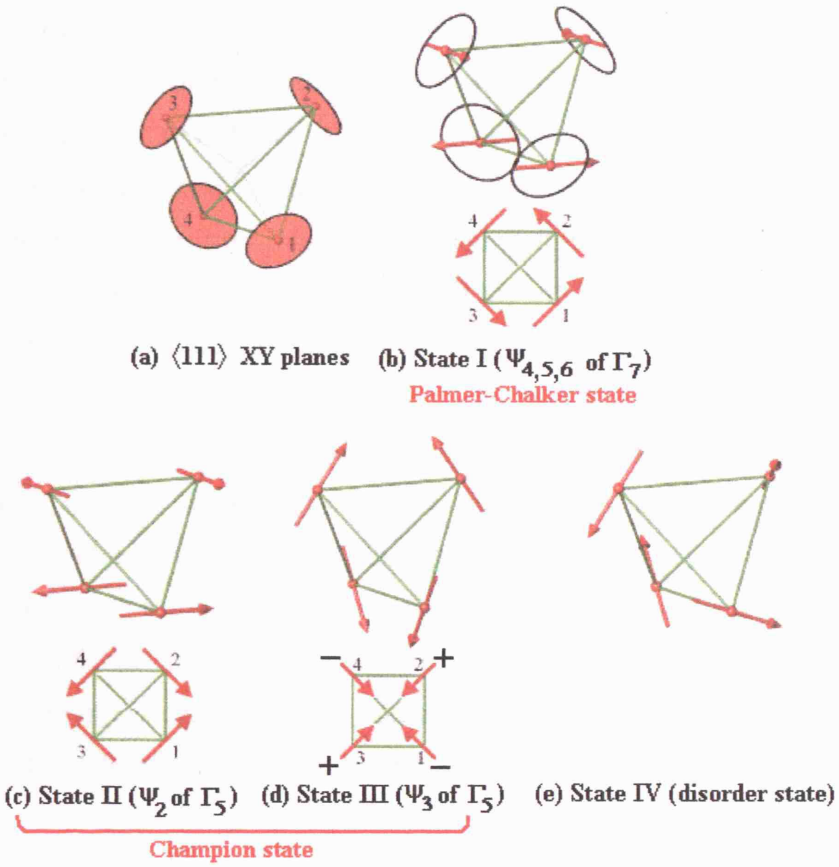

Figure 2.14: (a) The ⟨111⟩ XY planes of the tetrahedron. **(b)-(e)** The basis vectors (states) that constitute the **q** = 0 ground state manifold for the pyrochlore ⟨111⟩ XY antiferromagnet. The small pictures beneath the tetrahedra are the basis projected down [001]. The states are labeled according to Ref. [2] with the corresponding basis vector (ψ_ν) labels belonging to the irreducible representation (Γ_n) deduced for the **q** = 0 order. It should be noted that State I corresponds to the ground state deduced for Heisenberg pyrochlore antiferromagnet with dipolar interaction (Palmer-Chalker state) [37] and State II and State III to the set of basis vectors that fit the $Er_2Ti_2O_7$ magnetic neutron diffraction pattern below T_N ~ 1.1 K (Champion state) [42].

2.4 Frustrated Ferromagnet – The Spin Ice

In the previous section, we have introduced the theoretical interpretations regarding the ground states of the pyrochlore system with the exchange coupling J being antiferromagnetic (AFM, $J < 0$). A fairly detailed follow up was attempted so far since the experimental systems we deal within this thesis are mainly pyrochlore antiferromagnets (AFMs). However, although it is not directly relevant, a basic reviewing of the pyrochlore ferromagnets (FM) will also be made in this short section for completeness of the subject. Specially, because of the weight it has on the history of frustrated magnetism and its conceptual elegance, it makes one difficult to talk frustrated magnetism without mentioning the concept –'*spin ice*'. The christening of the name '*spin ice*' happened in 1997, realized by Harris and Bramwell [38,44]. Since then, the subject has received substantial attention from both theoreticians and experimentalists and the resulting deepness and diversity of the understanding of the subject made itself an irreplaceable 'icon' in the field of frustrated magnetism. There are number of reviews specifically treating this subject [3,45] and the reader should refer to them for the detailed work. This section is aimed only to introduce the reader to the remarkable 'bridging' that was made between the physics of water ice and magnetism in deriving the concept of spin ice.

The history of crystalline (water) ice goes back to the 1930's when Giauque and co-workers measured the residual (zero-point) entropy of it, identifying it to be the first frustrated system in history [46]. This enabled Pauling [48] to explain the origin of this entropy using the Bernar and Fowler 'ice rules'[47] –those rules that require two protons to be near and two further away from each oxide ion in the crystal structure of hydrogen-bonded H_2O ice (see Fig.2.11). Pauling noticed that the ice rules do not give enough constraint to the system, hence, no unique ordered structure is selected for the protons. Instead, the ground state of water ice is macroscopically degenerate with degeneracy of the order $\sim (3/2)^{N/2}$ for a sample with $N \sim 10^{24}$ molecules [48]. This leads to a theoretical zero-point entropy of $S_0 \sim (R/2)\ln(3/2)$ where R is the molar gas constant, which indeed agrees well with the measured value [46,48].

In 1996, Harris and co-workers initiated an experimental investigation into the compound $Ho_2Ti_2O_7$, a system with magnetic rare earth ions (Ho^{3+}) occupying the trigonal 16*c* sites of the space group $Fd\bar{3}m$ forming a pyrochlore lattice [44]. Their μSR [43] and neutron scattering experiments [43-44] established the absence of long-range order (LRO) down to ~50 mK. Two other information that were initially used to deduce the spin correlations in $Ho_2Ti_2O_7$ were (i) the early susceptibility study showing a peak at ≈ 1 K (suggesting AFM interactions) [49] and (ii) the strong easy-axis anisotropy of the order of $T \approx 300$ K present along the ⟨111⟩ axes [30, 44, 50]. The later is a consequence of the trigonal crystal field splitting of the $^5I_8$ free ion state of Ho^{3+} such that the ground state is an almost pure $|J, M_J\rangle = |8, \pm 8\rangle$ doublet with ⟨111⟩ quantization axis [30, 50]. The existence of this ⟨111⟩ easy-axis is also manifested in the bulk high field magnetization [51], where the moment measured for Ho^{3+} is a little over half the theoretical free ion value of $\mu = 10.61\ \mu_B$. Combining the above two conditions makes the system into a ⟨111⟩-Ising AFM for which a selection of unique ground state (the all spins in/out FeF_3 state) is predicted. Thus the absence of LRO gives dilemma.

The turning point to the scenario happened when Harris *et al.* realized that the Curie-Weiss temperature of $Ho_2Ti_2O_7$ can actually be $\theta_{CW} = +1.9$ (1) K if a careful demagnetization correction is applied [44]. This changes the question into a new one; 'why does not this *ferromagnet* order at a low temperature?'- it was not clear how a ferromagnet could be subject to geometrical frustration. Calculation was performed immediately to verify the ground state of the ⟨111⟩-Ising FM [38] and this revealed a ground state in which two spins point 'in' and two spins 'out' of the centre of each tetrahedron. This 'two-in, two-out' was the 'key' word to solve the whole question. Harris and Bramwell came to discover this unexpected analogy to the ice rules, leading to state that the ground state of the nearest-neighbour ⟨111⟩-Ising FM is, like that of ice, macroscopically degenerate [38, 44]. The name 'spin ice' was thus christened to describe this magnetic analog of water ice and the absence of LRO in $Ho_2Ti_2O_7$ was finally explained. The validity of this explanation was reinforced by the consistency of the field-induced ordering patterns observed by neutron scattering

[44]. The spin ice mapping of spins on the pyrochlore lattice is shown in Fig.2.15 together with the arrangements of protons in water ice overlaid to see the direct correspondence of the two systems. It should be emphasized that this pyrochlore ⟨111⟩-Ising model is an unusual example in which FM is more frustrated than the AFM.

A direct experimental evidence of the macroscopic degeneracy associated with the spin ice conjecture raised by Harris/Bramwell was given by the specific measurements on $Dy_2Ti_2O_7$ by Ramirez and co-workers [52-53]. $Dy_2Ti_2O_7$ is another example deduced to be a spin ice material, having a strong ⟨111⟩ Ising anisotropy [30,50,54] and θ_{CW} = + 0.5 K [51-52]. Ramirez *et al.* determined the ground state entropy by integrating the magnetic specific heat between T_1 = 300 mK in the spin ice regime and T_2 = 10 K in the paramagnetic regime (where the expected two-state system entropy should be $R \ln 2$) and comparing it to $S = R \ln 2$. The difference was ≈ $(R/2)\ln(3/2)$; a value close enough to the Pauling's estimate of the residual entropy for water ice [52]. This is shown in Fig.2.16.

As a final point on the topic, we will introduce the dipolar spin ice model, argued by den Hertog and Gingras [55]. This argument was brought in to try to explain the origin of the small, positive θ_{CW} of the spin ice materials. They attribute this ferromagnetism to the dominant dipolar term. Monte Carlo simulation using the Ewald infinite summation method [55,57] gives a ferromagnetic dipolar term ($D > 0$) which exceeds the nearest-neighbor exchange term, which is now negative for both $Ho_2Ti_2O_7$ (J_{nn} ~ -0.52 K) [58] and $Dy_2Ti_2O_7$ (J_{nn} ~ -1.24 K) [55]. This work shows that the spin ice state can exist for $J_{nn} \gtrsim$ - 0.91[55]. Although there are conflicts when to cut the summation (Siddharthan *et al.* chose to truncate the interaction up to 5th and 12th nearest neighbour in their Monte Carlo simulation [56]), the dipolar spin ice model is in its strong position as it accurately fits the $Dy_2Ti_2O_7$ specific heat curve (Fig.2.16 (*Left*)) as well as predicting the $Ho_2Ti_2O_7$ single crystal scattering patterns in zero field (Fig.2.16 (*Right*)) [58] and the magnetization data in applied magnetic fields for $Dy_2Ti_2O_7$ [59].

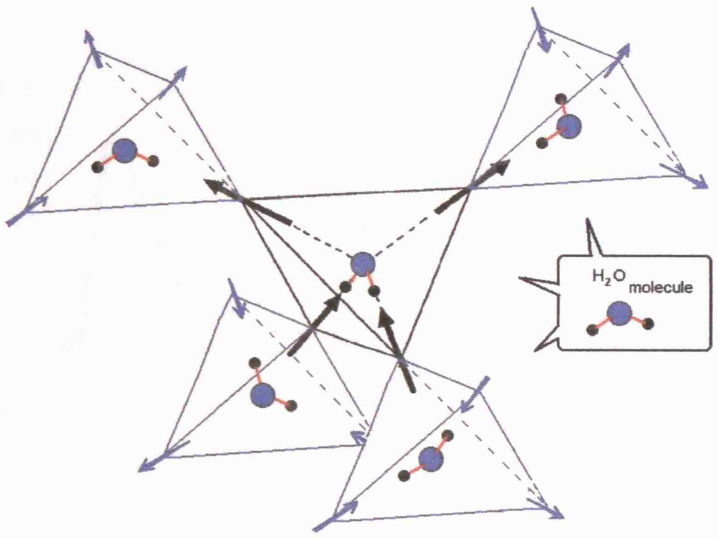

Figure 2.15: The spin ice model as the proposed ground state of $Ho_2Ti_2O_7$. The spins of Ho^{3+}(represented in black/blue arrows) are at the vertices of the tetrahedra that constitutes the cubic pyrochlore lattice. This two-in-two-out configuration of ferromagnetically coupled ⟨111⟩ Ising spins is directly mapped onto the two-near-two-far proton arrangements around an oxygen atom.

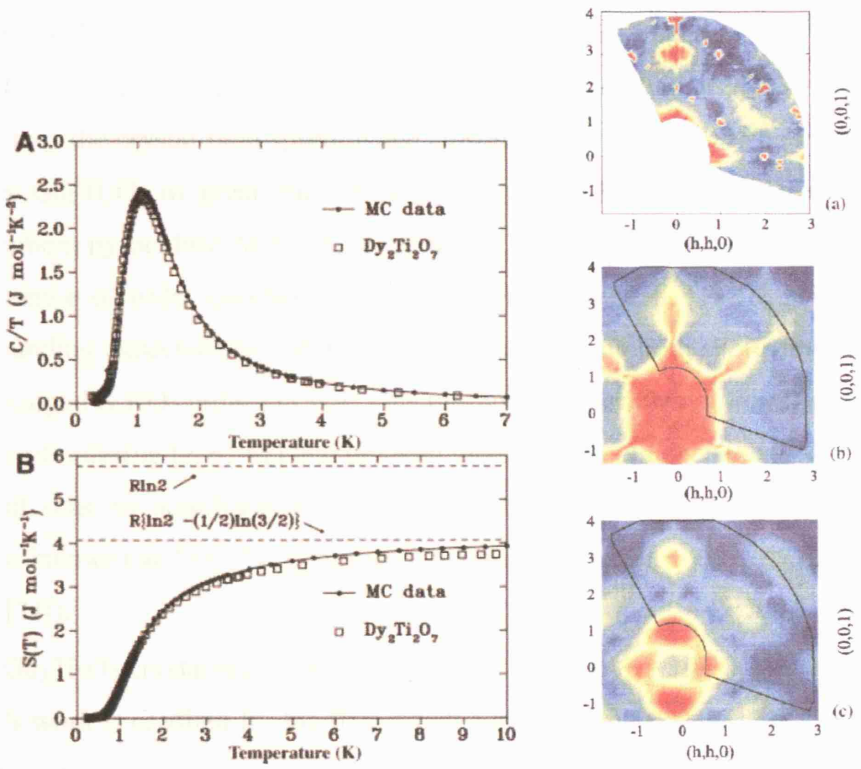

Figure 2.16 – *Left:* (A) Specific heat and (B) entropy data for the spin ice compound $Dy_2Ti_2O_7$ [52]. There is no indication of transition to an ordered state. The entropy reaches the value calculated based on Pauling's cubic (I_h) ice entropy. The fitted line shows the Monte Carlo simulation results for the dipolar spin ice model [55], with J_{nn} = - 1.24 K, D_{nn} = 2.35 K and system size of 1024 spins.

Figure 2.16 – *Right*: Comparison of neutron scattering pattern for $Ho_2Ti_2O_7$ (taken in the *hhl* plane at T = 50 mK)[58] (*Top*) with the calculated neutron scattering pattern for the nearest-neighbor spin ice model (*Middle*) and for the dipolar spin ice model (*Bottom*). The red zones have the highest intensities and the blue the lowest. The sharp red spots are the nuclear Bragg peaks with no magnetic components. The dipolar spin ice model predicts a pattern that is closer to the experimentally observed pattern than the simple nearest-neighbor model.

2.5 Gadolinium Titanate: $Gd_2Ti_2O_7$

In this section we briefly review the work done on the material $Gd_2Ti_2O_7$. The Gd^{3+} ion ($4f^7$, $S = 7/2$, $L = 0$, $J = 7/2$) is a spin only S-state ion with a $^8S_{7/2}$ single ion ground state, thus the crystal field splitting and anisotropy are expected to be minimized. This makes $Gd_2Ti_2O_7$ of great interest as it is expected to be an ideal realization of an Heisenberg pyrochlore AFM, in which theory predicts a spin liquid ground state with an absence of order (neither by OBD) down to $T = 0$ K [15-16, 21-22]. However, confounding expectations, $Gd_2Ti_2O_7$ was found to show both short-ranged (SRO) and long-ranged (LRO) order [35, 60]. This motivated experimental investigations into the nature of ordering [2, 61-62] and invoked theoretical challenges to ascribe this ordered ground state to additional weak perturbations (such as single ion anisotropy and dipole interaction [35,37,72], further neighbor interaction [60, 63, 73] and magnetic field [74]).

$Gd_2Ti_2O_7$ crystallizes in space group $Fd\bar{3}m$ with $a = 10.18(1)$ Å at 300 K. Raju *et al.*'s work is credited for the first detailed study of the system [35]. From their bulk dc susceptibility measurement (shown in Fig.2.17-*Left*), the Curie-Weiss temperature was found to be $\theta_{CW} = -9.6(3)$ K and the effective moment was $\mu_{eff} = 7.7\ \mu_B$, close to the free ion value $\mu_{freeion} = g_J\sqrt{J(J+1)} = 7.94\ \mu_B$. Although the dc susceptibility curve follows the Curie-Weiss law down to ~ 10 K, no evidence of magnetic order was observed down to ~ 1 K [35]. The ratio $|\theta_{CW}|/T_c$ that measures the level of frustration [11,13] is ~10 for the system, hence, $Gd_2Ti_2O_7$ is classified as a system with high level of frustration. A similar measurement on a diluted sample $(Y_{0.98}Gd_{0.02})_2Ti_2O_7$ shows that θ_{CW} essentially becomes zero, indicating that the crystal field contribution to θ_{CW} for this material can be ignored in accord with expectations [35]. In contrary to the dc susceptibility, the ac susceptibility and the specific heat measurements (Fig.2.17-*Right*) revealed two types of ordering; a LRO that develops at $T_c = 0.97$ K and a (possible) SRO that is present above 1 K that may persist up to ~ 30 K [35]. However, the diffuse contribution to the heat capacity could be due to sample disorder effects.

The measured θ_{CW} should be a measure of the energy scale for the overall magnetic interactions. This includes contributions from the exchange interaction (θ_{CW}^{J}), crystal field (θ_{CW}^{CEF}), and dipolar interaction (θ_{CW}^{dip}). The dipolar contribution to the measured θ_{CW} is a difficult problem to assess as an infinite lattice sum is involved and the sample-shape dependent demagnetizing factor must be considered. The closest one can approximate is probably to work out the upper and lower bounds; which is - 2.4 K $\leq \theta_{CW}^{dip} \leq$ 1.2 K [64]. Therefore, with the θ_{CW}^{CEF} being negligible, it shows that θ_{CW}^{J} is the dominant component.

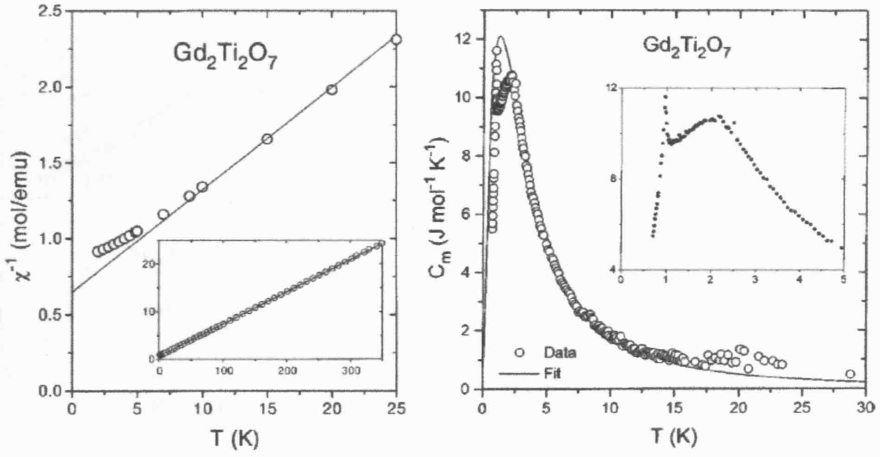

Figure 2.17 - ***Left***: Inverse molar susceptibility $1/\chi$ of powder $Gd_2Ti_2O_7$ against temperature. It shows that the Curie-Weiss law is obeyed down to ~10 K ($\approx \theta_{CW}$) with no sign of ordering down to ~ 1K [35].

Figure 2.17 - ***Right***: Magnetic specific heat C_m (obtained by subtracting the lattice contribution C_l from the measured C_p). The solid line represents the theoretical that simulates distribution of internal magnetic field [35]. There is a sharp transition into an ordered state at ~ 1K (seen better in the blown up inset). Also the presence of the broad peak around ~ 2 K and the approximately 50 % recovery of the entropy at ~1K may indicate the presence of short-range order [35].

In a more recent ac susceptibility and specific heat measurements both on a powder sample [60] (Fig.2.18-Left) and on a single crystal (Fig.2.18-Right) [66], two phase transitions into a LRO state below 1 K were reported in zero field; at T_{N1} = 0.97 K [60] (1.02 K [66]) and T_{N2} = 0.6K [60] (0.74 K [66]). The broad peak observed in the measurement in Ref.[35] peaked around 2 K is not observed in the latter measurements [60,66]. Also, it is noticed that, while in Raju *et al.*'s measurement there is some significant magnetic entropy contribution up to ~ 30 K [35], for the latter measurements [60,66] the entropy recovery (towards the expected $2R$ ln $(2S+1)$) is almost complete when the temperature reaches ~ 5 K.

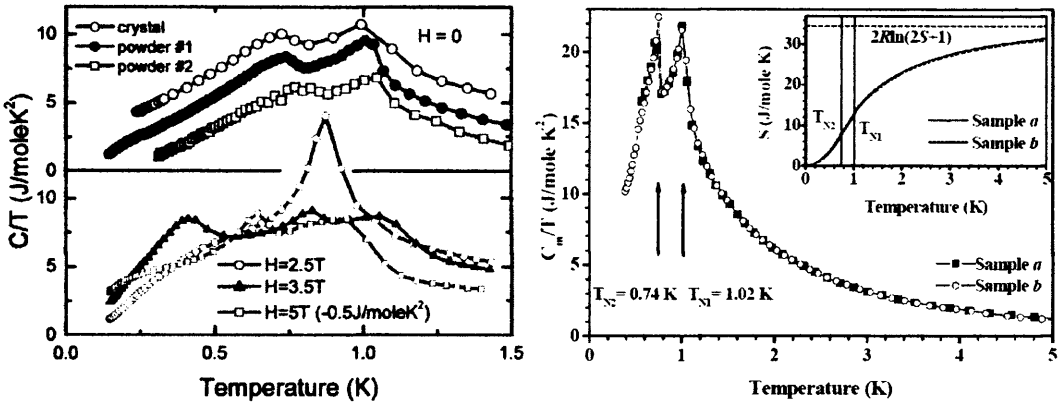

Figure 2.18 - ***Left***: Specific heat divided by temperature $C(T)/T$ for powder sample of $Gd_2Ti_2O_7$ at various applied fields. The top panel shows the zero-field measurements for three different samples. The two transitions (T_1 = 0.97 K, T_2 = 0.6 K) are clearly seen. The bottom panel shows the measurement for the three different applied fields and it shows how the application of the magnetic field induces different phase transitions [60].

Figure 2.18 - ***Right***: Temperature dependence of the specific heat divided by temperature, $C(T)/T$, measured for a single crystal of $Gd_2Ti_2O_7$ in zero applied field. The magnetic entropy curve is shown in the inset. Two measurements on different samples are shown in order to show the reproducibility of the data [66]. Approximately 90% of the expected entropy, $2R\ln(2S+1) = 34.6$ $Jmol^{-1}K^{-1}$, is recovered at $T \sim 5$ K.

The nature of the two orderings (T_{N1} and T_{N2}) was disclosed by the two subsequent experiments that uses the combined power of neutron scattering and symmetry analysis [2,61-62]. Both experiments were carried out on a powder sample of isotopically substituted $^{160}Gd_2Ti_2O_7$ to overcome the high absorption of neutron beam by the natural ^{157}Gd [2, 61-62]. In the first measurement by Champion *et al.*, the data collected from the POLARIS diffractometer at ISIS (Oxford) at 50 mK were used to analyze the ordered magnetic structure by the application of the representational analysis method described in Chapter 3. As a result, an exotic magnetic order with the propagation vector $\mathbf{k}$ = ½½½ was deduced. That is, the 3/4 of the Gd^{3+} spins are ordered within the kagomé planes (corresponding to a $\mathbf{k}$ = 000 order of kagomé AFM described in section 2.3.1), while the 1/4 remaining 'interstitial' spins are disordered [2, 61] – see Fig.2.19-(a). In this structure, all the spins are perpendicular to a single global [111] crystallographic direction and thus is called the '1-*k* (single-*k*) structure' [62].

The later neutron scattering experiment carried by Stewart *et al.* [62] confirmed the basic scenario of this ordering pattern, except that the possibility of 'multi-*k*' structures was now put into the equation. When neutron diffraction technique is employed for systems of high symmetry, alternative structures described by one or several symmetry-related propagation vectors *k* cannot be distinguished as they give identical diffraction patterns as a result of powder averaging (or the formation of '*k*-domain' in single crystals) [62,65]. The authors of the published work, ref [62], tackled this scientifically challenging problem in a fascinatingly smart way, leading to the rather solid conclusion that the system has a 4-*k* ordered structure below T_2 (~ 0.725 ± 0.025 K). The method they used is as follows. The authors focused on the diffuse-part of the scattering pattern and fitted the magnetic diffuse scattering measured on D7 diffractometer (ILL, Grenoble) using both the 1-*k* and 4-*k* structures. The 4-*k* structure has all spins perpendicular to the *local* trigonal ⟨111⟩ axes and is shown in Fig.2.19-(b). The diffuse scattering analysis involves only the partially ordered ('interstitial') spins, hence, it gives rise to a significant difference in the 1-*k* and 4-*k* patterns. This is because these spins are completely different in spatial distribution; the nearest-neighbour distances (R_{nn}) between these partially ordered

spins in 1-*k* and 4-*k* are R_{nn}^{1k} = 7.2 Å and R_{nn}^{4k} = 3.6 Å, respectively. The outcome was clear enough to evidence the 4-*k* ordering at T = 46 mK [62].

Looking at the diffraction patterns, Stewart *et al.* also realized the presence of the new weak Q = ½½½ reflection below T_2 [62]. Since this reflection only gains intensity when the interstitial spins are ordered, the transition happening at T_2 was immediately attributed to the ordering of the interstitial spins. The maximum ordered moments of the three kagomé spins and the single interstitial spin was deduced to be $7.0 \pm 0.1\mu_B$ (fully ordered) and $1.9 \pm 0.1\mu_B$ (~27 % ordered) , respectively [62]. It was also found that the partial ordering of the interstitial spins cause the remaining three kagomé spins to cant by ~ 9° from its **k** = 000 (120°) position within the [111] plane [62].

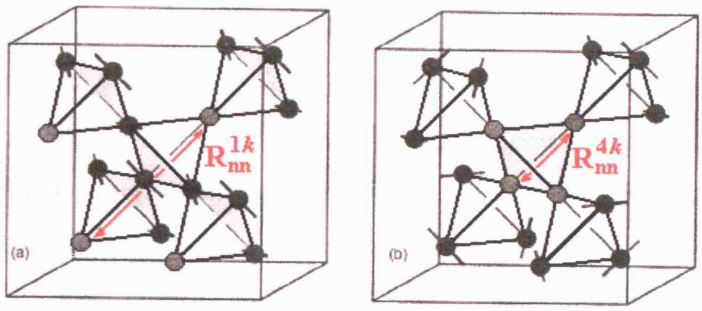

Figure 2.19: (a) The 1-*k* magnetic structure for $Gd_2Ti_2O_7$ [2,61]. The spins on the dark spheres represent Gd^{3+} spins that have (**k** = 000 or 120°) coplanar ordering on the kagomé planes perpendicular to the global [111] axis and the ordered moment is 6.73 ± 0.05 μ_B [2,61].The grey spheres are the 'interstitial' (or the inter-planar) Gd^{3+} that carry no thermally averaged moment. (b) The 4-*k* structure that is derived from its 1-*k* variant [62]. The dark spheres represent Gd^{3+} ions with a full ($7.0 \pm 0.1\mu_B$) ordered moment that while the grey spheres are the partially ordered ($1.9 \pm 0.1\mu_B$) spins. The kagomé spins (dark spheres) are now perpendicular to their own *local* ⟨111⟩ axis. The magnetic structure for $Gd_2Ti_2O_7$ for T_1(= T_N = 1.1 K) > T > T_2 (= 0.7 K) is consistent with (a) whereas below T_2 the structure is determined to be of (b), with partial ordering of the interstitial spins and a ~9° canting of the three kagomé spins within the [111] plane [62]. The nearest-neighbour distance of the disordered (grey) spins, R_{nn}, that differentiates the two structures, are also indicated in both pictures.

Having neglected the single ion anisotropy so far for the *S*-state Gd^{3+} ion, the true extent of anisotropy in $Gd_2Ti_2O_7$ is another issue that is giving conflict arguments in recent studies. Although natural instinct tells us that the anisotropy should be unimportant in materials containing the *S*-state Gd^{3+} ion (indeed, the typical anisotropy of Gd^{3+} is $\approx$ 0.3 K [68]), several experiments support the opposite case. For example, the ESR experiment carried out on a single crystal of $Gd_2Ti_2O_7$ demonstrates strong temperature dependent uniaxial anisotropy with respect to a specific [111] crystallographic direction below T = 80 K [67]. The anisotropy is augmented as the temperature is lowered and at 4 K it becomes as big as $\approx$ 5 K which is of the order of the exchange energy found from the bulk dc susceptibility [67]. The suggestion that $Gd_2Ti_2O_7$ has a unique [111] axis of these authors are compatible with the 1-*k* structure, but does not reconcile with the 4-*k* structure. The authors of Refs.[62] and [66] argue that this might be because the ESR results were obtained in high field at $T > 4.2$ K and hence might not be directly comparable with their results [62]. On the other hand, Mössbauer measurements supports another type of anisotropy for the single ion; the four spins of the tetrahedra having the same length and being perpendicular to the local trigonal ⟨111⟩ axis, this is consistent with the 4-*k* description of the structure [69]. Also, the most recent study about the Gd^{3+} anisotropy in $Gd_2Ti_2O_7$ points out that the single ion ground state might be a intra-shell mixture of $^8S_{7/2}$ and $^6P_{7/2}$, thus the ground state admixture containing some $L \neq 0$ states becomes susceptible to the surrounding crystal field [75]. This EPR study on a diluted single ion of $(Y_{1-x}Gd_x)_2Ti_2O_7$ showed the extent of anisotropy, D, comparable to the exchange integral, J; $D/J \sim 0.7$ (corresponding to a planar anisotropy) [75] and exceeds the dipole interaction. Thus in a future approach this single ion anisotropy should be placed as a serious perturbation to the Heisenberg model.

Finally, we will summarize the complex behavior of $Gd_2Ti_2O_7$ in field. The field-temperature phase diagram for the powder sample was constructed from the specific heat and ac susceptibility measurements [60] – this is shown in Fig.2.20. The complexity of it is clear; with at least five phases present. A similar process was repeated for a single crystal [66] with three principal field directions; [111], [112] and

[110] chosen. These will be discussed in Chapter 8 with regards to our results, so the reader should refer to Fig.8.10 later in the thesis.

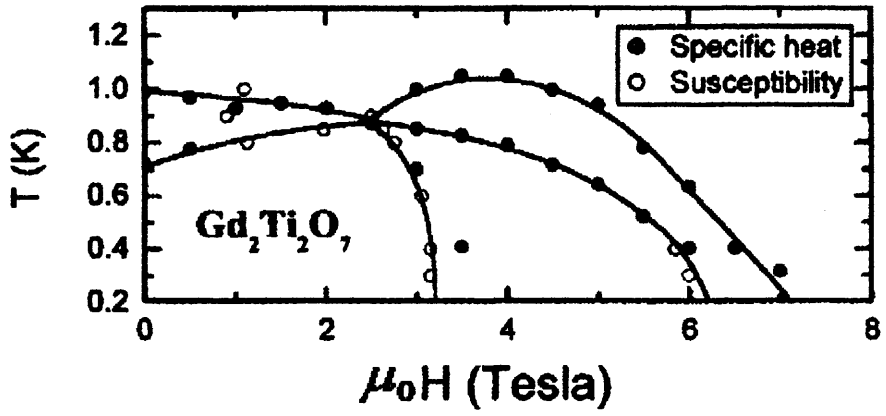

Figure 2.20: Temperature-field phase diagram constructed based upon the specific heat and susceptibility measurements of the polycrystalline $Gd_2Ti_2O_7$ sample. [60]

2.6 Erbium Titanate and Stannate: $Er_2(Ti/Sn)_2O_7$

Finally, we introduce the reader to the erbium titanate, $Er_2Ti_2O_7$, and erbium stannate $Er_2Sn_2O_7$, the materials we will devote the longest time during the rest of the thesis.

The three main early works concerning $Er_2Ti_2O_7$ were published during the late 1960's; these are the crystal structure determination by Knop *et al.*[70], susceptibility and demagnetization experiments by Van Genus [71] and the specific heat measurement carried out by Blöte *et al.*[71]. By comparing the calculated nuclear structure factors to those observed in neutron and x-ray diffraction, Knop determined the crystal structure of the $Er_2Ti_2O_7$ to be a cubic pyrochlore ($Fd\bar{3}m$). Also, similar work on other rare earth titanates are listed within Knop's work thus this reference still stands as the basic reference for the structural work of these materials.

The heat capacity of $Er_2Ti_2O_7$ shown in Fig.2.21 below shows a definite singularity at T = 1.25 K [71]. Blöte *et al.* calculated the entropy change involved during this transition and found it to be $\Delta S \approx 0.97\ R \ln 2$, a very close value to that involved in a system which has a doublet ground state. Therefore, it is assumed that

this transition at T_N = 1.25K involves a magnetic long-ranged ordering (LRO) of the ground state Kramers doublet. The d.c. susceptibility measured by these authors are also shown in Fig.2.21-*Left*. Two peaks are observed at T_N ~ 1.25 K and ~ 0.3 K. The nature of the second peak is still unclear since it becomes appreciably low in an applied magnetic field of 800 Oe, and also, chemical inhomogeneity is suspected for the used sample [62]. An existence of weak ferromagnetism is also suggested in this reference [62].

The Curie-Weiss temperature of $Er_2Ti_2O_7$ was determined from the susceptibility measurement by Van Genus to be very large and negative, θ_{CW} = - 22 K [62]. Blöte suspected that this was too large to be due solely to antiferromagnetic exchange interactions and postulated the effect of crystal field interactions. They proposed the existence of a low-lying doublet crystal field excitation about 1 meV (10 K) above the ground state Kramers doublet of Er^{3+}, such that the combined effect of the two doublets on the powder susceptibility manifests as an approximated free ion behavior [62]. However, this idea was disproved to be true in a later neutron scattering experiment; the two lowest excitations were at 6-8 meV (60-80K) [42] and it is unlikely that these excitations can account for the large θ_{CW}.

The free ion ground state term of the Er^{3+} ion is $^4I_{15/2}$ ($4f^{11}$, L = 6, S = 3/2, J = 15/2, g_J = 1.2) with a free ion magnetic moment of $g_J\sqrt{J(J+1)} = 9.59\mu_B$. As contrary to the case of Gd^{3+} ion (L = 0), the large orbital moment of Er^{3+} ion suggests significant anisotropy to be present in the system. The existence of the magnetic transition just in itself does not lead us to know whether the type of this anisotropy is uniaxial or planar, since transitions are observed in real [41] and theoretical antiferromagnets (see section 2.3.4) with either type of anisotropy. The hint to differentiate the two was found in the neutron diffraction pattern [43]. Neutron scattering experiments on both powder and single crystal of $Er_2Ti_2O_7$ confirm $\mathbf{k}$ = 000 ordering below T_N ~ 1.2 - 1.4 K [2,42,43]. This is shown in Fig.2.22. For this case of pyrochlore $\mathbf{k}$ = 000 AFM, when the anisotropy is ⟨111⟩-Ising the system should order into a FeF_3 structure (all spins pointing into or away from the centre of every tetrahedron – see Fig.2.12). This should give a magnetic diffraction pattern with the (1,1,1) magnetic Bragg peak absent [41]. However, in the $Er_2Ti_2O_7$ diffraction pattern

this peak has intensity, leading one to suspect that $Er_2Ti_2O_7$ might have a ⟨111⟩-planar anisotropy [43]. A strong support was later given to this speculation by directly measuring and interpreting the crystal field of the material [30, 43].

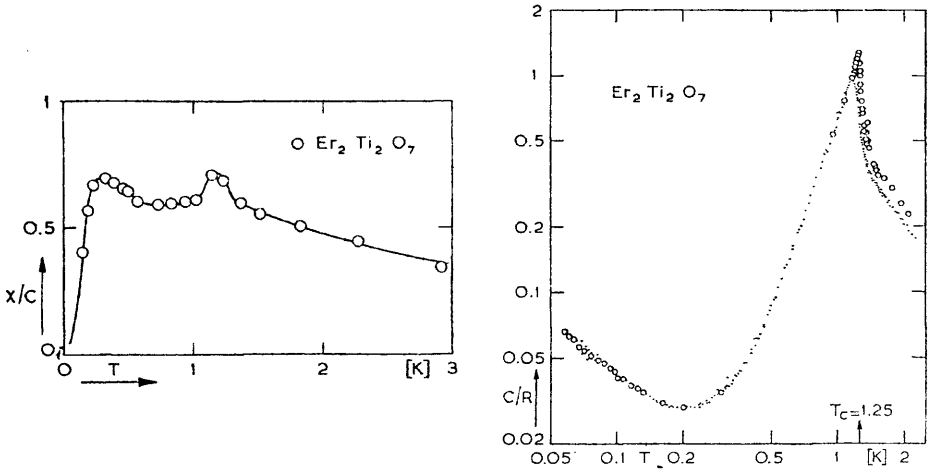

Figure 2.21-*Left*: d.c. susceptibility, χ, of the powder $Er_2Ti_2O_7$ sample divided by the Curie constant, C (C was determined for 1.5 K < T < 4 K) [62].

Figure 2.21-*Right*: Heat capacity measured for the powder $Er_2Ti_2O_7$ sample. The different markers represent two different measurements; the agreement is good below 1K [62].

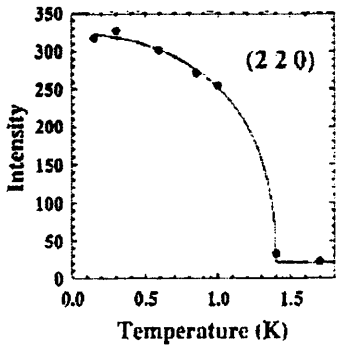

Figure 2.22: The temperature dependence of the (2,0,0) Bragg peak intensity in the neutron diffraction for the single crystal of $Er_2Ti_2O_7$ in zero field. The rapid increase in intensity below T_N = 1.4 K represents a (second order) phase transition to an ordered state.[43]

The actual ordered magnetic structure of $Er_2Ti_2O_7$ in zero field was determined by Champion *et al.* in 2003, using neutron scattering [2, 42]. They employed the representational analysis method (described in section 3.4.2.2) to determine the basis vectors that can fit the powder diffraction data taken at 50 mK. This revealed the two basis vectors ψ_2 and ψ_3 that belong to the same irreducible representation Γ_5 (see Fig.2.14 and Chapter 5 for full description) being consistent with the magnetic intensity [2, 42]. In Fig.2.23-(c), the powder neutron profile refined using ψ_2 and ψ_3 is shown – the powder profile is said to be fitted well with the 'Champion model'. One should note that, although the true ground state of $Er_2Ti_2O_7$ is found to be represented by the basis vector ψ_3 (see section 2.3.4.2), in a powder measurement any mixing ratio of ψ_2 and ψ_3 give the same predicted pattern and hence it is not possible to separate the two basis vectors. Therefore, further neutron scattering experiments were carried out by the same authors, now using a single crystal of $Er_2Ti_2O_7$ in order to distinguish between the two structures [42]. They chose to apply a magnetic field along the [1 -1 0] direction in order to suppress the formation of multidomains that occur due to the cubic symmetry of the system. It was observed that, below T_N, the field of 0.5 T caused the (2,2,0) magnetic Bragg peak to almost double in intensity while the rest of the peaks remained unchanged. This indicated the formation of the monodomain of ψ_3 ground state, leading the authors to conclude that the zero field ordering pattern is also described by ψ_3 [42]. The reader should notice that this ψ_3 structure correspond to the symmetric solution, state III, of the ⟨111⟩-XY AFM problem discussed in section 2.3.4.2, and therefore, a remarkable agreement between theory and experiment is shown here.

The ordered moment of Er^{3+} ions at 50 mK (where ordering is essentially complete) was demonstrated to be 3.01 ± 0.05 μ_B per atom [2, 42]. This is about 1/3 of the free ion value (9.59 μ_B). This suppression of single ion moment occurs due to the crystal electric field (CEF) interactions on the magnetic ion, and this is indeed confirmed by the analysis on the predicted CEF scheme of $Er_2Ti_2O_7$ [42]. Using the CEF parameters for $Ho_2Ti_2O_7$ derived from experiment carried out by Rosenkrantz, Hodges *et al.* derived the corresponding CEF parameters, thus, the CEF ground state for $Er_2Ti_2O_7$. The predicted single ion Kramers doublet ground state wave function is

then of the form [42]

$$\psi_0 = -0.5428|-{}^{11}/_2\rangle - 0.2384|-{}^{5}/_2\rangle + 0.5628|{}^{1}/_2\rangle + 0.3876|{}^{7}/_2\rangle - 0.426|{}^{13}/_2\rangle. \qquad (2.11)$$

This corresponds to moments of 3.8 μ_B and 0.12 μ_B perpendicular and parallel to the local $\langle 111 \rangle$ axis, giving an overall moment with the size consistent with the observed 3.01 μ_B [42].

With a moment of ~ 3 μ_B, the near neighbor dipolar interaction is calculated to be + 0.06 K per spin for structures $\psi_{2,3}$ (and – 0.32 K per spin for structure $\psi_{4,5,6}$ – see section 2.3.4.2)[42] and thus should be considered as a major perturbation to the model Hamiltonian. If this is the case, and assuming that $Er_2Ti_2O_7$ have $D_{dd}/J_1 << 5.7$ (D_{dd} = dipolar constant, J_1 = nearest-neighbor exchange constant), theory predicts ordering into the ground state of the *dipolar* Heisenberg pyrochlore AFM; the 'Palmer-Chalker state' (state I or structure $\psi_{4,5,6}$) described in section 2.3.3. Since this is not the observed result, one might have to speculate other perturbations or mechanisms causing the selected order, ψ_3. Champion *et al.* attribute the ordering of $Er_2Ti_2O_7$ to its stabilization by zero-point quantum fluctuations, in other words, the existence of soft modes (in their classical spin wave modelling) selecting the ψ_3 state over the others [2, 42]. Therefore, it is considered to be a novel example of *quantum* order by disorder. Two points should however be noticed as the failure of their analysis [42]; first is that they fail to simulate the T^3 dependence of specific heat and secondly, the continuous ordering transition contradicts the theory which predicts first order transition [39].

Inelastic neutron scattering experiments were also carried out by Champion *et al.*[42] The spectra for the powder and single crystal samples of $Er_2Ti_2O_7$ are both shown in Fig.2.23-(a)(b), below. The principal feature of these spectra are; (i) the lowest excitation levels present at 6.3 meV (~ 60 K) and 7.3 meV (~ 70 K) and (ii) a 'shoulder' on the elastic line extending out to ~ 1.5 meV was revealed [42].

A final remark about $Er_2Ti_2O_7$ is its behavior in applied magnetic field; no detailed study is yet made apart from the one in Ref. [43] which states that there is a further phase transition that occurs in a magnetic field. This is in some sense similar to the case for $Ho_2Ti_2O_7$, however, with a different character [43].

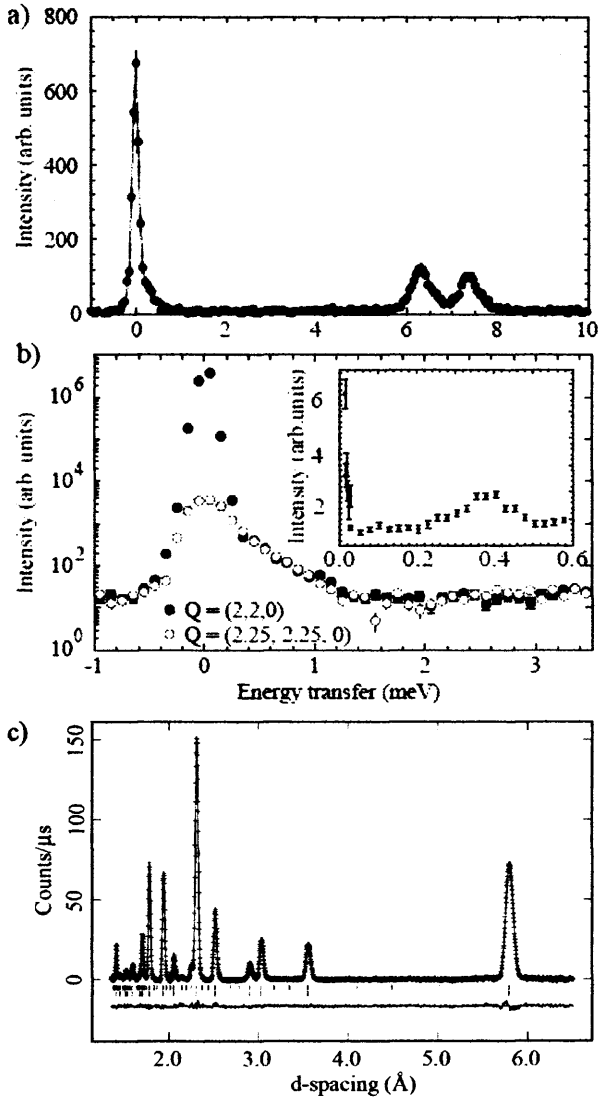

Figure 2.23: (a) Powder inelastic spectrum for $Er_2Ti_2O_7$ taken at $T = 1.8$ K (PRISMA, $|\mathbf{Q}| = 1.1$ Å^{-1}). (b) Single crystal inelastic spectrum for $Er_2Ti_2O_7$ taken at $T = 100$ mK (IN14). The strong elastic signal is the Bragg peak and a 'shoulder' is observed to this Bragg peak up to ~ 1 meV. Inset: Powder inelastic spectrum (IRIS, 50 mK) for $Er_2Ti_2O_7$ integrated over 15 spectra from $|\mathbf{Q}| = 0.4$ to 1 Å^{-1}. It resolves the low lying shoulder of the elastic Bragg peak into a weak excitation around 0.2 ~ 0.5 meV. (c) powder neutron profile refinement using the irreducible representation Γ_5 (ψ_2 and ψ_3) for $Er_2Ti_2O_7$ at 50 mK. The upper and lower ticks below the profile are the predicted magnetic and nuclear Bragg peak positions, respectively. [42]

We now turn our attention to the other related pyrochlore material containing Er^{3+} ions; the erbium stannate, $Er_2Sn_2O_7$. $Er_2Ti_2O_7$ and $Er_2Sn_2O_7$ are chemically very similar. They both adopt the pyrochlore structure with the magnetic Er^{3+} ions and non-magnetic Ti^{4+} or Sn^{4+} ions occupying lattices of corner-linked tetrahedra. Neither Ti^{4+} nor Sn^{4+} ions are expected to participate significantly in the magnetic properties. Their Curie-Weiss temperatures are both antiferromagnetic and are of the same order; θ_{CW} ($Er_2Ti_2O_7$) ~ - 22 K [51,71] and θ_{CW} ($Er_2Sn_2O_7$) = -14.32 K [76]. Also, their effective paramagnetic moment sizes of the Er^{3+} ions are similar (and close to the $^4I_{15/2}$ free ion value $g_J \sqrt{J(J+1)} = 9.59\mu_B$); $\mu_{eff}(Er_2Ti_2O_7) = 9.34\ \mu_B$ [51] and $\mu_{eff}(Er_2Sn_2O_7) = 9.55\ \mu_B$ [76].The only difference is the ion sizes of Ti^{4+} or Sn^{4+} ions, hence the lattice sizes. For the other members of the rare earth pyrochlore series the titanates and stannates show similar behaviors [14]. Therefore, it was a major surprise to discover that the low temperature bulk magnetic behavior of the two compounds $Er_2Ti_2O_7$ and $Er_2Sn_2O_7$ differs significantly; while $Er_2Ti_2O_7$ shows continuous magnetic ordering at T_N ~ 1.2 - 1.4 K [2,42,43], $Er_2Sn_2O_7$ remains disordered and fluctuating down to the lowest measured temperature T ~ 150 mK [76]. The powder neutron diffraction on $Er_2Sn_2O_7$ carried out by Bramwell *et al.* (on POLARIS diffractometer, ISIS, U.K) confirms the absence of order down to ~ 50 mK [78].

In order to verify this discrepancy, a μSR study of both materials were carried out by Lago and co-workers [77]. This μSR work confirmed the magnetic ordering in $Er_2Ti_2O_7$ around T_N = 1.1 K by a sharp increase in the muon depolarization rate at ~ 1 K. This is consistent with the dynamical slowing down at the ordering transition. However, it should be also noted that there remains a component of the spins quite strongly fluctuating down to ~ 50 mK (which is in turn consistent with the large susceptibility at low temperatures for this material [71]). A rather confusing result is obtained for the $Er_2Sn_2O_7$; although the spins are found to remain disordered fluctuating down to ~ 20 mK, there is a significant slowing down of spin dynamics at 1.1 K – similar to what happens in $Er_2Ti_2O_7$. These results are shown in Fig.2.24.

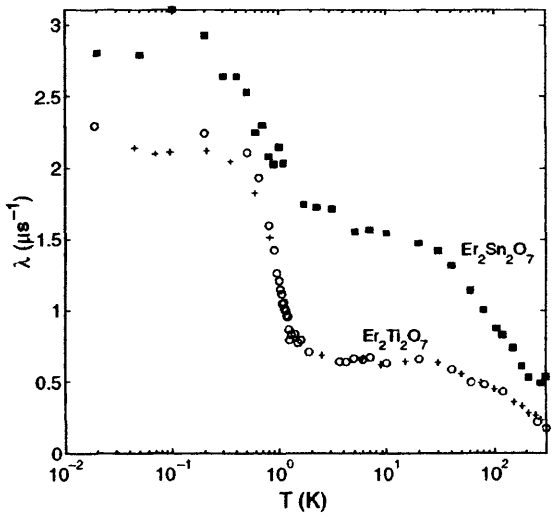

Figure 2.24: μSR depolarization rate of $Er_2Ti_2O_7$ and $Er_2Sn_2O_7$ showing sharp depolarization of the muons in both materials around $T_N(Er_2Ti_2O7) \sim 1.1$ K [77]. (circles and crosses respond to PSI and ISIS data, respectively.)

3. Aim and Plan of this Thesis

So far, we have listed the basic knowledge necessary to follow the science in this thesis; starting from the introduction to the general theory of magnetism and condensed matter in Chapter 1, it was followed by Chapter 2 that addressed the brief reviewing of the field of frustrated magnetism. In the upcoming Chapter 3, the readers will be guided through the technique of neutron scattering and how the obtained data will be analyzed in this work. Chapter 4 is devoted to show the experimental details regarding sample syntheses. Chapter 5 to 8 are the results chapters.

The three result chapters, 5, 6, and 7, are devoted to investigate the magnetic order properties of the series $Er_2Ti_{2-x}Sn_xO_7$ as a function of x ($x = 0 \sim 2$). From the anomalous results obtained in the comparison between the two end compounds,

$Er_2Ti_2O_7$ and $Er_2Sn_2O_7$ –where $Er_2Ti_2O_7$ magnetically orders at $T_N \sim 1.1$ K [42,71] but $Er_2Sn_2O_7$ remains disordered down to $T \sim 150$mK [76]- these materials are considered to be in the vicinity of a quantum critical point, where small changes in a parameter (such as the magnetic exchange or the crystal field parameters) influence the low temperature magnetic properties hugely. In this case, the nature of the transition is thought to be driven from a classical Néel-type order (in $Er_2Ti_2O_7$) to a fluctuating "quantum spin liquid" state (in $Er_2Sn_2O_7$). Our aim is to test this idea from different angles; first by looking at the magnetic diffraction patterns for the $Er_2Ti_{2-x}Sn_xO_7$ series (Chapter 5), secondly by searching the exact critical composition, $x_{critical}$, which gives the quantum critical point (Chapter 6) and finally by directly measuring and analyzing the crystal electric field of the $Er_2Ti_{2-x}Sn_xO_7$ series (Chapter 7). The question we ask ourselves is; 'What is the origin of the disappearance in the detected order in $Er_2Sn_2O_7$ in contrast to the observed order in $Er_2Ti_2O_7$? Are the single-ion moments of the Er^{3+} ions changing in size by the crystal electric field (i.e. is it a single-ion effect?) or do the moments remain constant in size but loses order because of the frustrated interactions (i.e. a collective effect?)?

The last result chapter (Chapter 8) will be devoted to describe the results obtained for the powder magnetic diffraction experiment in applied magnetic fields for the material $Gd_2Ti_2O_7$. The presence and the qualitative classification of the various phases present in the field-temperature phase diagram of $Gd_2Ti_2O_7$ will be investigated.

Finally, the summary of the thesis and some possible suggestions for the future work will be given in Chapter 9.

References for Chapter 2

[1] W.G.V.Rosser, *An Introduction to Statistical Physics*, Ellis Horwood ltd. Chicheste,1982.

[2] J.D.M.Champion, *Ph.D thesis,* University College London, 2002.

[3] S.T.Bramwell, M.J.P. Gingras, Science **294**, 1495 (2001).

[4] J.E.Greedan, J.Mater.Chem.**11**, 37 (2001).

[5] G.Toulouse, Commun.Phys. **2**, 115 (1977).

[6] P.W.Anderson, Phys.Rev. **102**, 1008 (1956).

[7] A.P.Ramirez, Ann.Rev.Mater.Sci. **24**, 453 (1994).

[8] J.E.Greedan, N.P.Raju, A.Maignan, Ch.Simon, J.S.Pedersen, A.N.Niraimathi, E.Gmelin, and M.A.Subramanian, Phys. Rev. B **54**, 7189 (1996).

[9] J.E.Greedan, M.Sato, N.Ali, and W.R.Datars, J. Solid State Chem. **68**, 300 (1987).

[10] J.E.Greedan,J.N.Reimers, C.V.Stagar, an L.Penny, Phys. Rev. B **43**, 5682 (1991).

[11] P.Schiffer and A.P.Ramirez, Comments Cond. Mat. Phys. **10**, 21 (1996).

[12] B.D.Gaulin, Hyperfine Inter. **85**, 159 (1994).

[13] A.P.Ramirez, Handbook Magn. Mater. **13**, 423 (2001).

[14] J.E.Greedan, J. Alloys. Comp. **408-412**, 444 (2006).

[15] J.Villain, Z.Phys.B **33**, 31 (1979).

[16] R.Moessner and J.T.Chalker, Phys. Rev. Lett. **80**, 2929 (1998).

[17] J.N.Reimers, A.J.Berlinsky, and A.C.Shi, Phys. Rev. B **43**, 865 (1991).

[18] R.Moessner, Can.J.Phys. **79**, 1283 (2001).

[19] J.T.Chalker, P.C.W.Holdsworth, and E.F.Shender, Phys. Rev. Lett. **68**, 855 (1992).

[20] References [20-23] of J.E.Greedan, J.Mater.Chem. **11**, 37 (2001).

[21] R.Moessner and J.T.Chalker, Phys. Rev. B **58**, 12049 (1998).

[22] J.N.Reimers, Phys. Rev. B **45**, 7287 (1992).

[23] Reference 1 of J.N.Reimers, Phys. Rev. B **45**, 7287 (1992).

[24] Reference 2 of J.N.Reimers, Phys. Rev. B **45**, 7287 (1992).

[25] Reference 14 - 16 of J.E.Greedan, J.Mater.Chem.**11**, 37 (2001).

[26] Reference 20 - 30 of J.E.Greedan, J.Mater.Chem.**11**, 37 (2001).

[27] Reference 20 - 30 of J.E.Greedan, J. Alloys. Comp. **408-412**, 444 (2006).

[28] Reference 31 - 39 of J.E.Greedan, J.Mater.Chem.**11**, 37 (2001).

[29] Reference 38 - 39 of J.E.Greedan, J.Mater.Chem.**11**, 37 (2001).

[30] S.Rosenkranz, A.P.Ramirez, A.Hayashi, R.J.Cava, R.Siddharthan, and B.S.Shastry, J.

Appl. Phys. **87**, 5914 (2000).

[31] Y.Qiu, *Ph.D thesis,* Johns Hopkins University, 2002.

[32] G.H.Wannier, Phys. Rev. **79**, 357 (1950).

[33] B.Canals and C.Lacroix, Phys. Rev. Let. **80**, 2933 (1998).

[34] B.Canals and C.Lacroix, Phys. Rev. B **61**, 1149 (2000).

[35] N.P.Raju, M.Dion, M.J.P.Gingras, T.E.Mason, J.E.Greedan, Phys. Rev. B **59**, 14489 (1999).

[36] J.N.Reimers, A.J.Berlinsky, and A.C.Shi, Phys. Rev. B **43**, 865 (1991).

[37] S.E.Palmer, J.T.Chalker, Phys. Rev. B **62**, 488 (2000).

[38] S.T.Bramwell and M.J.Harris, J. Phys.: Condens. Mat. **10**, L215 (1998).

[39] S.T.Bramwell, M.J.P.Gingras, and J. N. Reimers, J. Appl. Phys. **75**, 5523 (1994).

[40] R.Liebmann, *Statistical Mechanics of Periodic Frustrated Ising Systems*, Springer, Berlin, 1986.

[41] G.Ferey, Rev.Chim.Miner. **23**, 474 (1986).

[42] J.D.M.Champion, M.J.Harris, P.C.W.Holdsworth, A.S.Wills, G.Balakrishnan, S.T.Bramwell, E.Čižmár, T.Fennell, J.S.Gardner, J.Lago, D.F.McMorrow, M.Orendáč, A.Orendăcová, D.McK. Paul, R.I.Smith, M.T.F.Welling, A.Wildes, Phys. Rev. B **68**, 020401 (2003).

[43] M.J.Harris, S.T.Bramwell, T.Zeiske, D.F.McMorrow, and P.J.C.King, J. Magn. Magn. Mater. **177**, 757 (1998).

[44] M.J. Harris, S.T. Bramwell, D.F. McMorrow, T. Zeiske, K.W. Godfrey, Phys. Rev. Lett. **79**, 2554 (1997).

[45] S.T.Bramwell, M.J.P.Gingras and P.C.W.Holdsworth, '*Frustrated Spin Systems*' edited by H.T.Diep, World Scientific Publishing Co.Pte.Ltd, 2004; Chapter 7.

[46] W.F.Giaque, M.F.Ashley, Phys. Rev. **43**, 81 (1933); W.F.Giaque, J.W.Stout, J. Am. Chem. Soc. **58** ,1144 (1936).

[47] D.Bernal, R.H.Fowler, J. Chem. Phys. **1**, 515 (1933).

[48] L.Pauling, J. Am. Chem. Soc. **57**, 2680 (1935).

[49] J.D.Cashion, A.H.Cooke, M.J.M.Leask, T.L.Thorp, and M.R.Wells, J. Mater. Sci. **3**, 402 (1968).

[50] Y.M.Jana and D.Ghosh, Phys. Rev. B **61**, 9657 (2000).

[51] S.T.Bramwell, M.N.Field, M.J.Harris, and I.P.Parkin, J. Phys.: Condens. Mat. **12**, 483 (2000).

[52] A.P.Ramirez, A.Hayashi, R.J.Cava, R.Siddharthan, B.S.Shastry, Nature **399**, 333 (1999).

[53] M.Harris, Nature **399**, 311 (1999).

[54] D.J.Flood, J. Appl. Phys.**45**, 4041 (1974).

[55] B.C.den Hertog, M.J.P.Gingras, Phys. Rev. Lett. **84**, 3430 (2000).

[56] R.Siddharthan, B.S.Shastry, A.P.Ramirez, A.Hayashi, R.J.Cava, and S.Rosenkranz, Phys. Rev. Lett. **83** (9), 1854 (1999); R.Siddharthan, B.S.Shastry, and A.P.Ramirez, Phys. Rev. B **63**, 184412 (2001).

[57] P.P.Ewald, Ann. Phys. **64**, 253 (1921).

[58] S.T.Bramwell, M.J.Harris, B.C.den Hertog, M.J.P.Gingras, J.S.Gardner, D.F.McMorrow, A.R.Wildes, A.L.Cornelius, J.D.M.Champion, R.G.Melko, and T.Fennell, Phys. Rev. Lett. **87**, 047205 (2001).

[59] H.Fukazawa, R.G.Melko, R.Higashinaka, Y.Maeno, M.J.P.Gingras, Phys. Rev.B **65**, 054410 (2002).

[60] A.P.Ramirez, B.S.Shastry, A.Hayashi, J.J.Krajewski, D.A.Huse, and R.J.Cava, Phys. Rev. Lett. **89** (6), 067202 (2002).

[61] J.D.M.Champion, A.S.Wills, T.Fennell, S.T.Bramwell, J.S.Gardner and M.A.Green, Phys. Rev. B **64,** 140407 (2001).

[62] J.R.Stewart, G.Ehlers, A.S.Wills, S.T.Bramwell and J.S.Gardner, J. Phys.: Condens. Matter **16,** L321 (2004).

[63] O.Cépas and B.M.Shastry, Phys. Rev. B **69,** 184402 (2004).

[64] M.J.P.Gingras, B.C.den Hertog, M.Faucher, J.S.Gardner, S.R.Dunsiger, L.J.Chang, B.D.Gaulin, N.P.Raju and J.E.Greedan, Phys. Rev. B **62**, 6496 (2000).

[65] J. Rossat-Mignod, in Magnetic Structures, Vol. 23 of *Methods of Experimental Physics*, edited by K. Sköld and D. L. Price, Academic Press, New York,1986.

[66] O.A.Petrenko, M.R.Lees, G.Balakrishnan, D.M.K.Paul, Phys. Rev. B **70,** 012402 (2004).

[67] A.K.Hassan, L.P.Levy, C.Darie, P.Strobel, Phys. Rev. B **67**, 214432 (2003).

[68] H.A.Buckmaster and Y.H.Shing, Phys.Status Solidi A **12**, 467 (1973).

[69] E.Bertin, P.Bonville, J.P.Bouchard, J.A.Hodges, J.P.Sanchez, and P.Vulliet, Eur. Phys. J.B **27**, 347 (2002); P.Bonville, J.A. Hodges, M.Ocio, J.P.Sanchez, P.Vulliet, S.Sosin and D. Braithwaite, J. Phys. Condes. Matter **15**, 7777 (2003).

[70] O.Knop, F.Brisse, L.Castelliz, and Sutarno, Can. J. Chem. **43**, 2812 (1965).

[71] H.W.J.Blöte, R.F.Weilinga, and H.Huiskamp, Physica **43**, 549 (1969).

[72] M.Enjalran and M.J.P.Gingras, Phys. Rev. B **70**, 174426 (2004).

[73] A.J.Garcia-Adeva and D.L.Huber, Phys. Rev. B **65**, 184418 (2002); C.Pinettes, B.Canals, and C.Lacroix, ibid. **66**, 024422 (2002).

[74] M.E.Zhitomirsky, A.Honecker and O.A.Petrenko, Phys. Rev. Lett. **85**, 3269 (2000); M.E.Zhitomirsky, Phys. Rev. B **67**, 104421 (2003).

[75] V.N.Glazkov, M.E.Zhitomirsky, A.I.Smirnov, H.A.Krug von Nidda, A.Loidl, C.Marin, and J.-P.Sanchez, Phys. Rev. B **72**, 020409 (2005).

[76] K.Matsuhira , Y.Hinatsu, K.Tenya , H.Amitsuka and T.Sakakibara, J. Phys. Soc. Japan **71**, 1576 (2002).

[77] J.Lago, T.Lancaster, S.J.Blundell, S.T.Bramwell1, F.L.Pratt, M.Shirai and C.Baines, J. Phys.: Condens. Matter **17**, 979 (2005).

[78] S.T.Bramwell, Unpublished work.

Chapter 3

Neutron Scattering

The neutron is a powerful probe with which to study condensed matter, and has significant advantages over other forms radiation in the study of microscopic structure and dynamics. Both elastic (*diffraction*) and inelastic (*spectroscopy*) neutron scattering technique combines to give detailed information about the microscopic behaviour of condensed matter, playing a major role in the development of experimental and theoretical understanding of materials ranging from magnetism and superconductivity to chemical surfaces and interfaces.

In this chapter the general theory of neutron scattering is introduced [1-6]. Following it, some theoretical background to the magnetic structure analysis using the *representational analysis* method carried out in our work is also stated [6-11].

3.1 The Neutron

A neutron is an uncharged subatomic particle with mass 1,839 times that of electron. When bound in an atomic nucleus neutrons are stable, whilst having a mean lifetime approximately 1000 seconds as a free particle. It was first discovered in 1932 (Nobel Prize to Chadwick in 1935 for their discovery. Radioactive decay of radium emits α-particles which in turn encounter beryllium: ${}^{9}_{4}\mathrm{Be}+{}^{4}_{2}\mathrm{He}\rightarrow({}^{13}_{6}\mathrm{C})\rightarrow{}^{12}_{6}\mathrm{C}+{}^{1}_{0}\mathrm{n}$, and four years later it was demonstrated that neutrons could be Bragg diffracted by solids. The early experiments struggled with low flux from the radium-beryllium sources. However, when Enrico Fermi and his co-workers succeeded in the construction of the

first "atomic pile" in 1942 by showing that neutrons from fission of uranium (^{235}U) nucleus support a controlled chain reaction, the future became assured. Subsequent reactors produced more and more neutrons, enabling routine powder diffraction studies to be carried out, and the latest generation of high-flux reactors built in the 1960s and early 1970s produces a copious number of neutrons, making inelastic scattering studies possible. The 1994 Nobel Prize in Physics was awarded to Brockhouse and Shull for their pioneering contributions to the development of elastic and inelastic neutron scattering. This in fact explicitly represents the fact that neutron scattering is now widely accepted as one of the most important and versatile technique for probing condensed matter.

There are several advantages on using neutrons as probes to examine matter due to their properties. Some of the properties of the neutron are listed below.

Mass	$m_n = 1.675 \times 10^{-27}$ kg
Charge	0
Spin	½
Magnetic charge	$\mu_n = -1.913$ nuclear magnetons, μ_N
Life time	10.6 min, $n \rightarrow p + e + \upsilon$

For the purpose of neuron scattering, neutrons are considered as particles with a de Broglie momentum p and kinetic energy E:

$$p = \frac{h}{\lambda}, \quad E = \frac{h^2}{2m\lambda^2}, \tag{3.1}$$

where h is the Planck's constant, m is the mass of neutron and λ is the wavelength. The thermal neutrons that come out of the moderator of the reactor have $E \sim 25$ meV corresponding to $\lambda = 1.8$ Å, which is of the same order of magnitude as the interatomic distances in solids and liquids enabling neutrons to be used in diffraction techniques to gain structural information of the scattering system. Also, the energies of the thermal neutrons are in an appropriate range (1 μeV - 1 eV) in order to study dynamical phenomena, or excitations, in condensed matter. Measurements of the neutron energies in inelastic neutron scattering experiments thus provide accurate information on the energies of the excitations, such as quantum tunneling (in μeV range), through

molecular translations, rotations, vibrations and lattice modes to transitions within the electronic structures (in eV range).

The second point to note is that the neutron is an uncharged particle. This leads to a very weak interaction with matter and allows it to penetrate deeply into the target. This is a very important experimental convenience that is unique to the neutron probe, allowing the investigation of the interior of materials, rather than the surface layers. This feature also makes complex sample environment possible, such as the use of cryostat, furnaces and pressure cells, enabling the measurement of bulk processes under realistic conditions. More importantly, with zero charge there is no Coulomb barrier to overcome, therefore neutrons are scattered by the nuclear forces rather than the electron clouds. (In magnetic scattering however, neutrons are scattered by the unpaired electron spins.) This means that the scattering power (cross section) of an atom is not associated with its atomic number, unlike X-rays where the scattering power increases in proportion to the number of electrons in the atom. This makes it possible to see light atoms, such as hydrogen which is virtually transparent to X-rays, specially even in the presence of heavier atoms. Also neighboring elements in the periodic table can be distinguished, generally having substantially different cross sections and the nuclear dependence of the scattering allows isotopes of the same element to have scattering length substantially different from each other. Hence, isotopic substitution can be an useful labeling technique where you label different parts of an molecule.

Thirdly, although described as an uncharged particle, the neutron in itself is made up of distinctive sub-particles as quarks and gluons giving it a spin $S = 1/2$ nature. This internal distribution of sub-particles gives the neutron a net magnetic moment of 1.931 μ_N. This magnetic moment interacts with unpaired electrons spins in magnetic atoms with strength comparable to that of the nuclear interaction. Therefore, making the neutron a powerful probe of magnetic properties of solids.

3.2 Basic Crystallography

In this section we review some basic concepts and definitions of crystallography used in order to determine the (nuclear and magnetic) crystalline structure.

A nuclear crystal structure can be described in terms of lattice translations of a unit cell. The atomic position in the nth unit cell is given by

$$\mathbf{R}_{nj} = \mathbf{t}_n + \mathbf{r}_j \tag{3.2}$$

with $$\mathbf{t}_n = n_1\mathbf{a} + n_2\mathbf{b} + n_3\mathbf{c} \tag{3.3}$$

and $$\mathbf{r}_j = x_j\mathbf{a} + y_j\mathbf{b} + z_j\mathbf{c} \tag{3.4}$$

where **a**, **b** and **c** are unit vectors of the nuclear cell defined according to the International Tables; n_1, n_2 and n_3 are integers and x_j, y_j and z_j are fractional numbers less than unity. See Fig.3.1 for a schematic representation of these positional vectors in a unit cell. When a unit cell contains only one atom, the cell is called the Bravais cell and when the cell contains more than one atom, it is the non-Bravais cell.

Another important definition in crystallography is that defines the reciprocal lattice:

$$\mathbf{a}^* = \frac{2\pi}{v_0}\,\mathbf{b}\times\mathbf{c}, \quad \mathbf{b}^* = \frac{2\pi}{v_0}\,\mathbf{c}\times\mathbf{a}, \quad \mathbf{c}^* = \frac{2\pi}{v_0}\,\mathbf{a}\times\mathbf{b} \tag{3.5}$$

where v_0 is the volume of the unit cell, $v_0 = \mathbf{a}\cdot(\mathbf{b}\times\mathbf{c})$. A reciprocal lattice vector $\boldsymbol{\tau}$ (relative to the real lattice vector $\mathbf{R}_{nj}$) is then defined as

$$\boldsymbol{\tau} = h_\tau\mathbf{a}^* + k_\tau\mathbf{b}^* + l_\tau\mathbf{c}^* \tag{3.6}$$

where h_τ, k_τ and l_τ are integer numbers (called the Miller indices).

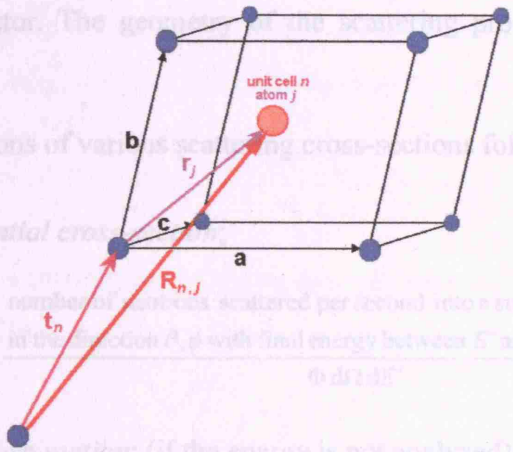

Figure 3.1: Position vectors $\mathbf{R}_{n,j} = \mathbf{t}_n + \mathbf{r}_j$ of the atom (n,j) for a non-Bravais crystal with unit vectors **a**, **b**, and **c** consisting the unit cell. The lattice vector $\mathbf{t}_n$ represents the position of the n-th unit cell and the position vector $\mathbf{r}_j$ defines the position of the atom j in the unit cell.

3.3 Nuclear Scattering

In this section a brief introduction to the formal derivation of neutron scattering equations is given. We first state the theory for the nuclear neutron scattering and proceed to magnetic neutron scattering in the next section,- section 3.4.

3.3.1 Scattering cross-sections

Consider a beam of monochromatic neutrons incident on some target scattering system. (The scattering system can be a crystal, an amorphous solid, a liquid or a gas.) Various types of measurement can be made on the neutron after they have interacted with the scattering system. The result in each case can be expressed in terms of a quantity known as a *cross-section*. Cross-sections are quantities that are actually measured during scattering experiments, hence, it is important to be able to calculate them.

In the scattering experiment, the number of neutrons scattered by the scattering

system in a given direction as a function of their final energy E' is counted using the neutron detector. The scattering angle $d\Omega$ is well defined by making the sample-detector distance large enough compared to the dimensions of both the sample and of the detector. The geometry of the scattering process is illustrated below in Fig.3.2.

Then the definitions of various scattering cross-sections follow as:

Partial differential cross-section;

$$\frac{d^2\sigma}{d\Omega\, dE'} = \frac{\text{number of neutrons scattered per second into a small solid angle } d\Omega \text{ in the direction } \theta,\phi \text{ with final energy between } E' \text{ and } E'+dE'}{\Phi\, d\Omega\, dE'} \tag{3.7}$$

Differential cross-section; (if the energy is not analyzed)

$$\frac{d\sigma}{d\Omega} = \frac{\text{number of neutrons scattered per second into } d\Omega \text{ in the direction } \theta,\phi}{\Phi\, d\Omega} \tag{3.8}$$

Total scattering cross-section; (if the energy nor the angle is analyzed)

$$\sigma_{tot} = \frac{\text{total number of neutrons scattered per second}}{\Phi} \tag{3.9}$$

where Φ is the flux of the incident neutrons. (Note: these cross sections do not take account of spin states of the neutron. However, this becomes important when one need to carry out polarization experiments.)

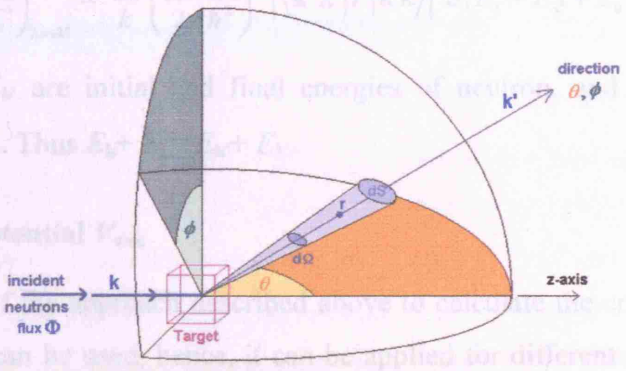

Figure 3.2: Geometry for scattering experiment.

The theory itself is a quantum mechanical scattering theory in which the state of the system and neutron before and after scattering are considered; $\lambda \rightarrow \lambda'$ for scattering system and $\mathbf{k} \rightarrow \mathbf{k}'$ for neutron. The sum in $(d\sigma/d\Omega)_{\lambda\rightarrow\lambda'}$ is taken over all the values of $\mathbf{k}'$ that lie in the small solid angle $d\Omega$ in the direction θ, ϕ, keeping the values of $\mathbf{k}$, λ and λ' constant. From the definitions of $d\sigma/d\Omega$ given in Eqn.3.8 this is

$$\left(\frac{d\sigma}{d\Omega}\right)_{\lambda\rightarrow\lambda'} = \frac{1}{\Phi}\frac{1}{d\Omega}\sum_{\mathbf{k}' \text{ in } d\Omega} W_{\mathbf{k},\lambda\rightarrow\mathbf{k}',\lambda'} \qquad (3.10)$$

where $W_{\mathbf{k},\lambda\rightarrow\mathbf{k}',\lambda'}$ is the number of transitions per second from the state $\mathbf{k},\lambda$ to the state $\mathbf{k}',\lambda'$. This can be evaluated using Fermi's golden rule and eventually gives

$$\left(\frac{d\sigma}{d\Omega}\right)_{\lambda\rightarrow\lambda'} = \frac{k'}{k}\left(\frac{m}{2\pi\hbar^2}\right)^2 \left|\langle \mathbf{k}'\lambda'|V|\mathbf{k}\lambda\rangle\right| \qquad (3.11)$$

where V is the potential for the neutron-nucleus system and m is the mass of neutron. What it is done here is to change the expression of $d\sigma/d\Omega$ involving sum over neutron states $\sum_{\mathbf{k}'}$ (Eqn.3.10) into an expression evaluated at a particular $\mathbf{k}'$. For fixed $\mathbf{k}$, λ, and λ', there is a very narrow range of $|\mathbf{k}'|$ values for which transitions are probable and the centre of this range is the value of $|\mathbf{k}'|$ corresponding to conservation of energy in the overall neutron-scatterer system. Thus, it is this particular $\mathbf{k}'$ which must be inserted in Eqn.3.11. Because of this, all the scattered neutrons in the $(d\sigma/d\Omega)_{\lambda\rightarrow\lambda'}$ cross section have the same energy. Consequentially the partial differential cross section is

$$\left(\frac{d\sigma}{d\Omega\, dE'}\right)_{\lambda\rightarrow\lambda'} = \frac{k'}{k}\left(\frac{m}{2\pi\hbar^2}\right)^2 \left|\langle \mathbf{k}'\lambda'|V|\mathbf{k}\lambda\rangle\right| \delta(E_\lambda - E_{\lambda'} + E_{\mathbf{k}} - E_{\mathbf{k}'}) \qquad (3.12)$$

where $E_{\mathbf{k}}$ and $E_{\mathbf{k}'}$ are initial and final energies of neutron, and E_λ and $E_{\lambda'}$ of the scattering system. Thus $E_{\mathbf{k}} + E_\lambda = E_{\mathbf{k}'} + E_{\lambda'}$.

3.3.2 Nuclear potential V_{nuc}

The usefulness of the approach described above to calculate the cross sections is that any potential V can be used, hence, it can be applied for different systems. The basic scheme can be followed for either nuclear of magnetic scattering with interchanged

potential functions.

The potential function used for the nuclear scattering is the Fermi pseudo-potential,

$$V(\mathbf{r}) = \frac{2\pi\hbar^2}{m} b\,\delta(\mathbf{r}) \tag{3.13}$$

where b is the scattering length, and the three-dimensional Dirac delta function $\delta(\mathbf{r})$ ensures the interaction to be very short ranged.

In an actual experiment we do not measure the cross-section for a process in which the scattering system goes from a specific state λ to another state λ'. Instead we measure the partial differential cross-section $(d^2\sigma/d\Omega dE_{k'})$. To obtain this quantity we must first sum $(d^2\sigma/d\Omega dE_{k'})_{\lambda\to\lambda'}$ over all final states λ', keeping the initial state λ fixed, and then average over all λ. This averaging is carried out using the probabilities of the system being in each state λ, given by the Boltzmann distribution.

3.3.3 Scattering length *b*

Here we look into the concept of scattering length b a bit closer by considering the scattering of neutrons by a single fixed nucleus. The nuclear forces which cause the scattering have a range about 10^{-14}-10^{-15} m; hence, is much shorter than the wavelengths of the thermal neutrons (~10^{-10} m). It is then easy to see that incoming neutron wavefunction ψ_{inc} is represented by a plane wave and the scattered wavefunction ψ_{sc} by spherically symmetric wave:

$$\psi_{inc} = \exp(ikz) \tag{3.14}$$

$$\psi_{sc} = -\frac{b}{r}\exp(ik'r) \tag{3.15}$$

where $k = k'$ since the scattering is elastic (the energy of the thermal neutron is too small to change the internal energy of the nucleus). Here, the origin is taken to be at the nucleus, z-axis is along the direction of the wavevector **k** and **r** is the position of the scattered neutron. The magnitudes of **k** and **r** are $k = 2\pi/\lambda$ and r, respectively. The scattering length can be real or complex. The imaginary parts of b corresponds to absorption, hence, nuclei with imaginary bs (e.g. ^{103}Rh, ^{113}Cd, ^{157}Gd, ^{176}Lu) strongly absorb neutrons. However, the majority of the nuclei have real b which is independent

of the energy of the neutron.

The value of the scattering length depends on the particular nucleus, and the spin state of the nucleus-neutron system. The neutron has spin ½. Suppose the nucleus has spin I (not zero). Then the spin of the nucleus-neutron system is either $I + ½$, or $I - ½$. Each spin state has its own value of b. Due to the lack of the proper theory of nuclear forces the values of b cannot be deduced theoretically and hence is found experimentally.

3.3.4 Coherent and incoherent scattering

Real scattering systems often have a variable scattering length b at different sites. This is because there is a distribution of nuclear spins and/or isotopes in the system. This separates the cross section into two terms, *coherent* and *incoherent*. Coherent scattering depends on the correlation between the positions of *same* nucleus at different times, and on the correlation between positions of the *different* nuclei at different times. It therefore gives interference effects. On the other hand, the incoherent scattering depends only on the correlation between the positions of the *same* nucleus at different times, and hence, it does not give interference effects.

Assuming there is no correlation between position and scattering length, the coherent scattering will depend on the average scattering length; $\sim (\overline{b})^2$. The incoherent scattering is due to the random distribution of deviations of the scattering lengths form the mean value and depends on $\sim (\overline{b^2} - (\overline{b})^2)$. One important example in neutron scattering that gives large incoherent scattering length is ^{1}H ($\sigma_{coh} = 1.8$, $\sigma_{inc} = 80.2$).

3.3.5 Nuclear Bragg scattering

After some long mathematical manipulations, the differential cross section of coherent elastic scattering from a crystalline system is expressed as

$$\left(\frac{d\sigma}{d\Omega}\right)_{coh\ el} = N\frac{(2\pi)^3}{v_0}\sum_{\tau}\delta(\mathbf{Q}-\boldsymbol{\tau})\left|F_N(\mathbf{Q})\right|^2 \qquad (3.16)$$

where $F_N(Q)$ is the nuclear unit cell structure factor given by

$$F_N(\mathbf{Q}) = \sum_j \bar{b}_j \exp(2\pi i \mathbf{Q}\cdot\mathbf{r}_j) \exp(-W_j) \qquad (3.17)$$

where $\bar{b}_j$ is the average scattering length of atom j, τ and $\mathbf{r}_j$ are the reciprocal lattice vector and the fractional coordinate vector of atom j, respectively (defined in section 3.2), and $\mathbf{Q}$ is the scattering vector; $\mathbf{Q} = \mathbf{k} - \mathbf{k}'$. W_j is the Debye-Waller factor of atom j, which reflects the thermal motion of the atom about its equilibrium position.

The scattering vector $\mathbf{Q}$ has dimensions of reciprocal length, hence can be expressed similarly to τ as

$$\mathbf{Q}\,(h_Q, k_Q, l_Q) = h_Q\,\mathbf{a}^* + k_Q\,\mathbf{b}^* + l_Q\,\mathbf{c}^*, \qquad (3.18)$$

$$\tau\,(h_\tau, k_\tau, l_\tau) = h_\tau\,\mathbf{a}^* + h_\tau\,\mathbf{b}^* + h_\tau\,\mathbf{c}^*, \qquad (3.19)$$

where h, k and ls are all integer numbers. The scalar $\mathbf{Q}\cdot\mathbf{r}$ in the interference term in the expression of structure factor (Eqn.3.17) becomes

$$\mathbf{Q}\,(h_Q, k_Q, l_Q)\cdot\mathbf{r}_j\,(x_j, y_j, z_j) \;=\; h_Q\,x_j + k_Q\,y_j + l_Q\,z_j. \qquad (3.20)$$

Eqn.3.16 tells us that the scattering occurs only when $\mathbf{Q} = \tau$. This condition is the same as Bragg's law for X-ray scattering. Thus, coherent elastic scattering is simply Bragg scattering. See Fig.3.3 below for the illustrative view. As the relations for the reciprocal lattice vector τ and **k**s

$$\tau = 2k\sin\theta/2, \quad \tau = n\,2\pi/d \qquad (3.21)$$

hold, where d is the spacing of the crystal planes and n is an integer, and since $k = 2\pi/\lambda$, these result in the expression

$$n\lambda = 2d\sin\theta/2, \qquad (3.22)$$

which is the familiar form of Bragg's law. Note that ½ θ is the angle between **k** and the crystal planes (Fig.3.3-(c)).

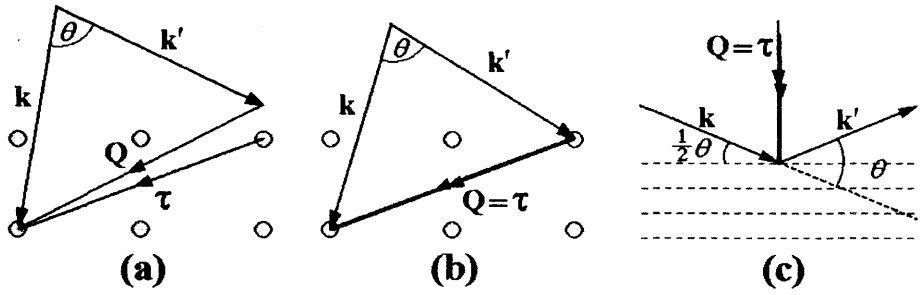

Figure 3.3: Bragg's law shown in reciprocal space. The grey circles are the reciprocal lattice points, **k** and **k'** are incident and scattered final wave vectors, respectively, and **Q** and τ are scattering vector and reciprocal lattice vector, respectively. (a) $Q \neq \tau$; no coherent elastic scattering. (b) $Q = \tau$; coherent elastic scattering occurs. (c) Relation of $\mathbf{Q} = \mathbf{k} - \mathbf{k'}$ shown in respect to the planes of atoms (dashed lines). [1]

Eqn.3.16 and 3.17 form the basis of calculating the intensity of a nuclear peak. If an intensity of a selected single reflection (particular **Q**) is to be calculated, then the sum over τ in Eqn.3.16 can be omitted. The δ-function simply adds the restriction that the equation should only work at the Bragg peak and the prefactor would eventually be absorbed into a scale factor.

3.4 Magnetic Scattering

This section is devoted to introduce one to the theory of magnetic neutron scattering. The section is divided into two sub-sections. In the first part the magnetic analogy to the nuclear scattering theory stated in the previous section is outlined. In the second part an approach to a magnetic structure analysis method, using a technique called the *representational analysis* method, is shown.

3.4.1 Magnetic neutron scattering theory

3.4.1.1 Magnetic potential V_{mag}

Despite its neutrality, the neutron has a magnetic moment, μ_n. This means that the neutron interacts with unpaired electrons. This interaction is the consequence of the energy of the neutron magnetic moment μ_n in the magnetic field **H** arising from the unpaired electrons. The magnetic field **H** is due to the contribution of the magnetic dipole (spin part) and the momentum of the electron that leads to a current (orbital part). For a single electron i in an atom with spin $\mathbf{s}_i$ and momentum $\mathbf{p}_i$ at a position $\mathbf{r}_i$, this interaction energy is expressed by

$$V_{mag}(\mathbf{r}) = -\boldsymbol{\mu}_n \cdot \mathbf{H} = -\mu_n \cdot \left(\text{curl} \frac{-2\mu_B \mathbf{s}_i \times \hat{\mathbf{r}}}{r^2} - \frac{2\mu_B \mathbf{p}_i \times \hat{\mathbf{r}}}{\hbar r^2} \right) \qquad (3.23)$$

where $\mu_n = -\gamma \mu_N \sigma$ (γ=1.9132), μ_N is the nuclear magneton, and σ is the Pauli spin operator for the neutron. Magnetic scattering is more complicated than nuclear because both the μ_n-$\mathbf{s}_i$ spin dipole-dipole interaction and the μ_n-$\mathbf{p}_i$ dipole-current interaction for orbital motion are long ranged and non-central. By non-central interaction we mean that the scattering amplitude is **Q**-(i.e. scattering angle) –dependent; the scattering gets weaker as 2θ gets large. This also means that, unlike the nuclear scattering where the scattering length is expressed by a constant value b, a **Q**-dependent form-factor $f(\mathbf{Q})$ must be introduced for magnetic scattering as for X-ray scattering. The appearance of the spin operator σ of the neutron in the magnetic potential makes the polarized neutron scattering such a powerful tool for the microscopic investigation of magnetic materials.

3.4.1.2 Magnetic Bragg scattering

With an unpolarized beam the scattering cross-section is simply a sum of the nuclear and magnetic parts;

$$\frac{d\sigma}{d\Omega}(\mathbf{Q}) = \frac{d\sigma_{nuc}}{d\Omega}(\mathbf{Q}) + \frac{d\sigma_{mag}}{d\Omega}(\mathbf{Q}); \qquad (3.24)$$

where

$$\frac{d\sigma_{mag}}{d\Omega}(\mathbf{Q}) = N\frac{(2\pi)^3}{v_0}\sum_{\tau}\sum_{\mathbf{k}}|\mathbf{F}_{M\perp}(\mathbf{Q})|^2\,\delta(\mathbf{Q}-\mathbf{k}-\tau) \qquad (3.25)$$

with

$$\mathbf{F}_{M\perp}(\mathbf{Q}=\tau+\mathbf{k}) = p\,f(\mathbf{Q})\sum_{j}\mathbf{S}_{\perp j}\exp 2\pi i\,\mathbf{Q}\cdot\mathbf{r}_j \qquad (3.26)$$

where $p = 0.2969\times10^{-12}$ cm represents the scattering amplitude at $Q = 0$ for a single magnetic moment of 1 μ_B and **k** is the ordering vector (or propagation vector) which will be explained in detail in the following section. One point worth noticing is that the magnetic structure factor is now a vector where the nuclear structure factor was a scalar quantity.

It turns out that magnetic scattering amplitude operator is related to the Fourier transform of the total (spin + orbital) magnetization component perpendicular to the scattering vector **Q**. This angular dependence of the scattering amplitude gives the possibility of determining both the amplitude and the orientation of the magnetic moment. The perpendicular spin component $\mathbf{S}_\perp$ in the expression of the magnetic structure factor (Eqn.3.25) can be found using the identity

$$\mathbf{S}_\perp = \mathbf{S} - (\mathbf{S}\cdot\hat{\mathbf{Q}})\hat{\mathbf{Q}}. \qquad (3.27)$$

The δ-function in Eqn.3.25 is different from that of nuclear scattering (compare with Eqn.3.16) This is due to the fact that the magnetic unit cell need not have the same size or symmetry as the nuclear one. When the magnetic structure is commensurate and not symmetry lowering (e.g. a ferromagnet), the magnetic Bragg peaks occur only on top of the nuclear peaks; it is said that the magnetic structure is related to the nuclear structure by the propagation vector **k** = 000. On the other hand, if the two structures are different then additional magnetic Bragg peaks (related by **k** ≠ 000) can occur. In general, each Brillouin zone will contain a single nuclear peak at the origin plus a number of magnetic Bragg peaks about it, related by each distinct **k**, and its symmetry equivalents. We shall look further into the use of this propagation vector **k** in describing the magnetic structure in the next section.

3.4.2 Magnetic structure analysis method

3.4.2.1 Ordering wave vector - k

Magnetic structures can be described by the periodic repetition of a magnetic unit cell, just as crystal structures are constructed by translation of a nuclear unit cell. Both nuclear and magnetic structures are periodic properties of the crystal, but they need not have the same periodicity. Instead, here we introduce the concept of the *ordering vector* (or *propagation vector*) **k**, a wave vector that connects the two periodicities. This accomplishment is due to the propagation vector **k** describing the relation between moment orientations of equivalent magnetic atoms in different nuclear unit cells. Instead of building a complete magnetic unit cell (which could contain thousands of magnetic atoms) the use of **k** with the knowledge of the nuclear unit cell provides us a simple and general formalism for the description of a magnetic structure. Usually, **k** is determined by carrying out a powder neutron experiment; it can be deduced from the Bragg angles of the magnetic peaks with respect to that of nuclear peaks.

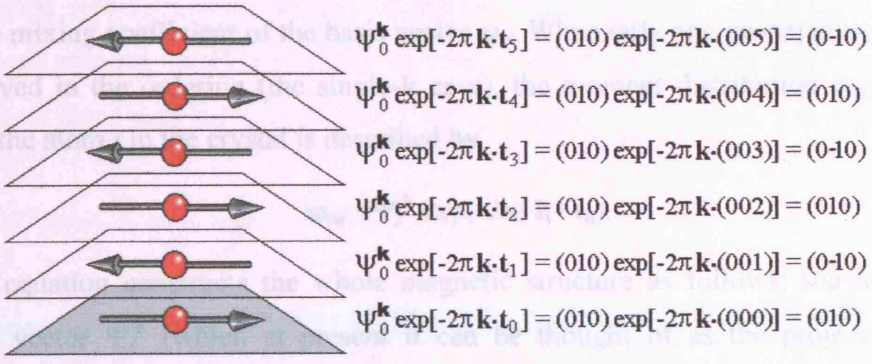

Figure 3.4: Description of translational properties of magnetic moments in the ordered structure with propagation vector **k**. In this example the basis vector for the moment in the zeroth cell is $\Psi_0^{\mathbf{k}}$ = (010) and **k** = 00½. Each plane corresponds to a lattice translation of **t** = 001.

3.4.2.2 Description of magnetic order

Any general magnetic order can be described by the distributions of magnetic moments $\mathbf{m}_j$. Let us first look at how the magnetic moment itself should be described. There are various ways and coordinate systems that can be used to describe a magnetic moment (e.g. Cartesian, polar or crystallographic coordinates). Here we choose to describe the projection of the moments along the crystallographic axes by a *basis vector* Ψ which has components along these axes. When a basis vector is real, like Ψ = (0,0,1), it simply corresponds to the projection of the moment along the different crystallographic axes, and so:

$$\mathbf{m}_j = \Psi_j. \tag{3.28}$$

The values Ψ_j will be taken as being those of atom j in the zeroth unit cell (i.e. the crystallographic unit cell). In actual cases, these projections of the moment are often not described just by one basis vector, but several:

$$\Psi_j^{\boldsymbol{k}} = \sum_{\nu} C_\nu \psi_\nu, \tag{3.29}$$

where ψ_ν represents the ν components of $\Psi_j^{\boldsymbol{k}}$ for a given propagation vector $\mathbf{k}$ and C_ν is the mixing coefficient of the basis vector ψ_ν. When only one propagation vector $\mathbf{k}$ is involved in the ordering (the single-$\mathbf{k}$ case), the moment distribution $\mathbf{m}_{nj}$ associated with the atom j in the crystal is described by

$$\mathbf{m}_{nj} = \Psi_j^{\mathbf{k}} \exp(-2\pi i\, \mathbf{k} \cdot \mathbf{t}_n). \tag{3.30}$$

This equation constructs the whole magnetic structure as follows; starting with the basis vector $\Psi_j^{\mathbf{k}}$ (which at present it can be thought of as the projections of the magnetic moment along the a, b, c crystallographic axes with relation to the atomic site j in the zeroth site) the translation properties in real space is described by the exponential term. This is best understood in reference to Fig.3.4. In this way, $\mathbf{k}$-defined translations of a basis vector of a unique site j will fill the whole space to describe the entire magnetic structure of the crystal; just as crystal structures are described by translations of a basic unit, the nuclear unit cell.

When the system is cooled and condenses into a state with magnetic order,

different types of magnetic structure results according to the way in which the magnetic energy is minimized. These are structures with ground state configuration characterized by (a) one **k** vector (single-**k** structure) or (b) several **k** vectors (multi-**k** structure). In order to see how multi-**k** situations occur we have to introduce ourselves the language of group theory. The propagation vector **k** is one member of a set of equivalent wave vectors $\mathbf{k}_p$ called the star of **k**. The other wave vectors in the star are obtained by applying the symmetry operations of the crystallographic space group G_0 to **k**. Multi-**k** structures often occur when Crystal Electric Field (CEF) or higher-order exchange interactions (e.g. quadrupole interaction) are dominant. When the system orders with a multi-**k** ground state, the moment distribution $\mathbf{m}_{nj}$ will be now expressed by the Fourier expansion;

$$\mathbf{m}_{nj} = \sum_{\mathbf{k}} \Psi_j^{\mathbf{k}} \exp(-2\pi i\, \mathbf{k} \cdot \mathbf{t}_n), \qquad (3.31)$$

where the summation is made over wave vectors **k** that are confined to the first Brillouin zone of the Bravais lattice j of the nuclear cell.

Many magnetically ordered structures are possible since there are 1421 magnetic symmetry groups. These magnetic symmetry groups are classified according to the crystallographic space group plus additional symmetry operations to take account the magnetic moment at each site. The ordered structure may be collinear, non-collinear, or helical depending on the basis function $\Psi_j^{\mathbf{k}}$ and the number of **k** involved.

3.4.2.3 Representational Analysis (RA)

Theory of RA method

As we have explained above, two pieces of information are required in order to express a magnetic structure: (1) the propagation vector(s) **k**, and (2) the coupling, orientation, and the value of the Fourier components $\Psi_j^{\mathbf{k}}$. Group theory cannot be of any help in determining **k** but it greatly simplifies the step of determining $\Psi_j^{\mathbf{k}}$ if the symmetry of both the paramagnetic space group G_0 and the magnetic sites are correctly taken into account. Specially, when a large number of magnetic atoms are present in the unit cell, group theory can be extremely useful in enumerating possible

magnetic structures compatible with the crystal symmetry.

Out of all the symmetry elements in paramagnetic space group G_0, those that leave **k** invariant form a sub-group of G_0; this is called '*little group* $G_{\mathbf{k}}$'. The power and utility of group theory calculations with regards to the determination of magnetic structures comes from the Landau theory of a second-order phase transition [11]. In simplest words, this states that a second-order magnetic phase transition can involve the build up of magnetic fluctuations that have the symmetry of only one irreducible representation (IR) of $G_{\mathbf{k}}$. Therefore, the resulting magnetic structure can be described by the basis vectors $\Psi_j^{\mathbf{k}}$ associated with only that IR. This greatly limits the number of possible magnetic models and the number of parameters that are involved in their refinement. (Note: even in the cases where the transition is first-order, nature is often kind to us and the structures that result are often the same as would be predicted for a second-order transition.)

The technique that is used in this thesis to calculate the magnetic structure is called the *Representational Analysis* method. This technique applies group theory to magnetic structures and allows the determination of the different symmetry- allowed magnetic structures given only the knowledge of (i) the crystallographic space group G_0, (ii) propagation vector **k** and (iii) the atomic coordinates of the magnetic atoms before the phase transition.

For a magnetic structure to be possible, it must be compatible with all of the symmetry operations of $G_{\mathbf{k}}$ simultaneously. The set of matrices that describes how the moments transform under all the symmetry operations g of $G_{\mathbf{k}}$ makes up a magnetic representation $\Gamma_{\mathbf{k}}$. This is decomposed into orthogonal IRs (Γ_θ) of $G_{\mathbf{k}}$:

$$\Gamma_{\mathbf{k}} = \sum_{\theta} n_\theta \Gamma_\theta \tag{3.32}$$

where the number of times, n_θ, that the IR Γ_θ appears in the magnetic representation $\Gamma_{\mathbf{k}}$ is given by

$$n_\theta = \frac{1}{|G_{\mathbf{k}}|} \sum_{g \in G_{\mathbf{k}}} \chi(g) \chi_\theta^*(g) \ . \tag{3.33}$$

Here, χ is the character of the magnetic representation $\Gamma_{\mathbf{k}}$, χ_θ is the character of the IR Γ_θ, and $|G_{\mathbf{k}}|$ is the order of $G_{\mathbf{k}}$ (i.e. total number of symmetry elements, g). The sum is

taken over all symmetry elements g in the little group $G_{\mathbf{k}}$.

Now, the μ unique basis vectors Ψ_v that transform according to the μ-dimensional IR $\Gamma_\theta{}^{(\mu)}$ are projected out of any given row of the representation matrix D_v using the projection operator formula

$$\psi_v^{i\lambda} = \sum_{h \in G_{\mathbf{k}}} D_v^{\lambda *} \sum_i \delta_{i,gi}\, \delta_h\, R^h\, \psi^{i\alpha} \tag{3.34}$$

where δ_h is the determinant of the representational matrix of rotational part h of the symmetry elements and $\lambda = 1, 2 \ldots \mu$. ψ^i is the column matrix of the spin component projected from the test function ψ^α.

Practical implementation of RA method

The symmetry calculations described above is complicated and is performed using a computer program 'SARA*h*-2K Representational Analysis' written by Andrew Wills [7]. Given only the information about (i) the paramagnetic space group, (ii) the magnetic atom positions and (iii) the propagation vector of the magnetic phase, the SARA*h* program calculates and computes out the list of symmetry-allowed basis vectors, Ψ_v. This software maximizes the power of the symmetry analysis in determining the magnetic structure and the advantage is that no knowledge of theoretical Hamiltonian or crystal field are necessary.

Once the symmetry-allowed basis vectors are computed out, the orientations of the atomic spins can be represented by summing up these basis vectors belonging to a specific irreducible representation;

$$S^i = \sum_v C_v^i\, \psi_v^i \tag{3.35}$$

where S^i is the atomic spin for the magnetic atom i and $C_v{}^i$ is the mixing coefficient for atom i of the basis vector v. SARA*h* is integrated with the standard structure analysis software package, GSAS [12] (and Fulprof [13]) and thus handling the refinement is straightforward. Once the irreducible representation (Γ) to be examined is chosen, the user should refine the orientation of the atomic moment by refining the mixing coefficients. Then this magnetic structure created by SARA*h* will be entered in to the

GSAS's .EXP file and an appropriate magnetic structure factor will be calculated. GSAS then performs a least-squares fit to the data, by refining the length of the magnetic moments (with the orientation fixed). Real examples of the representational analysis of the neutron scattering data using SARA*h* will be shown in the result chapters; Chapter 5.

Reference for Chapter 3

[1] G.L.Squires, *Introduction to the Theory of Thermal Neutron Scattering*, Cambridge Univ. Press, 1978.

[2] J.Rossat-Mignot, *Methods in Experimental Physics*, ed. K.Scöld and D.L. Price, Academic Press, 1987.

[3] S.W.Lovesey, *International Series of Monographs on Physics 72, Theory of Neutron Scattering from Condensed matter* Vol.1, Oxford University Press, Inc.,1984.

[4] S.W.Lovesey, *International Series of Monographs on Physics 72, Theory of Neutron Scattering from Condensed matter* Vol.2, Oxford University Press, Inc.,1984.

[5] G.E.Bacon, *Neutron Diffraction*, Clarendon Press, Oxford, 1955.

[6] C.Kittel, *Introduction to Solid State Physics*, 7th ed., John Wiley & Sons, Inc., 1996.

[7] A.S.Wills, Physica B **276**, 680 (2000).

[8] A.S.Wills, Phys. Rev. B **63**, 064430 (2001);
program available from ftp://ftp.ill.fr/pub/dif/sarah/..

[9] E.F.Bertaut, Acta. Cryst A **24**, 217 (1968).

[10] Yu.A.Izyumov, V.E.Naish and R.P.Ozerov, *Neutron Diffraction of Magnetic Materials*, Consultants Bureau, New York, 1991.

[11] Y.A.Izyumov, V.E.Naish, J. Magn. Magn. Matter **12**, 239 (1979).

[12] A.C. Larsen and R.B. von Dreele, *General Structure Analysis System,* Lansce, Los Alamos National Laboratory, Los Alamos, 1994.

[13] J. Rodriguez-Carvajal, Physica B **192**, 55 (1993).

Chapter 4

Sample Synthesis

In this chapter we summarize the methods taken and results obtained during the synthesis and the characterization of the samples made. Two batches of samples with the formula $Er_2Ti_{2-x}Sn_xO_7$ are synthesised and characterized. [Batch (i): x = 0, 0.5,1, 1.5 and 2 and batch (ii): x = 1.5, 1.55, 1.6.....1.95, and 2.0.]

4.1 Solid State Synthesis: Preparation Methods for Powder Samples

All the samples used in this project were prepared in powder state using standard solid synthesis method. The method is called *solid state reaction* where stoichiometric quantities of the starting powder materials are mixed and ground together and then heated in a furnace for prolonged periods. This old, simple and not very sophisticated method is intrinsically slow because the reactants are not very homogeneously mixed at the atomic levels even though they seem well-mixed at particle levels (~1μm-10^{-2}mm). Therefore, thorough grinding plays an important role in this method. Also, by pressing them into pellets, the distances between the reactant particles are reduced, hence the reaction is enhanced.

The required stoichiometric quantities of the powder reactants, Er_2O_3, TiO_2 and/or SnO_2 were weighed out accurately (to ±0.0005 g) and were ground together using an agate mortal and pestle (for about 15 minutes) until a homogeneous fine powder was obtained. The powder was pressed into pellets (7-10 tonnes), and the palletized reactants were then placed in a high density alumina boat which was then placed in a furnace and heated at a temperature range T = 1200 ~ 1400 °C. After the initial

20-24 hours of heating, the pellets were taken out of the furnace and were reground together, then placed back in the furnace and heated for shorter periods (from 12 up to 20 hours). This process was repeated 3-4 times to ensure the resulting product is well homogenous and impurity free.

X-ray diffraction (XRD) patterns of the prepared samples were measured and were used as an indication for the quality of the samples prepared, i.e. to verify whether the sample was of homogeneous phase with no reactants left nor contaminated with impurities. Further attempts with prolonged firing times and higher temperatures were then made if necessary, according to the XRD patterns.

In this thesis, two batches of $Er_2Ti_{2-x}Sn_xO_7$ samples were synthesized. The first batch with x = 0 (labelled SN0) , 0.5 (SN50), 1 (SN100), 1.5 (SN150) and 2 (SN200) was made in bulk quantities, ~30g per compound to be used in the neutron experiments. The second batch with x = 1.5 (SN150), 1.55 (SN155), 1.6 (SN160), 1.65 (SN165), 1.7 (SN170), 1.75 (SN175), 1.8 (SN180), 1.85 (SN185), 1.9 (SN190), 1.95 (SN195) and 2 (SN200) was synthesized for magnetization measurements; hence was made ~ 2 g per compound.

4.2 X-ray Diffraction

4.2.1 X-rays as a probe

All the structures of the compounds synthesized in this thesis were examined using powder X-ray diffraction. X-rays are electromagnetic radiation with wavelength ~ 1 Å (10^{-10} m), which may be produced by bombarding a metal with high-energy electrons. The high-energy electron expels the core electron of the metal, the electron of outer shell then falls into the resulting vacancy and X-rays are emitted as the transition energy. The wavelength dimension of X-ray is similar to that of typical interatomic separations (~ 2–3 Å) in crystals, hence X-rays are widely used in diffraction techniques for crystalline compounds.

4.2.2 Diffraction and Braggs law

Here we quickly recap the concept of diffraction. Diffraction of a monochromatic radiation interacting with the samples arises due to the constructive interference of elastically scattered waves by the atoms in the crystals. Because the wavelength of the probing X-ray beams are comparable to the separation of lattice planes, X-ray diffraction method has grown to a extremely powerful method in crystal structure analysis. By regarding crystals as stacks of reflecting (as from mirrors) lattice planes of separation d_{hkl}, Bragg showed that the angular distribution of the scattered could be understood, hence calculated the angle of crystal must take to the incoming beam of X-rays for constructive interference to happen. This condition for the Bragg's reflection is shown in Fig.4.1. In Fig.4.1, the path-length difference between the two rays reflected at adjacent lattice planes is

$$AB + BC = 2d_{hkl} \sin\theta \qquad (4.1)$$

which should also be a multiple of integer number of its wavelength in order for constructive interference to happen. Thus, Eqn.4.1 takes the form of the Braggs law;

$$n\lambda = 2d_{hkl} \sin\theta . \qquad (4.2)$$

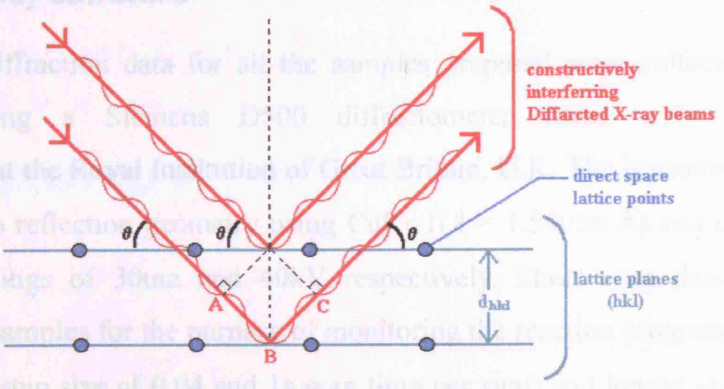

Figure 4.1: Braggs reflection in real space.

In the diffraction experiment, the position (2θ) and the intensity (I_{hkl}) of the diffracted beams are measured. The intensity of each reflection is a result of interference between waves scattered by different atoms within the unit cell and hence is related to the structure factor (F_{hkl}) by;

$$I_{hkl} = s \cdot Lp \cdot |F_{hkl}|^2 \qquad (4.3)$$

(s = scale factor, Lp = Lorenz polarization geometrical correction factor)
where structure factor F_{hkl} is the overall amplitude of a wave diffracted by a particular (hkl) plane;

$$F_{hkl} = \sum_i f_i e^{-i\phi_i} \cdot e^{-W_i} \text{ with } \phi_i = 2\pi(hx_i + ky_i + lz_i) \qquad (4.4)$$

and ϕ_i is the phase factor with (x_i, y_i, z_i) being the partial coordinates of atoms i within the unit cell. Scattering factor (f_i) is the scattering power of an isolated atom i, hence larger the scattering factor, the stronger the atom contributing to scattering of X-rays. Atomic displacements from their equilibrium positions in the crystal occurs due to thermal motions of the lattice and it results in an reduction of reflection intensity. This effect is incorporated in the Eqn.4.4 as the Debye-Waller isotropic temperature factor, W_i.

4.2.3 Powder X-ray diffraction

Powder X-ray diffraction data for all the samples prepared were collected at room temperature using a Siemens D500 diffractometer fitted with a primary monochromator at the Royal Institution of Great Britain, U.K. The instrument operates in Bragg-Bretano reflection geometry using CuKα1(λ = 1.54056 Å) and tube current and voltage settings of 30ma and 40kV respectively. Short scan data sets were collected for all samples for the purpose of monitoring the reaction progress (range 10° $\leq 2\theta \leq$ 70° with step size of 0.04 and 1s scan time per step) and longer scan data sets (range 18° $\leq 2\theta \leq$ 90° with step size of 0.01 and 12 seconds scan time per step) were obtained for some samples in order to perform a structural refinement based on them. The XRD Patterns obtained for all samples were Rietveld refined using the GENLES

routine of the structure refinement program GSAS. As a result of the refinement, lattice parameters and idealized x-coordinates for the oxygen O(2) were calculated.

4.3 Rietveld Refinement

The Rietveld method [1] is an analysis procedure that addresses the problem associated with peak overlap in a powder diffraction pattern by treating each point in the pattern as an individually observed intensity. During Rietveld refinement the intensity at each point in the diffraction pattern is calculated using the following expression

$$I_c^i = I_b^i + s \sum_k A L_k |F_k|^2 G_k^i \qquad (4.5)$$

where

I_c^i = calculated intensity at point i in the diffraction pattern,
I_b^i = background intensity at point i in the diffraction pattern,
s = scale factor
A = absorption coefficient
L_k = Lorentz polarization and multiplicity factors
G_k^i = normalised peak profile function at point i for reflection k, and
F_k = structure factor of the k^{th} Bragg reflection.

Hence, through the knowledge of certain diffractometer parameters describing the reflection shape and width, and sample parameters that define positions and intensities of the reflections, a powder diffraction pattern can be modelled. This model is then tested against the experimentally observed data by least square methods t obtain a best fit. Here, the quantity minimised is

$$S_I = \sum_i w_i (I_{exp}^i - I_c^i)^2 \qquad (4.6)$$

where I_{exp}^i and I_c^i are experimentally observed and calculated intensity for i^{th} step, respectively, and $w_i = 1/ I_{exp}^i$. These residuals are calculated after each iterative refinement cycle, and are used to calculate shifts that are applied to the initial parameters to improve the model. The process is then repeated. The refinement program is designed so that the residuals are minimised and the so called R-factors are

calculated in order for the users quantify the goodness of the fit hence judge the adequacy of the model. There are several R-factors, including the main R-factor

$$R_{wp}= \left\{ \frac{\sum_i w_i \left(I^i_{exp} - I^i_c\right)^2}{\sum_i w_i \left(I^i_{exp}\right)^2} \right\}^{\frac{1}{2}}. \qquad (4.7)$$

However, just looking at the R-factors can often be misleading. For example, a high and well fitted background with large numbers of background coefficients employed could lead to low R_{wp} values. Therefore, together with the R-factors we use the associated χ^2 of the least square fit

$$\chi^2 = \frac{\sum_i w_i \left(I^i_{exp} - I^i_c\right)^2}{N_{exp} - N_{var}} \qquad (4.8)$$

where N_{exp} and N_{var} are the number of experimental and varying points respectively. The Rietveld method is a structure refinement method, hence it is designed for the purpose of *refinement* but not to *solve* the structure from *ab initio*. Therefore, sufficient knowledge of the crystal structure of the material to be analysed should be known in order to commence the refinement.

4.4 Results

First in section 4.4.1 we present the XRD patterns for the bulk samples (synthesized in ~30 g quantity each) prepared for the neutron experiments. They are x = 0. 0.5, 1, 1.5 and 2 members of the $Er_2Ti_{2-x}Sn_xO_7$ series. Fig.4.2 and Fig.4.3 are the XRD patterns. From first inspection it is seen that the phases are pure without significant impurity contribution present and the variation of the patterns through x is smooth.

Secondly the XRD patterns of the samples with small increments of x (x = 1.5, 1.55, 1.6,.....1.95 and 2) are shown in section 4.4.2. Again, they are phase pure and the variation of the peak positions with x is gradual, proving the solid solution is successfully formed through the series.

4.4.1 XRD patterns for $Er_2Ti_{2-x}Sn_xO_7$ (x = 0, 0.5, 1, 1.5, 2)

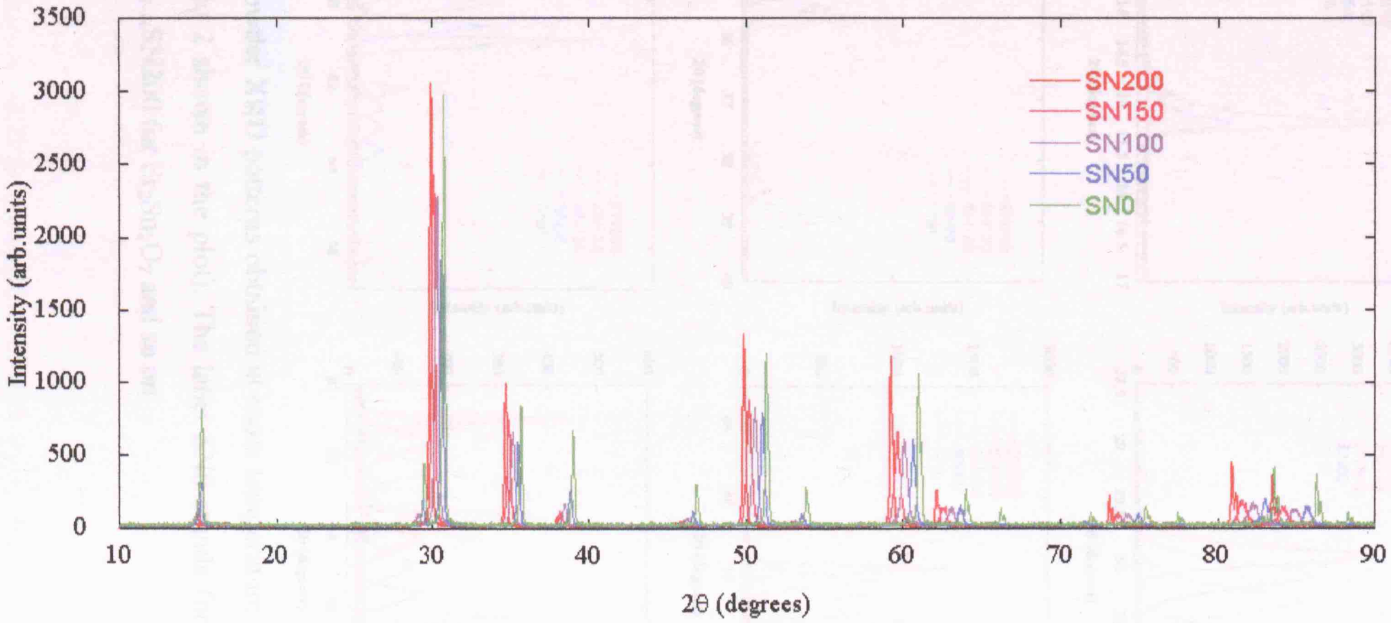

Figure 4.2: Powder XRD patterns obtained at room temperature for the $Er_2Ti_{2-x}Sn_xO_7$ series (x = 0 to 2 shown in the plot). The label SN0 stands for $Er_2Ti_2O_7$, SN50 for $Er_2Ti_{1.5}Sn_{0.5}O_7$...SN200 for $Er_2Sn_2O_7$ and so on.

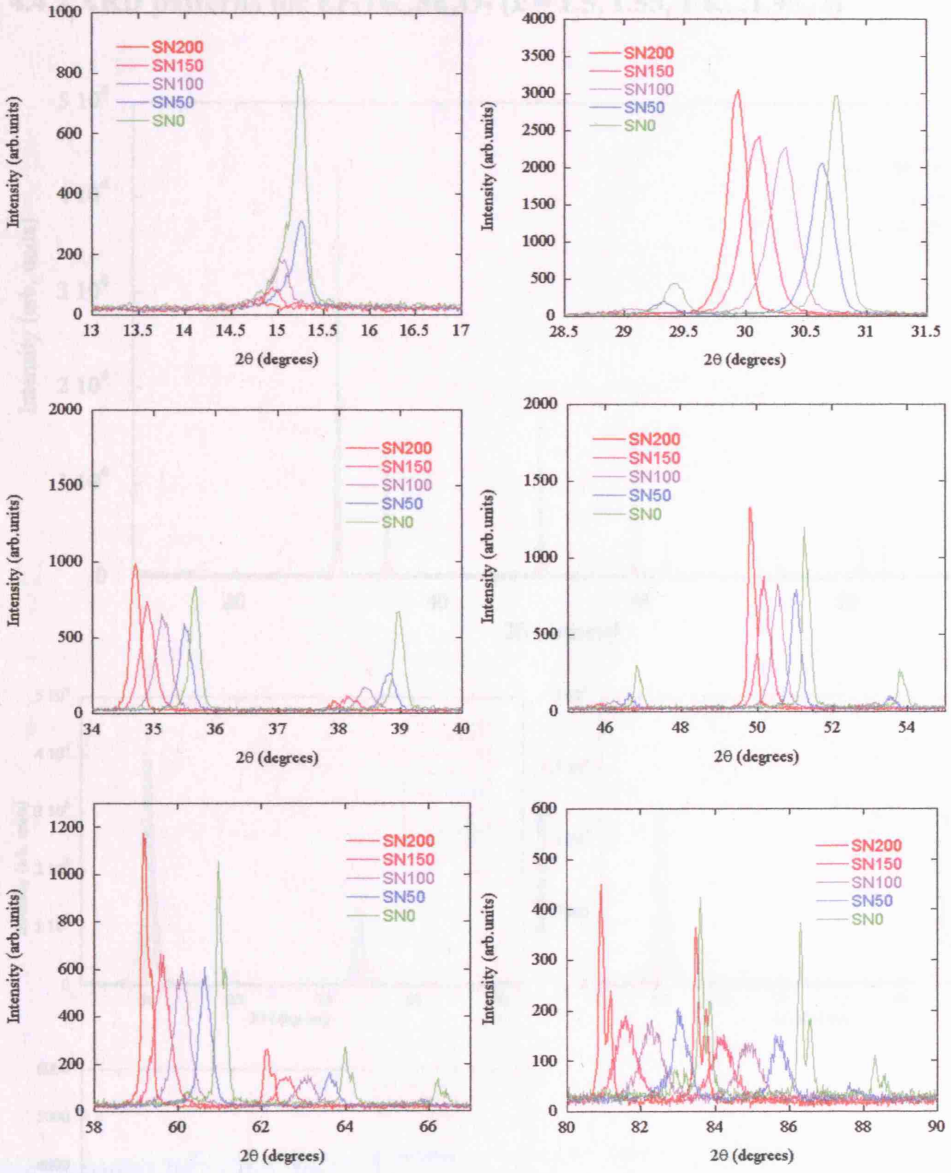

Figure 4.3: Powder XRD patterns obtained at room temperature for the $Er_2Ti_{2-x}Sn_xO_7$ series (x = 0 to 2 shown in the plot). The label SN0 stands for $Er_2Ti_2O_7$, SN50 for $Er_2Ti_{1.5}Sn_{0.5}O_7$...SN200 for $Er_2Sn_2O_7$ and so on.

4.4.2 XRD patterns for $Er_2Ti_{2-x}Sn_xO_7$ (x = 1.5, 1.55, 1.6....1.95, 2)

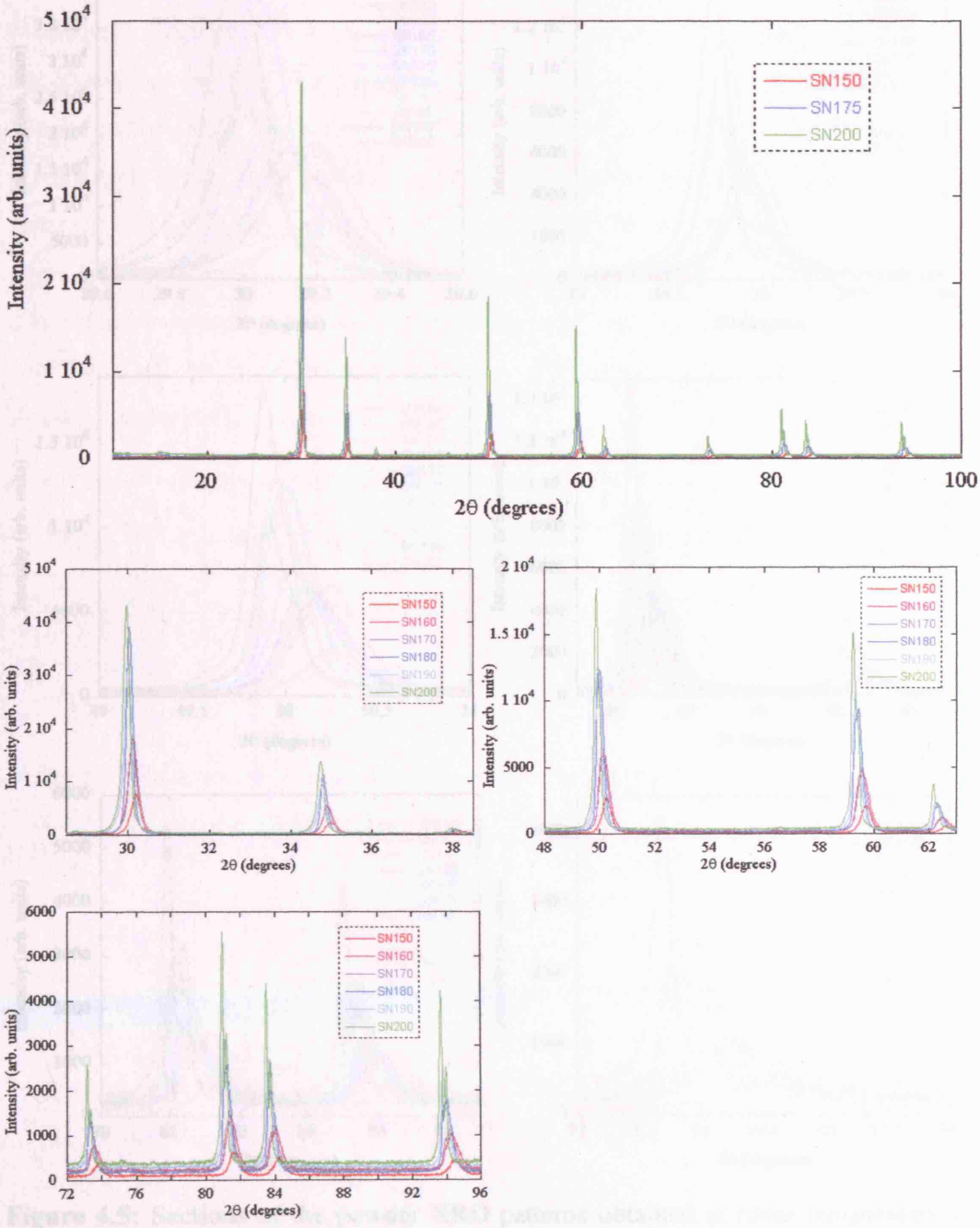

Figure 4.4: Powder XRD patterns obtained at room temperature for the $Er_2Ti_{2-x}Sn_xO_7$ series (x = 1.5 to 2 shown in the plot). The label SN150 stands for $Er_2Ti_{0.5}Sn_{1.5}O_7$, SN170 for $Er_2Ti_{0.3}Sn_{1.7}O_7$...SN200 for $Er_2Sn_2O_7$ and so on.

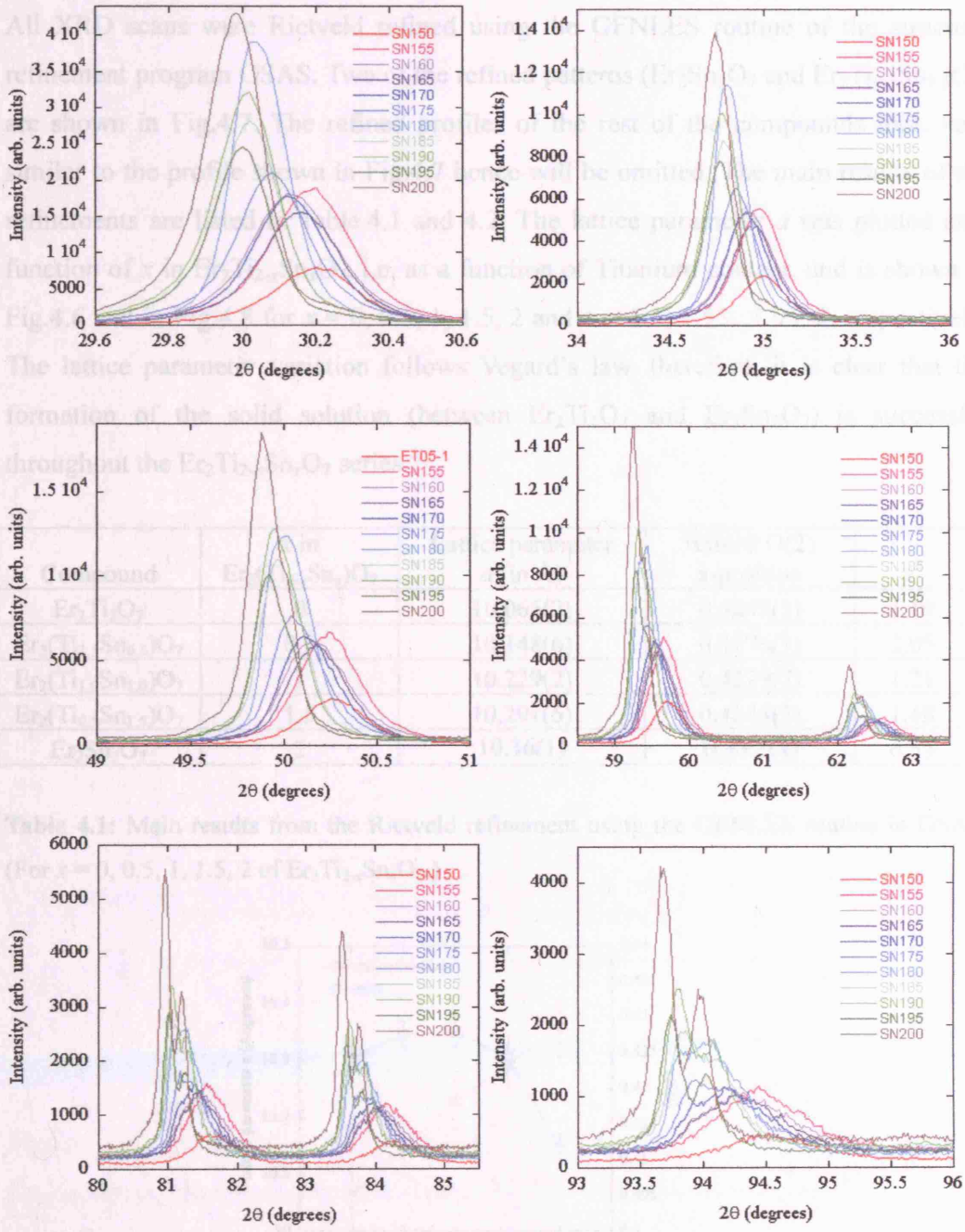

Figure 4.5: Sections of the powder XRD patterns obtained at room temperature for the $Er_2Ti_{2-x}Sn_xO_7$ series. The label SN150 stands for $Er_2Ti_{0.5}Sn_{1.5}O_7$, SN160 for $Er_2Ti_{0.4}Sn_{1.6}O_7$...SN200 for $Er_2Sn_2O_7$ and so on.

4.4.3 Rietveld refinement of the XRD patterns

All XRD scans were Rietveld refined using the GENLES routine of the structure refinement program GSAS. Two of the refined patterns ($Er_2Sn_2O_7$ and $Er_2Ti_{0.5}Sn_{1.5}O_7$) are shown in Fig.4.7. The refined profiles of the rest of the compounds look very similar to the profile shown in Fig.4.7 hence will be omitted. The main results of the refinements are listed in Table.4.1 and 4.2. The lattice parameter a was plotted as a function of x in $Er_2Ti_{2-x}Sn_xO_7$, i.e. as a function of Titanium content, and is shown in Fig.4.6 and in Fig.4.8 for $x = 0$, 0.5, 1, 1.5, 2 and $x = 1.5$, 1.55...1.95, 2, respectively. The lattice parameter variation follows Vegard's law, therefore, it is clear that the formation of the solid solution (between $Er_2Ti_2O_7$ and $Er_2Sn_2O_7$) is successful throughout the $Er_2Ti_{2-x}Sn_xO_7$ series.

Compound	x in $Er_2(Ti_{2-x}Sn_x)O_7$	Lattice parameter a (in Å)	refined O(2) x-position	χ^2
$Er_2Ti_2O_7$	0	10.065(2)	0.4243(3)	1.19
$Er_2(Ti_{1.5}Sn_{0.5})O_7$	0.5	10.148(6)	0.4276(3)	2.05
$Er_2(Ti_{1.0}Sn_{1.0})O_7$	1	10.229(2)	0.4279(7)	1.21
$Er_2(Ti_{0.5}Sn_{1.5})O_7$	1.5	10.291(6)	0.4243(2)	1.48
$Er_2Sn_2O_7$	2	10.36(1)	0.412(1)	6.53

Table 4.1: Main results from the Rietveld refinement using the GENLES routine in GSAS. (For $x = 0$, 0.5, 1, 1.5, 2 of $Er_2Ti_{2-x}Sn_xO_7$.)

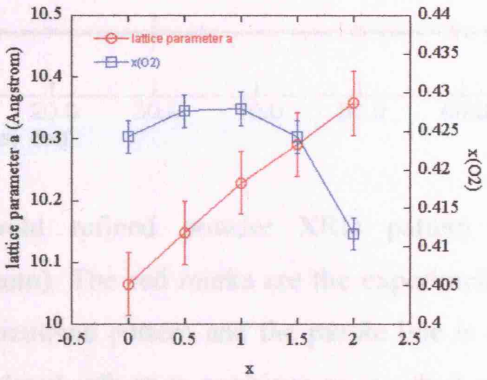

Figure 4.6: The variation in lattice parameter a (red circle) and x(O2)-position (blue square) as a function of x of $Er_2Ti_{2-x}Sn_xO_7$ ($x = 0$, 0.5, 1, 1.5, 2). The lattice parameter variation is a straight line hence obeying the Vegard's law of ion substitution.

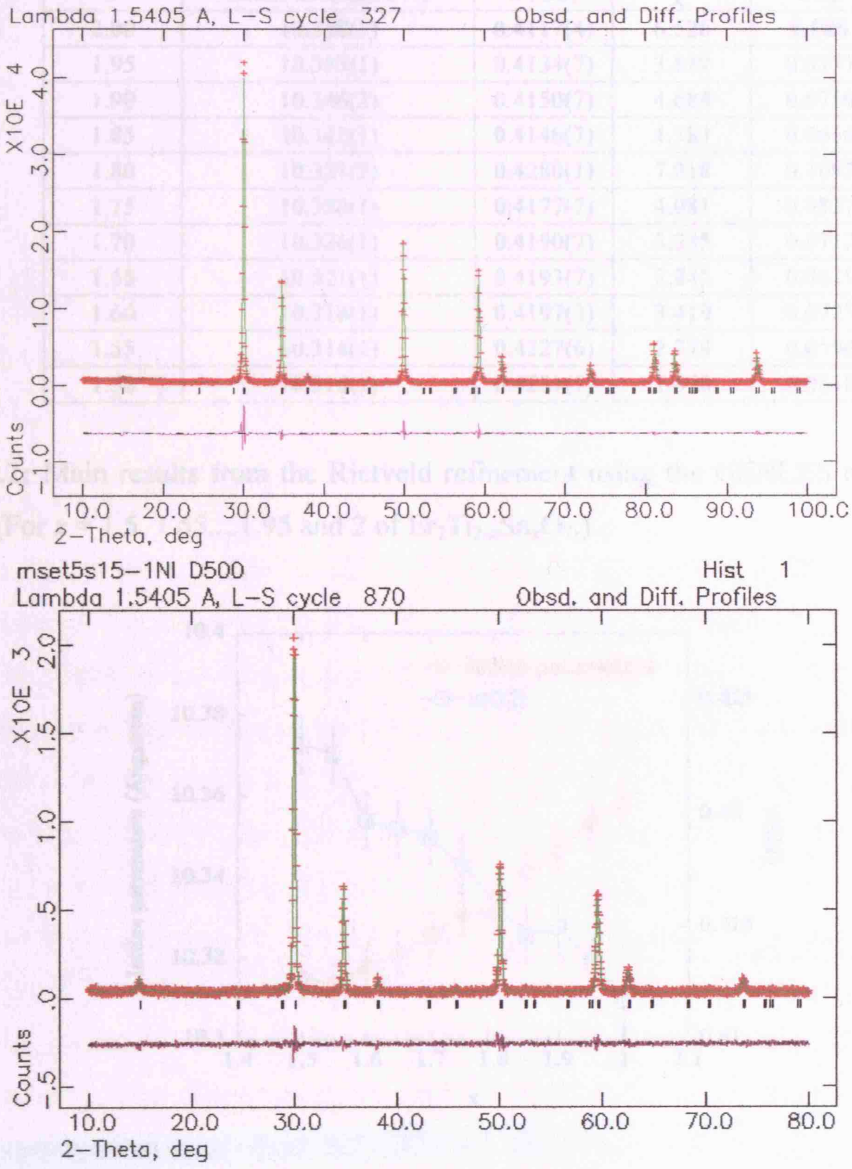

Figure 4.7: Rietveld refined powder XRD pattern for $Er_2Sn_2O_7$ (top) and $Er_2Ti_{0.5}Sn_{1.5}O_7$ (bottom). The red marks are the experimentally observed pattern, the green line is the calculated pattern and the purple line is the difference between the two. Also the calculated reflection positions are marked with black marks under the peaks.

x	lattice constant a /Å	x (O2)	χ^2	wRp
2.00	10.358(1)	0.4117(4)	6.526	0.086
1.95	10.353(1)	0.4134(7)	3.819	0.0777
1.90	10.346(2)	0.4150(7)	4.688	0.0719
1.85	10.341(1)	0.4146(7)	4.383	0.0656
1.80	10.331(2)	0.4280(1)	7.018	0.1092
1.75	10.330(1)	0.4177(7)	4.081	0.0837
1.70	10.326(1)	0.4190(7)	3.235	0.0712
1.65	10.321(1)	0.4193(7)	2.845	0.0619
1.60	10.318(1)	0.4197(3)	3.419	0.0725
1.55	10.314(1)	0.4227(6)	2.779	0.0596
1.50	10.316(1)	0.4231(7)	1.698	0.0618

Table 4.2: Main results from the Rietveld refinement using the GENLES routine in GSAS. (For x = 1.5, 1.55....1.95 and 2 of $Er_2Ti_{2-x}Sn_xO_7$.)

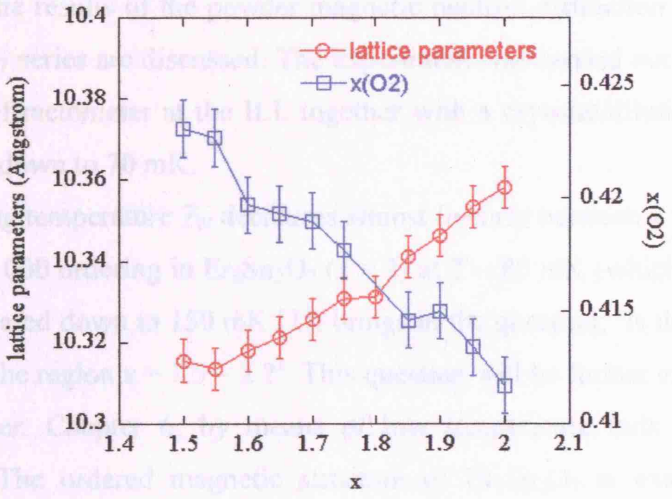

Figure 4.8: The variation in lattice parameter a (red circle) and x(O2)-position (blue square) as a function of x of $Er_2Ti_{2-x}Sn_xO_7$ (x = 1.5, 1.55....1.95 and 2). The lattice parameter variation is a straight line hence obeying the Vegard's law of ion substitution.

References for Chapter 4

[1] H.M.Rietveld, Acta.Cryst.**22**, 151 (1967); J.Appl.Cryst.**2**, 65 (1969).

Chapter 5

Magnetic Diffraction of $Er_2Ti_{2-x}Sn_xO_7$

In this chapter the results of the powder magnetic neutron diffraction experiment on the $Er_2Ti_{2-x}Sn_xO_7$ series are discussed. The experiment was carried out using the D20 high-intensity diffractometer at the ILL together with a cryostat/dilution refrigerator insert that cools down to 70 mK.

The ordering temperature T_N decreases almost linearly between $x = 0$ to 1.5. The reveal of an $\mathbf{k} = 000$ ordering in $Er_2Sn_2O_7$ ($x = 2$) at $T \sim 80$ mK (which was expected to remain disordered down to 150 mK [1]) brings in the question; 'is there a quantum critical point in the region $x = 1.5 \sim 2$?'. This question will be further examined in the following chapter, Chapter 6, by means of low temperature bulk magnetization measurements. The ordered magnetic structure of $Er_2Sn_2O_7$ is examined by the representational analysis method and was concluded to be described by the Palmer-Chalker model [2] with a small allowance of mixing with other basis vector.

5.1 Experimental Details

5.1.1 Sample environment

In this experiment, five different powder samples were used. These are the members of the series $Er_2Ti_{2-x}Sn_xO_7$ with x = 0, 0.5, 1, 1.5 and 2. The syntheses of these samples are discussed in Chapter 4. About 9 ~ 10 g of the samples were placed in a cylindrical copper sample holder (diameter ~ 10 mm, height ~ 8 cm) which filled up the holder up to the top. This was then attached to the dilution refrigerator insert and was cooled down to 70 mK inside a general cryostat. Detailed zero field temperature scans were taken in the range T = 70 mK ~ 1.2 K with temperature increments of 0.015 ~ 0.05 K and average counting time of 1200 seconds per scan (24 hours per sample, including the sample change and cooling time), and less detailed scans for T = 1.2 K ~ room temperature with temperature increments of 0.2 ~ 5 K and counting time of 300 seconds per scan were taken. All scans were obtained for the range $0° \leq 2\theta \leq 160°$.

5.1.2 D20 high-intensity two-axis diffractometer

D20 is a very high intensity 2-axis diffractometer with high neutron flux of up to 10^7 - 10^8 n s^{-1} cm^{-2}. D20 is equipped with a 1600 cell curved position sensitive detector (PSD) filled with a mixture of ^3He and CF_4. A picture of this PSD bank is shown in Fig.5.1 below together with the schematic diagram of the D20 whole geometry. The complete diffraction pattern at 1536 positions, covering a scattering range of 153.6 °, can be obtained in a matter of seconds. The variety of choices of monochromators adds flexibility to the instrument as the take-off angle can be varied between 26 - 120°, corresponding to the incident neutron of wavelength variance of λ = 0.82 - 2.41 Å. In our experiment, a pyrolitic graphite HOPG (002) monochromator was used to give a wavelength of 2.4 Å at a take-off angle of 42°.

5.1.3 Method used for the diffraction patterns analysis

The details of the refinements will be given in the later sections where appropriate. Here we however, state the details of the method (the steps and programs used) in which all the diffraction patterns were analysed.

For all the compounds, both nuclear structures at $T > T_N$ and magnetic structures at $T < T_N$ were refined. First, the nuclear structures factors were calculated using the GENLES routine of the GSAS Suite [3] and the resulting refined parameters (such as x(O2), U_{iso}, and peak profile function coefficients) were used as the starting parameters for the magnetic refinements. These parameters were kept constant during the magnetic refinements to maximum extent.

For the magnetic structure, the refinements were repeated twice for a given condition (i.e. for same compound / same counting time / same temperature) using two different data sets. These are (i) the non-subtracted data containing both the nuclear and magnetic peaks, and (ii) the subtracted data ($T < T_N - T > T_N$) containing only the magnetic information. The reason for the repetition was to ensure correct scaling of the magnetic profiles with respect to the nuclear profiles as this becomes crucial in determining the refined magnetic moment size. The usage of the non-subtracted data ensures this. However, the reason for the usage of the subtracted data is in the difference in intensity size between nuclear and magnetic patterns. The substantially smaller intensity of the magnetic peaks occurring on top of the large nuclear peaks often makes the fitting biased towards the nuclear profile. The consequence is that the calculated magnetic structure factor could end up having poor accuracy. The usage of subtracted data at least ensures that the fitting is carried out solely on the magnetic peaks. The subtracted patterns also have an advantage over the non-subtracted ones such as the removal of the background noise. Again, if one wants to see the science lying beneath the background, such as the diffuse scattering, it is maybe wiser not blindly getting rid of the background but to observe directly at the non-subtracted data.

During the magnetic refinements, the moment size was allowed to be refined using the GENLES routine of the GSAS Suite [3] while the moment orientations were controlled and refined separately by the simulated annealing-based program SARA*h*-Refine for GSAS [4, 5].

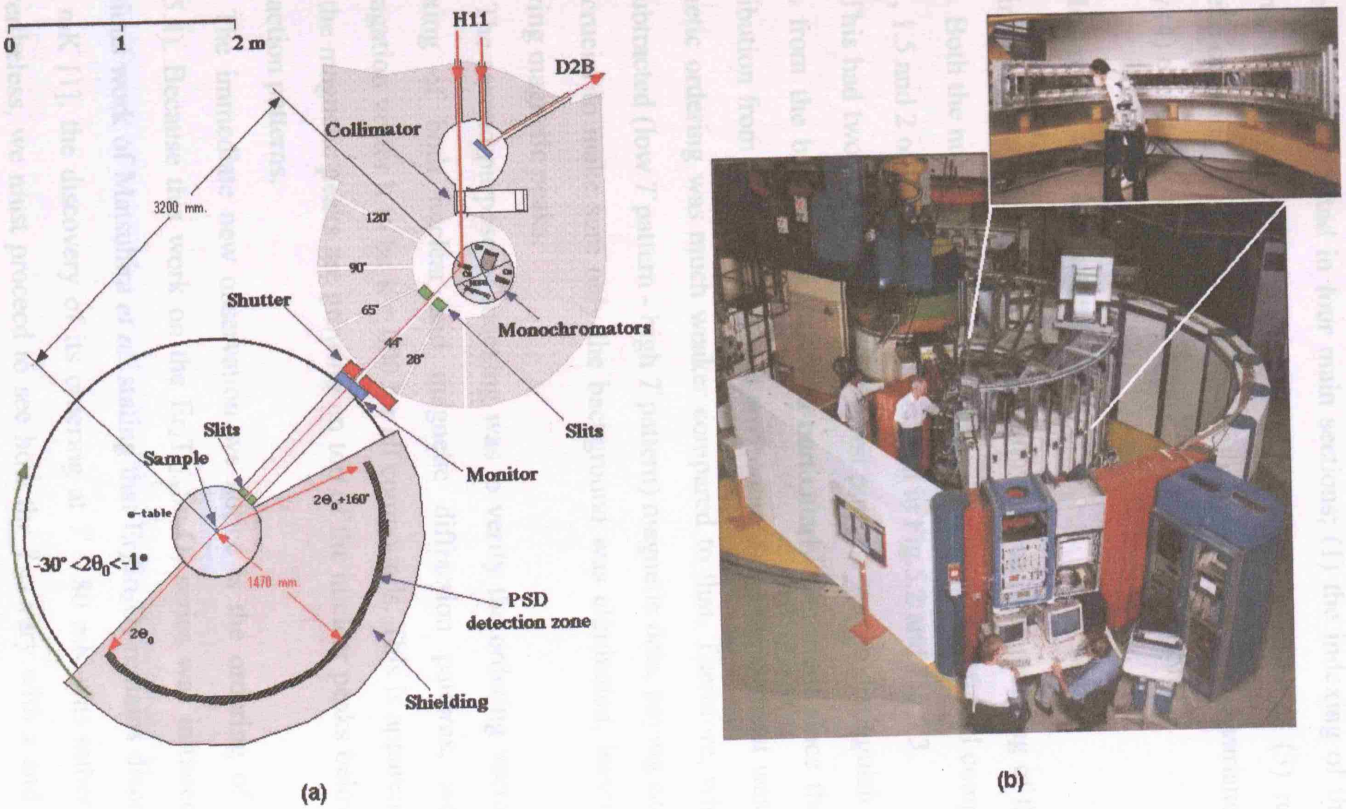

Figure 5.1: (a) Schematic diagram of D20 geometry at the ILL. (b) Photo of D20 with a focus on the 1600 cell cured PSD bank.

5.2 Results

The results are separated in four main sections; (1) the indexing of the diffraction patterns, (2) looking at the T_N variantion with composition x, (3) reviewing the magnetic ordering of $Er_2Ti_2O_7$ together with the ordering profile variance with x and finally (4) examination of the new magnetic ordering of $Er_2Sn_2O_7$.

5.2.1 Indexing of diffraction patterns

The first analysis that was carried out on the data was the indexing of the diffraction peaks. Both the nuclear and magnetic patterns were indexed for all compounds (x = 0, 0.5, 1, 1.5 and 2 of $Er_2Ti_{2-x}Sn_xO_7$) and shown in Fig.5.2 and Fig.5.3.

This had two major purposes; the first purpose was to distinguish the structural peaks from the background -this was particularly important since the background contribution from the copper sample environment and the cryostat was huge and the magnetic ordering was much weaker compared to that. Therefore, when looking at the subtracted (low T pattern - high T pattern) magnetic data, paying careful attention was crucial to make sure only the background was eliminated, leaving the weakly ordering magnetic peaks.

The second purpose of indexing was to verify the ordering vector **k**. From the indexing of both nuclear and magnetic diffraction patterns, we deduce the propagation vector **k** to be **k** = 000 for all compounds. This is apparent from the fact that the magnetic peaks are growing on top of the nuclear peaks below T_N in all the diffraction patterns.

The immediate new observation we notice is the ordering of $Er_2Sn_2O_7$ (see Fig.5.4). Because this work on the $Er_2Ti_{2-x}Sn_xO_7$ series was initiated based on the previous work of Matsuhira *et al.* stating that $Er_2Sn_2O_7$ remains disordered down to 150 mK [1], the discovery of its ordering at $T \sim 80$ mK was rather disappointing. Nevertheless, we must proceed to see how the T_Ns vary with x and investigate the nature of the ordering of the $Er_2Sn_2O_7$.

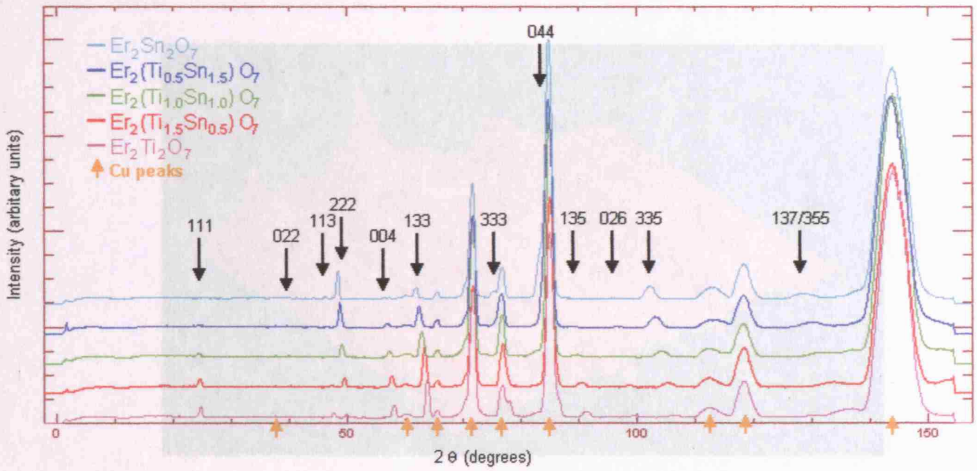

Figure 5.2:. Nuclear diffraction patterns taken at temperatures above T_Ns; T = 1.497, 1.288, 1.104, 1.100, 1.002 K for x = 0, 0.5, 1, 1.5 and 2, respectively, of $Er_2Ti_{2-x}Sn_xO_7$. The purpose of this figure is to index the nuclear peaks and distinguish from those Cu peaks.

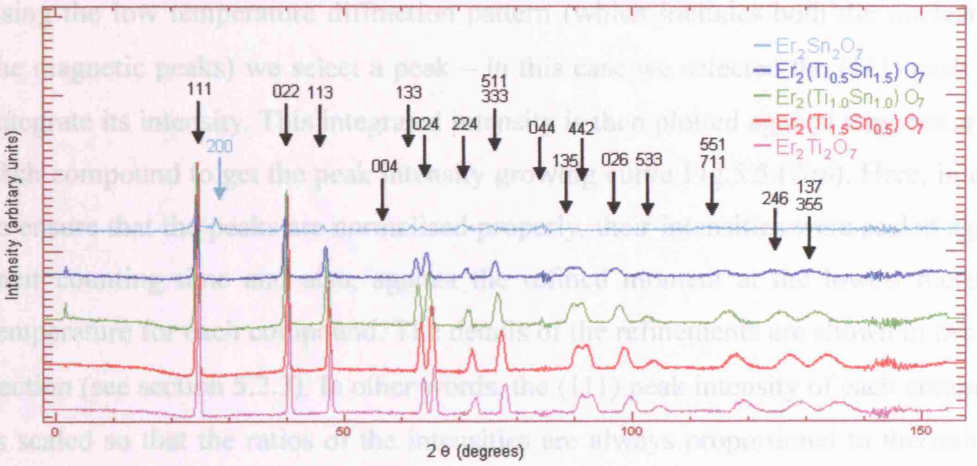

Figure 5.3: Magnetic ($T < T_N - T > T_N$ subtraction) diffraction patterns taken at temperatures below T_Ns; T = 0.1, 0.1, 0.1, 0.069, 0.070 K for x = 0, 0.5, 1, 1.5 and 2, respectively, of $Er_2Ti_{2-x}Sn_xO_7$. This figure shows the indexing of magnetic peaks. The peak labelled in light blue colour [2,0,0] is the new magnetic peak appeared for $Er_2Sn_2O_7$ that are not present in the rest of the compounds.

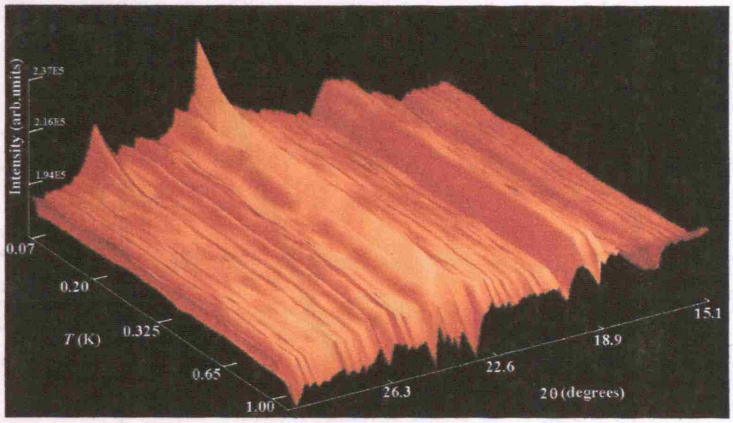

Figure 5.4: Figure showing the ordering of the $Er_2Sn_2O_7$ around $T_N = 0.1$ K.

5.2.2 T_N variation with x of $Er_2Ti_{2-x}Sn_xO_7$ series

Now we should determine the T_Ns of the compounds. The method is as follows; using the low temperature diffraction pattern (which includes both the nuclear and the magnetic peaks) we select a peak – in this case we selected the ⟨111⟩ peak- and integrate its intensity. This integrated intensity is then plotted against temperature for each compound to get the peak intensity growing curve Fig.5.5 (*Top*). Here, in order to ensure that the peaks are normalised properly, their intensities were scaled against their counting time and also, against the refined moment at the lowest measured temperature for each compound. The details of the refinements are shown in the later section (see section 5.2.3). In other words, the ⟨111⟩ peak intensity of each compound is scaled so that the ratios of the intensities are always proportional to the ratios of squared moment between the compounds, i.e. maximum intensity $\propto$ (refined maximum moment)^2. Secondly, a tangent that gives the steepest gradient is chosen and was fitted to this peak growing curve. The ordering temperature T_N is then taken to be the mid point of this tangent for each compound – see Fig.5.5 (*Bottom*). Finally, T_Ns for each compound are plotted in Fig.5.6.

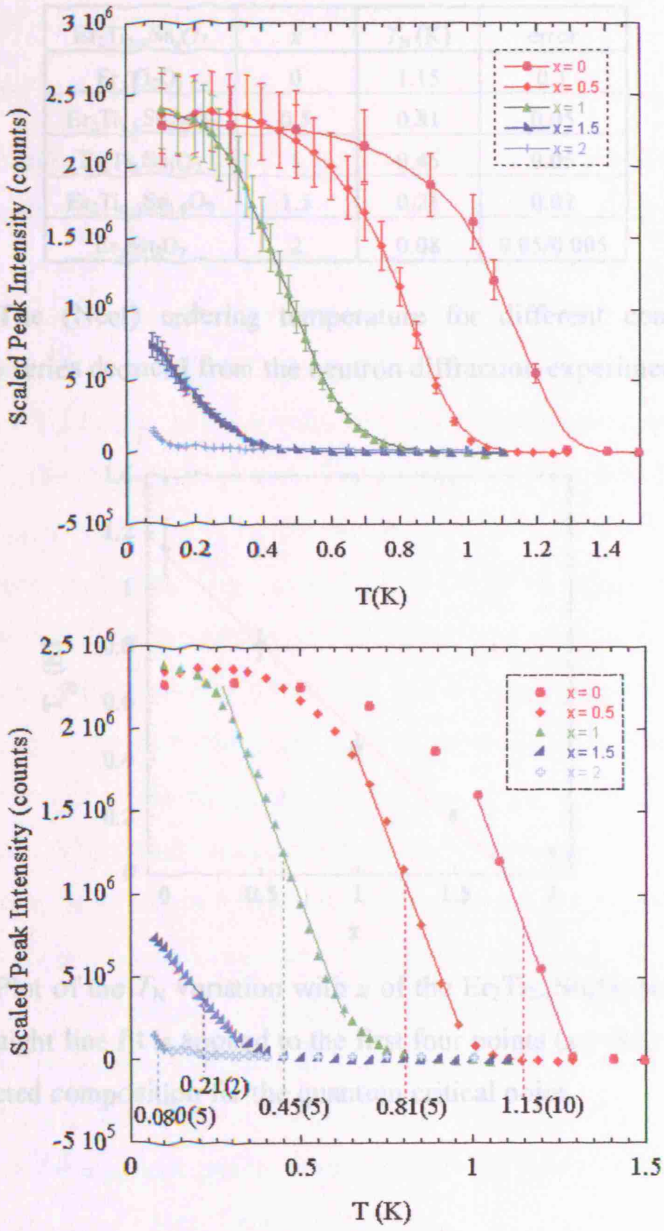

Figure 5.5: Integrated peak intensity variation of the ⟨111⟩ peak (Nuclear + Magnetic) with temperature for the $Er_2Ti_{2-x}Sn_xO_7$ series (x = 0, 0.5, 1, 1.5, 2). All data are scaled with counting time and the ratios of the peak intensities are fixed so that the maximum intensity ∝ (refined maximum moment)^2 –see later section for refinement details. *Top*: smooth curve fit applied to all data. *Bottom*: a steepest tangent is selected and fitted to the curve and the mid point of that tangent is taken as the transition point, T_N.

$Er_2Ti_{2-x}Sn_xO_7$	x	T_N (K)	error
$Er_2Ti_2O_7$	0	1.15	0.1
$Er_2Ti_{1.5}Sn_{0.5}O_7$	0.5	0.81	0.05
$Er_2Ti_1Sn_1O_7$	1	0.45	0.05
$Er_2Ti_{0.5}Sn_{1.5}O_7$	1.5	0.21	0.02
$Er_2Sn_2O_7$	2	0.08	0.05/0.005

Table 5.1: The (Néel) ordering temperature for different compositions of the $Er_2Ti_{2-x}Sn_xO_7$ series deduced from the neutron diffraction experiment.

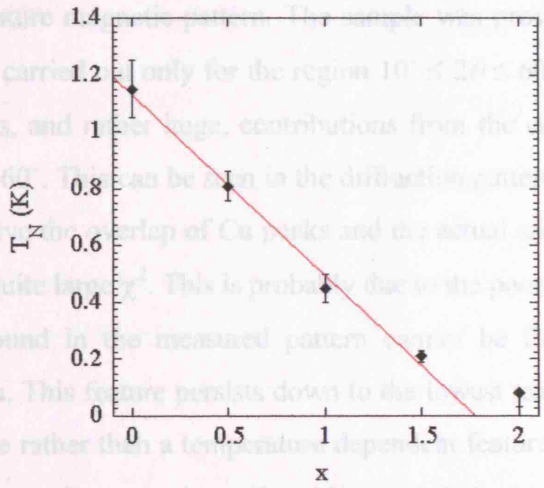

Figure 5.6: Plot of the T_N variation with x of the $Er_2Ti_{2-x}Sn_xO_7$ series (x = 0, 0.5, 1, 1.5, 2). A straight line fit is applied to the first four points (x = 0 to 1.5) as a guidance for the predicted composition for the quantum critical point.

After the disappointment of $Er_2Sn_2O_7$ ordering, an interesting question comes back into the light. The dropping in T_N with increase in x looks fairly linear up to x = 1.5. If this is the case, how would this T_N - x curve behave above x = 1.5? Would this line curve upwards giving always finite T_Ns? or is this going to keep falling towards zero? If so, will there be 'a quantum critical point' in this region $1.5 < x < 2$ where $T_N \rightarrow 0$? This question is investigated in detail in the next chapter, Chapter 6.

5.2.3 Ordering patterns of $Er_2Ti_{2-x}Sn_xO_7$ (x = 0, 0.5, 1, 1.5)

5.2.3.1 Nuclear structure analysis

From the diffraction patterns shown in section 5.2.1, we can assume that the magnetic structures remain the same for x = 0, 0.5, 1, 1.5 of the $Er_2Ti_{2-x}Sn_xO_7$ series. Therefore, we start with the refinement for $Er_2Ti_2O_7$. First, nuclear diffraction pattern ($T > T_N \sim$ 1.2 K) was analysed using the GENLES routine of the GSAS Suite [3]. The optimum refined profile is shown in Fig.5.7. The refinement parameters derived from this step, shown in Table 5.2 below, was then used later as the starting parameters when refining the low temperature magnetic pattern. The sample was proved to be phase pure. The refinement was carried out only for the region $10^\circ \leq 2\theta \leq 60^\circ$ because of the presence of the numerous, and rather huge, contributions from the copper sample holder (and cryostat) above 60°. This can be seen in the diffraction pattern above (Fig.5.2); it is too difficult to resolve the overlap of Cu peaks and the actual sample peaks. The resulting fit still gives a quite large χ^2. This is probably due to the poor fit of the background; the humpy background in the measured pattern cannot be fitted with any reasonable smooth function. This feature persists down to the lowest temperature scan, hence it is a systematic one rather than a temperature dependent feature inherent to the structure. There are yet some Cu peaks (e.g. $2\theta \sim 38^\circ$ and 44°) in the refined region. However, the validity of the refinement is shown by the agreement of the refined parameter x(O2) with the previously studied results of Knop *et al.* [6] and Champion *et al.* [7] within 3 ~ 5 e.s.d. We might comment at this point that the refinement improves dramatically in the magnetic pattern since general background information (Cu peaks) is removed in the low T - high T data subtraction.

Similar nuclear refinements were carried out on the rest of the samples; x = 0.5, 1, 1.5 and 2 in $Er_2Ti_{2-x}Sn_xO_7$, and the refinement parameters for all compounds are listed in Table 5.3. The lattice parameter a_o variance and the x(O2) position (of oxygen atoms at 48*f* site) variance with x of $Er_2Ti_{2-x}Sn_xO_7$ are plotted in Fig.5.8. A linear increase in lattice parameter is observed as Sn is substituted for Ti. This shows that the system obeys Vegard's law, hence the substitution is successfully homogeneous.

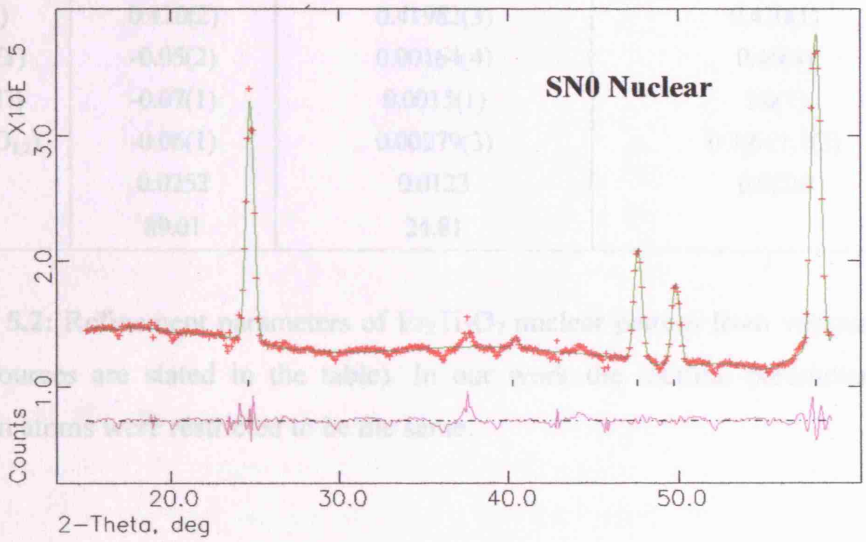

Figure 5.7: Refined profile for data collected from D20 instrument for $Er_2Ti_2O_7$ at 1.497 K; the nuclear diffraction pattern.

One point to mention is the negative isotropic thermal parameters U_{iso} in some of the refinements. An attempt was made to make this value positive by adding a linear absorption correction. However the refinement still converged to give the best fit with negative U_{iso}s. Therefore, we used the (negative) U_{iso} values derived in these nuclear refinements in the following magnetic refinements.

$Er_2Ti_2O_7$	This work	Champion's work [7]	Knop [6] / Brixner [13]'s work
T	1.497 K	4.85 K	Room T
a_o	10.0601(5)	10.0476(1)	10.076(1) / 10.069(1)
x(O2)	0.420(2)	0.41982(3)	0.420(1)
U_{iso}(Er)	-0.05(2)	0.00164(4)	0.46(4)
U_{iso}(Ti)	-0.07(1)	0.0015(1)	1.0(1)
$U_{iso}(O_{1,2})$	-0.06(1)	0.00279(3)	0.3(6),1.1(3)
R_{wp}	0.0252	0.0123	0.0225
χ^2	89.01	24.81	

Table 5.2: Refinement parameters of $Er_2Ti_2O_7$ nuclear pattern from various sources (the sources are stated in the table). In our work the thermal parameters of the oxygen atoms were restricted to be the same.

	$Er_2Ti_2O_7$	$Er_2Ti_{1.5}Sn_{0.5}O_7$	$Er_2Ti_1Sn_1O_7$	$Er_2Ti_{0.5}Sn_{1.5}O_7$	$Er_2Sn_2O_7$
T	1.497 K	1.288 K	1.104 K	1.100 K	1.002 K
a_o	10.0601(5)	10.1373(2)	10.2127(3)	10.2493(3)	10.3580(3)
x(O2)	0.420(2)	0.418(1)	0.415(2)	0.416(2)	0.420(1)
U_{iso}(Er)	-0.05(2)	-0.03(2)	-0.02(4)	0.03(4)	0.042(3)
U_{iso}(Ti)	-0.07(1)	-0.090(7)	-0.09(5)	0.08(2)	
U_{iso}(Sn)		-0.08(2)	-0.08(3)	0.02(5)	0.036(4)
$U_{iso}(O_{1,2})$	-0.06(1)	-0.04(1)	-0.04(3)	0.00(2)	0.028(3)
R_{wp}	0.0252	0.0266	0.0234	0.0231	0.0304
χ^2	89.01	115.4	90.95	87.55	189.9

Table 5.3: Refinement parameters of $Er_2Ti_{2-x}Sn_xO_7$ (x = 0, 0.5, 1, 1.5 and 2) nuclear diffraction patterns. In our work the thermal parameters of the oxygen atoms were restricted to be the same.

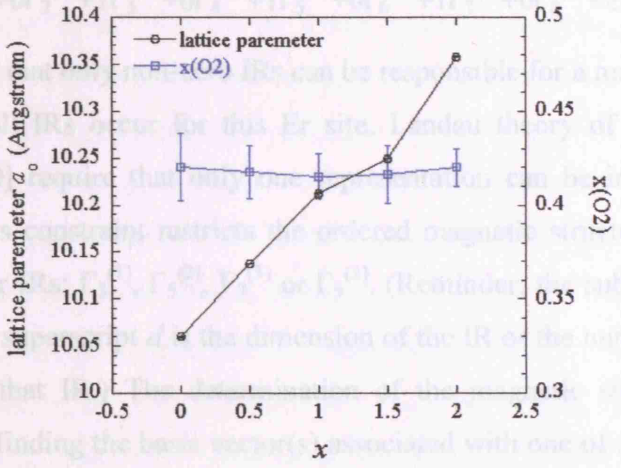

Figure 5.8: Plot showing the variation of the lattice parameters a_o (open circles) and the x(O2) positions of the oxygen atoms at 48*f* site (open squares) with stoichiometry x of the $Er_2Ti_{2-x}Sn_xO_7$ series. Error bars are also plotted for each point. There is a linear increase in the unit cell size with Sn substitution for Ti. The x(O2) variance is less clearly defined because of the large errors.

5.2.3.2 Magnetic structure analysis

As previously reported [8,9] the magnetic diffraction peaks of $Er_2Ti_2O_7$ could be indexed on a **k** = 000 propagation vector. This was also shown to be the case for our work (see section 5.2.2). In this section the representational analysis method outlined in section 3.4.2 is applied to the case of **k** = 000 for the spins on the 16*c* sites of the space group $Fd\bar{3}m$. This follows the work of Champion [7].

Decomposition of the magnetic representation

The magnetic representation, Γ_{Er}, of the Er site (16*c* in $Fd\bar{3}m$) can be decomposed in terms of irreducible representations (IRs) of $G_{\mathbf{k}}$ where $G_{\mathbf{k}}$ is defined as the little group of symmetry elements that leave **k** invariant. The application of the symmetry operations of $G_{\mathbf{k}}$ to the four tetrahedral Er positions results in a single orbit. For these sites the decomposition of the magnetic representation Γ_{Er} is :

$$\Gamma_{Er} = 0\Gamma_1^{(1)} + 0\Gamma_2^{(1)} + 1\Gamma_3^{(1)} + 0\Gamma_4^{(1)} + 1\Gamma_5^{(2)} + 0\Gamma_6^{(2)} + 1\Gamma_7^{(3)} + 0\Gamma_8^{(3)} + 2\Gamma_9^{(3)} + 0\Gamma_{10}^{(3)}. \quad (5.1)$$

We know that only non-zero IRs can be responsible for a magnetic structure. We see that not all IRs occur for this Er site. Landau theory of second order phase transitions [10] require that only one representation can be involved in a critical transition. This constraint restricts the ordered magnetic structure to correspond to one of the four IRs; $\Gamma_3^{(1)}$, $\Gamma_5^{(2)}$, $\Gamma_7^{(3)}$ or $\Gamma_9^{(3)}$. (Reminder: the subscript i of $\Gamma_i^{(d)}$ is the IR's label, the superscript d is the dimension of the IR or the number of basis vectors belonging to that IR.) The determination of the magnetic structure can now be proceeded by finding the basis vector(s) associated with one of the IRs that gives the best fitting magnetic pattern. The four IRs with their associated basis vectors are listed in Table 5.4 and the visual representations of these basis vectors are shown in Fig.5.9.

Landau theory states that only one representation can be involved in a critical transition. With this constraint it is possible to reduce the number of possible magnetic structures in which the system can order down to four. These are discussed below with reference to visual representations of the most characteristic basis vectors (see Fig.5.9).

Irreducible representation (IR) Γ_3 is one-dimensional represented by a single basis vector ψ_1. This corresponds directly to the FeF_3 ordered magnetic structure with all spins pointing into or out of the tetrahedron, along the easy-axes.

IR Γ_5 is two dimensional and therefore the possible directions for one particular site will all be in a plane when the two orthogonal basis vectors ψ_2 and ψ_3 are linearly combined. This in fact maps out arrangements in which the spins are lying on the $\langle 111 \rangle$ planes of the tetrahedron. We call the resulting spin arrangements the '*Champion model*' after Champion *et al.*'s work on $Er_2Ti_2O_7$ [7,9]. It is worth noticing that these two basis vectors are members of the eight basis vectors that define the ground state of the $\langle 111 \rangle$ XY antiferromagnet; ψ_2 = State II, and ψ_3 = State III (see Chapter 2) [7,9].

IR Γ_7 is three dimensional, with three non-orthogonal basis vectors, ψ_4, ψ_5 and ψ_6 associated with it. Here it is worth noticing that linear combinations of non-orthogonal basis vectors will result in configurations of spins with different lengths. Given the assumption that all the moments of a given crystallographic site have equal lengths, as is typical for an insulator, only linear combinations which involve single basis vectors are of interest. Therefore, it is reasonable not to mix the three non-orthogonal basis vectors in the Γ_7. The moments associated with each of these basis vectors again lie in the $\langle 111 \rangle$ easy-planes of the XY-model, choosing two sets of antiparallel spins which in turn are orthogonal to each other. This is a favored ground state for Heisenberg pyrochlore antiferromagnet with dipole-dipole interactions taken into account, derived by Palmer and Chalker and hence we call this the '*Palmer-Chalker model*' (see Chapter 2) [2]. Again, these basis vectors correspond to State I discussed in chapter 2, one of the ground state for the $\langle 111 \rangle$ XY AFM.

It becomes very important to notice the similarities and differences between the Champion state and the Palmer-Chalker state. A best picture that describes this is perhaps Fig.2.14 in Chapter 2. Being the basis vectors that constitute the ground state of $\langle 111 \rangle$ XY AFM, both states have spins lying on the $\langle 111 \rangle$ easy-planes, however, if the system chooses the Palmer-Chalker state over the Champion state, then it is indicative of dipole interactions playing an important role in the ordering process.

IR Γ_9 is much more complicated. As in the case of Γ_7, the six basis vectors ψ_7, ψ_8, ψ_9, ψ_{10}, ψ_{11}, and ψ_{12} are not all orthogonal to one another. The basis vectors can be classified into two sets; ψ_7, ψ_9 and ψ_{11} and ψ_8, ψ_{10} and ψ_{12}. Here, all three basis vectors in a given set have identical spin arrangements but with different choices of crystallographic axes (x, y or z-axis) in which the spins are aligned along. The first set [ψ_7, ψ_9 and ψ_{11}] have ferromagnetic spin configurations, and the second set [ψ_8, ψ_{10} and ψ_{12}] consists of two pairs of mutually orthogonal antiferromagnetic spins that lie along the edges of the tetrahedron. In fact, mixing the two different types of basis vectors (the FM one and the AFM one) in equal proportion gives us the familiar '*Spin-ice*' configuration! Therefore, we label the sets of basis vectors associated with Γ_9 as: 'Spin-ice (FM)' = [ψ_7, ψ_9 and ψ_{11}] and 'Spin-ice (AFM)' = [ψ_8, ψ_{10} and ψ_{12}].

The last remark to give about this Γ_9 is again the orthogonality of the basis vectors. As it is now easy to see, there are three pairs of orthogonal vectors: ψ_7, ψ_8, ψ_9, ψ_{10} and ψ_{11}, ψ_{12}, (the FM-AFM orthogonal pairs). There is also one orthogonal triplet: ψ_7, ψ_9, ψ_{11} ,(the FM triplet).

IR	Basis Vector	Atom1			Atom 2			Atom 3			Atom 4		
		m_x	m_y	m_z	m_x	m_y	m_z	m_x	m_y	m_z	m_x	m_y	m_z
Γ_3	ψ_1	1	1	1	-1	-1	1	-1	1	-1	1	-1	-1
Γ_5	ψ_2	1	-1	0	-1	1	0	-1	-1	0	1	1	0
	ψ_3	1	1	-2	-1	-1	2	-1	1	2	1	-1	2
Γ_7	ψ_4	0	1	-1	0	1	1	0	-1	-1	0	-1	1
	ψ_5	-1	0	1	-1	0	-1	1	0	-1	1	0	1
	ψ_6	1	-1	0	-1	1	0	1	1	0	-1	-1	0
Γ_9	ψ_7	1	0	0	1	0	0	1	0	0	1	0	0
	ψ_8	0	1	1	0	1	-1	0	-1	1	0	-1	-1
	ψ_9	0	1	0	0	1	0	0	1	0	0	1	0
	ψ_{10}	1	0	1	1	0	-1	-1	0	-1	-1	0	1
	ψ_{11}	0	0	1	0	0	1	0	0	1	0	0	1
	ψ_{12}	1	1	0	-1	-1	0	1	-1	0	-1	1	0

Table 5.4 [7]: Non-zero IRs and associated basis vectors ψ_v for the space group *Fd-3m* with **k** = 000 calculated using the program SARAh-Representational Analysis. [4, 5]. The labelling of the propagation vectors and the IRs follows the scheme of Kovalev [11].

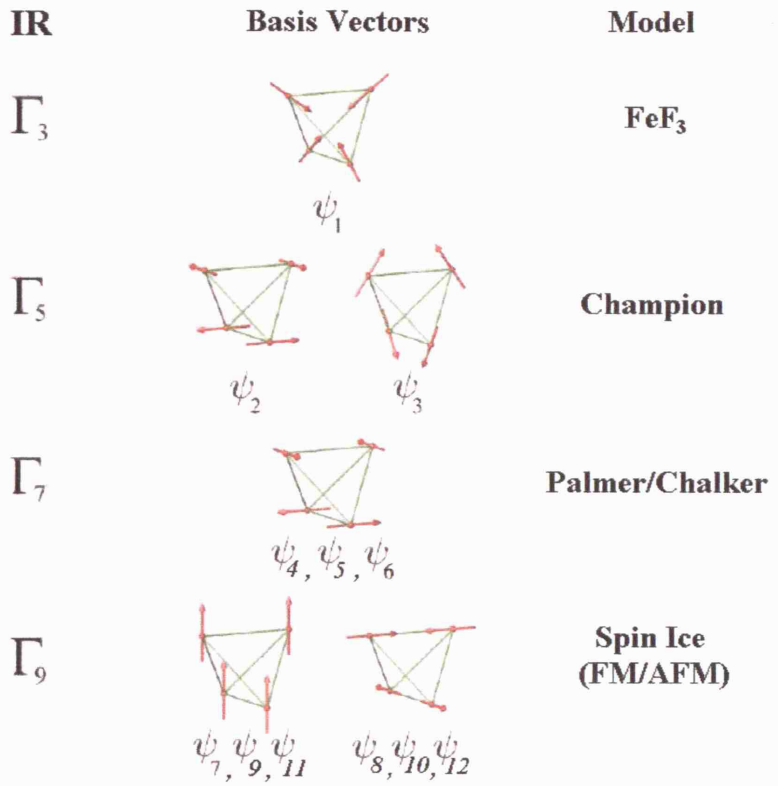

Figure 5.9 [7]: Graphical representation of the basis vectors ψ_v listed in Table 5.4. Names are given for the models represented by the basis vector(s). The ψ_vs not shown in the figure are identical arrangements with alignment along different axes. The basis vectors belonging to the Champion state (Γ_5) and Palmer-Chalker state (Γ_7) are all members of the solution to the ground state of $\langle 111 \rangle$ XY antiferromagnet (as described in the text in Chapter 2) [7]. The only difference is that the Palmer-Chalker state is favored over Champion state when dipole interactions are considered [2].

Fitting magnetic patterns using Champion model

The magnetic pattern of $Er_2Ti_2O_7$ is now fitted using the Champion model. This is to confirm the work done by Champion *et al.* on the ordering of $Er_2Ti_2O_7$ [7,9]. Both the non-subtracted pattern (0.1 K – 1.497 K) and the subtracted pattern are refined by using Γ_3 ($\psi_2 + \psi_3$) in SARA*h*-Refine program [4,5] controlling the mixing ratio of the basis vectors (i.e. to control the moment orientations). Note that powder neutron diffraction gives the average scattering over all crystallites in the sample, and thus the scattering intensity is the same for all linear combinations of the basis vectors $\psi_2 + \psi_3$.

The moment sizes were refined next using the GENLES routine of GSAS Suite [3]. The resulting refined profiles can be seen in Fig.5.10 below. During the refinement only the background and the lattice parameters were allowed to be refined apart from the magnetism. It is shown that the refinement is reproducible and the agreement with the previous work [7,9] is excellent. As a reassurance, attempts were also made to fit the data using different models (i.e. using basis vectors from Γ_1, Γ_3 or Γ_7), however, since the fit was significantly worse than in the case for Γ_2 the details will not be presented in this work. The refined ordered moment size for $Er_2Ti_2O_7$ was 3.40 (1) μ_B using the subtracted data and 3.51 (4) μ_B for the non-subtracted data. The agreement lies within their 3 e.s.d.

Now the same procedure is repeated for the other compounds; $x = 0.5$, 1 and 1.5 of $Er_2Ti_{2-x}Sn_xO_7$. The refinement using Champion model was again successful; the refined profiles are presented in Fig.5.11, Fig.5.12, and Fig.5.13.

The moment sizes are now tabulated in Table 5.5 and to see their variance with x better Fig.5.14 is plotted. From this, one can see that the moment size does not vary linearly with x. This gives a good contrast to the linear variation in T_N we saw in the previous section (Fig.5.6).

Finally, equipped ourselves with the refined magnetic moment sizes, we can now replot the ordering parameter growth, now using ordered moment size as the y-axis. This is shown in Fig.5.15. It is interesting to note that up to $x = 1$, substitution in Sn for Ti in $Er_2Ti_{2-x}Sn_xO_7$ have no effect of the ordered moment size but lowers T_N substantially.

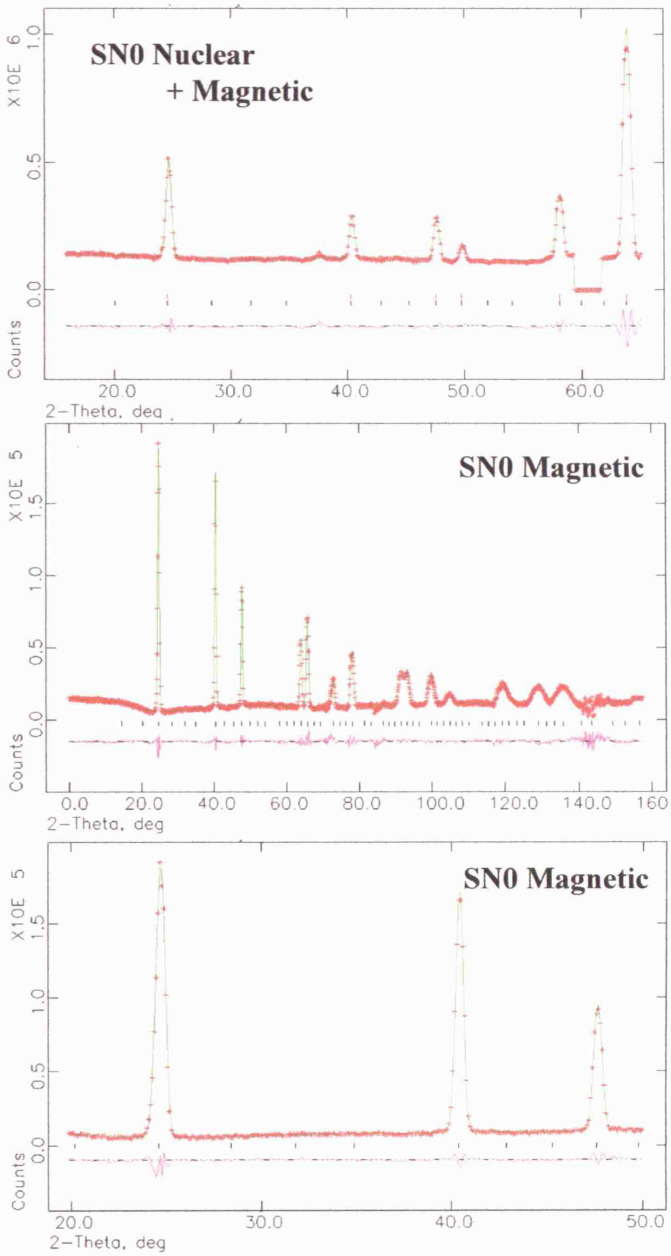

Figure 5.10: Magnetic diffraction pattern of $Er_2Ti_2O_7$ fitted with Champion model (use of any combination of basis vectors ψ_2 and/or ψ_3 belonging to the irreducible representation Γ_5). *Top* pattern: using Nuclear + Magnetic (non-subtracted) data taken at T = 0.1 K. The calculated reflections are shown by two types of markers; top = magnetic, bottom=nuclear reflections. *Middle* and *Bottom* patterns: using Magnetic (subtracted) data (T = 0.1 K - 1.497 K).

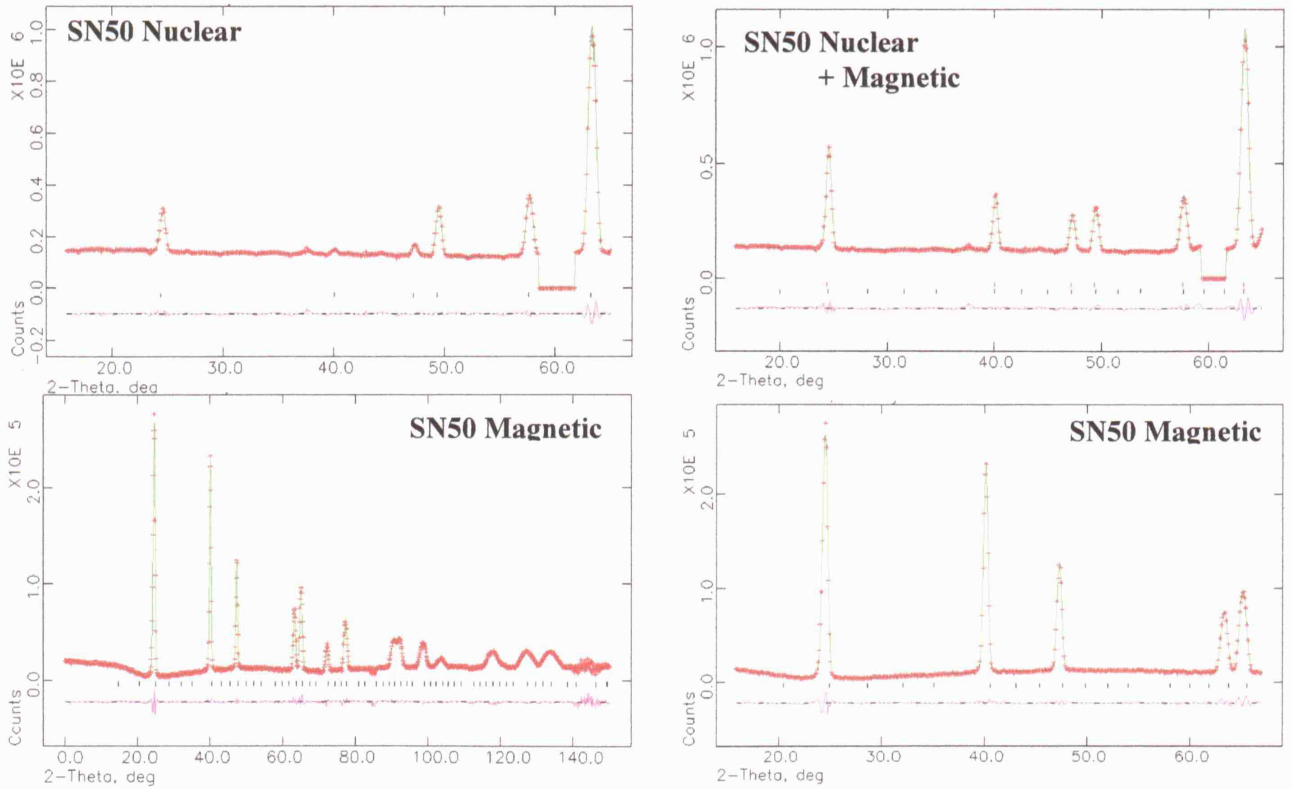

Figure 5.11: Nuclear ($T = 1.288$ K) and magnetic ($T = 0.1$ K) diffraction patterns of $Er_2Ti_{1.5}Sn_{0.5}O_7$ (SN50) fitted with Champion model (use of any combination of basis vectors ψ_2 and/or ψ_3 belonging to the irreducible representation Γ_5). Magnetic profiles use the subtracted data.

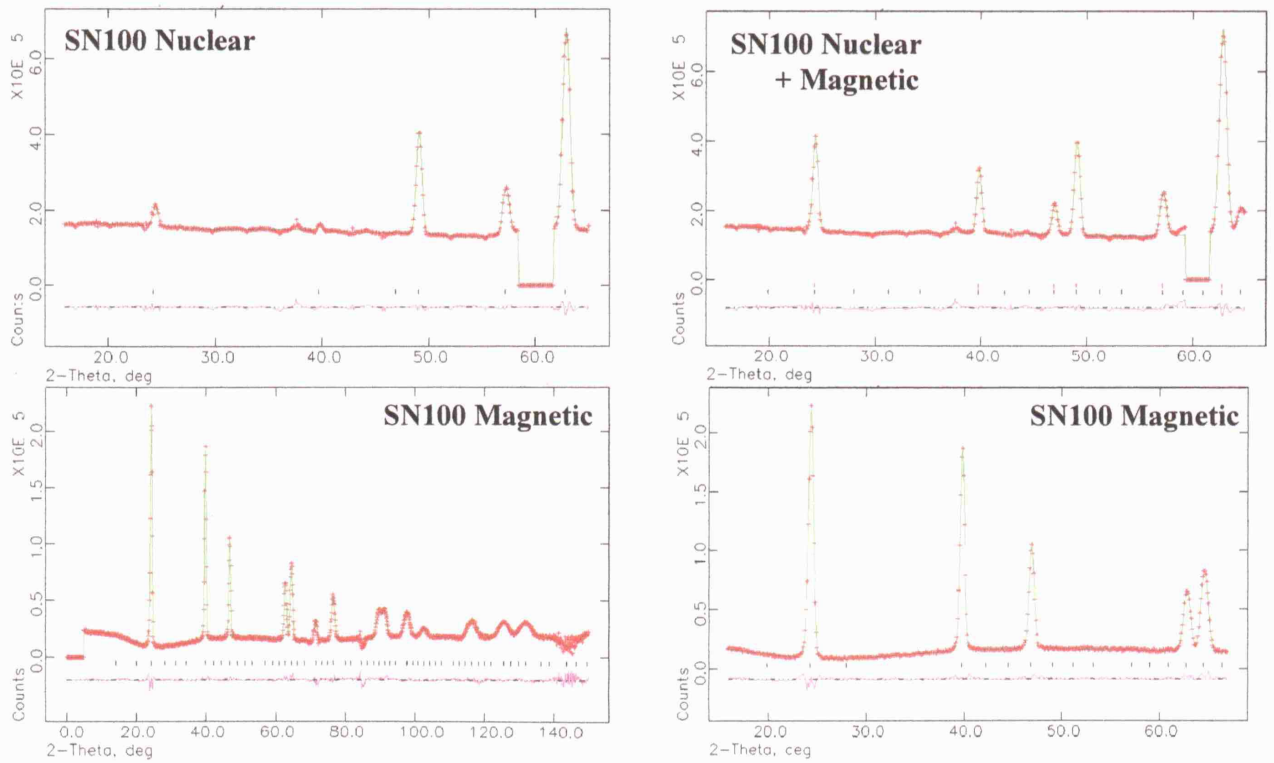

Figure 5.12: Nuclear ($T = 1.104$ K) and magnetic ($T = 0.1$ K) diffraction patterns of $Er_2Ti_1Sn_1O_7$ (SN100) fitted with Champion model (use of any combination of basis vectors ψ_2 and/or ψ_3 belonging to the irreducible representation Γ_5). Magnetic profiles use the subtracted data.

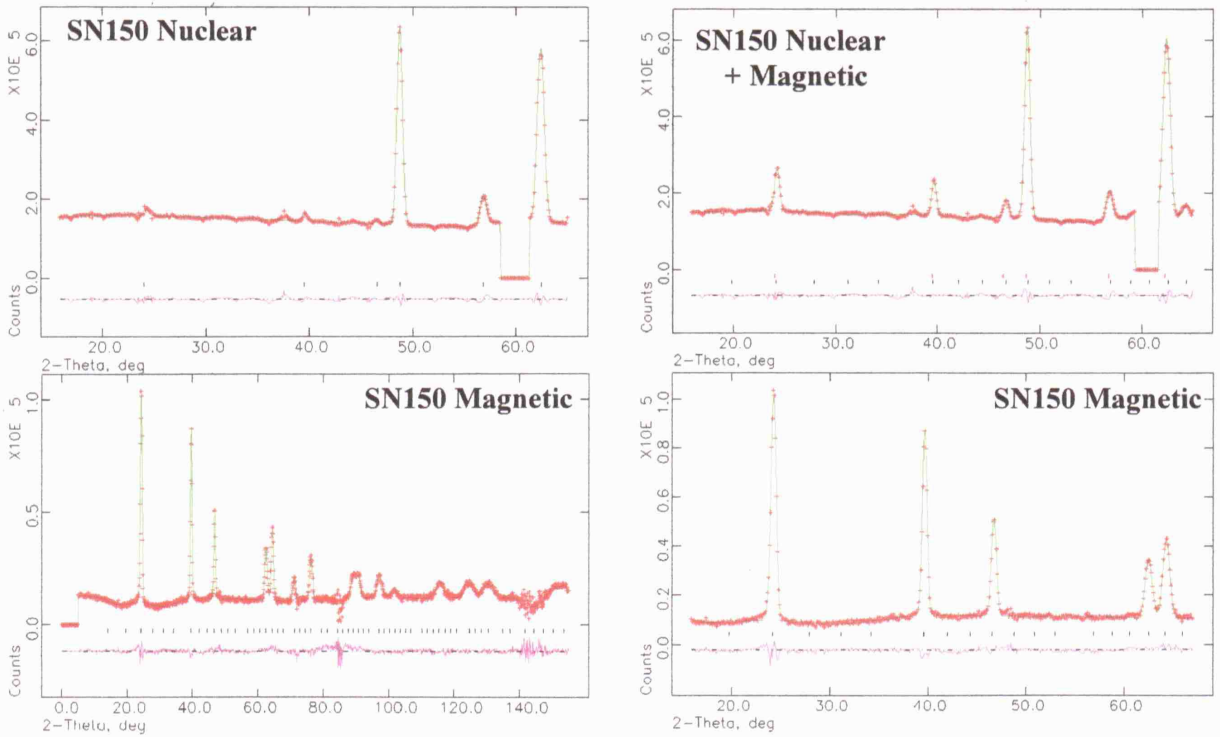

Figure 5.13: Nuclear (T = 1.1 K) and magnetic (T = 0.069 K) diffraction patterns of $Er_2Ti_{0.5}Sn_{1.5}O_7$ (SN150) fitted with Champion model (use of any combination of basis vectors ψ_2 and/or ψ_3 belonging to the irreducible representation Γ_5). Magnetic profiles use the subtracted data.

	$Er_2Ti_2O_7$	$Er_2Ti_{1.5}Sn_{0.5}O_7$	$Er_2Ti_1Sn_1O_7$	$Er_2Ti_{0.5}Sn_{1.5}O_7$	$Er_2Sn_2O_7$
T	0.1 K	0.1 K	0.1 K	0.069 K	0.070 K
Model	Champion	Champion	Champion	Champion	Palmer/Chalker*
Magnetic only (2θ= 15 - 150°)					
μ / μ_B	3.40(1)	3.46(1)	3.49(1)	1.94(1)	0.87(1)
R_{wp}	0.1061	0.0779	0.0784	0.1103	0.0518
χ^2	161.5	112.5	131.6	168.9	43.71
Nuclear + Magnetic (2θ= 15 - 65°)					
μ / μ_B	3.51(4)	3.56(3)	3.48(3)	1.99(2)	0.34(1)
R_{wp}	0.0424	0.0368	0.0326	0.0256	0.0232
χ^2	275.6	218.2	177.2	106.7	113.0

Table 5.5: Refined magnetic moment size of $Er_2Ti_{2-x}Sn_xO_7$ (x = 0, 0.5, 1, 1.5 and 2). The moment orientations for each refinement are fixed according to the model used. Two sets of refinements were carried out for each compound; one using subtracted data (magnetic peaks only) and the other using non-subtracted data (magnetic + nuclear). All magnetic refinements are scaled with the corresponding nuclear refinements. *See next section for refinement details.

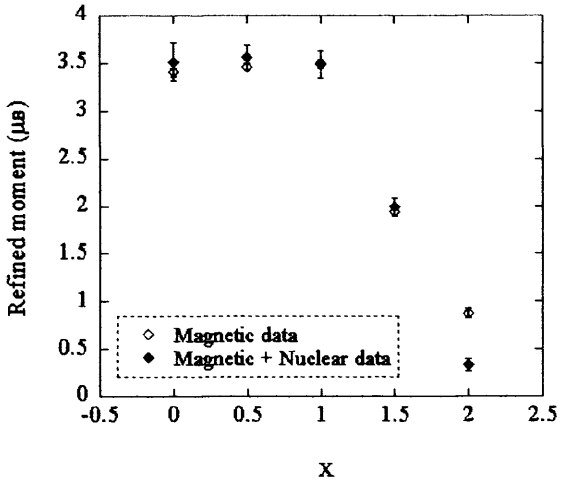

Figure 5.14: Refined ordered moment size for the series $Er_2Ti_{2-x}Sn_xO_7$ at T = 0.1 K (x = 0), 0.1 K (x = 0.5), 0.1 K (x = 1), 0.069 K (x = 1.5), and 0.07 K (x = 2). The same refinements were repeated twice using different data sets; using (i) low T – high T subtracted magnetic data (open diamond) and (ii) low T non-subtracted magnetic + nuclear data (black diamond).

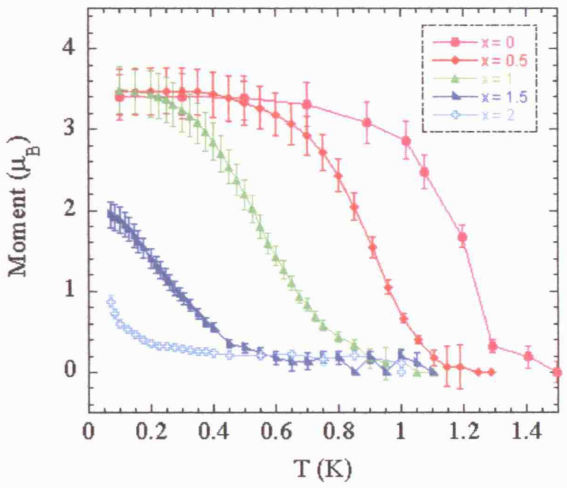

Figure 5.15: Ordered moment variation for the series $Er_2Ti_{2-x}Sn_xO_7$ (x = 0, 0.5, 1, 1.5, 2) with temperature. The ratios of the moment size between different compounds are based on the magnetic refinement (using the subtracted data) at each compound's lowest measured temperature.

5.2.4 Ordering pattern of $Er_2Sn_2O_7$ ($x = 2$)

5.2.4.1 Nuclear structure analysis

Now we move on to $Er_2Sn_2O_7$ and examine its ordering. As it was done previously, first the nuclear pattern is refined. This is shown in Fig.5.16. The refined parameters are listed in Table 5.3 together with those for the rest of the series. In the magnetic refinement, the refined nuclear profiles were used as a starting point. Then, only the lattice parameters and the background were allowed to be refined apart from the moment orientation and moment size. From the nuclear refinements, again, the compound was proved to be phase pure. Hence we now proceed to the final stage of this chapter; to investigate the magnetic structure of $Er_2Sn_2O_7$.

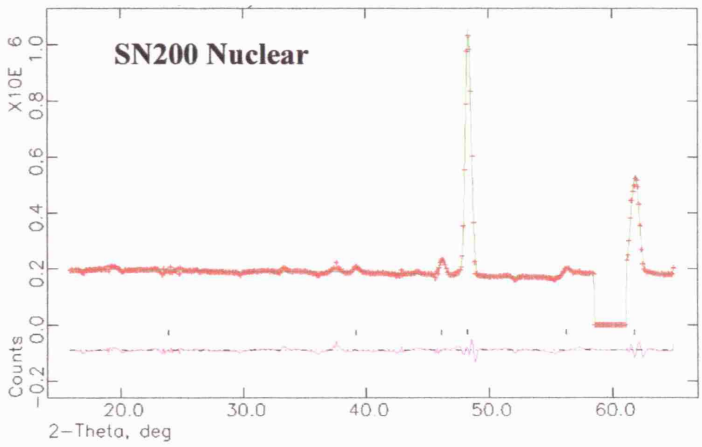

Figure 5.16: Refined profile for data collected from D20 instrument for $Er_2Sn_2O_7$ at 1.1 K; the nuclear diffraction pattern.

5.2.4.2 Magnetic structure analysis

As it was verified in the previous section (section 5.2.1), the magnetic diffraction peaks of $Er_2Sn_2O_7$ could also be indexed on a **k** = 000 propagation vector. It is noted that, as it was the case for $Er_2Ti_2O_7$, in this $Er_2Sn_2O_7$ the [111] magnetic Bragg peak was also observed. As magnetic scattering intensity (I_{hkl}) measures the magnetic moment component which is perpendicular to the scattering vector **Q** (*h k l*), this is an indication that the spins have components perpendicular to the ⟨111⟩ axes.

In this section the same procedure for the magnetic structure analysis shown for $Er_2Ti_2O_7$ above (section 5.2.3) is followed, except that we present the representational analysis results in more detail; all the tested combinations of basis vectors will now be shown.

To simplify the refinement a major approximation was made. That is, assuming equal moment sizes at the four tetrahedron sites only orthogonal sets of basis vectors were chosen to be mixed. All other combinations that lead to unequal moment sizes were not tested, apart from few exceptions that were thought to be interesting to test. All the results together with the models (combinations of the basis vectors) used are

listed in Table 5.6. The outcome is that it is the Palmer-Chalker model which orders within representation Γ_7 that gives the best fit. The refined profile for the Palmer-Chalker model is shown in Fig. 5.19 and the remaining profiles for the other models are shown in Fig.5.17 for comparison. Powder averaging leads to the structures described by basis vector ψ_4, ψ_5 and ψ_6 being indistinguishable by neutron diffraction and prevents contributions of the individual basis vectors from being refined. For this reason only ψ_4 (out of the three basis vectors) was used in the refinement whenever mixing of Palmer-Chalker state and other state(s) were intended.

Although the pure Palmer-Chalker state (modeled by the usage of either of ψ_4, ψ_5 or ψ_6) gives the best fit to the magnetic data, some allowance of mixing in other state(s) exists. In other words, mixing basis vector(s) from other IR(s) up to certain extent still results in the same refinement result. The allowed extent in mixing is shown by the plots in Fig.5.18. It is shown that the minimum in χ^2 occurs when the mixing coefficient of the Palmer-Chalker basis vector ($c\psi_4$, $c\psi_5$ or $c\psi_6$) is unity. This minimum has a flat bottom and it extends up to ~10% of the mixing coefficients. This can be used as indications of (i) error size in which mixing coefficients are refined, or (ii) extent in which other basis vectors are allowed to mix in.

Choosing the Palmer-Chalker model to fix the moment orientations, finally the ordered moment size was refined using the GENLES routine of GSAS Suite [3]. The ordered moment at T = 70 mK was 0.87 (1) μ_B and 0.34 (1) μ_B for the subtracted (magnetic only) and non-subtracted (nuclear + magnetic) data, respectively. This is less than 1/10 of the maximum ordered moment that can be observed by neutron at low T for Er (= $g_J J = 9\ \mu_B$). Therefore, it is observed that the moments of the Er^{3+} ion in $Er_2Sn_2O_7$ are either highly disordered or are reduced in size fundamentally due to its environment (i.e. the crystal field). The origin of this reduced ordered moment will be investigated further in Chapter 7.

Model	Basis vectors	mixing ratio	orthogonality	Cycle	χ^2_{min}
FeF_3	Γ(3) Ψ(1):		-	5	263.8
FeF_3	Γ(3) Ψ(1):		Yes	100	157.2
JDMC	Γ(5) Ψ(3):		Yes		
JDMC	Γ(5) Ψ(2):	0~1	Yes	100	156.9
	Γ(5) Ψ(3):	1~0	Yes		
JDMC	Γ(5) Ψ(2):		Yes	200	155.2
	Γ(5) Ψ(3):		No		
Spin ice (FM)	Γ(9) Ψ(7):		Yes		
Champion	Γ(5) Ψ(2):		Yes	100	155.2
Spin ice (FM)	Γ(9) Ψ(7):		Yes		
Champion	Γ(5) Ψ(2):		Yes	100	99.02
Spin ice (AFM)	Γ(9) Ψ(8):		Yes		
Champion	Γ(5) Ψ(2):	~ 0.1	No	100	49.01
Palmer Chalker	Γ(7) Ψ(4):	~ 0.9	No		
Champion	Γ(5) Ψ(2):	~ 0.1	No	100	49
Palmer Chalker	Γ(7) Ψ(5):	~ 0.9	No		
Champion	Γ(5) Ψ(2):	~ 0.1	No	100	49
Palmer Chalker	Γ(7) Ψ(6):	~ 0.9	No		
Champion	Γ(5) Ψ(2):		Yes	300	74.36
Spin ice (FM)	Γ(9) Ψ(7):		Yes		
Spin ice (AFM)	Γ(9) Ψ(8):		Yes		
Champion	Γ(5) Ψ(3):	~ 0.1	Yes	100	49
Palmer Chalker	Γ(7) Ψ(4):	~ 0.9	Yes		
Champion	Γ(5) Ψ(3):	~ 0.1	Yes	100	49
Palmer Chalker	Γ(7) Ψ(5):	~ 0.9	Yes		
Champion	Γ(5) Ψ(3):	~ 0.1	Yes	100	49
Palmer Chalker	Γ(7) Ψ(6):	~ 0.9	Yes		
FeF_3	Γ(3) Ψ(1):	~ 0.1	Yes	300	49.37
Champion	Γ(5) Ψ(3):	~ 0.1	Yes		
Palmer Chalker	Γ(7) Ψ(4):	~0.9	Yes		
Palmer Chalker	Γ(7) Ψ(4):		-	5	49
Palmer Chalker	Γ(7) Ψ(5):		-	5	49
Palmer Chalker	Γ(7) Ψ(6):		-	5	49
Palmer Chalker	Γ(7) Ψ(4):	~ 0.9	Yes	100	49.02
Spin ice (FM)	Γ(9) Ψ(7):	~ 0.1	Yes		
Palmer Chalker	Γ(7) Ψ(4):	~ 0.9	Yes	100	49
Spin ice (AFM)	Γ(9) Ψ(8):	~ 0.1	Yes		
Palmer Chalker	Γ(7) Ψ(4):	~ 0.9	Yes	300	51.27
Spin ice (FM)	Γ(9) Ψ(7):	~ 0.1	Yes		
Spin ice (AFM)	Γ(9) Ψ(8):	~ 0.1	Yes		
Spin ice (FM)	Γ(9) Ψ(7):		Yes	100	73.01
Spin ice (AFM)	Γ(9) Ψ(8):		Yes		

Table 5.6: Goodness of fit parameters χ^2 for each of the possible combinations of basis vectors ψ(ν), for $Er_2Sn_2O_7$ magnetic diffraction pattern measured on D20 at 0.07 K. To define the model used a name is given to every IR Γ(n); see text for definitions. The orthogonality of the mixed ψ(ν)s and number of Reverse Monte Carlo cycles are also indicated. For the models with lowest χ^2s, the ratios of the mixing coefficients of ψ(ν)s that give the lowest χ^2 are also shown.

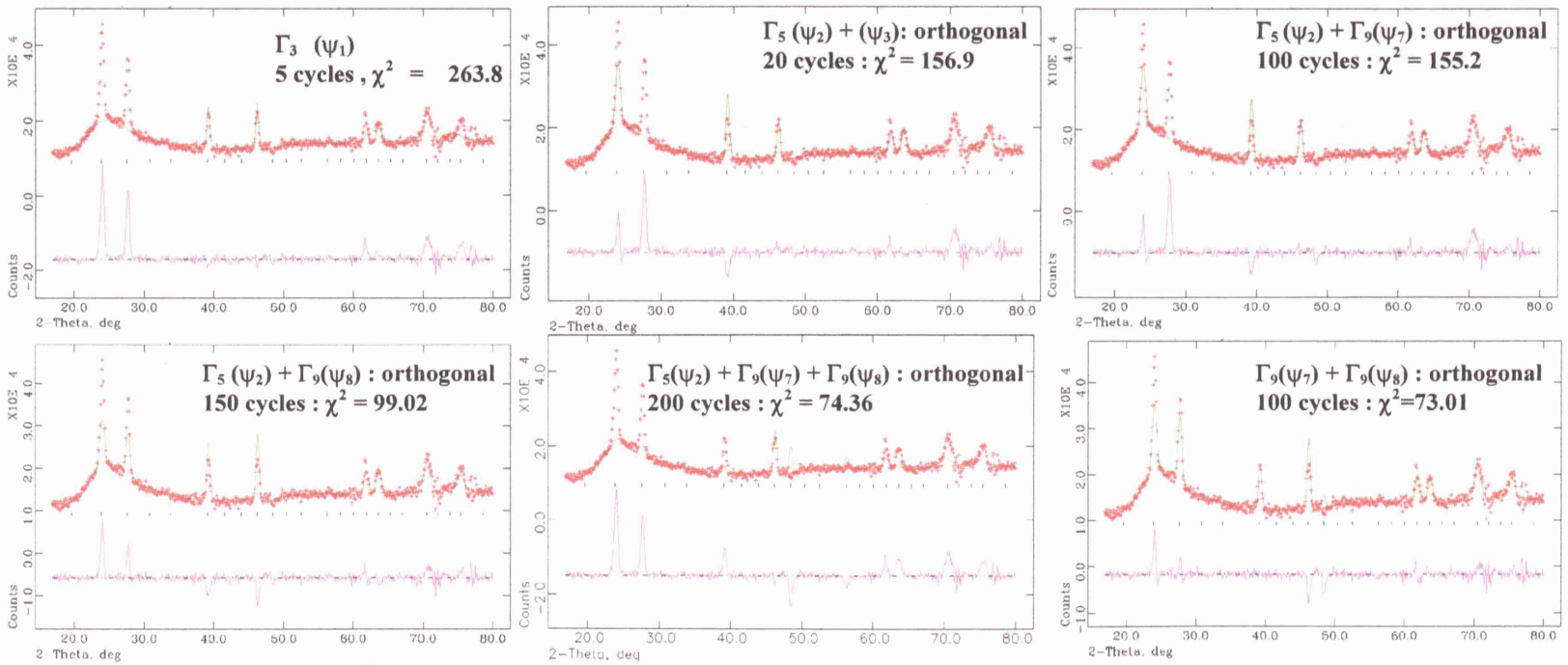

Figure 5.17: Refined magnetic profiles for $Er_2Sn_2O_7$ using different combinations of basis vectors, ψ_v. Mainly, combinations of orthogonal basis vectors are chosen and tested. These poor fitting profiles contrast with the good fit achieved using the Palmer-Chalker model ($\psi_4 + \psi_5 + \psi_6$ of Γ_7) shown in Fig.5.19.

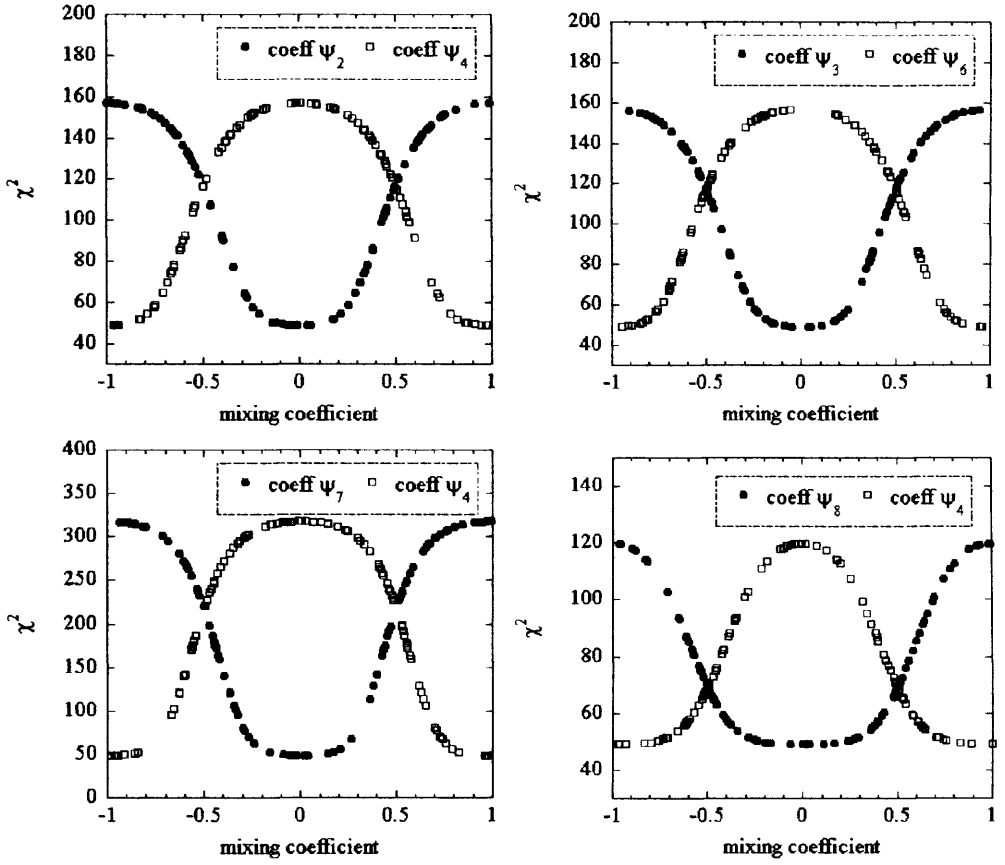

Figure 5.18: Plot showing the mixing ratio of different basis vectors ψ_vs in order to achieve the best magnetic pattern refinement for $Er_2Sn_2O_7$. One of the basis vectors are taken from the Palmer-Chalker state (one of the ψ_4, ψ_5 or ψ_6) and is mixed with another basis vector; ψ_2 or ψ_3 from the Champion state or ψ_7 or ψ_8 from the spin ice (FM or AFM) state. The χ^2 variation with the mixing coefficients for the Palmer-Chalker basis vectors are plotted in black circles and open squares are used for the other basis vector. It is shown that the minimum in χ^2 occurs when the mixing coefficient of the Palmer-Chalker basis vector is 1. This minimum extends up to ~ 10 % of the mixing coefficients. This can be used as indications of (i) error size in which mixing coefficients are refined, or (ii) extent in which other basis vectors are allowed to mix in.

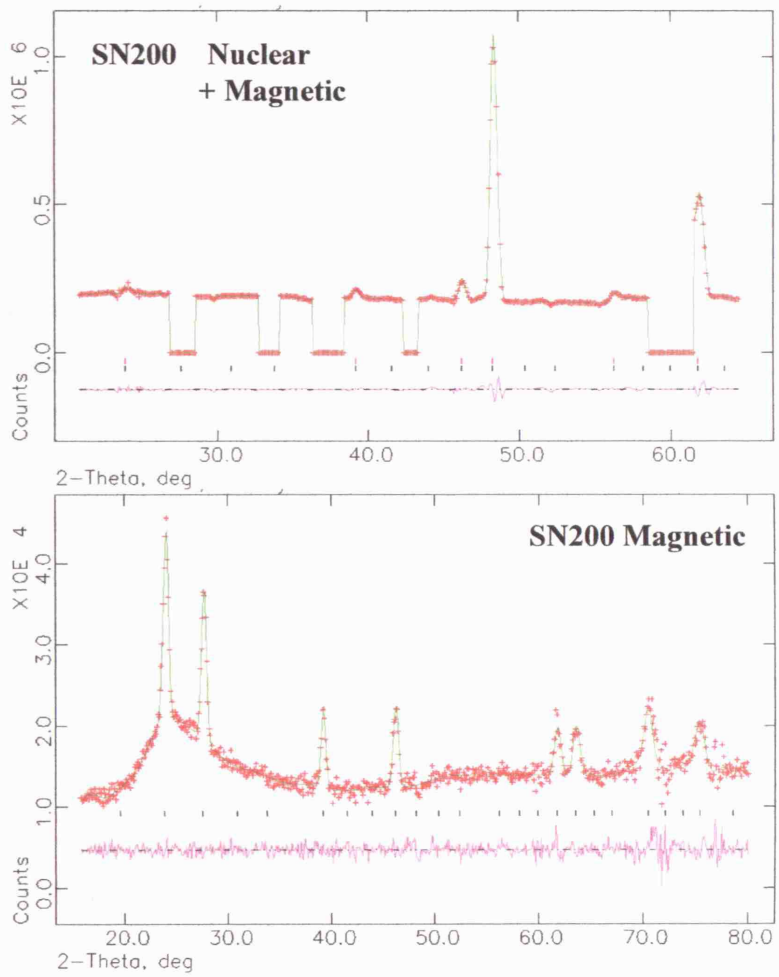

Figure 5.19: Magnetic diffraction pattern of $Er_2Sn_2O_7$ fitted with Palmer-Chalker model (use of one of the basis vectors ψ_4, ψ_5 or ψ_6 belonging to the irreducible representation Γ_7). *Top* pattern: using Nuclear + Magnetic (non-subtracted) data taken at T = 0.07 K. The calculated reflections are shown by two types of markers; top = magnetic, bottom = nuclear reflections. *Bottom* pattern: using Magnetic (subtracted) data (T = 0.07 K - 1.002 K).

5.3 Conclusions

Here we summarize the results obtained in this chapter.

(i) The indexing of the diffraction patterns confirmed the ordering of all the samples (including $Er_2Sn_2O_7$ which was not known to order) with the ordering vector **k** = 000. Also the presence of the ⟨111⟩ magnetic Bragg peaks in all samples indicates that the ordering happens in the ⟨111⟩ easy plane (i.e. all ordered spin components should lie perpendicular to the local ⟨111⟩ axes of the tetrahedra.). The first four compounds with x = 0, 0.5, 1 and 1.5 of $Er_2Ti_{2-x}Sn_xO_7$ give rise the same magnetic diffraction pattern, indicating that the ordered structure is the same for these four. For $Er_2Sn_2O_7$ (x = 2) a new magnetic Bragg peak [002] was observed, suggestive of it having a different structure to the rest of the series.

(ii) From the T_N v.s. x plot (Fig.5.6), one can see a linear drop in T_N with increasing x (i.e. higher Sn substitution for Ti). However, it is not certain whether there exist a point in which T_N drops to zero or not. If exists, this is an example of a quantum critical point and is worth a further investigation. This will be examined further in Chapter 6.

(iii) The diffraction patterns of the four compounds x = 0 ($Er_2Ti_2O_7$), 0.5, 1 and 1.5, assumed to have the same ordered magnetic structure, was fitted against the Champion model; the ordering happening within the irreducible representation (IR) Γ_5 ($\psi_2 + \psi_3$). This showed excellent agreement with the previous work by Champion *et al.*[7,9] done on $Er_2Ti_2O_7$ and gave good fit for all the four compounds. See Fig.2.14 and Chapter 2 for full description of this Champion model. The ordered moment size show peculiar variance with x (Fig.5.14) ; its size remains at a constant value of ~ 3.5 μ_B (about 1/3 of the full moment of Er^{3+}) for x = 0, 0.5 and 1 but decreases dramatically for x = 1.5 (~2 μ_B). This sudden drop in ordered moment contrasts with the linear variance of T_N with x.

(iv) Following Champion's work [7,9], the ordered magnetic structure of $Er_2Sn_2O_7$ was investigated by the use of the representational analysis method described

in section 3.4.2.3. Different combinations of basis vectors (mainly focusing on the orthogonal combinations) were fitted to the magnetic diffraction pattern and this gave the conclusion that the ordering pattern of $Er_2Sn_2O_7$ is best described by the Palmer-Chalker model. This belongs to the IR Γ_5 (ψ_4 or ψ_5 or ψ_6) – see Chapter 2 (section 2.3.3) and Fig 2.10 for description. This Palmer-Chalker state correspond to the ground state for the Heisenberg pyrochlore antiferromagnet (AFM) with dipolar interactions [2]. The refined ordered moment of the Er^{3+} in $Er_2Sn_2O_7$ was found to be 0.34 (1) or 0.87 (1) μ_B, depending on which data is refined upon (the subtracted or non-subtracted diffraction data). The origin of this minute moment size is not known yet. It must either be due to the disorder induced by zero-point fluctuations, which are a general property of AFMs [12,13], or otherwise the size of the individual moment of Er^{3+} is reduced by its crystal field environments. This if further investigated in the crystal field study carried out on the $Er_2Ti_{2-x}Sn_xO_7$ series in Chapter 7.

One final point to mention is the possibility of mixing other basis vectors to describe the ordered magnetic structure of $Er_2Sn_2O_7$. Up to ~10 % of mixing other basis vectors such as the spin ice basis vectors (ψ_7 or ψ_8 of Γ_9) to the Palmer-Chalker state gives the same χ^2, hence it can not be distinguished from the pure Palmer-Chalker state. As a consequence, a possibility of including a small ferromagnetic contribution (e.g. ψ_7) in the system remains.

References for Chapter 5

[1] K.Matsuhira, Y.Hinatsu, K.Tenyai, H.Amitsuka and T.Sakakibara, J. Phys. Soc. Japan **71**(6), 1576 (2002)

[2] S.E.Palmer and J.T.Chalker, Phys. Rev. B **62**(1), 488 (2000)

[3] A.C.Larsen and R.B.von Dreele, General Structure Analysis System, Lansce, Los Alamos National Laboratory, Los Alamos, 1994.

[4] A. S. Wills, Phys. Rev. B **63**, 064430 (2001).

[5] A. S. Wills, Physica B **680**, 276 (2000), program available from ftp://ftp.ill.fr/pub/dif/sarah/.

[6] O.Knop. F.Brisse, L.Castelliz and Sutrano, Can. J. Chem. **43**, 2812 (1965).

[7] J.D.M.Champion, Ph.D. Thesis, Univ. London, (2001).

[8] M.J.Harris, S.T.Bramwell, T.Zeiske, D.F.McMorrow, and P.J.C.King, J. Magn. Magn. Mater. **177**, 757 (1998).

[9] J.D.M.Champion, M.J.Harris, P.C.W.Holdsworth, A.S.Wills, G.Balakrishnan, S.T.Bramwell, E..Cizmar, T.Fennell, J.S.Gardner, J.Lago, D.F.McMorrow, M.Orendac, A.Orendacova, D.M.Paul, R.I.Smith, M.T.F.Telling and A.Wildes, Phys. Rev. B **68**, 020401 (2003).

[10] Y.A.Izyumov, V.E.Naish, J.Magn.Magn.Matter **12**, 239 (1979).

[11] O. V. Kovalev, *Representations of the Crystallographic Space Groups*, 2 ed., Gordon and Breach Science Publishers, Switzerland, 1993.

[12] P.W.Anderson, Phys. Rev. **102**, 1008 (1956).

[13] R.M.White, *Quantum Theory of Magnetism,* McGraw-Hill, New York,1970.

[14] L.H.Brixner, Inorg. Chem. **3**, 1065 (1964).

Chapter 6

Low Temperature Magnetization of $Er_2Ti_{2-x}Sn_xO_7$

In this chapter we present the results of magnetization measurements carried out on the $Er_2Ti_{2-x}Sn_xO_7$ series with x over 1.5 up to 2. This has two purposes. One is to verify whether $Er_2Sn_2O_7$ ($x = 2$) orders at a temperature lower than the previously measured T = 150 mK [4] where no ordering transition was observed. The second is, as it was derived from the previous chapters, for the purpose of looking into the high Sn concentration region, $x = 1.5 \sim 2$, where one might expect a quantum critical point to occur. Therefore, samples with finer increments of x (of 0.05) were synthesized (about 2 g each, see Chapter 4 for details) and were used in the measurements.

In this work, magnetizations and susceptibilities of the samples were measured using the Faraday force magnetometer constructed by Sakakibara *et al.* at the Institute for Solid State Physics, Tokyo University. This magnetometer operating in the dilution refrigerator realizes accurate measurement of magnetic moment with a high resolution; of better than 1×10^{-7} Am^2 (1×10^{-4} emu) at ultra low temperatures down to ≤ 25 mK and in fields up to 9 T. Here we briefly show the mechanism of the equipment and of the measurement [1].

6.1 Faraday Force Magnetometer

Among the various methods for magnetization measurement, inductive methods (sample extraction, vibrating sample and field modulation techniques) are most commonly used. However, moving the sample inside a pick up coil in order to drive a time-varying magnetic flux results in heating the system and is not ideal for very low temperature measurements. Even in the field modulation (ac) method where the sample is held static, heating due to the time-varying modulation field is not negligible for metallic samples. Moreover, this method does not suit the measurement of irreversible phenomena with hysteresis in the magnetization.

Here instead, we measure the magnetization by measuring the forces exerted on a specimen situated in a spatially varying magnetic field; the use of Faraday method. As this method can be done with an infinitesimal displacement of the sample, a heating-free measurement of the magnetization is realizable. The magnetic force is measured using capacitors in the equipment used.

6.1.1 Method of measurement

Fig.6.1 schematically follows the principle of the measurement. A sample that gives magnetization **M** is mounted on a small load-sensing device (called the 'load cell') made of a parallel-plate variable capacitor. This load cell is schematically shown in Fig.6.2. The powder sample was ground together with silver powder to improve thermal conductivity and was loaded into a silver sample holder which was in turn fixed to the stage of the movable plate of the load cell using some varnish. The capacitor plate on the top has a diameter of 10 mm and is suspended by two sets of perpendicularly crossing (in x- and y-directions) phosphor bronze wires (0.1 - 0.2 mm diameter) with small tension of ~ 0.1 N. The wires act as elastic springs making the top plate movable in the z-direction only. On the other hand, the bottom plate is fixed to the cell, 3 mm apart from the movable plate along the z-direction. The displacement δ of the plate by the force along z-direction, F_z, can be estimated from the formula for the

1 mm / N. The sensitivity of the load cell is calibrated using a specimen whose magnetization is known, such as Ni.

Now we go back to discuss what causes the plate movement in the z-direction. When the sample is subject to a spatially varying magnetic field **B**, it experience a force

$$\mathbf{F} = (\mathbf{M} \cdot \nabla)\mathbf{B}. \tag{6.1}$$

Suppose that **F** is directed along the z-direction, the displacement of the plate is proportional to **F** and can be detected as a change in capacitance ΔC; $\Delta C = C_1 - C_0$ where C_1 is the capacitance measured with the field gradient $G > 0$ on and C_0 is the capacitance where $G = 0$. The field gradient G_0 at the specimen (at $z = 0$) defined as

$$G_0 = (\partial B_Z / \partial z)_{z=0} \tag{6.2}$$

was produced by the use of a set of gradient coils. The superconducting magnet used here is schematically drawn in Fig.6.3 together with the spatial variance in **B**. The main coil produces magnetic fields B_0 up to 9 T, whose homogeneity at the centre is better than 10^{-5} within a 10 mm diameter spherical volume. (Note: from now on, the magnetic field will be denoted by an *italic B*, representing just the magnitude of the field, $|\mathbf{B}| = B$, since the direction is not important in an experiment using powder sample. The same notation scheme will be applied whenever a vector quantity is described.) The gradient coils are wound outside the main coil, and can provide vertical field gradient G_0 up to 10 T/m, whose uniformity along the axis is better than 0.5% over ±5 mm from the centre. It is indeed an elegant way of exerting a field gradient without actually adding value to the field at the sample B_0. The magnetic field from the gradient coil has $B_{grad} = 0$ at the sample while $G_0 = (\partial B_Z/\partial z)_{z=0}$ can be set to be a finite value. On the other hand, the magnetic field from the main coil applied to the sample B_{main} contributes directly to B_0 while its field gradient is null.

Now finally ΔC can be transformed to the displacement Δd of the plate by the simple formula

$$\Delta d = \varepsilon_0 S (C_0^{-1} - C_1^{-1}) \tag{6.3}$$

where S denotes the area of the plate. From this value Δd together with the information obtained from the calibration done on Ni one can obtain the magnetization of the

specimen in question.

Another important factor to be determined is the spring constant K of the load cell. The force F acting on a spring can be formulated using

$$F = K \cdot \Delta d \tag{6.4}$$

where K is the spring constant of the spring and Δd is the length change of the spring. This equation together with Eqn.6.1, 6.2 and 6.3 gives

$$M_z = K \{\varepsilon_0 \cdot S (C_0^{-1} - C_1^{-1})\} / G_0 \tag{6.5}$$

where M_z is the magnetic moment component in z-direction. Therefore, in order to determine the absolute value of the moments, the knowledge of the precise value of K is essential.

6.1.2 Installation in a dilution refrigerator

The load cell was installed in a Kelvinox$^{\text{AST Minisorb}}$ dilution refrigerator which operates by cryogenically circulating the ^{3}He using double sorption pumps built into the insert. This is schematically drawn in Fig.6.4 below. Its cooling power is of 40 μW at 100 mK and the base temperature reachable is ≤25 mK.

The properties of the liquids in the dilution refrigerator are described by quantum mechanics: the details will not be described here. However, it is important to know that below a tri-critical point of 0.86 K, the ^{3}He/^{4}He liquid mixture may separated into two phases; one rich in ^{4}He (the heavier *dilute phase*) and one rich in ^{3}He (the lighter *concentrated phase*). Because ^{3}He has lower density, it floats on top of the ^{4}He rich liquid. As the temperature goes down, the ^{3}He rich phase becomes pure ^{3}He but surprisingly, the dilute phase does not become pure ^{4}He, rather there is 6.4% ^{3}He left in it (at vapor pressure) even at T = 0 K. This finite solubility is of utmost importance for dilution technology. The ^{4}He which makes up the majority of the dilute phase is inert, and the ^{3}He gas moves through the liquid ^{4}He without interacting with it at all. This phase boundary is set to occur in the 'mixing chamber' of the dilution refrigerator, and the cooling obtained by this process, which is analogous to evaporation at a liquid surface, is used to cool a sample.

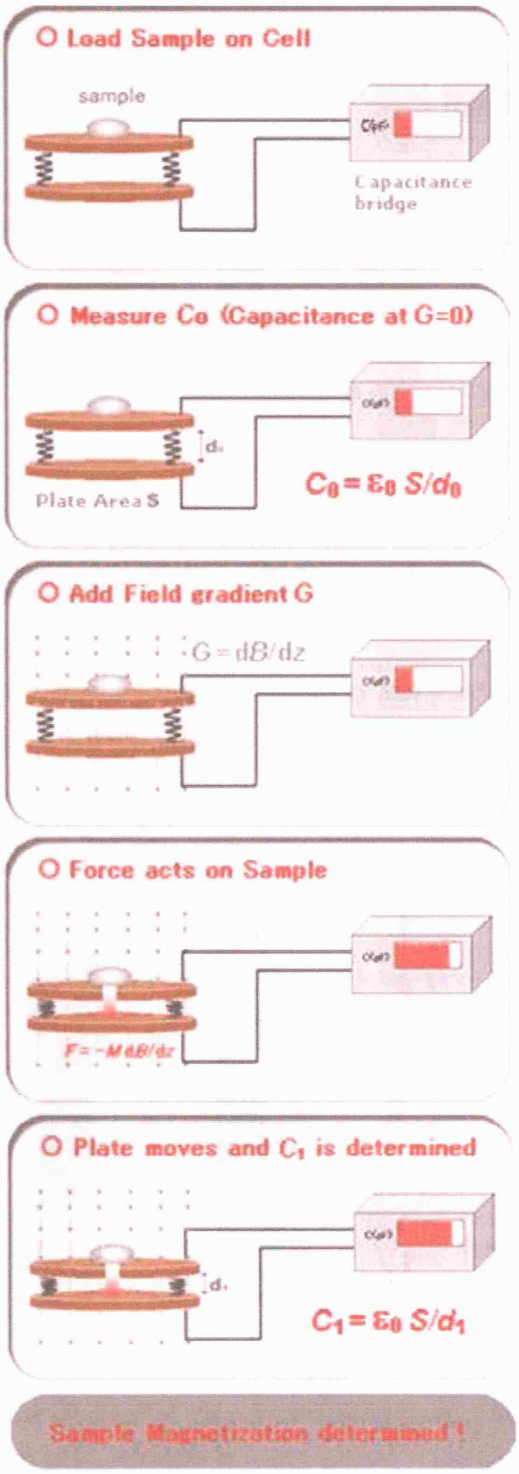

Figure 6.1: Schematic flow chart showing the principle of magnetization measurement using the Faraday force magnetometer consisting of a load sensing device (the load cell) and a capacitance bridge.

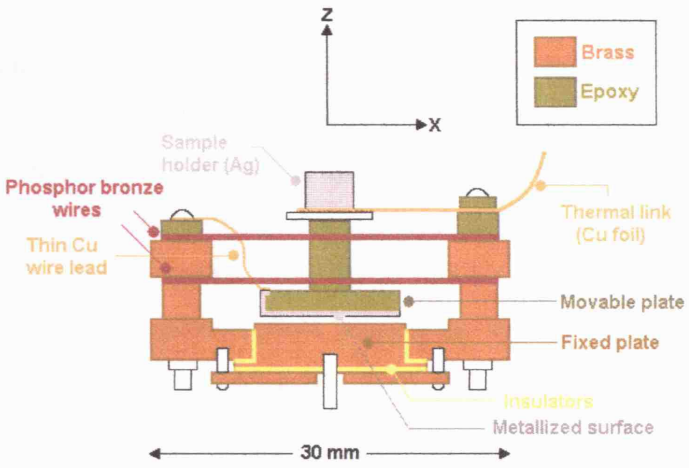

Figure 6.2: Cross-sectional view of the load-sensing device (load cell) loaded into the dilution refrigerator. The movable plate is suspended by two sets of phosphor bronze wires from *x*- and *y*-directions allowing its movement only along the *z*-direction. The sample was ground together with silver powder to improve thermal conductivity and was loaded into a silver sample holder which was in turn fixed to the stage of the movable plate.

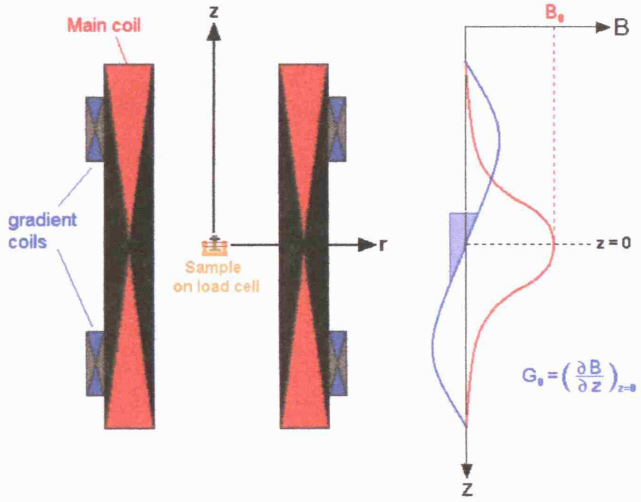

Figure 6.3: Schematic diagram of a superconducting magnet for a Faraday magnetometer. The spatial variance of the magnetic field **B** is also shown. It can be seen that the applied field $\mathbf{B}_{main}$ from the main coil does not contribute to the field gradient G_0 at the sample ($z = 0$) but $\mathbf{B}_{grad}$ from the gradient coils does.

When the refrigerator is started the '1K pot' cooled to ~1.2K by pumping ^{4}He is used to condense the ^{3}He/^{4}He mixture. Then using an external pumping system the mixture is cooled down below 0.86 K (the tri-critical point) in the 'still'. The ^{3}He concentration and the volume of mixture are correctly chosen so that the phase boundary is inside the mixing chamber and the liquid surface is in the still. In a continuously operating system, the ^{3}He should be extracted from the dilute phase and returned into the concentrated phase keeping the system in a dynamic equilibrium. The ^{3}He is preferentially pumped away from the liquid surface in the still which is maintained at 0.6~0.9K using the two sorption pumps because at this temperature the vapor pressure of the ^{3}He is much higher than that of ^{4}He. The sorption pumps are made of charcoal and work by adsorbing the ^{3}He when cooled and releasing it when heated. The use of double sorption pumps enables one of it to cool down while the other heats up, hence it is very time efficient. The concentration of the ^{3}He in the dilute phase in the still therefore becomes lower than it is in the mixing chamber, and consequent osmotic pressure drives a flow of ^{3}He to the still. The ^{3}He leaving the mixing chamber is used to cool the returning flow of concentrated ^{3}He in a series of heat exchangers.

The load cell with the sample on it is thermally connected to the mixing chamber of the dilution refrigerator with a bundle of Cu wires of 0.1 mm diameter and with Cu foil of 10 μm thickness. This is also shown in Fig.6.5.

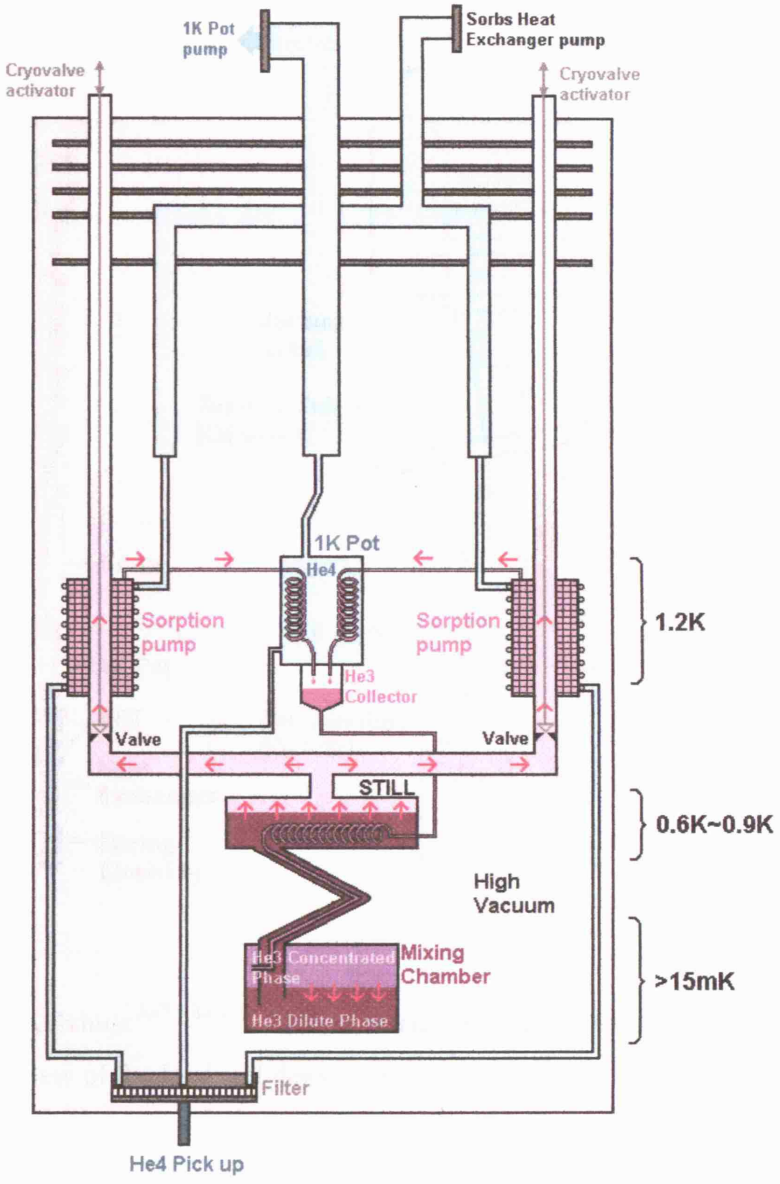

Figure 6.4: Principle of operation of dilution refrigerator with double sorption pumps (Kelvinox$^{AST\ Minisorb}$ in our work). The arrows indicate the flow of ^{3}He in the system.

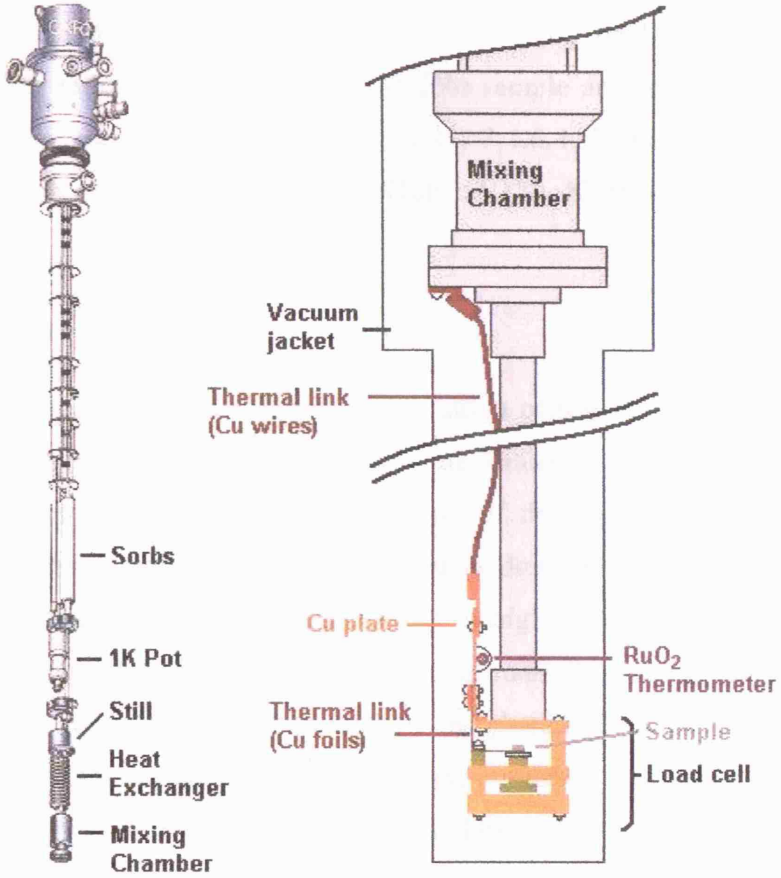

Figure 6.5: The Kelvinox$^{AST\ Minisorb}$ dilution refrigerator insert used in this work (Left) and a schematic view of the load cell deice installed in a dilution refrigerator (Right).

6.2 Results

Here we present the results of the magnetization and susceptibility measurements. The section is separated into three sub-sections; a part describing the details of calibration, a part showing the results for the $Er_2Sn_2O_7$ (SN200) sample and finally a part showing the results for the rest of the samples; $x = 1.9, 1.8, 1.7, 1.6, 1.55$ and 1.5 of $Er_2Ti_{2-x}Sn_xO_7$ series where they are labeled SN190, SN180, SN170, SN160, SN155 and SN150, respectively.

6.2.1 Calibration

As it was explained in section 6.2, the determination of the spring constant K of the load cell is essential in determining the absolute values of the magnetic moments. Another factor that influences the determination of the absolute magnitude of the measurement is the capacitance without the field gradient (G) applied, C_0. It is found from experience that the measured magnetization is highly sensitive to the experiment set up, and the value of C_0 does indeed jump with a small disturbance to the equipment such as the helium transfer to the cryomagnet or changing samples (or even small earthquakes during the measurements!). Therefore, in theory, it is desirable to calibrate (i.e. measure the K value and the C_0) every time these small disturbances are applied. However, in our case, there were too many sample changes and He transfers for this calibration to be repeated every time. Instead, K values were measured only once per sample (except for SN170, SN180 and SN190) and the K value determined for a particular sample was used throughout the analysis for the same sample (both in the analysis of $M(T)$ and $M(B)$).

The K values are determined as follows. First, the field dependence of the magnetization $M(B)$ of a particular sample is measured using the SQUID magnetometer (MPMS, Quantum Design Inc.) at $T = 4.2$ K (or 2 K) in order to obtain a reference $M(B)$ curve with absolute moment size determined. Then the sample is transferred into the magnetometer in the dilution refrigerator and the $M(B)$ curve is measured there at a temperature also of 4.2 K (or 2 K). Finally, by comparing these two $M(B)$ curves one can

determine the K value of the capacitance cell used in the Faraday force magnetometer. In other words, the $M(B)$ curve scaled using this determined K value should be the same to the one measured in SQUID. This is shown in Fig.6.6 (*Left*), for SN200.

The K values in theory should be fairly constant as it is an intrinsic property of the capacitance cell. However, during the experiment it was found that this value fluctuated about $\pm 20\%$ depending on the measurement. Hence, we consider this error size to be the appropriate scale for the error for the absolute measured moment.

For the samples SN170, SN180 and SN190, the calibration measurements were not actually made. Instead, the K values were estimated for these samples by adjusting their saturation moment (in $M(B)$ curve) to be the same for the calibrated sample's saturation value. Again, this is based on the assumption that the $M(B)$ curves of any sample will saturate to a same value ($\sim 4.5\,\mu_B$) and this may add extra error to the accuracy of the measurement. Although, the $M(B)$ curves for the calibrated samples (SN200, SN150, SN155 and SN160) all saturated to this value and therefore, it should be reasonably safe to take this assumption. (We present the $M(B)$ curves for the calibrated samples in Fig.6.6 (*Right*).)

Another useful error analysis might be the comparison of the moment value obtained by the field dependent $M(B)$ and temperature dependent $M(T)$ measurements. The comparison is given in Fig.6.7. The difference in the moment values given by the two different measurements indicates the error that may arise when He transfer is carried out.

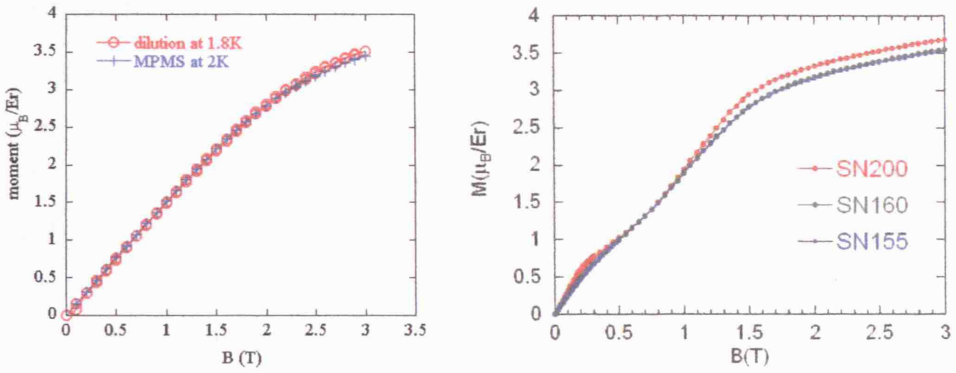

Figure 6.6 - ***Left***: $M(B)$ plots measured by the Faraday magnetometer (in dilution refrigerator) and by the SQUID magnetometer at $T = 1.8$ K and 2 K, respectively for the SN200 sample. The magnetization of former is scaled with the K value of $K_{SN200}^{1.8K} = 2413546$ dyne cm^{-1}. ***Right:*** $M(B)$ plots of calibrated SN200, SN150 and SN160 measured at the $T = 50$ mK showing the saturation values to be approximately equal.

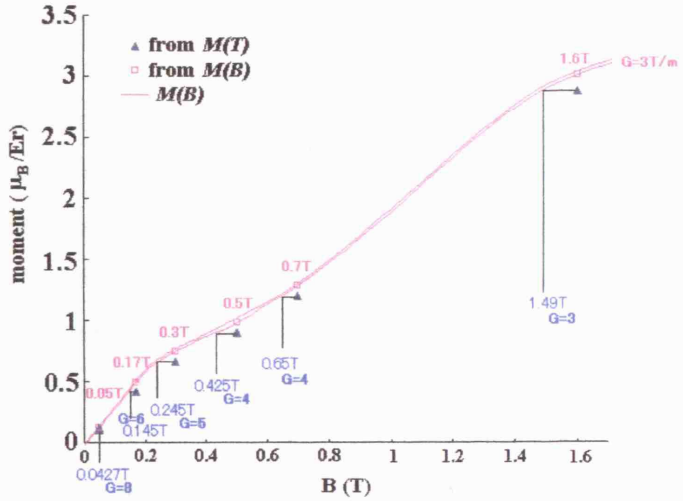

Figure 6.7: Comparison of the moments measured in $M(T)$ and $M(B)$ for SN200 at 50 mK. The difference stands for a measure of the error size. The applied set field for the $M(T)$ measurements are indicated (in pink) together with the corresponding actual field in which the moment was experiencing (in blue). Also the field gradients in which the $M(T)$s were measured are indicated (in blue).

6.2.2 Magnetization of $Er_2Sn_2O_7$

In this section we present the magnetization curves measured for the $Er_2Sn_2O_7$ sample. First, the field variances of the magnetization, $M(B)$-plots, at temperatures T = 50, 120, 130, 140, 400 and 1800 mK will be presented. For these $M(B)$ curves, the differentiation plot dM_Z/dB will also be plotted on the same plot to aid following the magnetization variance with field B in more detail. Secondly, the susceptibility v.s. temperature plot, the $M(T)$-plots, are plotted for $Er_2Sn_2O_7$ at applied field of B = 50, 100, 170, 300, 500, 700 and 1600 mT (milli Tesla).

There are three points worth making notes which are the followings:

(i) The spring constant $K_{SN200}{}^{1800mK}$ = 2413546 dyne cm^{-1} determined in the calibration process using the $M(B)$ curves taken at 1800 mK was used through out the data analysis

(ii) All $M(B)$ curves were measured in rising fields first and then in falling fields and the $M(T)$ curves were first measured for the zero-field-cooled (ZFC) sample and then instead of the 'proper' field-cooled (FC) measurement (which in principle should be measured *after* the sample been cooled in a field) $M(T)$ was measured *while* the sample was cooling in the applied field.

(iii) Note that there are no indications of error size in any of the plots. This is (as it was explained in the section of calibration) because the absolute values of the measurements have not been determined accurately enough. One needs more frequent calibrations in order to decide the absolute moment. However, because the $M(B)$ curves for any measurement ended up giving the same saturation value (independent of the temperature and also of the sample used!) it may be secure to assume that the error in the $M(B)$ plots are minor compared to the $M(T)$ plots.

6.2.2.1 *M*(*B*) plots

In Fig.6.8 and Fig.6.9 we present the $M(B)$ and $dM(B)/dB$ plots, respectively, for $Er_2Sn_2O_7$ (SN200) taken at T = 50, 120, 130, 140, 400 and 1800 mK. Here we summarize the points we learn from the $M(B)$ measurements of $Er_2Sn_2O_7$:

- Except for the T=1800 mK data, there exist two main transitions in all the $M(B)$ plots; these are (i) a well defined transition at $B \sim 0.15$ T that leads $M(B)$ into a plateau and (ii) a very broad transition around $B \sim 1.1$ T (extending over ± 0.5 T). Apart from these strong features, there is a small anomaly just at the commencing of the transition (ii), around $B \sim 0.5$ T (this is best resolved in the dM/dB curves).
- Looking more closely at each transition; transition (i) shows some hysterisis when the measurement is done in rising/falling field. This difference is best shown in Fig.6.9 (*Top*: rising *B*. *Bottom*: falling *B*). The transitions are clearer in the falling field. On the other hand, transition (ii) is broad and although its shape being similar to that of first order, there is no hysterisis.
- The transition (i) persists up to 140 mK but it becomes less clear above 400 mK and disappears at 1800 mK. On the other hand, the transition (ii) is still clearly present at 400 mK and disappears also at 1800 mK.
- The $M(B)$ curve for T=1800 mK has a form of a simple Brillouin curve without any obvious transition, however, the saturation moment is approximately half the free ion maximum $\mu_{Jmax} = 9\mu_B$ [Er^{3+}, $4f^{11}$, $^4I_{15/2}$; S=3/2, L=6, J=15/2, g_J = 1.2, $\mu_{Jmax}/\mu_B = g_J J$]. This is consistent with previously reported result [3]. In fact, all $M(B)$ curves saturate at this value $M \sim 4.5\,\mu_B$.

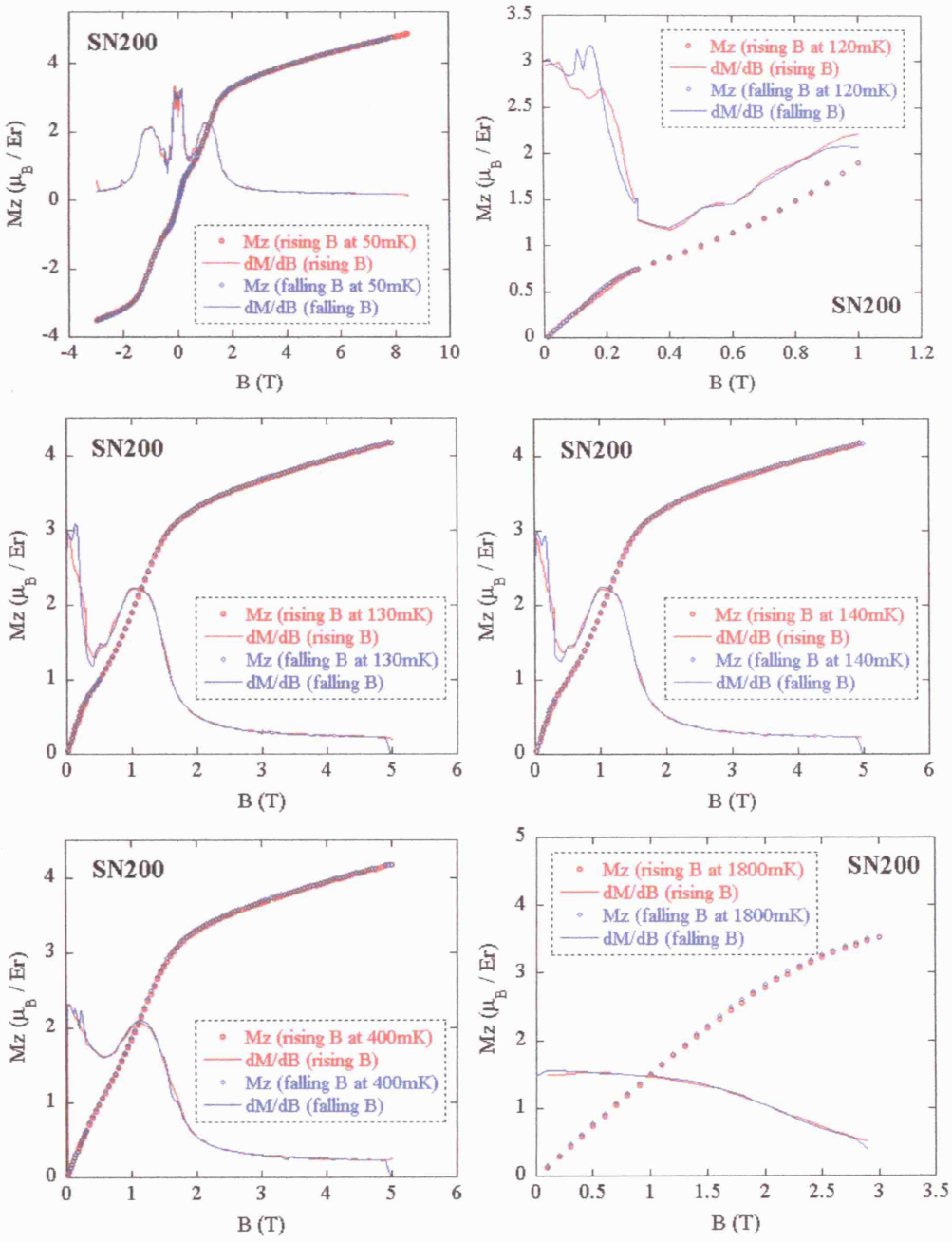

Figure 6.8: Magnetization versus applied field B for $Er_2Sn_2O_7$ at $T = 50$, 120, 130, 140, 400 and 1800 mK (open circles). The full lines are the differentiation $dM(B)/dB$.

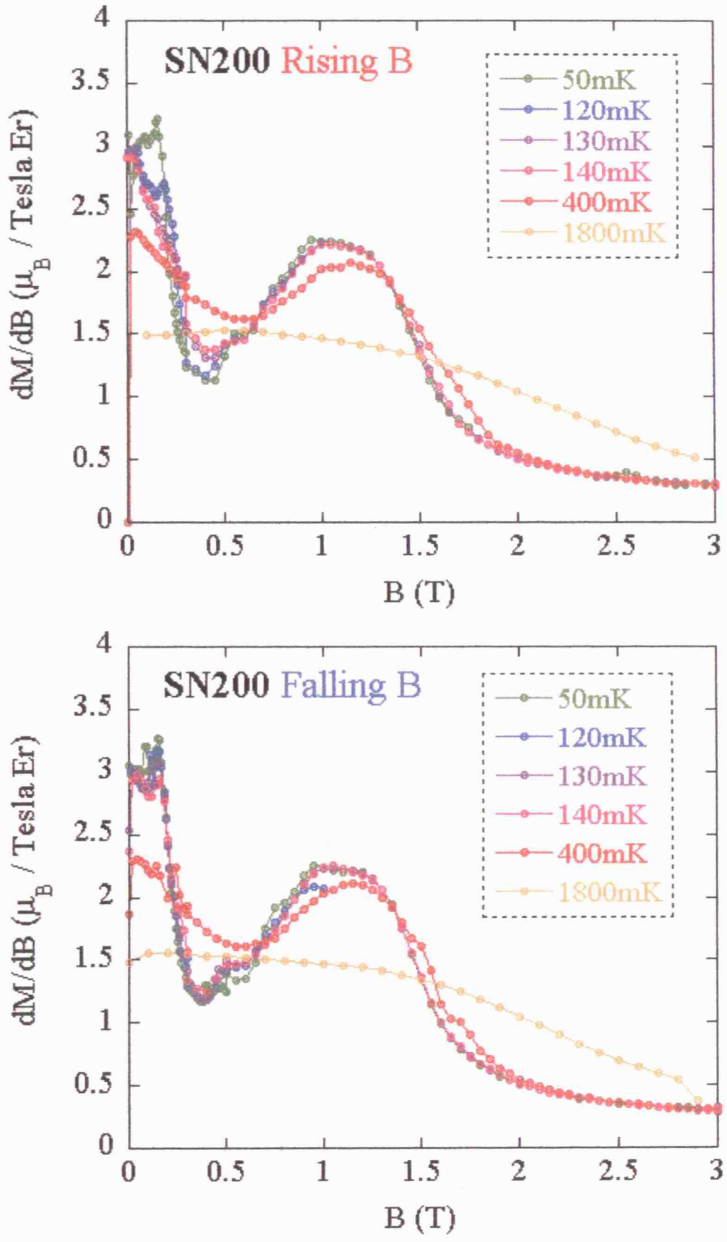

Figure 6.9: The (d*M*/d*B*) differentiation curves for $Er_2Sn_2O_7$ at T = 50, 120, 130, 140, 400 and 1800 mK measured with rising B (Top) and with falling B (Bottom). The transitions occurring at $B \sim 0.2$ T are shown more clearly in the falling B plot.

6.2.2.2 *M*(*T*) plots

In Fig.6.11 (a) and Fig.6.11 (b) we present the *M*(*T*) plots for $Er_2Sn_2O_7$ (SN200) taken at applied fields $B = 50, 100, 170, 300, 500, 700$ and 1600 mT. Here we summarize the points we learn from the *M*(*T*) measurements of $Er_2Sn_2O_7$:

- First of all, the *M*(*T*) plot of $B = 50$ mT shows features of phase transitions. This is consistent with the neutron measurements shown in Chapter 5. This measurement was repeated four times, in principle all measurements were made at the same applied field $B = 50$ mT. However, one can see from these plots (Fig.6.11(a):*Top*) how sensitive the absolute value of the moment can be to the experiment condition.
- The *M*(*T*) plot of $B = 50$ mT has double transitions occurring at $T = 0.1$ and 0.13 K. This is a feature that was not observed in the neutron experiment. The transition occurring at the higher temperature (0.13 K) is second order in nature with fairly small hysterisis. Then as the temperature is lowered, the second transition (at 0.1K) occurs. This transition gives a jump in the measured magnetization hence will be best described by a first order transition. It also involves substantial hysterisis character in it.
- As we move up in applied field, this double transition feature diminishes. The second order transition becomes less and less clear as *B* is increased and at $B = 300$ mT the *M*(*T*) curve ends up showing only the first order transition. In another words, the lower temperature (first order) transition point moves up in temperature as the applied field is raised, finally 'swallowing' the second order transition.
- However, after these double transitions merging into a single point, the *M*(*T*) plots at higher *B*s start showing more anomalies. At $B = 500$ mT, the nature of the transition changes dramatically from that at $B = 300$ mT. In *M*(*T*) at 300 mT, the moment showed a jump to a higher value as the transition was crossed from the high *T* side but in the *M*(*T*) at 500 mT the susceptibility bends down at the transition. This 'second-order' type of transition that dominates the *M*(*T*) at 500 mT persists in higher fields. Finally, the transition disappears at $B = 1600$ mT.
- A quick analysis was done to estimate the size of the ferromagnetic contribution to

the ordering. This is easiest to refer to Fig.6.10 below. If the ordering was purely antiferromagnetic, the moment is expected to fall to 2/3 of the peak value as $T \rightarrow 0$. In this case $(2/3) \times 0.098 = 0.0653\ \mu_B$/Er. Hence, the actual ordered moment at the lowest measured temperature is anticipated to have a ferromagnetic contribution of about $0.098 - 0.0653 \approx 0.033\ \mu_B$/Er. This is too small to be seen in the neutron experiment. That is why the ferromagnetic component was only seen as a possible perturbation to the ground state basis functions – see Chapter 5.

- The Curie-Weiss analysis [$\mu_J = g_J \mu_B \sqrt{J(J+1)}$] was not done on the $M(T)$ plots because the measured range of temperature did not extend to a high enough value to do a reasonable (i.e. paramagnetic) analysis.

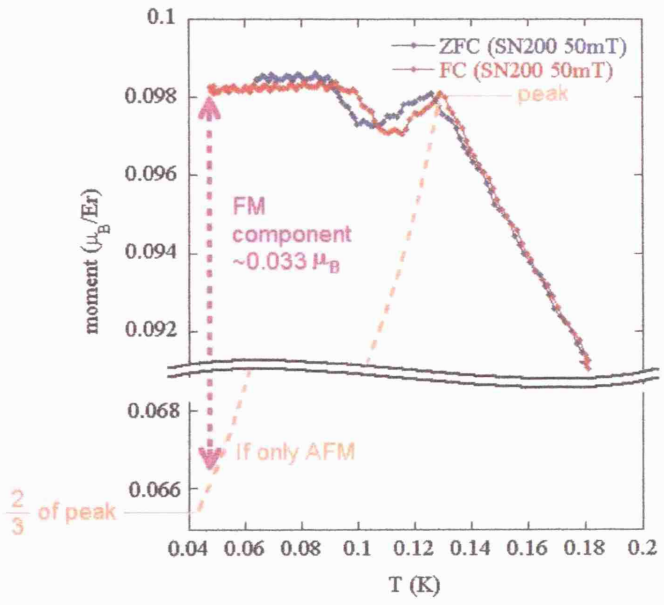

Figure 6.10: Extent of ferromagnetic component of the ordered moment estimated from a simple analysis of the $M(T)$ plot of SN200 at $B = 50$ mT.

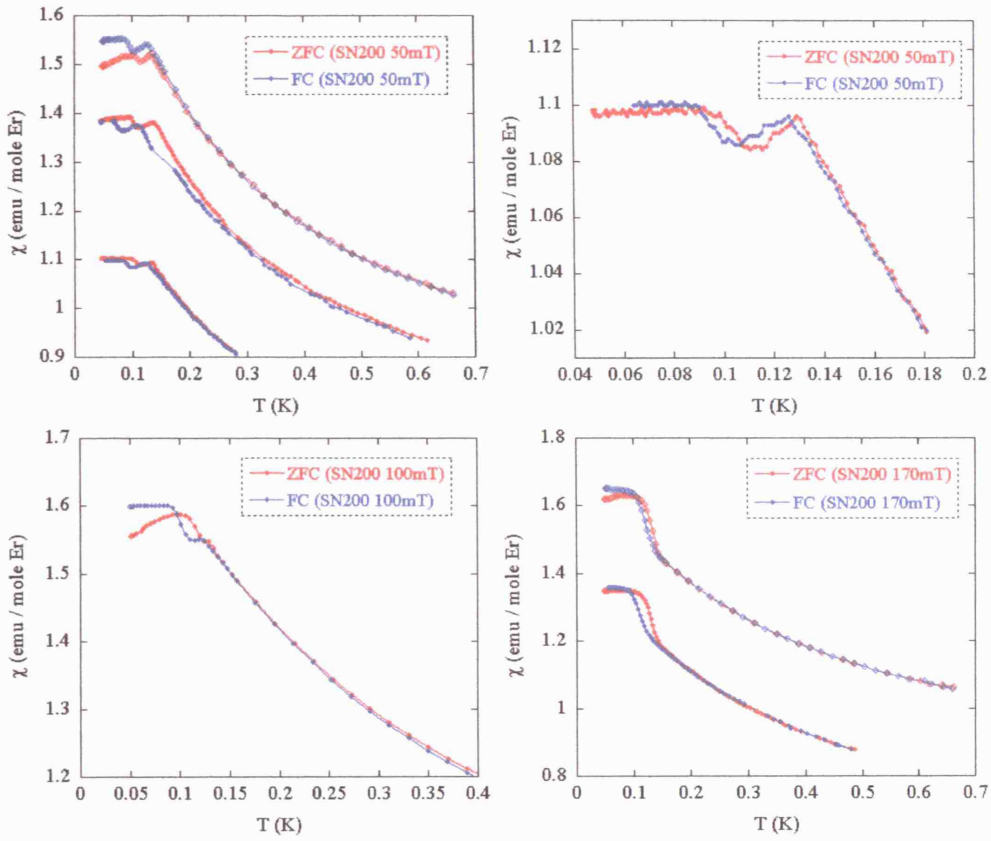

Figure 6.11 (a): Susceptibility versus temperature for $Er_2Sn_2O_7$ at applied fields B = 50, 100, and 170 mT. (See Fig.6.11(b) for B = 300, 500, 700 and 1600 mT data sets.) The zero-field-cooled (ZFC) measurements were made while heating as expected, however, the field-cooled (FC) measurements were made while cooling as opposed to the 'proper' FC measurements. More than one set of curves plotted on the same plot represents repeated measurements at the same conditions. This can be used to estimate the errors on the absolute values of χ (or moment), hence shows the need for calibration (to determine the spring constant K) each time the measurement is carried out if the absolute moments are to be determined with better accuracy.

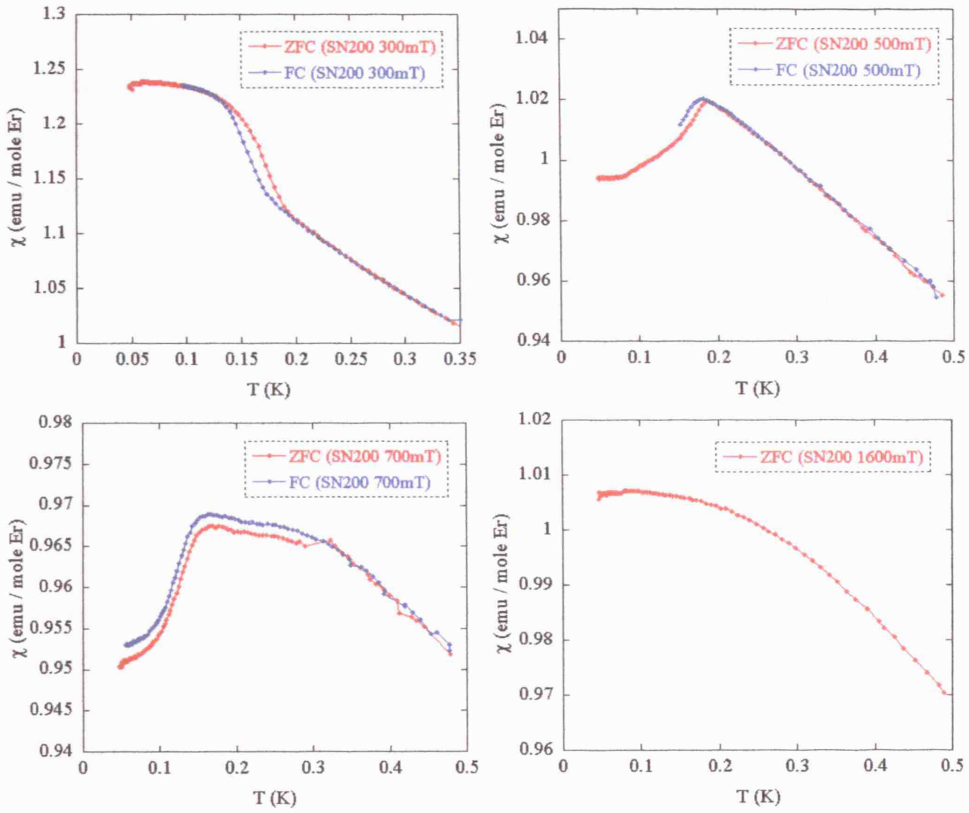

Figure 6.11 (b): Susceptibility versus temperature for $Er_2Sn_2O_7$ at applied fields B = 300, 500, 700 and 1600 mT. The zero-filed-cooled (ZFC) measurements were made while heating as expected, however, the field-cooled (FC) measurements were made while cooling as opposed to the 'proper' FC measurements. Note that the difference in ZFC/FC curves at 700 mT is not a real effect but may be attributed to a jump in the capacitance value (of the capacitance cell) occurred at the Helium transfer.

6.2.2.3 *B* -*T* phase diagram of $Er_2Sn_2O_7$

Finally, in Fig.6.12 we present the field-temperature phase diagram constructed for $Er_2Sn_2O_7$ (SN200). A comparison is made to the phase diagram of $Gd_2Ti_2O_7$[2]. Similarities are observed. The 'double transition' occurring at the zero field is the main feature that is shared between the two phase diagrams. In the case of $Gd_2Ti_2O_7$, as the transitions are approached from the high T end, the first transition is attributed to the ordering of 3/4 of the Gd^{3+} spins (corresponding to the spins in the kagomé layers) leaving the 1/4 interstitial spins disordered [5]. The second (lower T) transition is then attributed to a partial (~ 27 %) ordering of these interstitial sites [6]. In the case of $Er_2Sn_2O_7$ the situation will be different as the ordering vector is $\mathbf{k}=000$ (whereas $\mathbf{k}=$ ½½½ for $Gd_2Ti_2O_7$) and hence the four Er^{3+} spins in the tetrahedral unit will not be split into two sets (called *orbits* in Ref.[5]) but all four will count as a single orbit (i.e. they are not distinguishable). From our neutron diffraction results (see Chapter 5) the ordering of the $Er_2Sn_2O_7$ is expected to be in the Palmer-Chalker state [7], with some possible allowance of ferromagnetic mixing. Although this double transition feature was not resolved in the neutron experiment, from the shape of the $M(T)$ plot at 50 mT (Fig.6.11(a); *Top*) one may come up with a possible interpretation of the nature of the transitions. That is, the high T transition being associated with an antiferromagnetic order and the low T transition associated with an ordering of some ferromagnetic nature.

Another similarity of the two phase diagrams is that there is a critical point which is shared between four to five phases. This is the point [H=2.5 T, T=0.85 K] and the point [H=0.17 T, T=0.12 K] in the $Gd_2Ti_2O_7$ and $Er_2Sn_2O_7$ phase diagram, respectively. The high B side of the $Er_2Sn_2O_7$ phase diagram becomes less clearly defined because the broad transition extending from B~0.5 T up to B~1.5 T starts overlapping to the other transitions.

The only feature not shown in the $Gd_2Ti_2O_7$ phase diagram but is present in the $Er_2Sn_2O_7$'s one is the strong transition occurring at B~1 T. This is a broad transition and it is present up to at least 400 mK. Considering the scale of the phase diagram, the $Gd_2Ti_2O_7$ one is much bigger than that of the $Er_2Sn_2O_7$, therefore, one may find this high B transition line for the $Gd_2Ti_2O_7$ if the measurement was extended to a higher B.

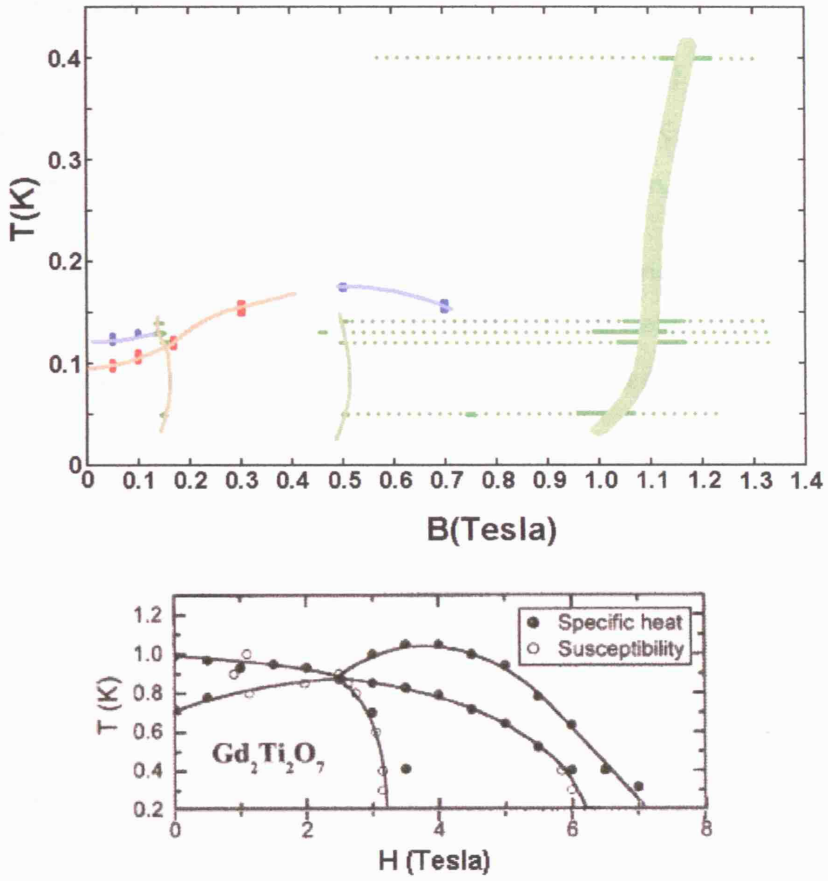

Figure 6.12: Field-temperature phase diagram constructed for $Er_2Sn_2O_7$ based on the low temperature magnetization measurements (*Top*). For the points obtained from the $M(T)$ plots, two types of transitions are distinguished; the red line represents the transition of first order in nature and the blue line of second order in nature. The green lines are drawn based on the $M(B)$ measurements; showing three characteristic lines at B= 0.15, 0.5 and 1.1 Tesla. The transition at 1.1 Tesla is very broad and the extended region of this transition is indicated by the green dots. The similar phase diagram for $Gd_2Ti_2O_7$ given by Ramirez *et al.*[2] is also shown for comparison (*Bottom*).

6.2.3 Magnetization of $Er_2Ti_{2-x}Sn_xO_7$ (x =1.5, 1.55, 1.6, 1.7, 1.8 and 1.9)

6.2.3.1 $M(B)$ Curve

In Fig.6.13 and Fig.6.14 we present the $M(B)$ and $dM(B)/dB$ plots, respectively, for $Er_2Ti_{2-x}Sn_xO_7$ (x= 1.9, 1.8, 1.7, 1.6, 1.55 and 1.5) at T = 50 mK. Here we summarize the points we learn from the $M(B)$ measurements of the $Er_2Ti_{2-x}Sn_xO_7$ series:

- The shapes of the $M(B)$ curves for the $Er_2Ti_{2-x}Sn_xO_7$ series are very similar to that of $Er_2Sn_2O_7$ described in section 6.3.2. Staring at zero field, once the field is raised, the magnetization goes into a plateau of about ~1 μ_B at B~0.25 T. Then there is the characteristic broad transition around B~1 T.
- However, the transition that leads to the plateau is only well defined in SN200 and in SN190 and for the rest of the samples this transition is less abrupt (see Fig.6.14 for best picture).

6.2.3.2 $M(T)$ Curve

In Fig.6.15 (a) to (e) we present the $M(T)$ plots for $Er_2Ti_{2-x}Sn_xO_7$ (x= 1.9, 1.8, 1.7, 1.6, 1.55, 1.5) taken at applied fields B = 50, 100 and 300 mT together with dM/dT plots for B = 50 mT to aid see the presence/absence of phase transitions. Here we summarize the points we learn from the $M(T)$ measurements of the $Er_2Ti_{2-x}Sn_xO_7$ series;

- First of all, none of the $M(T)$ plots the $Er_2Ti_{2-x}Sn_xO_7$ series except SN200 has the double transition feature at B = 50 mT.
- Looking at the $M(T)$ plots of B=50 mT, a clear phase transition was observed for SN190 and SN180 but for SN170 the transition becomes less clear and for SN160 and SN155 there were no clear sign of any phase transition down to 40mK. Hence, the quantum critical point is expected to exist at the composition x= 1.55 ~ 1.6.
- In general, as the applied field B is raised, the transition temperature increases. The change of shape of the curves is interesting; the transition is second-order-like at low B but as B is increased the shape changes as if the transition starts to become first order.

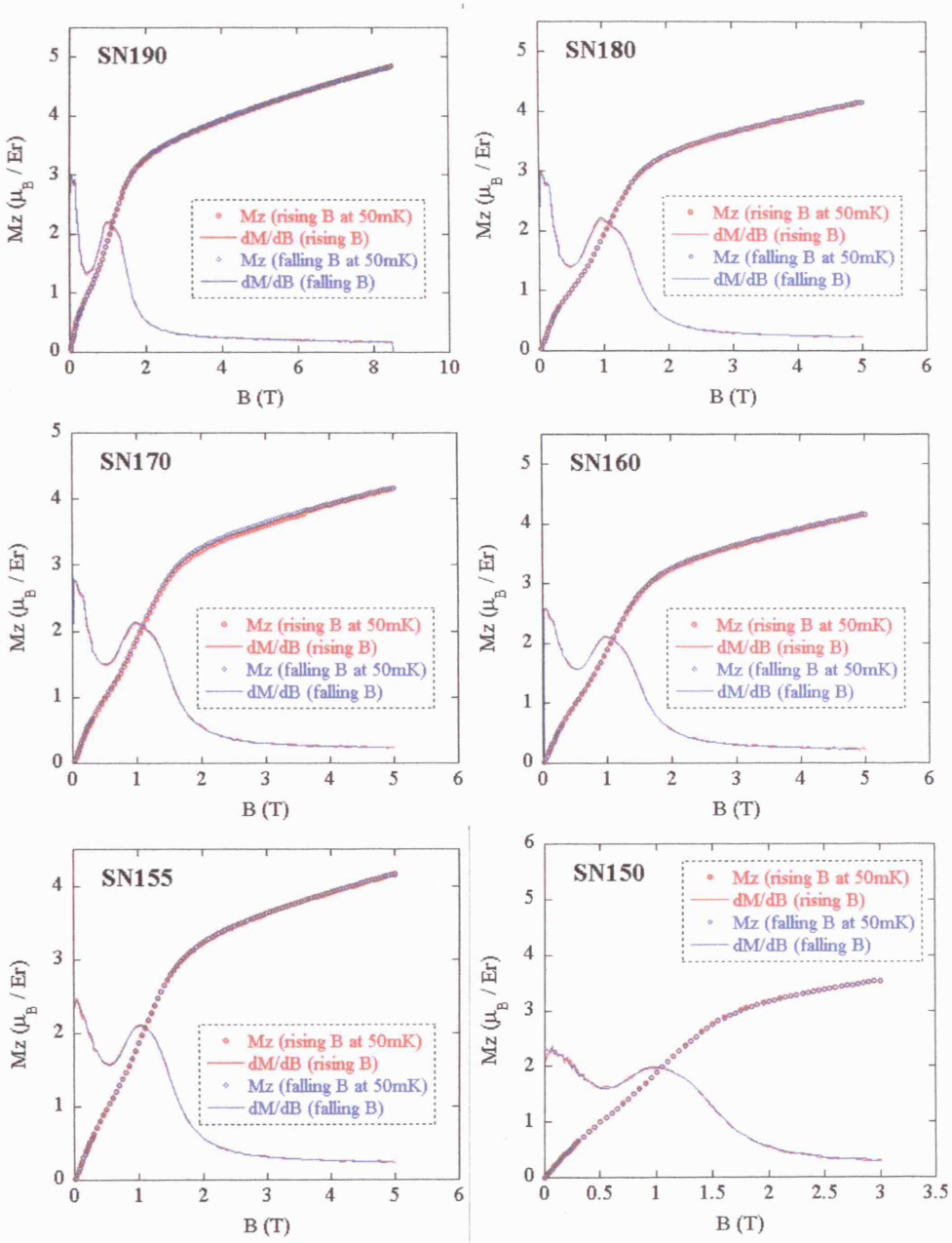

Figure 6.13: Magnetization versus applied field B for $Er_2Ti_{2-x}Sn_xO_7$ (x=1.9, 1.8, 1.7, 1.6, 1.55 and 1.5) at T=50 mK (open circles). The full lines are the differentiation d$M(B)$/dB.

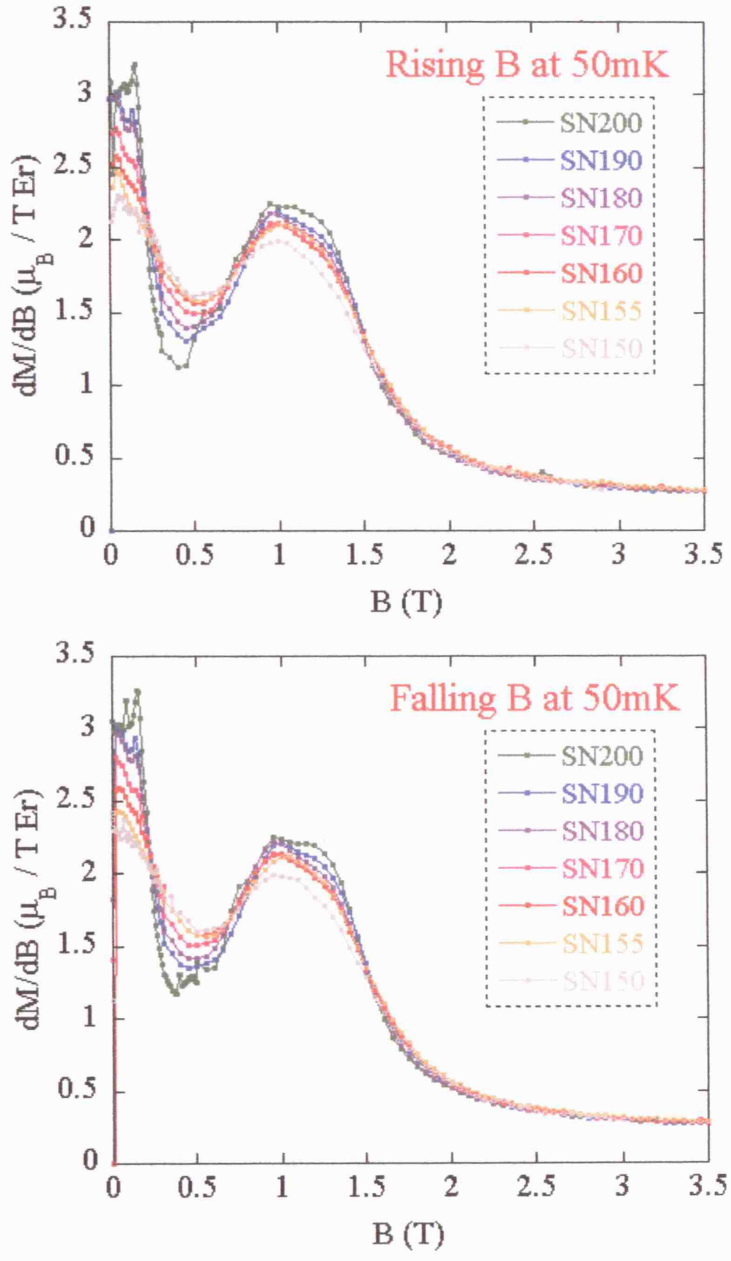

Figure 6.14: The (d*M*/d*B*) differentiation curves for $Er_2Ti_{2-x}Sn_xO_7$ (x = 1.9, 1.8, 1.7, 1.6, 1.55 and 1.5) at T = 50 mK measured with rising B (Top) and with falling B (Bottom).

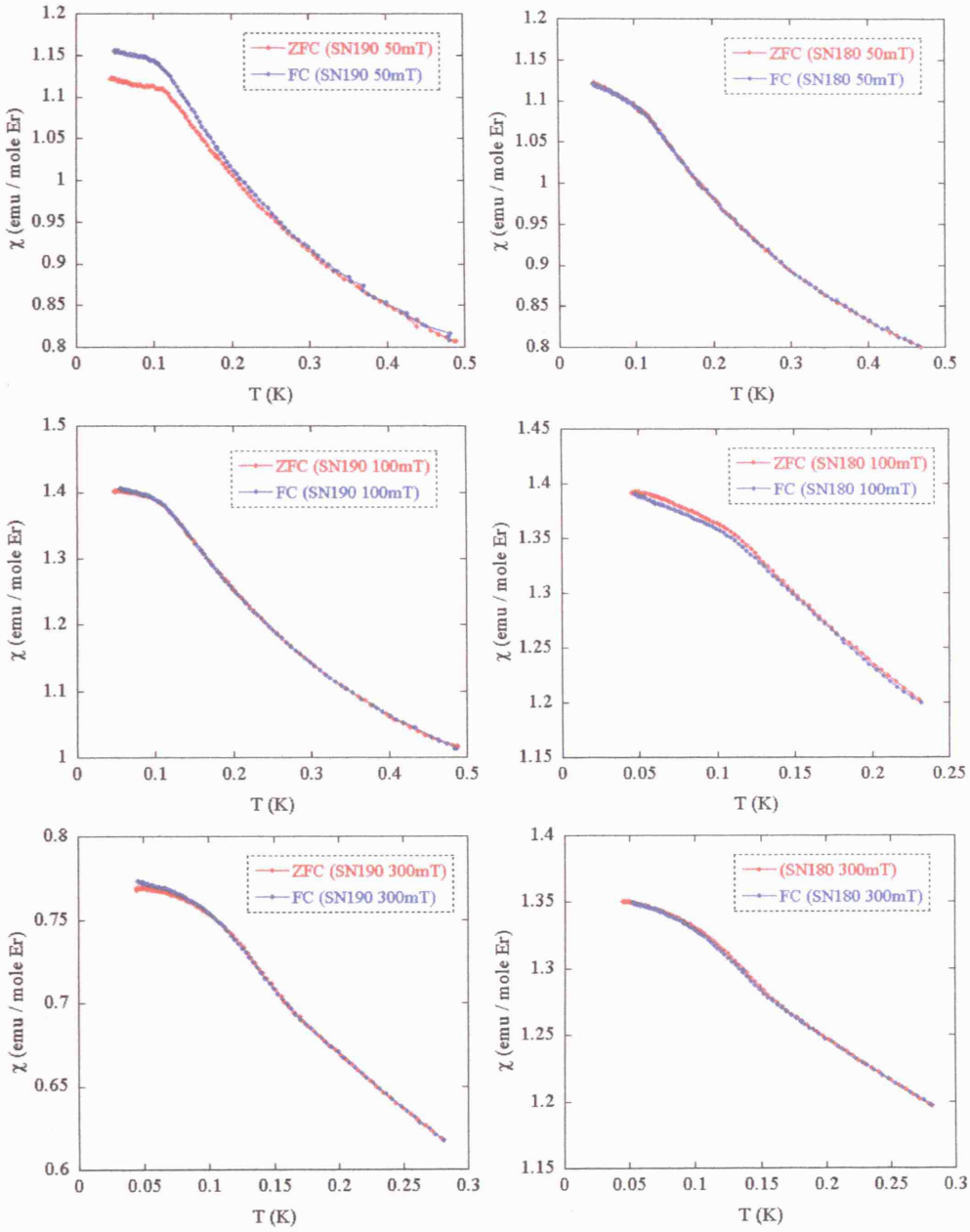

Figure 6.15 (a): Susceptibility versus temperature for $Er_2Ti_{2-x}Sn_xO_7$ (x = 1.9 and 1.8) at applied fields B = 50, 100, and 300 mT. The zero-field-cooled (ZFC) measurements were made while heating as expected, however, the field-cooled (FC) measurements were made while cooling as opposed to the 'proper' FC measurements.

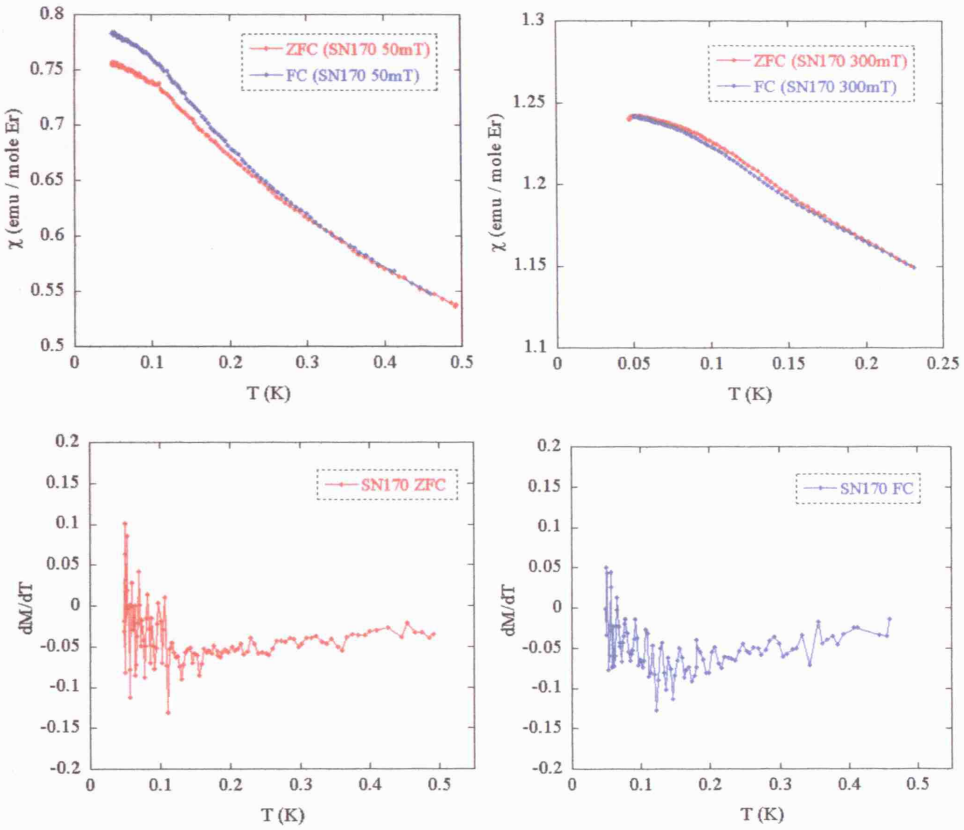

Figure 6.15 (b): Susceptibility versus temperature for $Er_2Ti_{2-x}Sn_xO_7$ (x = 1.7) at applied fields B = 50 and 300 mT (*Top left and right*). The zero-field-cooled (ZFC) measurements were made while heating as expected, however, the field-cooled (FC) measurements were made while cooling as opposed to the 'proper' FC measurements. The dM/dT plots for B = 50 mT for both ZFC and FC are shown in order to aid the observation of the phase transition happening (*Bottom left and right*).

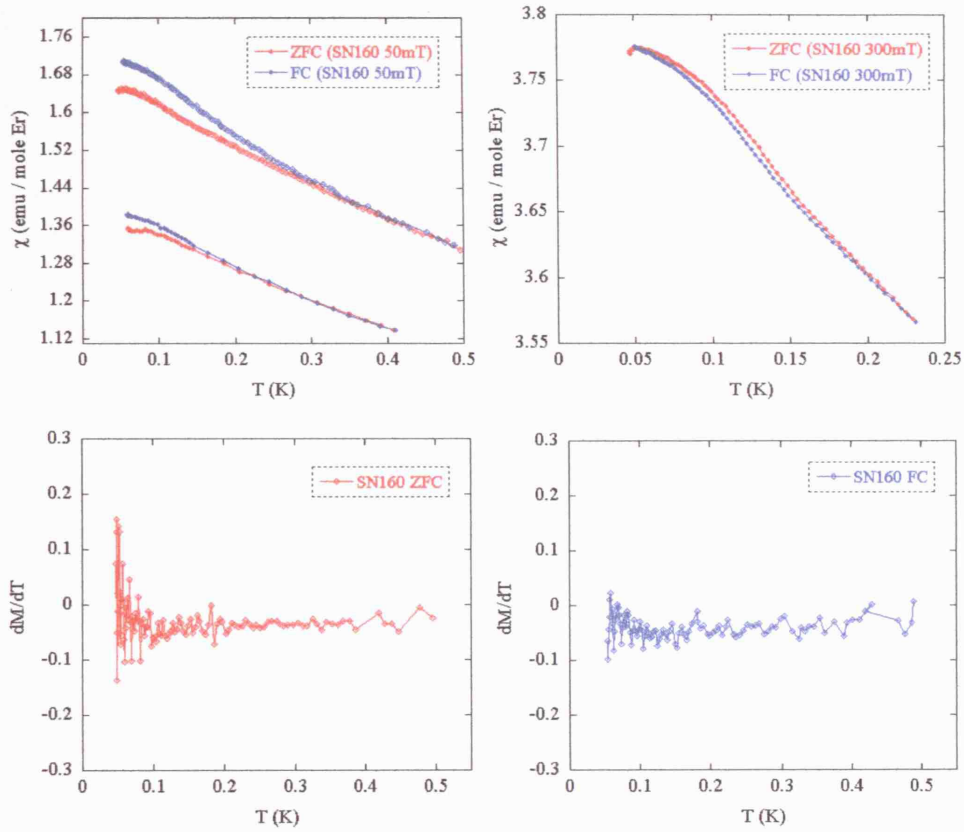

Figure 6.15 (c): Susceptibility versus temperature for $Er_2Ti_{2-x}Sn_xO_7$ (x = 1.6) at applied fields B = 50 and 300 mT (*Top left and right*). The zero-filed-cooled (ZFC) measurements were made while heating as expected, however, the field-cooled (FC) measurements were made while cooling as opposed to the 'proper' FC measurements. The dM/dT plots for B = 50 mT for both ZFC and FC are shown in order to help seeing the absence of the phase transition happening in this compound (*Bottom left and right*).

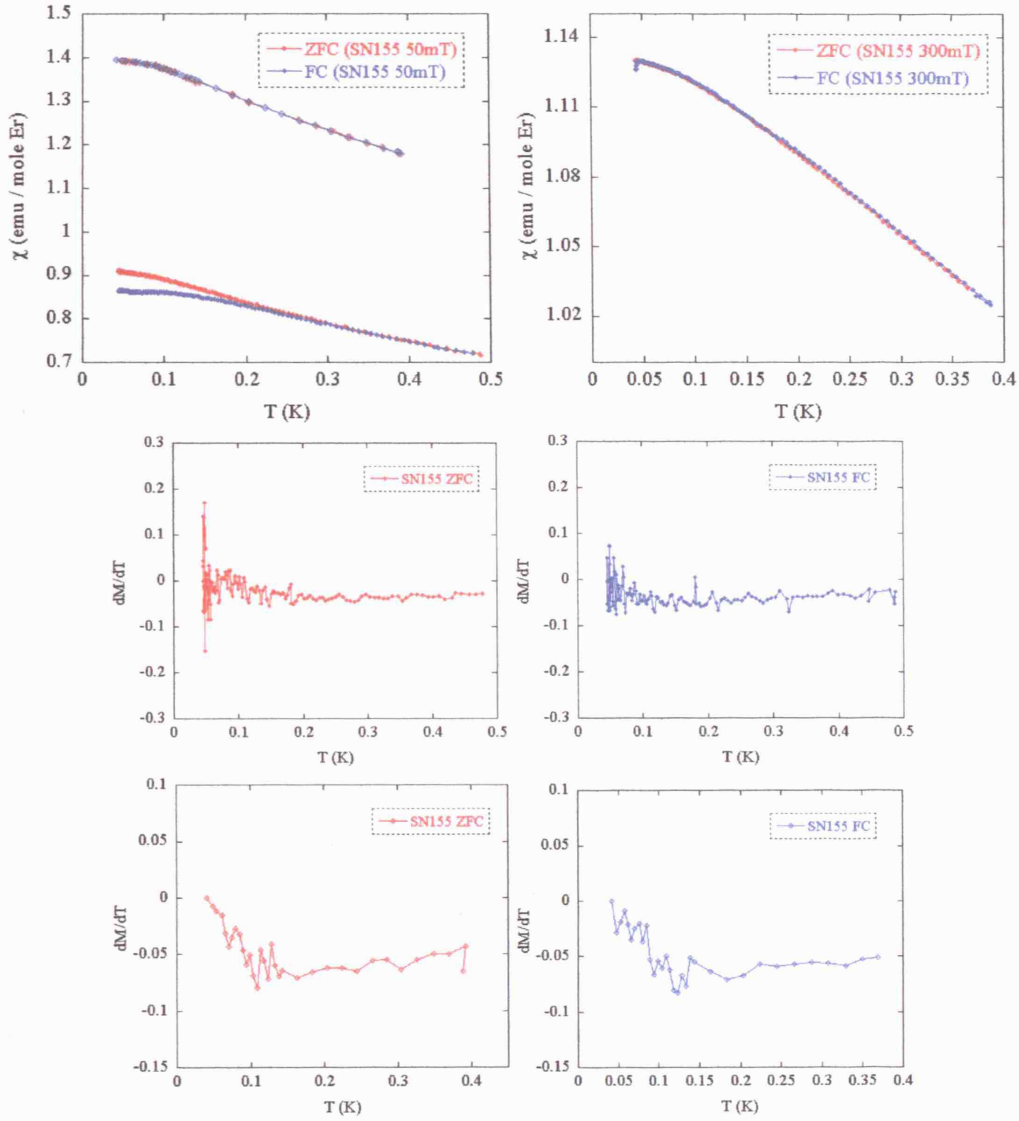

Figure 6.15 (d): Susceptibility versus temperature for $Er_2Ti_{2-x}Sn_xO_7$ (x = 1.55) at applied fields B = 50 and 300 mT (*Top left and right*). The zero-field-cooled (ZFC) measurements were made while heating as expected, however, the field-cooled (FC) measurements were made while cooling as opposed to the 'proper' FC measurements. Two sets of dM/dT plots for B = 50 mT for both ZFC and FC (for the two repeated measurements) are shown in order to help seeing the absence of the phase transition happening in this compound (*Middle/Bottom row, left and right*). (However, the dM/dT curves of the second measurement (*Bottom*) show sort of transitions.)

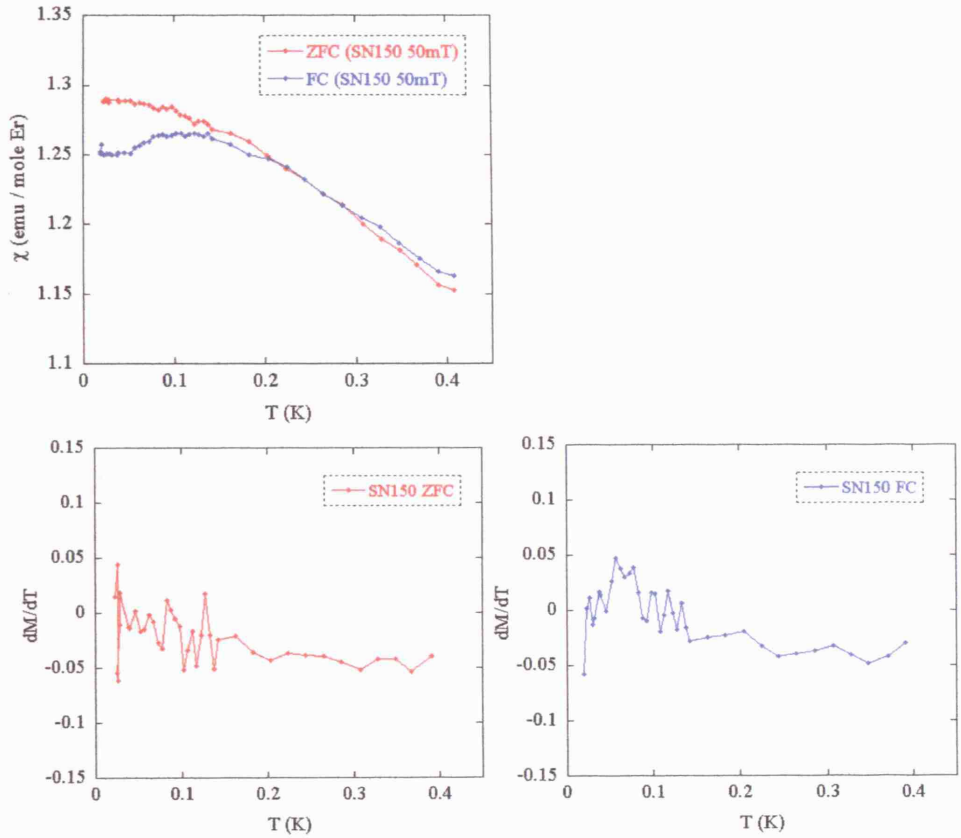

Figure 6.15 (e): Susceptibility versus temperature for $Er_2Ti_{2-x}Sn_xO_7$ (x = 1.5) at applied fields B = 50 mT (*Top*). For this measurement, both the zero-field-cooled (ZFC) and field-cooled (FC) measurements were made while heating as expected. The dM/dT plots for B = 50 mT for both ZFC and FC are shown in order to help seeing the presence of the phase transition happening in this compound (*Bottom left and right*). An ordering transition is clearly observed in the neutron diffraction measurements (see Chapter 5) while it is not very clearly shown in this magnetization measurement.

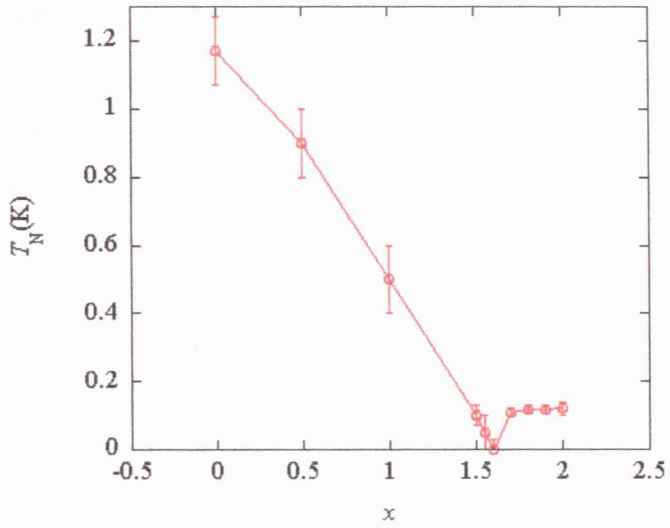

Figure 6.16: Transition temperature T_N v.s. x for the $Er_2Ti_{2-x}Sn_xO_7$ series. The points below $x = 1.5$ is taken from the neutron results in Chapter 5. It shows that the ordering diminishes around the critical composition $x = 1.55 \sim 1.6$. This is hence considered to be the quantum critical point.

6.2.4 T_N plot for the $Er_2Ti_{2-x}Sn_xO_7$ series

Finally, the entire T_N-plot can be constructed for the whole $Er_2Ti_{2-x}Sn_xO_7$ series ($x = 0 \sim 2$). This is shown in Fig.6.16. The data below $x = 1.5$ are taken from the D20 diffraction results (Chapter 5). It gets very difficult to distinguish the presence of the phase transition from its absence when the nature of transition gets very 'mild' in character, opposing the abrupt, clear transitions that are observed in high T_N systems. In order to aid see the change in magnetization, the first derivative dM/dT is plotted for those compounds that are expected to be around the quantum critical point (i.e. $x = 1.7 \sim 1.5$, Fig.6.15(b)-(e)). Judging from these plots, the T_N plot was made.

6.3 Conclusions

In this chapter, the results of low temperature magnetization measurements carried out on the $Er_2Ti_{2-x}Sn_xO_7$ series with x over 1.5 up to 2 have been presented. These ultra low temperature magnetization measurements (down to ~ 20 mK) were realized by the use of the Faraday force magnetometer which operates within the dilution refrigerator. Below we summarize the results gained in this chapter.

First of all, the ordering transition observed in the neutron experiment (Chapter 5) for the compound $Er_2Sn_2O_7$ was also confirmed by this magnetization measurement. In fact, the transitions were 'double' in nature, one occurring at $T_N \sim 0.13$ K and the second follows just below it, at $T_C \sim 0.1$ K. The first transition (at T_N) is second-order and antiferromagnetic (AFM) in nature, whereas the lower T transition (at T_C) has a more first-order feature and is ferromagnetic (FM) in nature. The FM component of the ordered moment was estimated to be of ~ 0.033 μ_B/Er. This is too small to be detected by the neutrons.

An interesting observation is made in the field-sweep measurements, $M(B)$. When the applied field is raised to a high enough level (>3 Tesla), independent of the temperature chosen, all samples showed the same saturation moment. This value, ~ 4.5 μ_B, is consistent with the measured single ion moment size defined by the crystal fields, ~ 5.5 μ_B, which was also constant for all x (of $Er_2Ti_{2-x}Sn_xO_7$).

Another common feature is shared in the $M(B)$ plots of all compounds measured at a low temperature (50 mK). That is; a plateau is reached at an intermediate field (around 0.1 ~ 0.5 Tesla) before it starts to rise again towards the saturation value of ~ 4.5 μ_B.

A field-temperature phase diagram of $Er_2Sn_2O_7$ was constructed based on our measurements and is plotted in Fig.6.12. There are many anomalous features observed in it. One such feature is the change in nature of transition line (from second-order to first-order) at a critical point. This phase diagram is compared to the corresponding phase diagram of $Gd_2Ti_2O_7$ [2], a pyrochlore Heisenberg AFM, and similar features are found between them; such as the occurrence of the critical point shared by more than four phases. The double transition in zero-field is another common feature shared

between the two compounds but its nature is unknown for the case of $Er_2Sn_2O_7$. The anisotropy of $Gd_2Ti_2O_7$ has various suggestions (see section 2.5) and it has not yet been given a definite answer. In order to compare the resemblance and/or the difference of the phase diagrams of the two materials ($Gd_2Ti_2O_7$ and $Er_2Sn_2O_7$) a proper determination of the crystal field of $Er_2Sn_2O_7$ is essential and this will be investigated in detail in Chapter 7.

Finally, T_Ns were plotted against composition x for the whole $Er_2Ti_{2-x}Sn_xO_7$ series. It is difficult to judge the 'absence' of ordering transition but it seems that for SN155 and SN160 the ordering feature becomes 'mild' enough to say that any ordering transition is absent. Therefore, $x = 1.55 \sim 1.6$ is thought to be the critical region where the quantum critical point might happen. However, we realize the necessity of measuring the sample SN150 ($Er_2Ti_{0.5}Sn_{1.5}O_7$) to show this material indeed orders at $T_N \sim 0.2$ K (the ordering T_N observed in neutron scattering work; Chapter 5) for the completeness of our work.

One final point to mention is that, unfortunately, the ordered moment sizes at low temperatures cannot be determined accurately enough to create a plot against x. This will be very useful once determined since one can compare with the ordered moments determined in the neutron work (Chapter 5). A more careful (more frequent) calibration is needed in order to determine the absolute magnitudes of the moments.

Reference for Chapter 6

[1] T.Sakakibara, H.Mitamura, T.Tayama and H.Amitsuka, Jpn. J. Appl. Phys. **33,** 5067 (1994).

[2] A.P.Ramirez, B.S.Shastry, A.Hayashi, J.J.Krajewski, D.A.Huse, R.J.Cava, Phys. Rev. Lett. **89,** 067202 (2002).

[3] S.T.Bramwell, M.N.Field, M.J.Harris and I.P.Parkin, J. Phys: Condens. Mater **12,** 483 (2000).

[4] K.Matsuhira, Y.Hinatsu, K.Tenya, H.Amitsuka and T.Sakakibara, J. Phys. Soc. Japan **71**(6), 1576 (2002).

[5] J.D.M.Champion, A.S.Wills, T.Fennell, S.T.Bramwell, J.S.Gardner, M.A.Green, Phys. Rev. B **64,** 140407R (2001).

[6] J.R.Stewart, G.Ehlers, A.S.Wills, S.T.Bramwell, J.S.Gardner, J. Phys. Condens. Matter **16,** L321 (2004).

[7] S.E.Palmer, J.T.Chalker, Phys. Rev. B **62,** 488 (2000).

Chapter 7

Crystal Field Measurement of $Er_2Ti_{2-x}Sn_xO_7$

7.1 Introduction

In this chapter the results of the crystal electric field (CEF) measurement of the $Er_2Ti_{2-x}Sn_xO_7$ series (x = 0, 0.5, 1, 1.5, 2) using inelastic neutron scattering (spectroscopy) are presented. The experiment was carried out using the HET spectrometer at the spallation source ISIS at the Rutherford Appleton Laboratory, Oxford, U.K. The experimental details are shown in the following section. The magnetic spectra obtained were analyzed using the interactive CEF parameter fitting program FOCUS written by P. Fabi (ISIS, RAL)[1]. In this program the CEF is treated by the Stevens' operator method [1, 3, 5-8]. The overview of the theory is summarized in the Appendix (A2). Finally, from the refined CEF parameters and ground state wavefunctions, the magnetic moments of the Er^{3+} ion in the CEF were calculated for all compounds.

7.2 Experimental Details

7.2.1 Sample environment

The $Er_2Ti_{2-x}Sn_xO_7$ series (x = 0, 0.5, 1, 1.5, 2) samples were prepared as a ceramic powder following standard solid synthesis technique described in Chapter 4. Approximately 15 g of the sample was enclosed in an aluminum foil in a flat-plate geometry of 38 mm×39 mm and mounted into a closed-cycle refrigerator on the neutron time-of-flight spectrometer HET (ISIS).

Spectra were recorded at incident energies E_i = 12, 25 and 120 meV and at temperatures T = 6, 30, 70 and 200 K, respectively. The counting time was about 1.5 hour per spectrum; hence, a day per sample was used. All spectra were taken in zero-field.

7.2.2 HET spectrometer

HET is a chopper spectrometer at the spallation source ISIS (Rutherford Appleton Laboratory, Oxford, U.K.) in which a single incoming energy is selected [2]. The final energy and momentum transfer is analyzed by time-of-flight and the detector angle. The schematic image is shown in Fig.7.1 below. It uses a Fermi chopper to monochromate the incident white beam. In our experiment, the chopper revolution frequencies of 100, 150 and 400 Hz were used for E_i = 10, 25 and 120 meV, respectively. The two monitors placed before and after the Fermi chopper count the time-of-flight between the two monitors and hence determine the incident energy. Once the monochromatic neutrons are scattered by the sample, they are detected by the arrays of ^{3}He detectors. The energies of the scattered neutrons are determined by the time taken to reach the detectors. The recorded spectra are grouped into seven workspaces (w1 to w7) according to the scattering angle; see Fig.7.2 for detail.

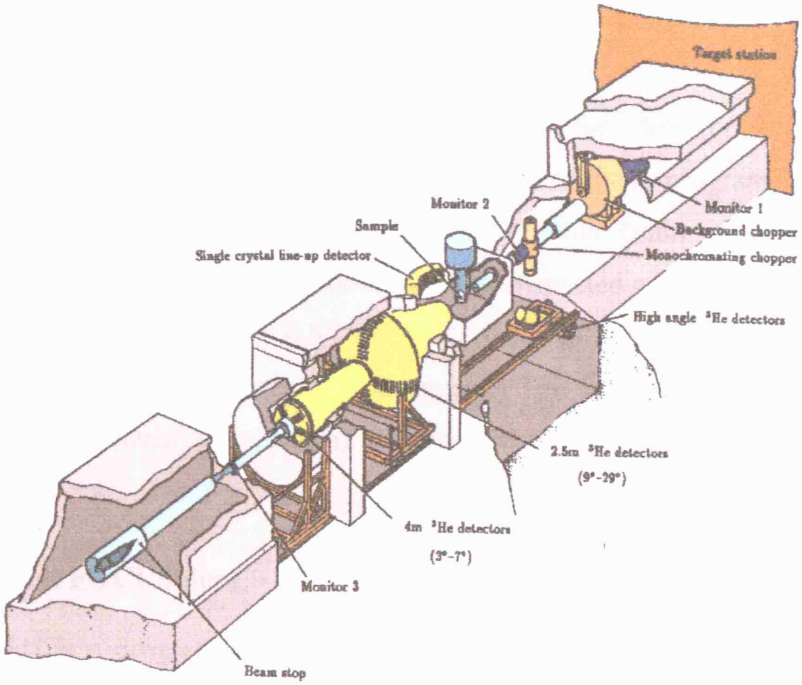

Figure 7.1: Schematic diagram of HET chopper spectrometer at ISIS (Rutherford Appleton Laboratory, Oxford, U.K.) [2].

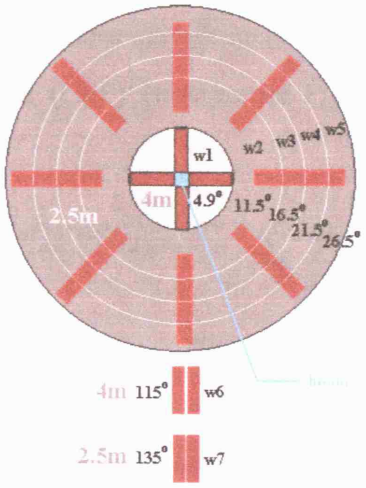

Figure 7.2: Schematic diagram of the detector arrangements of HET spectrometer. There are four sets of detector banks; 4 m low angle bank (w1), 2.5 m low angle bank (w2 - w5), 4 m high angle bank (w6) and 2.5 m high angle bank. The 2.5 m and 4 m represent the distance of the detectors from the sample.

7.2.3 Data analysis

The raw data were normalized and corrected for detector efficiency and time-independent background using the HET data analysis program HOMER [2]. The instrumental resolution was determined using white beam vanadium runs. The spectra collected at different detector banks were inspected and we decided to use the spectra collected at the w1 = 4.9° low angle bank as the spectra peaks were best resolved. (See Fig.7.2 for detector bank layout.) The normalized spectra were then fitted to the calculated spectra using the interactive CEF parameter fitting program FOCUS [1].

7.2.3.1 What FOCUS does

FOCUS [1] is a program designed to determine the CEF parameters of rare earth containing materials by fitting the calculated spectra to the inelastic neutron spectra. It calculates the CEF Hamiltonian in two different ways; the first method uses Stevens' operator- equivalents [1,3-8] whilst the second applies 3*j*-symbols [1,11-12]. In this work we only used the first method hence the remaining discussion will be solely based on the Stevens' operator-equivalents method.

The crystal electric field (CEF) Hamiltonian $\hat{V}_{CEF}$ used in Stevens' operator-equivalent notation is

$$\left\langle Jm_J \left| \hat{V}_{CEF} \right| Jm_J' \right\rangle = \sum_{n=2,4,6} B_n^{\,0} \left\langle Jm_J \left| \hat{O}_n^{\,0}(\mathbf{J}) \right| Jm_J' \right\rangle + \frac{1}{2} \sum_{n=2,4,6} \sum_{\substack{m=-n \\ m\neq 0}}^{n} B_n^{\,m} * \left\langle Jm_J \left| \hat{O}_n^{\,m}(\mathbf{J}) \right| Jm_J' \right\rangle \quad (7.1)$$

where the $B_n^{\,m}$ are complex CEF parameters and the $\hat{O}_n^{\,m}(\mathbf{J})$ are full *Stevens' operator-equivalents*. The sum over *m* only takes those values which are not forbidden by the point symmetry of the rare earth ion. FOCUS has all rare earth ions Ln^{3+} implemented and computes out the CEF Hamiltonians depending on the point symmetry of the CEF. In our case, the CEF point symmetry is chosen to be of D_{3d} point group. (See section 2.2.3, Fig.2.5 for the symmetry of the environment around Ln^{3+} ion.)

7.2.3.2 Starting CEF parameters B_n^m

In order to start the fitting, it is desired to have a good starting model, in other words, a physically sensible set of CEF parameters B_n^m. These starting CEF parameters were derived from the B_n^m (B_k^q in their notation) given by Rosenkrantz. *et al.*'s neutron scattering work on $Ho_2Ti_2O_7$'s crystal field [13].

The CEF parameter B_n^m is defined by

$$\hat{V}_{CEF} = \sum_{nm} B_n^m O_n^m \tag{7.2}$$

where $B_n^m = A_n^m \langle r_n \rangle \theta_n$ ($\theta_2 = \alpha_J$, $\theta_4 = \beta_J$, $\theta_6 = \gamma_J$) in Stevens' notation. Here, θ_n is the Stevens' multiplicative factor which is listed in Table VI (page 252) of Ref [3] and $\langle r_n \rangle$ is the radial integral that can also be found in the literature [9]. Therefore, it is possible to derive a set of B_n^m for Er^{3+} from those of Ho^{3+} by exchanging these ion dependent constants appropriately. Also, the B_k^q in Rosenkrantz's work [13] does not account for the effect of summing over magnetic electrons, hence, it is also necessary to adjust for this by dividing B_k^q by an appropriate conversion prefactor A_n^m. The derivation procedure for the CEF parameters B_n^m for Ho^{3+}, Er^{3+}, and Dy^{3+} from the original form B_k^q given by Rosenkrantz [13] is summarized in Table 7.4 .

7.3 Results

In this results section we will follow the order in which the analysis was done and present all results in sequence. In the first part, the spectra of $Er_2Ti_{2-x}Sn_2O_7$ (x = 0, 0.5, 1, 1.5 and 2) will be presented. This is the starting point of the analysis since one can get qualitative information regarding the energy levels. In the second part of the result analysis, a test calculation based on our converted B_n^m is made on Ho^{3+} and Dy^{3+} (in $Ho_2Ti_2O_7$) and the predicted energy level schemes are compared to those in the literature [10,13]. Once this test is approved, we start fitting the spectra of the $Er_2Ti_{2-x}Sn_xO_7$ series. From the refined CEF parameters the energy levels for the $Er_2Ti_{2-x}Sn_xO_7$ series will be deduced. Finally, from the computed wavefunctions the magnetic moments of the Er^{3+} ions in different crystal fields will be calculated.

7.3.1 Spectra of $Er_2Ti_{2-x}Sn_xO_7$ (x = 0, 0.5, 1, 1.5 and 2)

Below we present the spectra taken for $Er_2Ti_2O_7$ (x = 0) and $Er_2Sn_2O_7$ (x = 2) at T = 6, 30, 70 and 200 K and with incident neutron energy of E_i = 25 and 120 meV. The spectra for the compounds with intermediate x (x = 0.5, 1 and 1.5) are attached to the Appendix A3.

First of all, the peaks are distinguished according to the nature of their transition. That is, whether the transition is from the ground state levels or it is a transition from one of the (thermally populated) excited states. This can be verified by looking at the intensity variation with the temperature. When the temperature is increased, higher energy levels will be more populated and the proportion of the transition from the excited states will increase. In contrast, the ground state will be depopulated at higher temperatures, hence the proportion of the transition from the ground state should decrease. Therefore, if the intensity of the peak grows with increasing temperature then it should be classified as the transition from the excited states into a higher level, and if the intensity of the peak grows with decreasing temperature then it should be classified as the transition from the ground state into a higher level. This classification is applied to the spectra of $Er_2Ti_2O_7$ and is schematically shown in Fig.7.3. Here the negative energy transfer side ($\Delta E < 0$) which corresponds to the transitions from a higher level to a lower level is omitted but they should be classified in a similar fashion to the positive energy transfer side. In Fig.7.5 and Fig.7.6, spectra of $Er_2Ti_2O_7$ and $Er_2Sn_2O_7$ are shown respectively with the labels corresponding to different transition (refer to Fig.7.3 for labeling). Fig.7.7 and Fig.7.8 compare the energy levels of the five different compounds of the $Er_2Ti_{2-x}Sn_xO_7$ (x = 0 to 2) series. From a quick inspection of the spectra, it seems that the energy level variance with x is fairly linear rather than showing any abrupt change. Therefore, assuming all samples (all x) have the same set of energy levels, the same labeling scheme was employed for both Fig.7.5 ($Er_2Ti_2O_7$) and Fig.7.6 ($Er_2Sn_2O_7$).

One point to note down about the $Er_2Ti_2O_7$ spectra is that anticipated

'shoulder' of the elastic peak [14-15] was not observed in any of the spectra taken, even using the incident energy of E_i = 8.5 meV. (The resolution of the HET instrument is not adequate to resolve such detailed feature.)

Before proceeding to the fitting process, it is worth taking a look at the two spectra taken (at a same temperature) with different incident energies; E_i = 25 and 120 meV. See Fig.7.4 for the comparison. It is clear that there is a shift in the high energy (E_i = 120 meV) spectra to a higher energy side compared to the low energy (E_i = 25 meV) spectra. This shift is due to the shift in the elastic peak. This happens on HET (also on other time of flight spectrometer) and is a systematic property of the spectrometer. The desirable solution to this problem would be either to fix the elastic peak position to E = 0 or to run fits simultaneously using both high and low energy data. However, in our analysis it was decided to focus on to the low energy spectra (where the spectra are not shifted) giving less priority to fit the high energy spectra.

7.3.2 Converting Rosenkrantz's B_k^q (Ho^{3+}) into B_n^m (Ho^{3+}/Er^{3+}/Dy^{3+})

As it was mentioned previously, the first step of the fitting process is the derivation of the starting CEF parameters. This was done by taking Rosenkrantz's CEF parameters B_k^q given in Ref. [13] for the Ho^{3+} ion in $Ho_2Ti_2O_7$ and converting it into appropriate form B_n^m that can be used in the FOCUS program. The steps taken in the conversion process are summarized in Table 7.4. The definitions of the constants used in the conversion were given in section 7.2.3 (and in the theory section given in the Appendix A2).

In order to test the validity of the converted starting parameters B_n^m the energy levels of the Ho^{3+} ion were first calculated using them. This is shown in Table 7.2 together with the energy level scheme given by Rosenkrantz (Fig.7.10) [13]. The agreement is very good, hence, proving the validity of the method (i.e. starting parameter conversion + FOCUS program) taken. Secondly, substituting Dy^{3+} for Ho^{3+}, the energy levels for Dy^{3+} in the same CEF were calculated. This is shown in Table 7.3 together with the reproduction of the energy level scheme calculated by Qiu (Fig.7.11) [10]. Again, this serves as an excellent example for the reproducibility of the calculation. The calculated wavefunctions (for all energy levels) for both ions Dy^{3+} and Ho^{3+} are listed in the Appendix (A3.2) section.

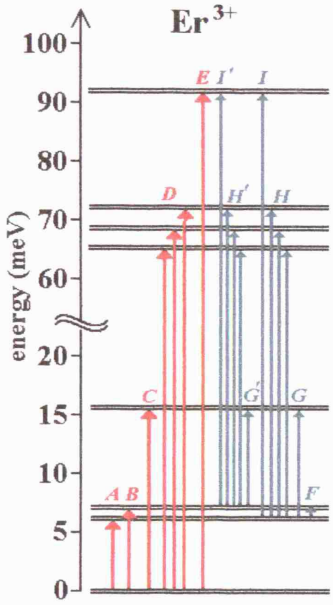

Figure 7.3: Schematic crystal field energy level scheme of the Er^{3+} measured for $Er_2Ti_2O_7$ in the inelastic neutron scattering experiment. The transitions from the ground states (labeled *A* to *E*) are distinguished from the transitions from the excited states (labeled *F* to *I*).

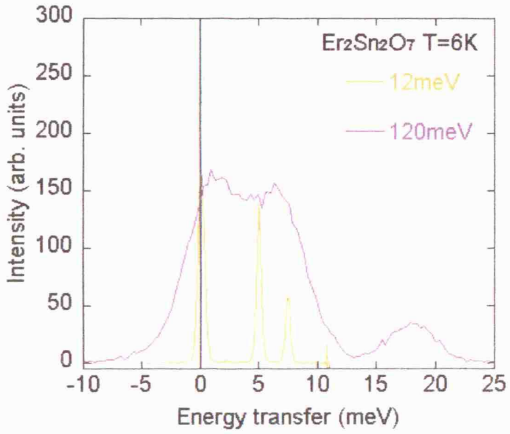

Figure 7.4: Overlaid spectra of $Er_2Ti_2O_7$ taken at T = 6 K with different incident energies; E_i = 12, 25 and 120 meV. It is clear that there is a shift in the spectrum taken at high E_i to a higher energy side compared to the low E_i spectra.

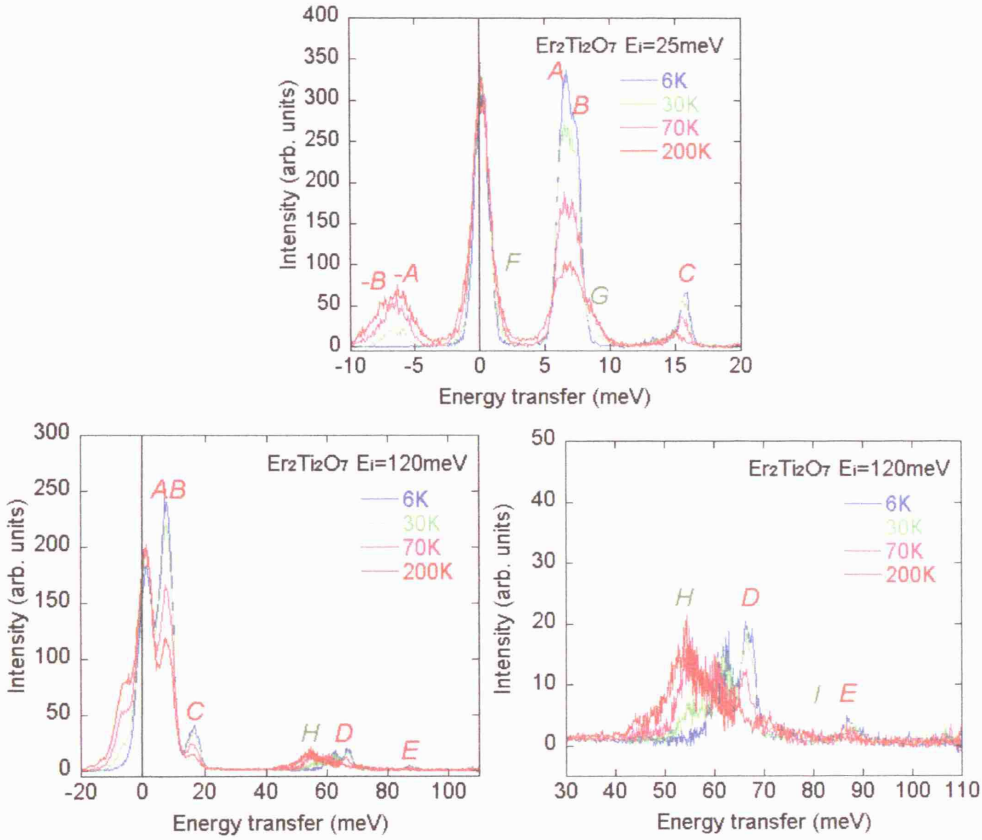

Figure 7.5: Energy spectra for $Er_2Ti_2O_7$ measured on HET with incident energy E_i = 25 meV (*Top Left*) and E_i = 120 meV (*Top Right* and *Bottom*) measured at T = 6, 30, 70 and 200 K. The peaks that grow in intensity with lowering the temperatures are E_i ~ 6.8 (*A*), 7.4 (*B*), 16 (*C*), 62.5 (*D*), 66.5 (*D*) and 87.3 (*E*) meV; hence attributed to transition from the ground state. The peaks that grow in intensity with increasing the temperatures are E_i ~ < 2 (*F*), 8.5 - 10 (*G*), 55 - 57 (*H*) meV; hence attributed to transition from the excited states.

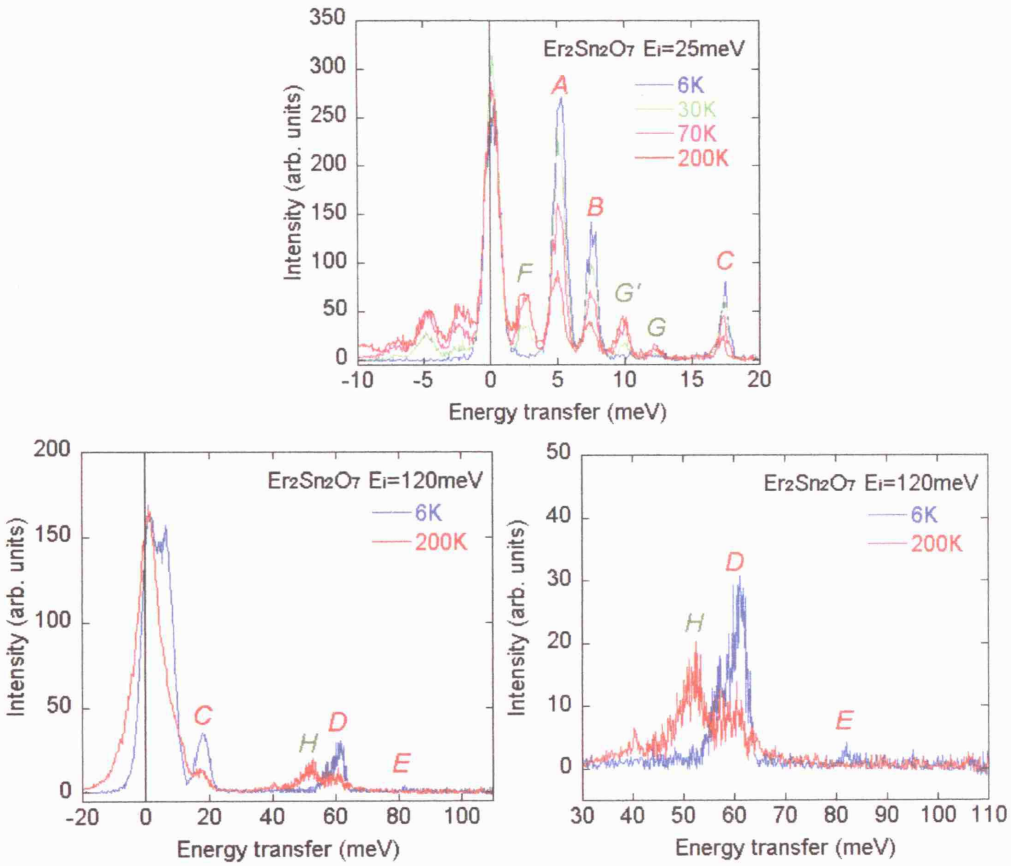

Figure 7.6: Energy spectra for $Er_2Sn_2O_7$ measured on HET with incident energy E_i = 25 meV (*Top Left*) and E_i = 120 meV (*Top Right* and *Bottom*) measured at T = 6, 30, 70 and 200 K. The peaks that grow in intensity with lowering the temperatures are E_i ~ 5.3 (*A*), 7.9 (*B*), 17.5 (*C*), 57.4 (*D*), 61.2 (*D*) and 82 (*E*) meV; hence attributed to transition from the ground state. The peaks that grow in intensity with increasing the temperatures are E_i ~ 2.8 (*F*), 10.1 (*G'*), 12.7 (*G*), 50-55 (*H*) meV; hence attributed to transition from the excited states.

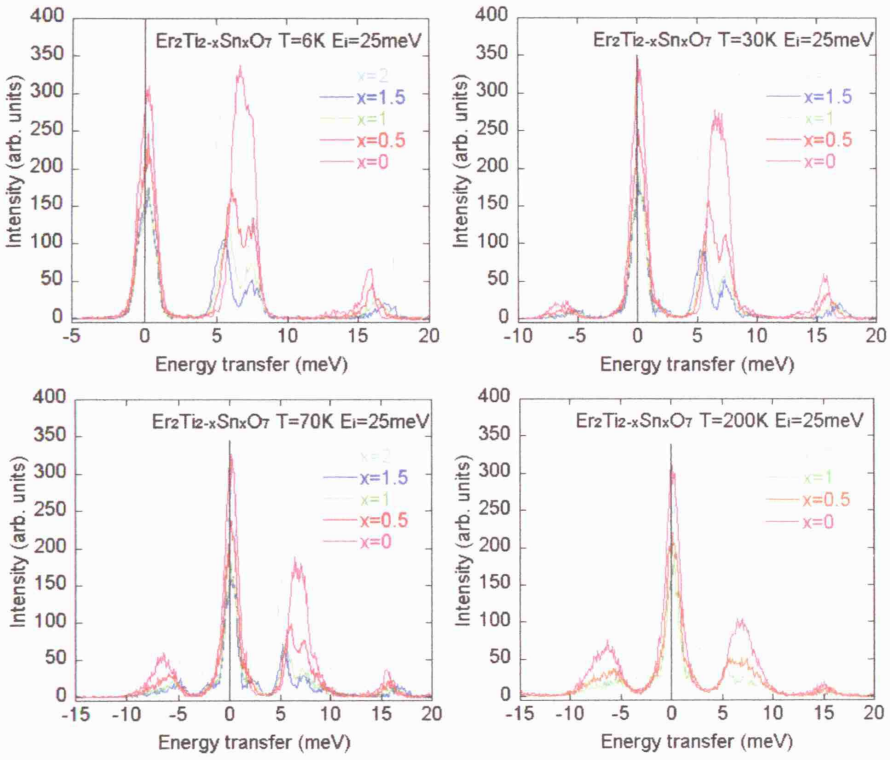

Figure 7.7: Energy spectra for $Er_2Ti_{2-x}Sn_xO_7$ (x = 0, 0.5, 1, 1.5 and 2) measured on HET with incident energy E_i = 25meV measured at T = 6, 30, 70 and 200 K. They show the gradual variation in peak positions and intensities as one moves across the series.

Fitted Energy Levels of Er^{3+} in $Er_2Ti_2O_7$ (meV)	
1 (2-fold)	0
2 (2-fold)	6.41
3 (2-fold)	7.34
4 (2-fold)	15.42
5 (2-fold)	66.27
6 (2-fold)	69.23
7 (2-fold)	71.96
8 (2-fold)	97.77

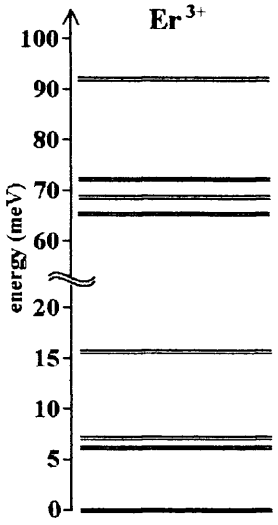

Table 7.1 (*Left*): Energy levels derived from the fitted spectrum of $Er_2Ti_2O_7$. The program FOCUS [1] refines the starting CEF parameters B_n^m (Er^{3+}) (derived from the parameters B_k^q (Ho^{3+}) given by Rosenkrantz [13]). The detail of the fitting is described in the text (section 7.3.3). **Figure 7.9 (*Right*):** The resulting refined energy levels for $Er_2Ti_2O_7$ is drawn schematically.

Finally, the energy levels for the ion Er^{3+} was calculated in the same way as described above. The result is shown in Table 7.5 (they are the *calculated* energy levels using the starting CEF parameters). To be more accurate about the point of discussion, in Table 7.1 and Fig.7.9, the energy levels for $Er_2Ti_2O_7$ with the refined CEF parameters (i.e. fitted to the actual spectra) are shown. In trigonal geometry, the free ion ground state term $^4I_{15/2}$ of Er^{3+} splits into eight doublets including the Kramers doublet ground state. The main difference from the energy level schemes of the Dy^{3+} and Ho^{3+} in the same CEF is that the lowest excited level in Er^{3+} is at $E \sim 6.41$ meV (~ 74.8 K) which is much lower compared to the other two ions. The two lowest energy levels at $E \sim 6.4$ and 7.3 meV are in accordance with the previous inelastic neutron scattering work. [14] The existence of low lying energy levels around 14 K (1.2 meV) was anticipated in previous susceptibility works on $Er_2Ti_2O_7$ [15-16] but this was not observed in our work. The calculated wavefunctions for the Er^{3+} will not be presented but instead the wavefunctions fitted to the actual spectra will be listed later in Table 7.9.

Predicted Energy Levels of Ho^{3+} in $Ho_2Ti_2O_7$ (meV)	
1 (2-fold)	0
2 (1-fold)	20.33
3 (2-fold)	21.87
4 (2-fold)	25.92
5 (1-fold)	27.65
6 (2-fold)	59.5
7 (1-fold)	69.31
8 (1-fold)	69.82
9 (2-fold)	71.47
10 (2-fold)	76.79
11 (1-fold)	80.48

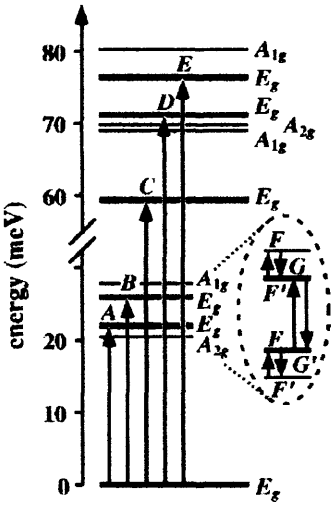

Table 7.2 (*Left*): Calculated energy levels of the Ho^{3+} ion in $Ho_2Ti_2O_7$ using the CEF parameters B_n^m (Ho^{3+}) derived from the parameters B_k^q (Ho^{3+}) given by Rosenkrantz [13]. This energy level scheme is then compared to the one given by Rosenkrantz [13] (**Figure 7.10 -*Right***). The agreement is perfect.

Predicted Energy Levels of Dy^{3+} in $Dy_2Ti_2O_7$ (meV)	
1 (2-fold)	0
2 (2-fold)	33.02
3 (2-fold)	43.31
4 (2-fold)	47.11
5 (2-fold)	58.52
6 (2-fold)	82.38
7 (2-fold)	95.16
8 (2-fold)	95.42

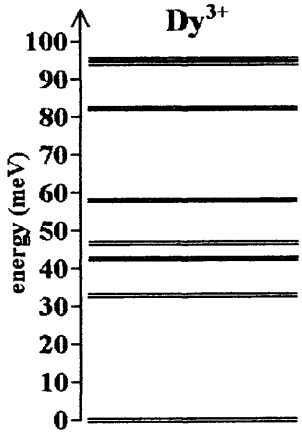

Table 7.3 (*Left*): Calculated energy levels of the Dy^{3+} ion in $Dy_2Ti_2O_7$ using the CEF parameters B_n^m (Dy^{3+}) derived from the parameters B_k^q (Ho^{3+}) given by Rosenkrantz [13]. This energy level scheme is then compared to the energy levels calculated by Qiu [10] (**Figure 7.11 -*Right***). The agreement is perfect.

	Rosenkrantz's Ho^{3+} B_k^q for an electron in CEF[13]	B_n^m converted in this work summed over all electrons	B_n^m converted in this work			conversion prefactor[4]	
			Er^{3+}	Ho^{3+}	Dy^{3+}		
B_2^0 (meV)	68.2	$B_2^0 * \alpha(Ln^{3+}) * \langle r^2(Ln^{3+})\rangle / \langle r^2(Ho^{3+})\rangle / p\_B_2^0 =$	0.082707	-0.075778	-0.227208	$p\_B_2^0$	2
B_4^0 (meV)	274.8	$B_4^0 * \beta(Ln^{3+}) * \langle r^4(Ln^{3+})\rangle / \langle r^4(Ho^{3+})\rangle / p\_B_4^0 =$	0.001405	-0.001144	-0.002219	$p\_B_4^0$	8
B_4^3 (meV)	83.7	$B_4^3 * \beta(Ln^{3+}) * \langle r^4(Ln^{3+})\rangle / \langle r^4(Ho^{3+})\rangle / p\_B_4^3 =$	-0.010124	0.008245	0.015996	$p\_B_4^3$	= -2 * SQRT(35) / 35
B_6^0 (meV)	86.8	$B_6^0 * \gamma(Ln^{3+}) * \langle r^6(Ln^{3+})\rangle / \langle r^6(Ho^{3+})\rangle / p\_B_6^0 =$	0.000010	-0.000007	0.000006	$p\_B_6^0$	16
B_6^3 (meV)	-62.5	$B_6^3 * \gamma(Ln^{3+}) * \langle r^6(Ln^{3+})\rangle / \langle r^6(Ho^{3+})\rangle / p\_B_6^3 =$	0.000148	-0.000104	0.000093	$p\_B_6^3$	= -8 * SQRT(105) / 105
B_6^6 (meV)	101.6	$B_6^6 * \gamma(Ln^{3+}) * \langle r^6(Ln^{3+})\rangle / \langle r^6(Ho^{3+})\rangle / p\_B_6^6 =$	0.000179	-0.000125	0.000112	$p\_B_6^6$	= 16 * SQRT(231) / 231

Steven's multiplicative factor [3]

	Ho^{3+}	Er^{3+}	Dy^{3+}
α_J (Ln^{3+})	=-1/(2*9*25)	=4/(9*25*7)	=-2/(9*5*7)
β_J (Ln^{3+})	=-1/(2*3*5*7*11*13)	=2/(9*5*7*11*13)	=-8/(27*5*7*11*13)
γ_J (Ln^{3+})	=-5/(27*7*121*169)	=8/(27*7*121*169)	=4/(27*7*121*169)

Radial Integral $\langle r^n \rangle$ [9]

	Ho^{3+}	Er^{3+}	Dy^{3+}
$\langle r^2 \rangle$	0.7446	0.7111	0.7814
$\langle r^4 \rangle$	1.379	1.27	1.505
$\langle r^6 \rangle$	5.379	4.816	6.048

Table 7.4: A summary of the conversion procedure of crystal field parameters B_n^m starting from the parameters given by Rosenkrantz *et al.*[13] for Ho^{3+} in $Ho_2Ti_2O_7$. Both effects of the summation over magnetic electrons and the exchanging ions (into Er^{3+} and Dy^{3+}) are taken into account in the conversion.

7.3.3 Fitting spectra of $Er_2Ti_2O_7$ and $Er_2Sn_2O_7$ from starting B_n^m

In this section the initial steps followed in fitting the calculated spectra to the actual data will be presented. The fitted results for all compounds (x = 0 to 2 of $Er_2Ti_{2-x}Sn_xO_7$) will be listed in the next section (section 7.3.4).

First of all, taking the converted starting parameters B_n^ms for the Er^{3+} ion from Table 7.4, the predicted spectra was calculated. The predicted energy levels are listed in Table 7.5. This starting spectrum was fitted to the experimentally obtained spectra and it was found that the predicted energy levels were closest to the levels of $Er_2Sn_2O_7$ rather than that of $Er_2Ti_2O_7$. Therefore, we start the refinement using the spectra of $Er_2Sn_2O_7$. The spectrum taken at T = 200 K was used first because there are more peaks to fit than in the low T spectra. The non-refined (fit of starting parameters) and refined fits are shown in Fig.7.12. Because the refinement was extremely sensitive to even a small change in the B_n^ms, the refinement was carried out manually with care, by refining one B_n^m at a time, keeping the rest fixed. The refined spectrum of the E_i = 25 meV was applied to the E_i = 120 meV spectrum to see the agreement, but because the spectrum with E_i = 120 meV is shifted towards higher energies the fitting was not as good as for the low incident energy spectra fit.

After the success of fitting the spectra of $Er_2Sn_2O_7$, the same fitting procedure was applied to the spectra of $Er_2Ti_2O_7$. Similarly as for the $Er_2Sn_2O_7$, the non-refined fits (using the same starting parameters) and the refined fits are shown in Fig.7.13.

The refined CEF parameters and the resulting properties will be discussed in the later sections (section 7.3.4~7.3.7).

Energy level	E (meV)	Degeneracy
1	0	2-fold
2	6.37	2-fold
3	8.69	2-fold
4	17.07	2-fold
5	49.89	2-fold
6	52.32	2-fold
7	57.16	2-fold
8	76.04	2-fold

Table 7.5: The predicted energy levels using the starting CEF parameters B_n^m for Er^{3+} taken from Table 7.4. These levels are taken as the starting template to fit the spectra for all samples containing Er^{3+} ion (i.e. for all x in $Er_2Ti_{2-x}Sn_xO_7$).

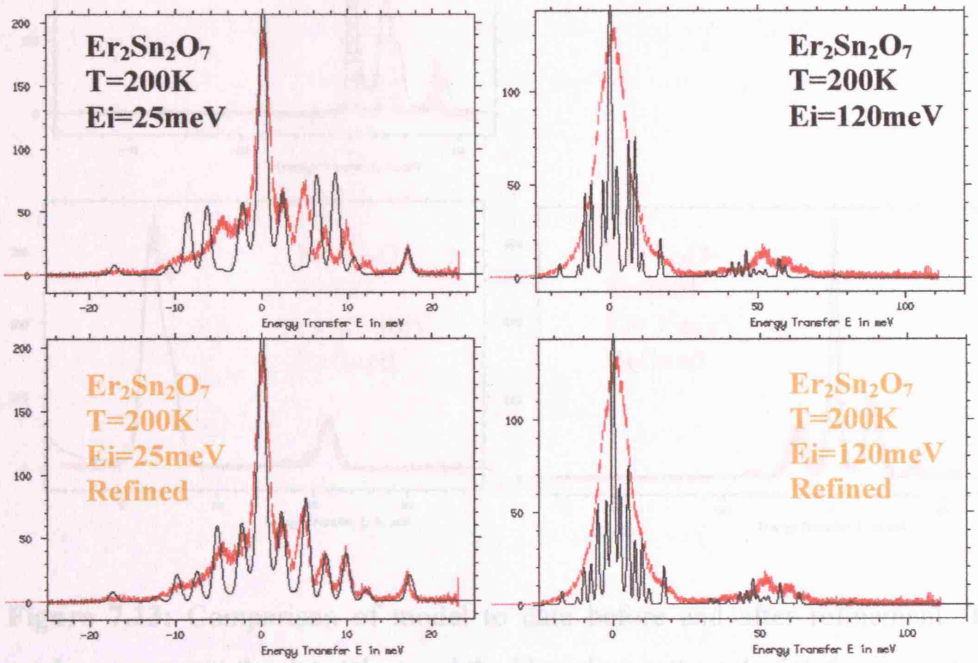

Figure 7.12: Comparison of model to data before (*Top*) and after (*Bottom*) refinement. The red markers represent the data taken and the black line is the calculated spectra. The spectra are of $Er_2Sn_2O_7$ taken at T = 200 K with incident energies E_i = 25 meV (*left*) and E_i = 120 meV (*right*). The starting model (*Top*) is calculated using the starting CEF parameters B_n^m given in Table 7.3.2. Because the spectra with E_i = 120 meV are shifted towards higher energies compared to those corresponding spectra with E_i = 25 meV, the fits of the high incident energy spectra are not as good as the lower energy ones.

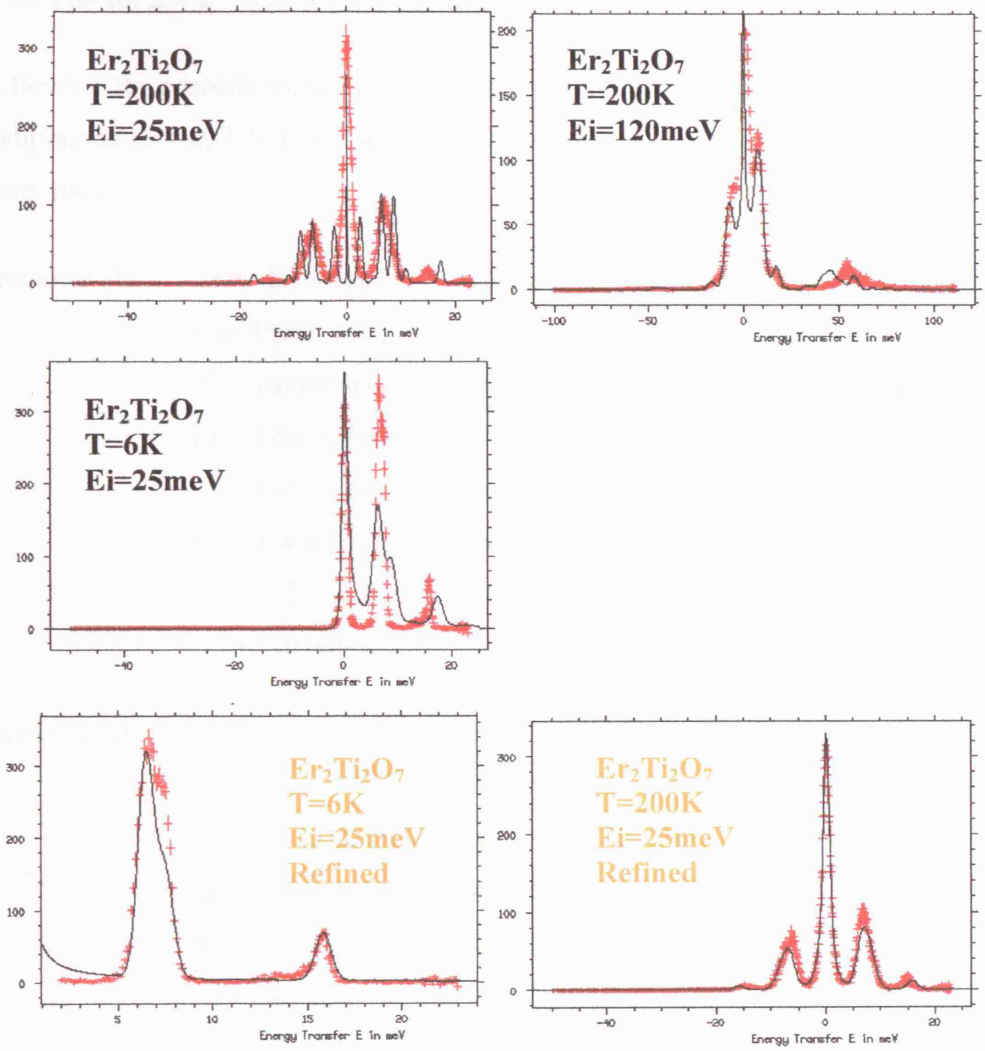

Figure 7.13: Comparison of model to data before and after refinement. The red markers represent the data taken and the black line is the calculated spectra.

Top and Middle rows - Spectra of $Er_2Ti_2O_7$ taken at $T = 200$ K and 6 K with incident energies $E_i = 25$ meV and 120 meV overlaid with the calculated pattern (from starting CEF parameters B_n^m given in Table 7.3.2).

Bottom row – Spectra of $Er_2Ti_2O_7$ taken at $T = 200$ K and 6 K with incident energies $E_i = 25$ meV overlaid with the refined fit.

7.3.4 Fits for $x = 2 \sim 0$ and their parameters

Following the procedures taken in the previous sections now fits were made for all the compounds (x = 2, 1.5, 1, 0.5 and 0). Two sets of attempts using different starting fits were made;

Sequence (I): first, the spectrum of $Er_2Sn_2O_7$ (x = 2) at T = 200 K with E_i = 25 meV was fitted using the starting parameters listed in Table 7.4 for Er^{3+}. The parameters are refined accordingly to give the best fit to this $Er_2Sn_2O_7$ spectrum. Then, using this refined parameters for $Er_2Sn_2O_7$ as a starting point, the spectra of the next compound $Er_2Ti_{0.5}Sn_{1.5}O_7$ (x = 1.5) was fitted and was refined. This was sequentially repeated for x = 1, 0.5 and 0. The results of this cascade of fitting will be shown below in sub-section 7.3.4.1.

Sequence (II): the second fitting sequence begins from the other end of the series; from the x = 0 compound, $Er_2Ti_2O_7$ in turn. The spectra for $Er_2Ti_2O_7$ taken at T = 200 K with E_i = 25 meV was first fitted using the calculated starting parameters listed in Table 7.4 for Er^{3+} and this was refined to give the best fit for this spectra. An additional reassurance step was taken in this sequence. That is, taking the refined parameters in the T = 200 K spectra, a fit was attempted to the low temperature T = 6 K spectra of the same sample. If the resulting fit was not good enough this was refined and the refined parameters were reapplied back to the T = 200 K spectra. This was repeated until a reasonable fit was achieved for both T = 200 K and T = 6 K spectra simultaneously using the same set of B_n^ms. This best set of B_n^ms were then taken as the starting parameters for the next compound x = 0.5 and the same fitting procedure was repeated. These fitting cycle was repeated for all compounds down to x = 2 ($Er_2Sn_2O_7$). The results are shown in sub-section 7.3.4.2.

7.3.4.1 Fitting starting from $Er_2Sn_2O_7$

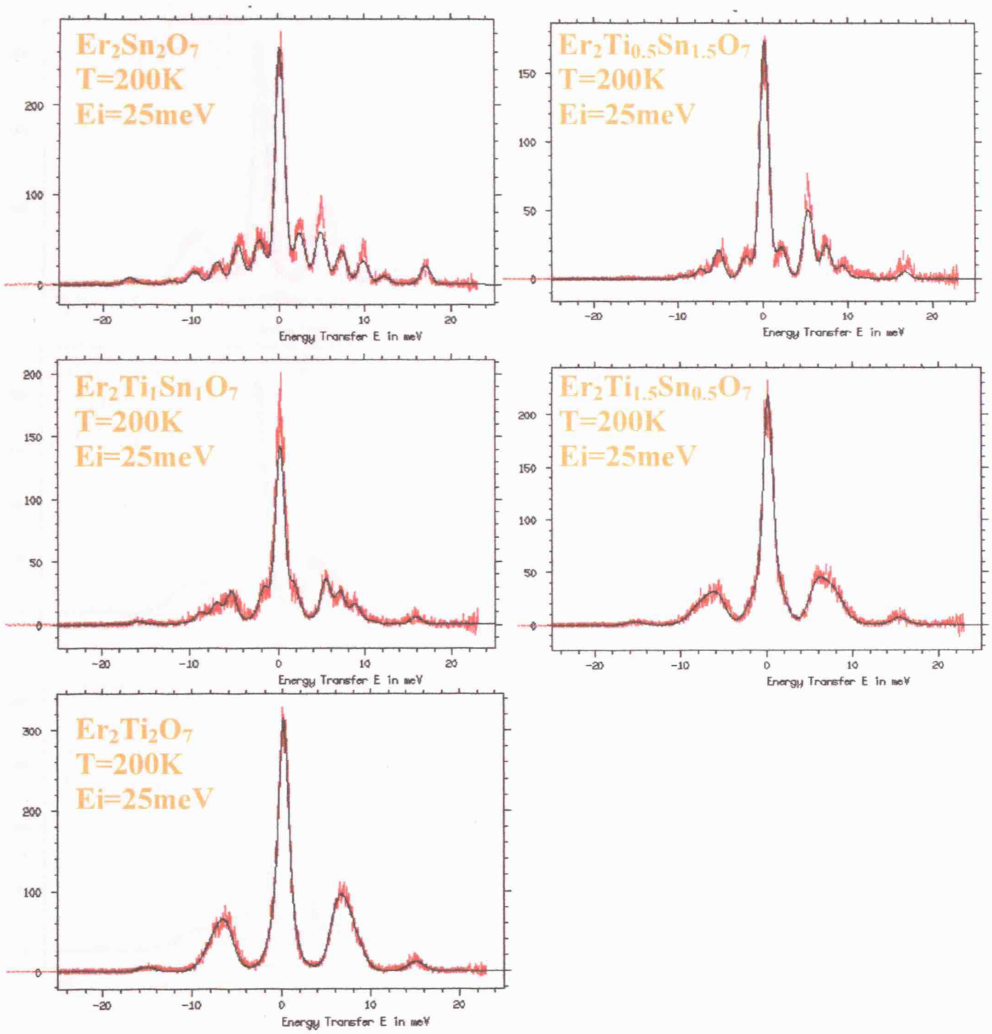

Figure 7.14: Fits of energy spectra for $Er_2Ti_{2-x}Sn_xO_7$ (x = 2, 1.5, 1, 0.5, 0) measured on HET (ISIS, U.K.); the red line is the measured spectra. The black solid line denotes the calculated spectra using the best fitted CEF parameters, including an intrinsic Lorentzian broadening of the transitions as well as the instrumental resolution. The fit was started with the x = 2 compound and the fitted parameters were used subsequently as the next fitting (x = 1.5) starting point and so on. Only the spectra taken at T = 200 K with E_i = 25 meV were used.

7.3.4.2 Fitting starting from $Er_2Ti_2O_7$

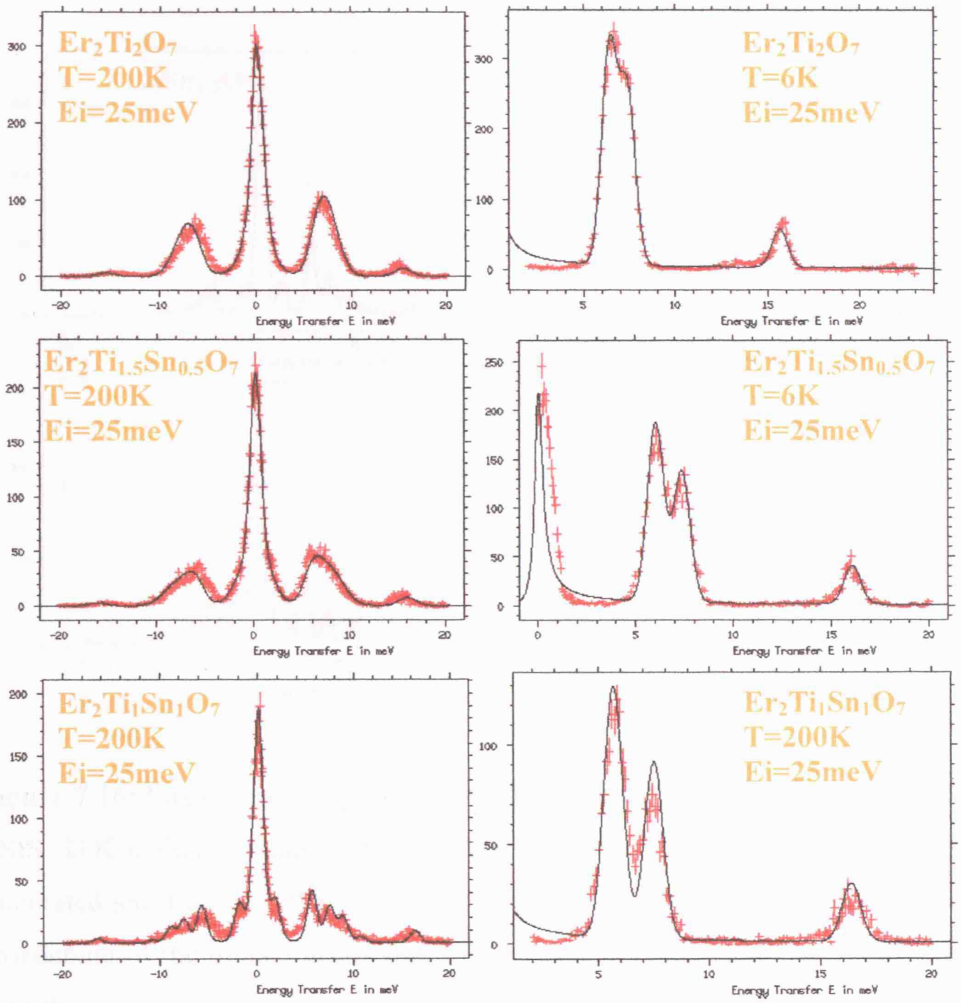

Figure 7.15: Fits of energy spectra for $Er_2Ti_{2-x}Sn_xO_7$ (x = 0, 0.5, 1) measured on HET (ISIS, U.K.); the red markers represent the measured spectra. The spectra for x = 1.5 and 2 continues in Fig.7.16. The black solid lines denote the calculated spectra using the refined CEF parameters, including an intrinsic Lorentzian broadening of the transitions as well as the instrumental resolution. The fit was started with the x = 0 compound and the fitted parameters were used subsequently as the next fitting (x = 1.5) starting point and so on. Spectra taken at T = 200 K and T = 6 K with E_i = 25 meV were fitted simultaneously.

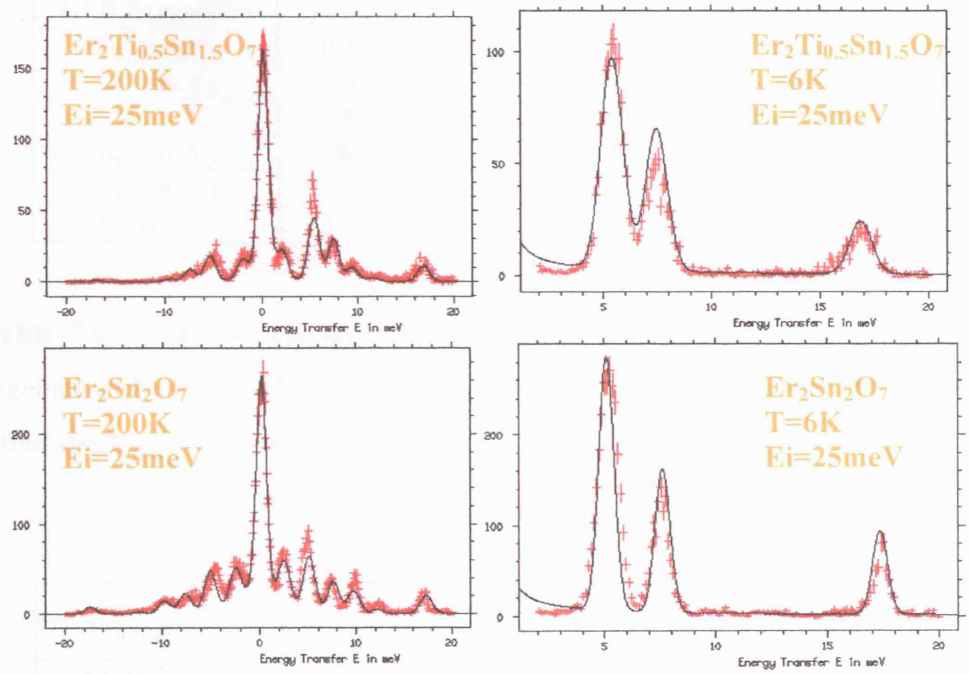

Figure 7.16: Fits of energy spectra for $Er_2Ti_{2-x}Sn_xO_7$ (x = 1.5 and 2) measured on HET (ISIS, U.K.); the red line is the measured spectra. The black solid lines denote the calculated spectra using the refined CEF parameters, including an intrinsic Lorentzian broadening of the transitions as well as the instrumental resolution. The fit was started with the x = 0 compound and the fitted parameters were used subsequently as the next fitting (x = 1.5) starting point and so on. Spectra taken at T = 200 K and T = 6 K with E_i = 25 meV were fitted simultaneously.

x	2	1.5	1	0.5	0
CEF Parameter	$\chi^2 = 2.9$	$\chi^2 = 1.5$	$\chi^2 = 2.0$	$\chi^2 = 1.3$	$\chi^2 = 1.7$
B_2^0 (meV)	0.131	0.171	0.161	0.138	0.151
B_4^0 (meV)	1.37E-03	1.39E-03	1.75E-03	1.58E-03	1.40E-03
B_4^3 (meV)	-3.78E-02	-3.72E-02	-3.60E-02	-3.81E-02	-3.97E-02
B_6^0 (meV)	1.18E-05	1.41E-05	1.39E-05	1.37E-05	1.45E-05
B_6^3 (meV)	9.42E-05	1.24E-04	1.23E-04	1.00E-04	7.69E-05
B_6^6 (meV)	1.62E-04	1.17E-04	1.27E-04	1.50E-04	1.49E-04

Table 7.6: Table of best fitted parameters for $Er_2Ti_{2-x}Sn_xO_7$ (x = 2, 1.5, 1, 0.5, 0) together with their goodness of the fit χ^2 for the fitting sequence (I). The corresponding fitted spectra are shown in Fig.7.14.

x	2	1.5	1	0.5	0
χ^2 (200K / 6K)	7.6 / 5.1	5.4 / 2.8	7.7 / 3.9	18.2 / 16.8	32.2 / 4.0
CEF Parameter					
B_2^0 (meV)	0.192	0.171	0.167	0.159	0.140
B_4^0 (meV)	1.97E-03	1.82E-03	1.78E-03	1.71E-03	1.62E-03
B_4^3 (meV)	-3.13E-02	-3.38E-02	-3.52E-02	-3.69E-02	-3.80E-02
B_6^0 (meV)	1.25E-05	1.26E-05	1.33E-05	1.38E-05	1.40E-05
B_6^3 (meV)	8.34E-05	8.25E-05	8.29E-05	8.28E-05	8.34E-05
B_6^6 (meV)	1.45E-04	1.47E-04	1.49E-04	1.52E-04	1.52E-04

Table 7.7: Table of best fitted parameters for $Er_2Ti_{2-x}Sn_xO_7$ (x = 0, 0.5 1, 1.5 2) together with their goodness of the fit χ^2 for the fitting sequence (II). The corresponding fitted spectra are shown in Fig.7.15 and Fig.7.16.

7.3.4.3 Fitted CEF Parameters (B_n^m) variation with x

The best fitted CEF parameters for all compounds ($x = 0 \sim 2$ of $Er_2Ti_{2-x}Sn_xO_7$) against x for both sequences (I) and (II) are now plotted in Fig.7.17. The variation have better trends for sequence (II) where fitting was applied to spectra at two temperatures (T = 200 K and 6 K) for each sample. In other words, the B_n^m variation with x for sequence (II) are more linear than those for sequence (I). Although the values of χ^2 are lower in sequence (I), we expect that the fitting results in sequence (II) are more reliable because of the reassurance procedure applied to it (-the detail of the procedure is given in section 7.3.5). Therefore, we take this linear trend of B_n^m variation with x as the starting point for the remaining magnetic property calculations. In the subsequent sections, the predicted energy levels (section 7.3.5), the calculated wavefunctions (section 7.3.6) and the derived magnetic moments (section 7.3.7) for the $Er_2Ti_{2-x}Sn_xO_7$ series will be presented and discussed, only based on the fits obtained for Sequence (II).

7.3.5 Energy levels of $Er_2Ti_{2-x}Sn_xO_7$ (x = 0, 0.5, 1, 1.5, 2)

The calculated energy levels from the refinements for all the compounds (x = 0, 0.5, 1, 1.5 and 2 of $Er_2Ti_{2-x}Sn_xO_7$) are listed in Table 7.8 and are plotted in Fig.7.18. (Reminder; only the results of the fits started from fitting $Er_2Ti_2O_7$ –i.e. Sequence (II)- are plotted.) All compounds have similar energy level scheme with eight doublets. The gradual shift in energy levels (which was previously noticed, although only qualitatively, in section 7.3.1) with x is reproduced.

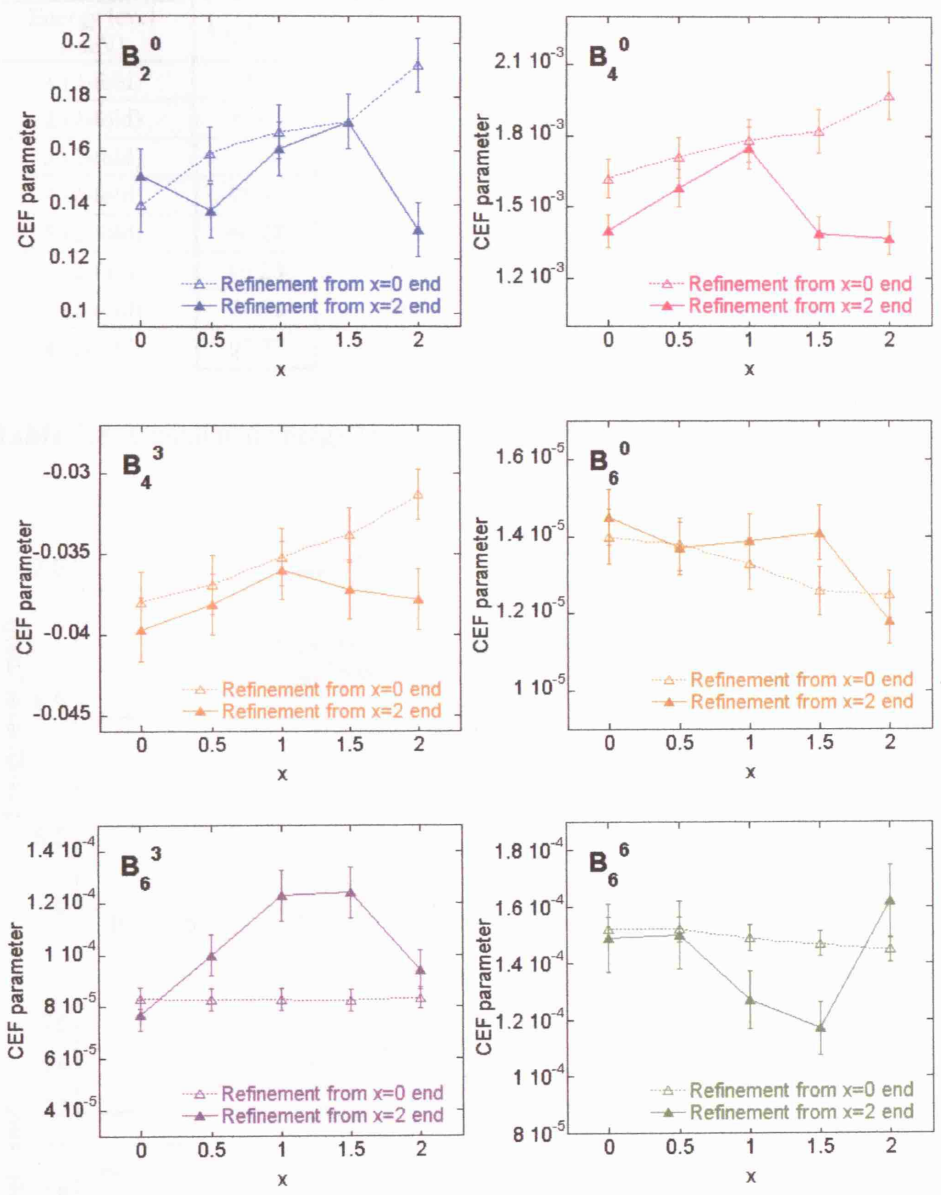

Figure 7.17: CEF parameter (B_n^m) variation with x for the series $Er_2Ti_{2-x}Sn_xO_7$. The solid lines represent results obtained from the fitting following Sequence (I); starting the fit from $Er_2Sn_2O_7$ and using only T = 200 K spectra. The dotted lines represent results obtained from the fitting following Sequence (II); starting the fit from $Er_2Ti_2O_7$ and using both T = 200 K and 6 K spectra to reassure the validity of the fitted parameters.

Energy level (meV)	$Er_2Ti_2O_7$	$Er_2Ti_{1.5}Sn_{0.5}O_7$	$Er_2Ti_1Sn_1O_7$	$Er_2Ti_{0.5}Sn_{1.5}O_7$	$Er_2Sn_2O_7$
1 (2-fold)	0	0	0	0	0
2 (2-fold)	6.41	6.02	5.69	5.4	5.08
3 (2-fold)	7.34	7.37	7.42	7.47	7.6
4 (2-fold)	15.42	16.06	16.46	16.83	17.34
5 (2-fold)	66.27	65.22	63.51	61.99	59.89
6 (2-fold)	69.23	68.12	66	64.39	61.93
7 (2-fold)	71.96	70.5	68.17	66.18	63.49
8 (2-fold)	97.77	100.67	101.12	100.75	104.43

Table 7.8: Calculated energy levels for the $Er_2Ti_{2-x}Sn_xO_7$ (x = 0, 0.5, 1, 1.5, 2).

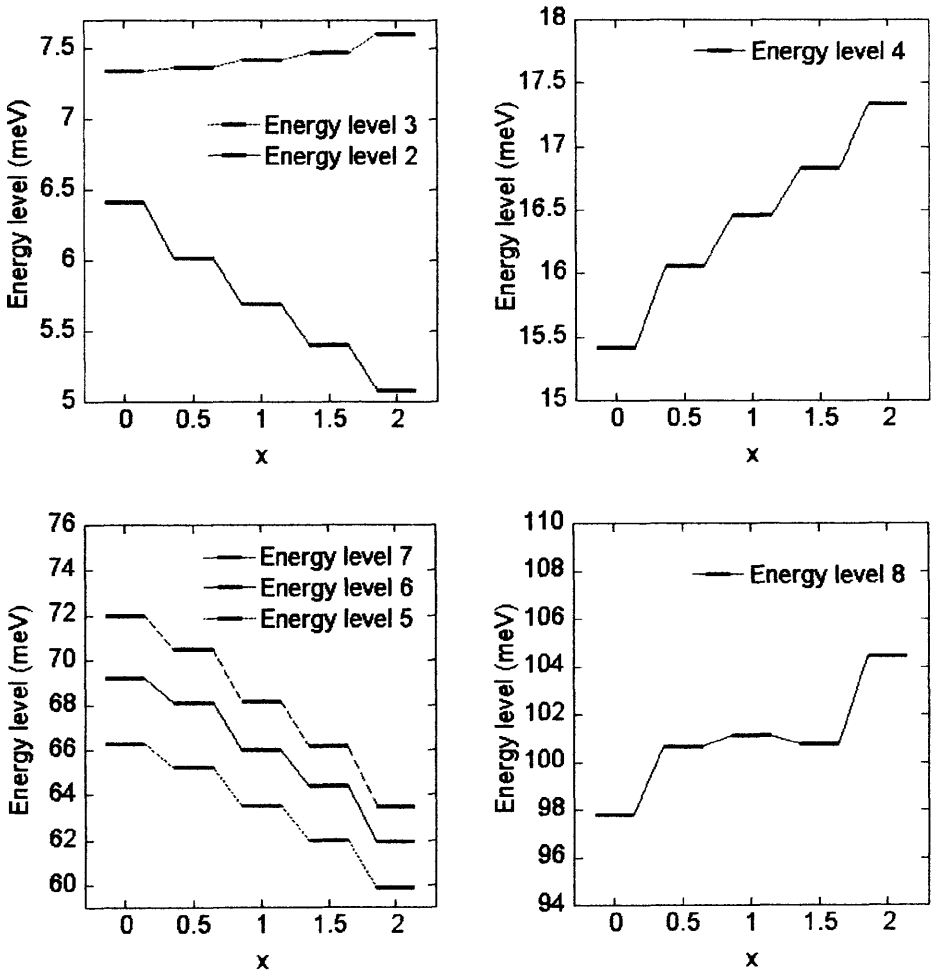

Figure 7.18: Calculated energy levels for the $Er_2Ti_{2-x}Sn_xO_7$ (x = 0, 0.5, 1, 1.5, 2).

7.3.6 Wavefunctions of $Er_2Ti_{2-x}Sn_xO_7$ (x = 0, 0.5, 1, 1.5, 2)

In this section we discuss about the wavefunctions of $Er_2Ti_{2-x}Sn_xO_7$ (x = 0, 0.5, 1, 1.5, 2) calculated from the fitted spectra. The wavefunctions are calculated by the FOCUS program using the refined B_n^m values. The whole wavefunction set for all energy levels for all compounds are listed in the Appendix (A3).

In Table 7.9 the ground state (Kramers doublets) wavefunctions calculated from the fitting for all five compounds are listed. This on its own is *not* wrong. However, as one might notice, all the $|m_J\rangle$ states in the J-manifold are present in the wavefunction representation whereas the wavefunction calculated by Hodges in Ref.[14] is represented by only $|m_J\rangle$s that differ by 6/2 (i.e. 3) ($|m_J\rangle$ = |-11/2⟩, |-5/2⟩, |1/2⟩, | 7/2⟩, |13/2⟩). This means the Hodges' wavefunctions are calculated using the 3-fold rotation ⟨111⟩ axis as the c-axis, hence $|m_J\rangle$s differing by 3 are only present. In our case, the FOCUS program chooses an arbitrary axis to be the c-axis (the quantization axis) and represents the wavefunction with respect to this axis. The consequence is that the wavefunction we get out of FOCUS is *rotated* with respect to the Hodges' wavefunction. In order to make a direct comparison of the two wavefunctions one need to *rotate* (back) our wavefunction so that it is represented in Hodges' format. This is not a rotation in direct space but is called a rotation in Hilbert space [17] and it corresponds to the diagonalization of the magnetic moment matrix (the details will be discussed in section 7.3.7); below we state how this is done.

7.3.6.1 Rotation of wavefunction in Hilbert space

Let $|\psi_+\rangle$ and $|\psi_-\rangle$ be the starting wavefunction pair [17];

$$|\psi_+\rangle = \sum_{J,m} C_{J,m} |J,m\rangle \tag{7.3}$$

$$|\psi_-\rangle = \Theta|\psi_+\rangle = \sum_{J,m} C_{J,m}{}^* (-1)^{J-m} |J,-m\rangle \tag{7.4}$$

where $C_{J,m}$ is the coefficient of the $|J,m\rangle$ state. When rotated these become $|\psi_+'\rangle$ and $|\psi_-'\rangle$;

$$|\psi_+'\rangle = a|\psi_+\rangle + b|\psi_-\rangle \tag{7.5}$$

$$|\psi_-'\rangle = \Theta|\psi_+'\rangle = -b^*|\psi_+\rangle + a^*|\psi_-\rangle . \tag{7.6}$$

The $|m_J\rangle$s that are present in our wavefunction and absent in Hodges' are; $|-13/2\rangle$, $|-7/2\rangle$, $|-1/2\rangle$, $|5/2\rangle$ and $|11/2\rangle$. Therefore, one needs to find the coefficients a and b that makes $C_{|-13/2\rangle} = 0$, $C_{|-7/2\rangle} = 0$, etc. For example, let the original wavefunctions be

$$|\psi_+\rangle = A|-13/2\rangle + B|-11/2\rangle + C|-7/2\rangle + \cdots + I|11/2\rangle + J|13/2\rangle \tag{7.7}$$

$$|\psi_-\rangle = -J|-13/2\rangle + I|-11/2\rangle + H|-7/2\rangle + \cdots + -B|11/2\rangle + A|13/2\rangle. \tag{7.8}$$

Then A, -J, C, H···· (the coefficients for $|m_J\rangle$ absent in Hodges' work) should be zero. The coefficients of the new (rotated) set of wavefunctions $|\psi_+'\rangle$ and $|\psi_-'\rangle$ then becomes

$$|\psi_+'\rangle = a|\psi_+\rangle + b|\psi_-\rangle = = a\,A\,|-13/2\rangle - bJ|-13/2\rangle = 0, \tag{7.9}$$

$$\text{so} \qquad a = \frac{1}{\sqrt{1 + A^2/J^2}} \qquad \text{and} \qquad b = \frac{A}{J\sqrt{1 + A^2/J^2}}. \tag{7.10}$$

In this way, the wavefunction pairs computed out of the FOCUS program can be converted into a pair that is in Hodges' format. The converted ground state wavefunctions for all compounds are listed in Table 7.9 together with the Hodges' $Er_2Ti_2O_7$ wavefunction [14].

7.3.7 Magnetic moment calculations for $Er_2Ti_{2-x}Sn_xO_7$ from their rotated wavefunctions

Finally, the magnetic moments for the Er^{3+} ions in the different CEF of the $Er_2Ti_{2-x}Sn_xO_7$ series are calculated from the ground state Kramers doublets. The magnetic moment operator $\hat{\mu}$ can be calculated using the so-called g-matrix (tensor);

$$\hat{\mu} = \begin{pmatrix} \hat{\mu}_x \\ \hat{\mu}_y \\ \hat{\mu}_z \end{pmatrix} = \begin{pmatrix} g_{x1} & g_{x2} & g_{x3} \\ g_{y1} & g_{y2} & g_{y3} \\ g_{z1} & g_{z2} & g_{z3} \end{pmatrix} \begin{pmatrix} \sigma_1 \\ \sigma_2 \\ \sigma_3 \end{pmatrix}, \tag{7.11}$$

where σs are the Pauli spin operators. Therefore,

$$\hat{\mu}_x = g_{x1}\sigma_1 + g_{x2}\sigma_2 + g_{x3}\sigma_3, \tag{7.12}$$
$$\hat{\mu}_y = g_{y1}\sigma_1 + g_{y2}\sigma_2 + g_{y3}\sigma_3, \tag{7.13}$$
$$\hat{\mu}_z = g_{z1}\sigma_1 + g_{z2}\sigma_2 + g_{z3}\sigma_3. \tag{7.14}$$

The g-matrix can be calculated using the following relations;

$$J_z|m_J\rangle = m_J|m_J\rangle \tag{7.15}$$
$$J_+|m_J\rangle = \sqrt{(J-m_J)(J+m_J+1)}\,|m_J+1\rangle \tag{7.16}$$
$$J_-|m_J\rangle = \sqrt{(J+m_J)(J-m_J-1)}\,|m_J-1\rangle \tag{7.17}$$

$$\langle\psi_+|J_z|\psi_+\rangle = g_{z3}, \tag{7.18}$$
$$\langle\psi_-|J_z|\psi_+\rangle = g_{z1} - ig_{z2}\,; \quad g_{z2} = 0, \tag{7.19}$$
$$\langle\psi_+|J_+|\psi_+\rangle = \langle\psi_+|J_x + iJ_y|\psi_+\rangle = g_{x3} + ig_{y3}\,; \quad g_{y3} = 0, \tag{7.20}$$
$$\langle\psi_-|J_+|\psi_+\rangle = \langle\psi_-|J_x + iJ_y|\psi_+\rangle = g_{x1} + g_{y2} + i(g_{y1} - g_{x2})\,; \quad g_{y1} - g_{x2} = 0, g_{y1} = g_{x2} \tag{7.21}$$
$$\langle\psi_+|J_-|\psi_+\rangle = \langle\psi_+|J_x - iJ_y|\psi_+\rangle = g_{x3} - ig_{y3}\,; \quad g_{y3} = 0, \tag{7.22}$$
$$\langle\psi_-|J_-|\psi_+\rangle = \langle\psi_-|J_x - iJ_y|\psi_+\rangle = g_{x1} - g_{y2} + i(g_{y1} + g_{x2})\,; \quad g_{y1} + g_{x2} = 0, g_{y1} = -g_{x2} \tag{7.23}$$
$$g_{y1} = g_{x2} = -g_{x2} = 0 \tag{7.24}$$

where all imaginary terms are zero. Then the g-matrix will be reduced into the form;

$$\hat{g}\text{-matrix} = \begin{pmatrix} g_{x1} & g_{x2} & g_{x3} \\ g_{y1} & g_{y2} & g_{y3} \\ g_{z1} & g_{z2} & g_{z3} \end{pmatrix} \Rightarrow \begin{pmatrix} g_{x1} & 0 & g_{x3} \\ 0 & g_{y2} & 0 \\ g_{z1} & 0 & g_{z3} \end{pmatrix}. \tag{7.25}$$

In order to find the magnetic moment out of the g-matrix, the g-matrix has to be diagonalized in the form

$$\hat{g}\text{-matrix} = \begin{pmatrix} g_{x1} & g_{x2} & g_{x3} \\ g_{y1} & g_{y2} & g_{y3} \\ g_{z1} & g_{z2} & g_{z3} \end{pmatrix} \Rightarrow \begin{pmatrix} g_{x1} & 0 & 0 \\ 0 & g_{y2} & 0 \\ 0 & 0 & g_{z3} \end{pmatrix}. \tag{7.26}$$

This is achieved when appropriate axes are chosen as x, y and z. The conversion of the axis made in section 7.3.6 should give this diagonal g-matrix. The calculated g-matrices for all compounds will now be listed below;

$$\hat{g}(Er_2Ti_2O_7) = \begin{pmatrix} 3.01 & 0 & 0.01 \\ 0 & -3.01 & 0 \\ 0 & 0 & -1.37 \end{pmatrix}, \quad (7.27)$$

$$\hat{g}(Er_2Ti_{1.5}Sn_{0.5}O_7) = \begin{pmatrix} 2.38 & 0 & 0.02 \\ 0 & -2.38 & 0 \\ 0.03 & 0 & -2.73 \end{pmatrix}, \quad (7.28)$$

$$\hat{g}(Er_2Ti_1Sn_1O_7) = \begin{pmatrix} -2.21 & 0 & -0.02 \\ 0 & 2.21 & 0 \\ 0.04 & 0 & -3.03 \end{pmatrix}, \quad (7.29)$$

$$\hat{g}(Er_2Ti_{0.5}Sn_{1.5}O_7) = \begin{pmatrix} -2.10 & 0 & 0.00 \\ 0 & 2.10 & 0 \\ 0.00 & 0 & -3.21 \end{pmatrix}, \quad (7.30)$$

$$\hat{g}(Er_2Sn_2O_7) = \begin{pmatrix} 1.75 & 0 & -0.01 \\ 0 & -1.75 & 0 \\ -0.04 & 0 & -3.71 \end{pmatrix}. \quad (7.31)$$

It should be noted that if a matrix is diagonal, any two of the diagonal terms can be reversed in sign (-this is only true for the Kramers doublet since the signs of the terms depend on which wavefunction one chooses out of the Kramers pair.). After these reversal of signs, all the above g-matrices will only contain positive diagonal terms. Another small detail to notice is that the g-matrices are not strictly diagonalized in some compounds and this is due to the mismatch between the chosen axis and the calculated wavefunction. However, the off-diagonal terms are small enough to be ignored and the corresponding magnetic moments will be calculated only from the diagonal terms.

$$\mu(\text{compound}) = (\mu_x, \mu_y, \mu_z); \quad |\mu| = \sqrt{\mu_x^2 + \mu_y^2 + \mu_z^2}\ \mu_B \qquad (7.32)$$

$$\mu(Er_2Ti_2O_7) = (3.61, 3.61, 1.65); \quad |\mu| = 5.36\ \mu_B \qquad (7.33)$$

$$\mu(Er_2Ti_{1.5}Sn_{0.5}O_7) = (2.86, 2.86, 3.28); \quad |\mu| = 5.20\ \mu_B \qquad (7.35)$$

$$\mu(Er_2Ti_1Sn_1O_7) = (2.66, 2.66, 3.63); \quad |\mu| = 5.23\ \mu_B \qquad (7.36)$$

$$\mu(Er_2Ti_{0.5}Sn_{1.5}O_7) = (2.52, 2.52, 3.85); \quad |\mu| = 5.24\ \mu_B \qquad (7.37)$$

$$\mu(Er_2Sn_2O_7) = (2.11, 2.11, 4.55); \quad |\mu| = 5.35\ \mu_B \qquad (7.38)$$

The way to interpret the above notations is as follows; μ_x and μ_y correspond to the components of the moment that are perpendicular to the ⟨111⟩ axis (the chosen *c*-axis) and μ_z is the moment parallel to ⟨111⟩. Then obviously, $|\mu|$ represents the actual moment length (size). For example, the Er^{3+} moment in the CEF of $Er_2Ti_2O_7$ (Eqn.7.33) is interpreted to have components of 3.61 μ_B and 1.65 μ_B perpendicular and parallel to ⟨111⟩. Although this proves the tendency of the spins to lie within the ⟨111⟩ easy-planes, they are not strictly confined in the planes. Thus, the assumption that the $Er_2Ti_2O_7$ being an experimental realization of the pyrochlore ⟨111⟩-XY antiferromagnet [14,18] is not strictly true. The variation in μ_x, μ_y, μ_z and $|\mu|$ against the composition x of $Er_2Ti_{2-x}Sn_xO_7$ is plotted in Fig.7.19 below.

Two crucial conclusions can be drawn from the above calculations of the magnetic moments. Firstly, focusing on the actual moment sizes, it is apparent that there is no obvious change within the series of compounds. The Er^{3+} moment size fixed by the surrounding CEF takes a constant value of ~ 5.2 - 5.35 μ_B despite of the system. (This is about half the free ion value of Er^{3+}; $g_J\sqrt{J(J+1)} = 9.59\ \mu_B$.)

Secondly, however more interestingly, the nature of the moment (therefore the spatial distribution / or the anisotropy of the moment) changes dramatically as we go across the series. From the plot in Fig.7.19 one can see that, for $x = 0$ ($Er_2Ti_2O_7$) the moments have a tendency to lie *perpendicular* to the ⟨111⟩ axis but they gradually change preference and as it approaches $x = 2$ ($Er_2Sn_2O_7$) they now start to lie *along* the ⟨111⟩. In other words, the system changes its anisotropy from having ⟨111⟩ easy- planes (i.e. XY-like) in $Er_2Ti_2O_7$, into a system having ⟨111⟩ easy-axes (i.e. Ising-like) in $Er_2Sn_2O_7$. This crossover in nature of anisotropy happens around $x = 0.5$.

$Er_2Ti_2O_7$

|1+>	=	-0.189	-13 /2 >	|1->	=	0.2	-13 /2 >
	+	0.51	-11 /2 >		+	0.482	-11 /2 >
	+	0.25	-7 /2 >		+	-0.264	-7 /2 >
	+	-0.388	-5 /2 >		+	-0.367	-5 /2 >
	+	-0.081	-1 /2 >		+	0.086	-1 /2 >
	+	0.086	1 /2 >		+	0.081	1 /2 >
	+	-0.367	5 /2 >		+	0.388	5 /2 >
	+	0.264	7 /2 >		+	0.25	7 /2 >
	+	-0.482	11 /2 >		+	0.51	11 /2 >
	+	0.2	13 /2 >		+	0.19	13 /2 >

$Er_2Ti_{1.5}Sn_{0.5}O_7$

|1+>	=	-0.015	-13 /2 >	|1->	=	0.248	-13 /2 >
	+	0.72	-11 /2 >		+	0.047	-11 /2 >
	+	0.023	-7 /2 >		+	-0.351	-7 /2 >
	+	-0.532	-5 /2 >		+	-0.035	-5 /2 >
	+	-0.007	-1 /2 >		+	0.1	-1 /2 >
	+	0.1	1 /2 >		+	0.007	1 /2 >
	+	-0.035	5 /2 >		+	0.532	5 /2 >
	+	0.351	7 /2 >		+	0.023	7 /2 >
	+	-0.047	11 /2 >		+	0.72	11 /2 >
	+	0.248	13 /2 >		+	0.016	13 /2 >

$Er_2Ti_1Sn_1O_7$

|1+>	=	0.22	-13 /2 >	|1->	=	-0.038	-13 /2 >
	+	0.131	-11 /2 >		+	0.733	-11 /2 >
	+	-0.329	-7 /2 >		+	0.059	-7 /2 >
	+	-0.093	-5 /2 >		+	-0.52	-5 /2 >
	+	0.076	-1 /2 >		+	-0.014	-1 /2 >
	+	0.014	1 /2 >		+	0.076	1 /2 >
	+	0.52	5 /2 >		+	-0.093	5 /2 >
	+	0.059	7 /2 >		+	0.329	7 /2 >
	+	0.733	11 /2 >		+	-0.131	11 /2 >
	+	0.039	13 /2 >		+	0.22	13 /2 >

$Er_2Ti_{0.5}Sn_{1.5}O_7$

|1+>	=	0.206	-13 /2 >	|1->	=	0.01	-13 /2 >
	+	-0.035	-11 /2 >		+	0.758	-11 /2 >
	+	-0.323	-7 /2 >		+	-0.015	-7 /2 >
	+	0.024	-5 /2 >		+	-0.522	-5 /2 >
	+	0.061	-1 /2 >		+	0.003	-1 /2 >
	+	-0.003	1 /2 >		+	0.061	1 /2 >
	+	0.522	5 /2 >		+	0.024	5 /2 >
	+	-0.015	7 /2 >		+	0.323	7 /2 >
	+	0.758	11 /2 >		+	0.035	11 /2 >
	+	-0.01	13 /2 >		+	0.206	13 /2 >

$Er_2Sn_2O_7$

|1+>	=	-0.089	-13 /2 >	|1->	=	0.145	-13 /2 >
	+	0.682	-11 /2 >		+	0.424	-11 /2 >
	+	0.147	-7 /2 >		+	-0.237	-7 /2 >
	+	-0.423	-5 /2 >		+	-0.263	-5 /2 >
	+	-0.006	-1 /2 >		+	0.009	-1 /2 >
	+	0.009	1 /2 >		+	0.006	1 /2 >

Table 7.9: Ground state Kramers doublet wavefunctions for $Er_2Ti_{2-x}Sn_xO_7$ ($x = 0 \sim 2$) listed in the format calculated in the FOCUS program.

$Er_2Ti_2O_7$ (our data with 3-fold axis chosen as the quantization axis)

|1+>	=	0.59	-11 /2 >	|1->	=	0.31	-13 /2 >
	+	-0.56	-5 /2 >		+	-0.44	-7 /2 >
	+	0.24	1 /2 >		+	0.24	-1 /2 >
	+	0.44	7 /2 >		+	0.56	5 /2 >
	+	0.31	13 /2 >		+	0.59	11 /2 >

$Er_2Ti_{1.5}Sn_{0.5}O_7$

|1+>	=	0.72	-11 /2 >	|1->	=	0.25	-13 /2 >
	+	-0.53	-5 /2 >		+	-0.35	-7 /2 >
	+	0.10	1 /2 >		+	0.10	-1 /2 >
	+	0.35	7 /2 >		+	0.53	5 /2 >
	+	0.25	13 /2 >		+	0.72	11 /2 >

$Er_2Ti_1Sn_1O_7$

|1+>	=	0.74	-11 /2 >	|1->	=	-0.22	-13 /2 >
	+	-0.53	-5 /2 >		+	0.33	-7 /2 >
	+	0.08	1 /2 >		+	-0.08	-1 /2 >
	+	0.33	7 /2 >		+	-0.53	5 /2 >
	+	0.22	13 /2 >		+	-0.74	11 /2 >

$Er_2Ti_{0.5}Sn_{1.5}O_7$

|1+>	=	0.76	-11 /2 >	|1->	=	0.21	-13 /2 >
	+	-0.52	-5 /2 >		+	-0.32	-7 /2 >
	+	0.06	1 /2 >		+	0.06	-1 /2 >
	+	0.32	7 /2 >		+	0.52	5 /2 >
	+	0.21	13 /2 >		+	0.76	11 /2 >

$Er_2Sn_2O_7$

|1+>	=	0.80	-11 /2 >	|1->	=	0.17	-13 /2 >
	+	-0.50	-5 /2 >		+	-0.28	-7 /2 >
	+	0.01	1 /2 >		+	0.01	-1 /2 >
	+	0.28	7 /2 >		+	0.50	5 /2 >
	+	0.17	13 /2 >		+	0.80	11 /2 >

$Er_2Ti_2O_7$ (Hodges' [14] data with 3-fold axis chosen as the quantization axis)

|1+>	=	-0.543	-11 /2 >	|1->	=	-0.426	-13 /2 >
	+	-0.238	-5 /2 >		+	-0.388	-7 /2 >
	+	0.5628	1 /2 >		+	0.5628	-1 /2 >
	+	0.3876	7 /2 >		+	0.2384	5 /2 >
	+	0.426	13 /2 >		+	0.5428	11 /2 >

Table 7.10: Ground state Kramers doublet wavefunctions for $Er_2Ti_{2-x}Sn_xO_7$ ($x = 0 \sim 2$) listed in the converted format following Hodges's choice of c-axis (the $\langle 111 \rangle$ 3-fold axes are chosen as the quantization axis) .

As an additional work, the *g*-matrices and the corresponding magnetic moments are calculated for the Er^{3+} in $Er_2Ti_2O_7$ from Hodges' wavefunctions [14], for the Ho^{3+} in $Ho_2Ti_2O_7$ from Rosenkrantz's B_k^q [13] and for Dy^{3+} in $Dy_2Ti_2O_7$ from the converted B_n^m given in section 7.3.2.

$$\hat{g}(Er_2Ti_2O_7)_{Hodges} = \begin{pmatrix} 3.18 & 0 & 0 \\ 0 & -3.18 & 0 \\ 0 & 0 & 0.1 \end{pmatrix} \quad (7.39)$$

$$\mu(Er_2Ti_2O_7)_{Hodges} = (3.81, 3.81, 0.12); \quad |\mu| = 5.39\ \mu_B \quad (7.40)$$

$$\hat{g}(Ho_2Ti_2O_7)_{Rosenkrantz} = \begin{pmatrix} 0 & 0 & 0 \\ 0 & 0 & 0 \\ 0 & 0 & 7.82 \end{pmatrix} \quad (7.41)$$

$$\mu(Ho_2Ti_2O_7)_{Rosenkrantz} = (0, 0, 9.38); \quad |\mu| = 9.38\ \mu_B \quad (7.42)$$

$$\hat{g}(Dy_2Ti_2O_7) = \begin{pmatrix} 0 & 0 & 0 \\ 0 & 0 & 0 \\ -0.01 & 0 & -7.40 \end{pmatrix} \quad (7.43)$$

$$\mu(Dy_2Ti_2O_7) = (0, 0, 8.88); \quad |\mu| = 8.88\ \mu_B \quad (7.44)$$

These show that almost the entire moment in Ho^{3+} and in Dy^{3+} lie parallel to the $\langle 111 \rangle$ axis. This is a confirmation of the Ising nature of the two ions in the $Ln_2Ti_2O_7$ (Ln = Ho, Dy) CEF. The agreement of our calculations to the previously reported results [10, 13-14] in each case is excellent, confirming again the validity of our calculations.

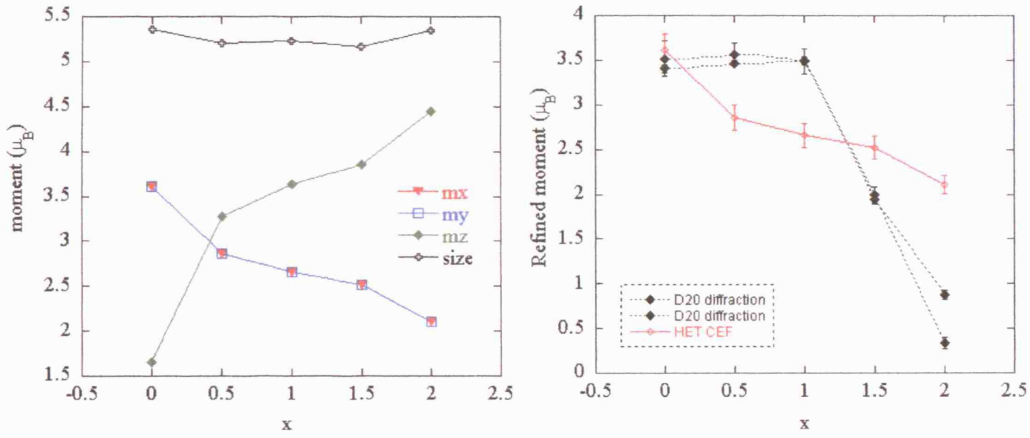

Figure 7.19- (Left): The variation in single ion moment anisotropies, μ_x, μ_y, μ_z, and moment size with composition x of $Er_2Ti_{2-x}Sn_xO_7$. μ_x and μ_y correspond to the components of the moment perpendicular to the ⟨111⟩ axis (the chosen c-axis in the CEF interpretation) and μ_z is the moment parallel to ⟨111⟩. While the moment size remains constant, the system gradually changes its single ion anisotropy from being XY-like in $Er_2Ti_2O_7$ into Ising-like in $Er_2Sn_2O_7$. The crossover in nature of anisotropy takes over around $x = 0.5$.

Figure 7.20- (Right): The comparison of the ordered moment in the ⟨111⟩-plane detected in the diffraction experiment (*black markers*) against the maximum orderable moment component in the ⟨111⟩-plane determined by the crystal field measurement (*red markers*). The actual ordered moment detected agrees well with the maximum orderable moment size for $Er_2Ti_2O_7$ (both ~ 3.5 μ_B) since $T_{measured} << T_N$. However, the order observed in $Er_2Sn_2O_7$ is much smaller (0.5 ~ 1 μ_B) than the maximum possible order allowed by its crystal field (~ 2.25 μ_B). This is possibly because the ordering was incomplete at the temperature where the diffraction experiment was carried out; the ordering temperature, T_N, $Er_2Sn_2O_7$ of is ~ 0.08 K, thus, $T_{measured} \sim T_N$.

7.4 Conclusions

In this chapter the crystal electric field (CEF) of the $Er_2Ti_{2-x}Sn_xO_7$ series (x = 0, 0.5, 1, 1.5, 2) was analyzed using the interactive CEF parameter fitting program FOCUS [1]. The CEF is treated by the Stevens' operator method [1, 3, 5-8]; in which the crystal field, which is the crystalline potential summed over magnetic electrons, is represented by simple operators involving only $\hat{J}^2, \hat{J}_x, \hat{J}_y, \hat{J}_z$ and $\hat{J}_\pm$ – see Appendix A2 for the follow up of the theory. Taking the Ho^{3+} ground state wavefunctions in $Ho_2Ti_2O_7$ [13] as a starting point, we deduced a set of CEF parameters B_n^m suitable for the corresponding Er^{3+} ion and used it to fit the energy spectra of the $Er_2Ti_{2-x}Sn_xO_7$ series. From the refined CEF parameters and ground state wavefunctions, the magnetic moments of the Er^{3+} ion in the CEF were calculated for all compounds.

This work revealed the linear variation in CEF parameters (B_n^ms) with composition x of $Er_2Ti_{2-x}Sn_xO_7$, hence proving that the CEF does not abruptly change between compounds. These linearity in variation is best seen in the plots Fig.7.17 and Fig.7.18. Another important information obtained is that the single ion moment of Er^{3+} has a constant magnitude (size) of ~ 5 μ_B for all x (Fig.7.19). This answers the question, 'is the single ion moment size changing due to the different CEF environments for different x ?'. The answer is 'no' and thus the change in single ion moment size is eliminated from the list of the possible origin in the decrease in ordered moment size detected in the diffraction experiment (Chapter 5). In this sense, one can conclude that the vanishing order with x is *not* a single ion effect.

However, if one focuses on the actual detail of the anisotropy (or the 'spatial symmetry') of the single ion moment, this gives a rather different interpretation. Referring to Fig7.19, one can follow the variation in the moment component (along and perpendicular to $\langle 111 \rangle$) variation with x. The system changes its single ion anisotropy from being XY-like in $Er_2Ti_2O_7$ into Ising-like in $Er_2Sn_2O_7$. The crossover in nature of anisotropy takes over around x = 0.5 and this coincides with the approximate composition in which the sudden drop in the ordered moment was observed, x ~ 1 (see Fig.7.20). If the single ion anisotropy of $Er_2Sn_2O_7$ is more Ising-like (i.e. moments

lying parallel to ⟨111⟩), then the system will be better described to be a pyrochlore ⟨111⟩-Ising AFM. However, a pyrochlore AFM with an Ising anisotropy along ⟨111⟩ is known to have a unique (hence ordered) ground state; the FeF_3 state (see section 2.3.4.1). Thus the connection of this Ising nature of the anisotropy in $Er_2Sn_2O_7$ with the Palmer-Chalker ordering established in Chapter 5 is unclear and has no straightforward explanation at present.

References for Chapter 7

[1] P.Fabi, *FOCUS Manual*, ISIS Science Division, Rutherford Appleton Laboratory, ISSN 1358-6254 (1995).

[2] http://www.isis.rl.ac.uk/excitations/het/.

[3] M.T.Hutchings, Solid State Phys.**16**, 227 (1964).

[4] B.G.Wybourne, *Spectroscopic Properties of Rare Earths*, Chap. 6, Interscience Publishers, New York (1965).

[5] K.W.Stevens, Proc. Phys. Soc. **A65**, 209 (1952).

[6] R.J.Elliott and K.W.H.Stevens, Proc. Roy. Soc. A **218**, 553 (1953).

[7] R.J.Elliott and K.W.H.Stevens, Proc. Roy. Soc. A **219**, 387 (1953).

[8] B.R.Judd, Proc. Roy. Soc. A **227**, 552 (1955).

[9] A.J.Freeman and J.P.Desclaux, J. Magn. Magn. Mater. **12**, 11 (1979).

[10] Y. Qiu, *PhD thesis*, Johns Hopkins University, Baltimore, Maryland (2002).

[11] C.W.Nielson and G.F.Koster, *Spectroscopic Coefficients for p^n, d^n and f^n Configurations*, MIT Press, Cambridge, Mass. (1964).

[12] Rotenberg, Bivins, Metropolis, and Wooten, *The 3-j and6-j symbols*, MIT Press, Cambridge, Mass. (1959).

[13] S.Rosenkrantz, A.P.Ramirez, A.Hayashi, R.J.Cava, R.Siddharthan and B.S.Shastry, J. Appl. Phys. **87**, 5914 (2000).

[14] J.D.M.Champion, M.J.Harris, P.C.W.Holdsworth, A.S.Wills, G.Balakrishnan, S.T Bramwell, E.Čižmár, T.Fennell, J.S.Gardner, L.Lago, D.F.McMorrow, M.Orendàč, A.Orendàčovà, D.McK.Paul, R.I.Smith, M.T.F.Telling, and A.Wildes, *Phys. Rev. B* **68**, 020401(R) (2003).

[15] S.T.Bramwell, M.N.Field, M.J.Harris, and I.P.Parkin, J. Phys.:Condens.Mat.**12**, 483 (2000).

[16] H.W.J.Blöte, R.F.Weilinga, and H.Huiskamp, Physica **43**, 549 (1969).

[17] A.Abragham and B.Bleaney, *Electron Paramagnetic Resonance of Transition Metal ions*, Clarendon, Oxford, p.650-651, (1970).

[18] M.J. Harris, S.T. Bramwell, T. Zeiske, D.F. McMorrow and P.J.C. King, J. Magn. Magn. Mater **177**, 757 (1998).

Chapter 8

Neutron Diffraction work on $Gd_2Ti_2O_7$ in Applied Fields

8.1 Introduction

In $Gd_2Ti_2O_7$, Gd^{3+} ions are in a state with $S = 7/2$ and $L = 0$, and the spins are coupled antiferromagnetically. This makes $Gd_2Ti_2O_7$ unique in terms of negligible single-ion anisotropy, and makes it an ideal model for Heisenberg antiferromagnet. The interest in low temperature properties, particularly the magnetic properties, of the geometrically frustrated pyrochlore oxide $Gd_2Ti_2O_7$ has blossomed over the past decade, and this is reviewed in section 2.5.

In this chapter we present the result of neutron diffraction of a powder $Gd_2Ti_2O_7$ with applied fields up to 5 Tesla. The aim of this work was to investigate into the different ordered phases of $Gd_2Ti_2O_7$ present in its previously reported field-temperature phase diagram [1-2]. Our neutron diffraction data confirm the main phase transitions previously reported by Ramirez *et al.*[1] in their specific heat and magnetization measurements. Our experimental set up was chosen so that the applied the magnetic field is perpendicular to the scattering vector, $\mathbf{H} \perp \mathbf{Q}$. The integrated intensity variation of the individual scattering vector, $I_{\langle hkl \rangle}$, in applied fields, was also compared with the corresponding single crystal phase diagram [2] (i.e. $\mathbf{Q}_{Powder} \perp \mathbf{H}_{SingleCrystal}$).

8.2 Experimental Method

Natural Gd is known to be unsuited for neutron experiments due to the high absorption cross section of ^{155}Gd and ^{157}Gd. Therefore, isotopically enriched polycrystalline sample of $^{160}Gd_2Ti_2O_7$ (~ 500 mg) described in Ref.[3] was used in this experiment.

Powder neutron diffraction data were collected using the D20 high-flux 2-axes diffractometer at the ILL reactor source neutron facility, Grenoble, using an incident wave length of 2.4 Å. The sample was contained in a vanadium can with ^4He exchange gas and mounted in a dilution refrigerator.

The experiment was set up so that the magnetic field, **H**, was applied always perpendicularly to the scattering plane, hence to the detected scattering vector, **Q** (see Fig.8.1). Data were collected for 40 hours in the temperature range 0.6 to 1.2 K in a magnetic field of up to 5 Tesla.

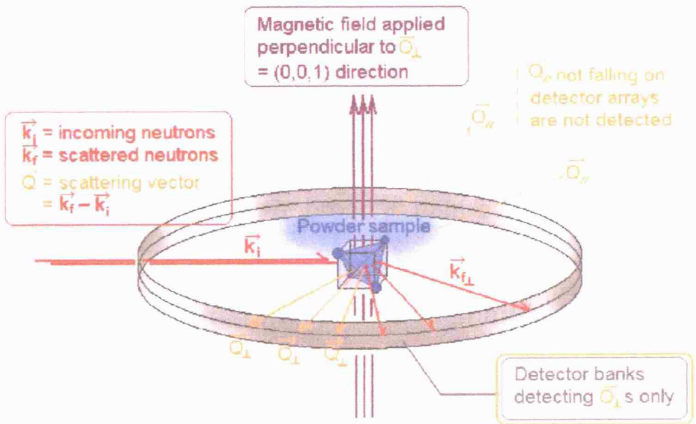

Figure 8.1: Experimental set up of D20 instrument. The experiment was set up so that the magnetic field was always applied perpendicularly to the detected scattering vector **Q**.

8.3 Results

8.3.1 Peak indexing

The magnetic peaks were first indexed. This revealed two categories of peaks; (i) peaks that can be indexed with a magnetic propagation vector of **k** = 000 (integer values of *h*, *k*, *l* – the ferromagnetic (FM) peaks), and (ii) peaks indexed with **k** = ½½½ (half integer values of *h*, *k*, *l* – the antiferromagnetic (AFM) peaks). This is shown in Fig.8.2 as the indexed diffraction pattern obtained at $T = 0.9$ K with applied fields of $H = 0 \sim 5$ T.

8.3.2 Peak intensity variation

All the peak intensities were integrated after subtracting the diffuse background. The peak intensity variation with field and temperature are plotted in Fig.8.3 and Fig.8.4 below. The **k** = ½½½ and **k** = 000 peaks are plotted in different graphs to see the effect of the AFM and FM component variance, respectively. The temperature dependence of the ferromagnetic peaks (**k** = 000) at $H = 1$ T and $H = 4$ T are expanded and plotted separately in Fig.8.5.

Phase transitions can be seen on all the plots. Although some of the transitions are clear (with intensities falling to zero), some are not as well defined as the others; for instance, the transitions defined by $Q_{hkl} = \langle {}^1/_2\ {}^1/_2\ {}^3/_2 \rangle$ intensity variation at both temperatures around 2 ~ 2.5 Tesla, are broad in nature and they do not completely fall to zero. Hence, it can be speculated that these ill-defined phase transitions are a result of superposition of multiple phases that go through different phase transitions, each arising from different crystallites in the sample.

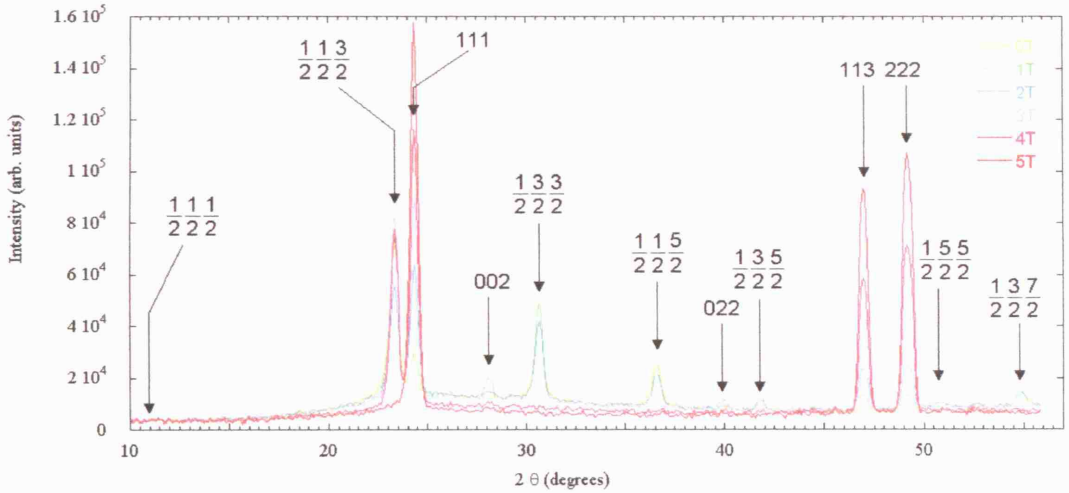

Figure 8.2: Magnetic diffraction pattern of $Gd_2Ti_2O_7$ at T = 0.9 K showing the coexistence of **k** = 000 and **k** = ½½½ peaks at the applied fields of 0 ~ 5 Tesla.

h	*k*	*l*	*d*/ Å	2θ/degrees
1/2	1/2	1/2	11.55	11.93
1/2	1/2	3/2	6.03	22.96
1	1	1	5.77	23.99
0	0	2	5.00	27.77
1/2	3/2	3/2	4.59	30.32
1/2	1/2	5/2	3.85	36.33
3/2	3/2	3/2	3.85	36.33
0	2	2	3.54	39.68
1/2	3/2	5/2	3.38	41.58
3/2	3/2	5/2	3.05	46.34
1	1	3	3.02	46.91
2	2	2	2.89	49.13
1/2	1/2	7/2	2.80	50.74
1/2	5/2	5/2	2.80	50.74
1/2	3/2	7/2	2.60	54.89
3/2	5/2	5/2	2.60	54.89
0	0	4	2.50	57.37
3/2	3/2	7/2	2.44	58.83

Table 8.1: List of reflections for $Gd_2Ti_2O_7$ (a = 10 Å) with both **k** = 000 and **k** = ½½½. The reflections (002) and (022) highlighted in red are systematic absent peaks which give zero intensity in zero field.

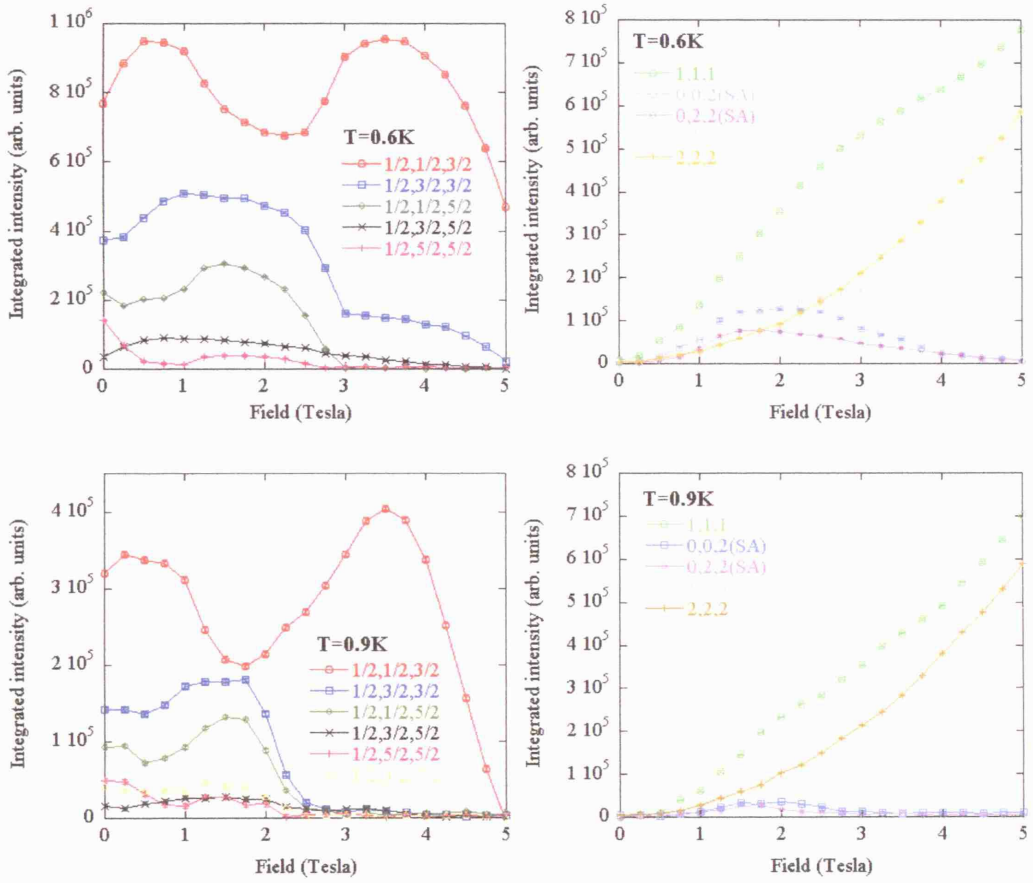

Figure 8.3: **k** = ½½½ and **k** = 000 integrated peak intensity variation with field at T = 0.6 K (*Top*) and 0.9 K (*Bottom*). Peaks ⟨002⟩ and ⟨022⟩ are the systematic absence peaks that give zero intensities in zero field. While the FM (**k** = 000 peaks) are present in all phases (except, of course, at H = 0), the systematic absence peaks are only present for $0 < H < 5$ T (at 0.6 K) and $0 < H < 3$T (at 0.9 K).

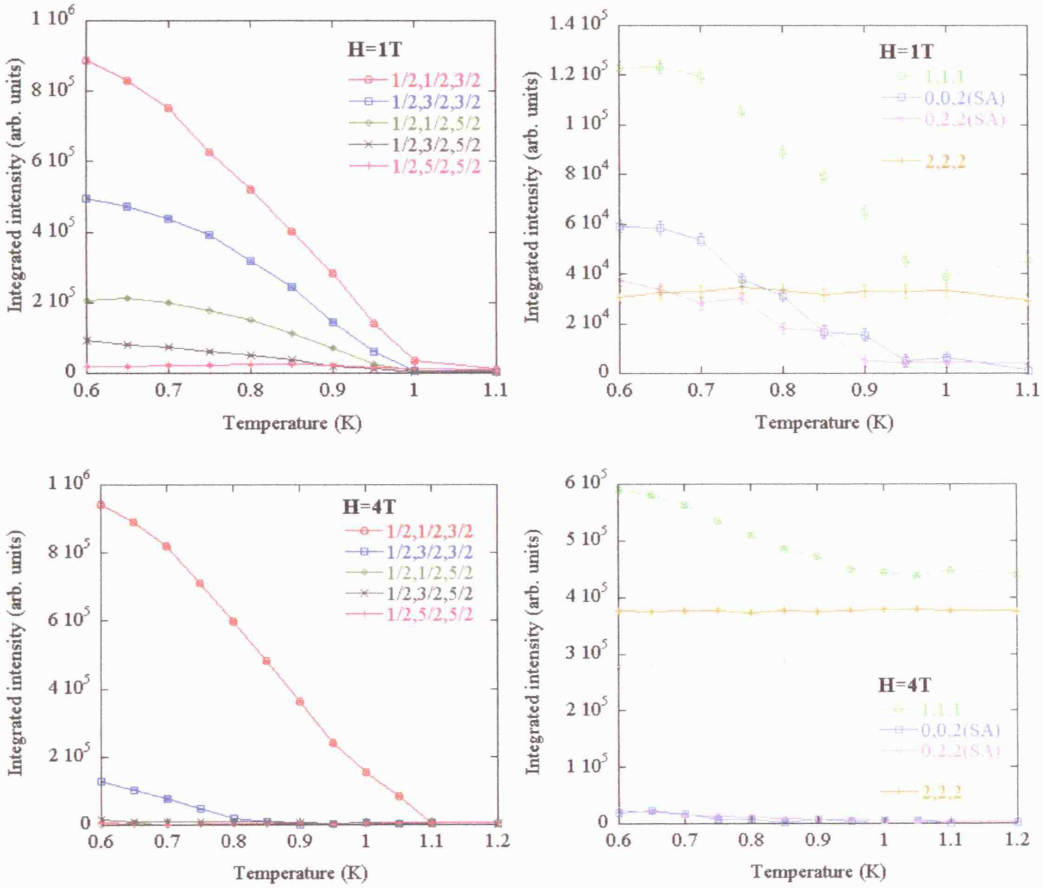

Figure 8.4: **k** = ½½½ and **k** = 000 integrated peak intensity variation with temperature in applied fields of H = 1T (*Top*) and 4T (*Bottom*). Peaks ⟨0 0 2⟩ and ⟨0 2 2⟩ are systematic absence peaks that give zero intensities in zero field.

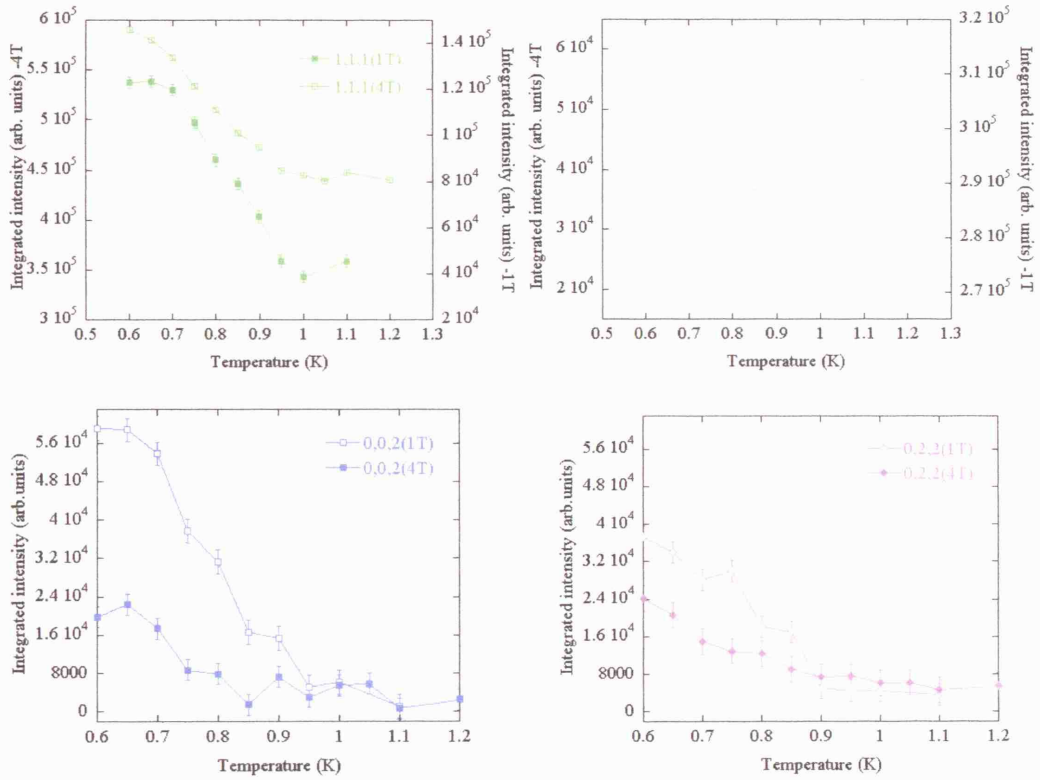

Figure 8.5: **k** = 000 (FM) integrated peak intensity variation with temperature in applied fields of H = 1 T and 4 T. Peaks ⟨002⟩ and ⟨022⟩ are systematic absence peaks that give zero intensities in zero field. While the FM (**k** = 000 peaks) are present in all phases (except, of course, at H = 0), the systematic absence peaks are only present for $T < 0.9$ K (at 1 T) and $T < 0.85$ K (at 4 T). Another unusual feature is the ⟨1 1 3⟩ peak variation; at H = 1 T the intensity decrease with temperature while at H = 4 T the peak grows in intensity with temperature.

8.3.3 Comparison of powder neutron diffraction data v.s. phase diagram based on powder bulk measurements

First we compared the phase transitions observed in our peak intensity variation plots with the field-temperature phase diagram constructed upon susceptibility and heat capacity measurements of the powder $Gd_2Ti_2O_7$ by Ramirez *et al.*[1]. This is shown in Table 8.2.

Because there is every possible orientation of the crystallites present in a powder sample, the application of a field to a powder sample means that the field is applied to 'all' directions with respect to the crystal axes. The measured quantity is hence an average quantity arising from these different crystallites with field applied to different directions. In our experimental set up, we chose particular sets of field directions; that is, fields perpendicular to **Q**. Consequently, the peak intensity of a particular Q reflection is a sum of intensities arising from different crystallites with field applied to different directions but now all perpendicular to **Q**.

The agreement of the phase transitions observed in the two sets of data (Table 8.2) is good enough to state that the set of field directions associated with Q chosen in the neutron experiment set up are enough to represent almost 'all' the directions in the bulk measurements.

The first observation made about the four distinct phases present in the $Gd_2Ti_2O_7$ phase diagram was that the number of **k** = ½½½ peaks observed that varies from phase to phase. This is shown in Fig.8.6. The first transition line you cross when increasing the temperature in the 0 – 2.5 Tesla region (between phase B and A in Fig.8.6) is a rather weak transition (this was also pointed out by Petrenko *et al.*[2]). The nature of this transition at zero field was attributed to the ordering of the subset of spins (these are the interstitial spins that lay between the kagomé layers) that is disordered in the region 1 K > T > 0.7 K [3-4]. This weak transition was not apparent in our result since it is only associated with a very small relative peak intensity change, and the two phases above and below this transition line share the same sets of Q peaks (Fig.8.6) except for the very weak $Q_{hkl} = \langle {}^1/_2\ {}^1/_2\ {}^1/_2 \rangle$ reflection that is only

present when the interstitial spins are ordered [4]. However, because $Q_{hkl} = \langle {}^1/_2\ {}^1/_2\ {}^1/_2 \rangle$ has very small intensity compared to the other peaks it was not resolved in our experiment.

The most remarkable point of Fig.8.6 is that the high temperature-high field phase (phase D) only consists of $Q_{hkl} = \langle {}^1/_2\ {}^1/_2\ {}^3/_2 \rangle$ peaks, apart from some negligible contributions from other peaks. This was thought to be the key fact in order to solve the nature of the phase D and attempts to derive structure factors that kill all other Q intensities but $Q_{hkl} = \langle {}^1/_2\ {}^1/_2\ {}^3/_2 \rangle$ were made. This is discussed further in the next section.

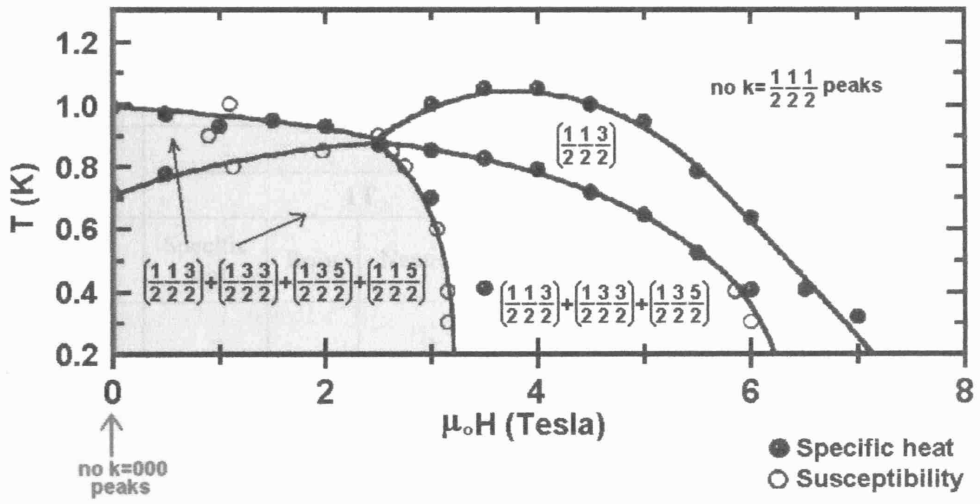

Figure 8.6: Ramirez's phase diagram [1] with the **k** = ½½½ (AFM) peak labels detected in our neutron scattering measurement. As for the **k** = 000 (FM) peaks, they are present in all phases (except at $H = 0$ where there is none of them) – apart from the systematic absence peaks, $\langle 0\,0\,2 \rangle$ and $\langle 0\,2\,2 \rangle$, that seem to be present only for phases A – C (and possibly D), not in the paramagnetic phase E.

	Observed phase transitions							
	0.6K				0.9K			
Scattering vector Q	Specific heat	Error	Neutron	Error	Specific heat	Error	Neutron	Error
$\langle 1/2\ 1/2\ 3/2\rangle$	3.05 T 5.2 T 6.1 T	0.1 0.1 0.1	>5 T? 2.5 T	- 0.25	0.9 T-2.5 T 5.1 T	0.1 0.1	1.75 T 5 T	0.25 0.125
$\langle 1/2\ 3/2\ 3/2\rangle$			3 T 5 T	0.125 0.125			2.5 T	0.125
$\langle 1/2\ 3/2\ 5/2\rangle$			5 T	0.125			2.75 T 4 T	0.125 0.125
$\langle 1/2\ 1/2\ 5/2\rangle$			1?	0.25			0.5?	0.25
$\langle 1\ 1\ 1\rangle$			3?	0.25			2.5?	0.25
$\langle 1\ 1\ 3\rangle$			3?	0.25				
$\langle 0\ 0\ 2\rangle$			2?	0.25			3?	0.25
$\langle 0\ 2\ 2\rangle$			1.5?	0.25			3?	0.25
	Observed phase transitions							
	1T				4T			
Scattering vector **Q**	Specific heat	Error	Neutron	Error	Specific heat	Error	Neutron	Error
$\langle 1/2\ 1/2\ 3/2\rangle$	0.82K 0.98K	0.05 0.05	1K	0.25	0.8 K 1.04 K	0.05 0.05	0.95K 1.1K	0.25 0.25
$\langle 1/2\ 3/2\ 3/2\rangle$			1K	0.25			0.8K	0.25
$\langle 1/2\ 3/2\ 5/2\rangle$			1K	0.25			0.95K	0.25
$\langle 1/2\ 1/2\ 5/2\rangle$			1K	0.25			-	-
$\langle 1\ 1\ 1\rangle$			1K	0.25			0.95K	0.25
$\langle 1\ 1\ 3\rangle$			0.5K 1K	0.25				
$\langle 0\ 0\ 2\rangle$			0.95K	0.25			0.85K	0.25
$\langle 0\ 2\ 2\rangle$			0.9K	0.25			0.9K	0.25

Table 8.2: Comparison of the observed phase transitions in powder neutron diffraction and in phase diagram based on susceptibility / heat capacity measurements by Ramirez *et al.* [1]. The agreement is good.

8.3.4 Fitting against calculated intensities

The next step of the result analysis was to try calculating the theoretical magnetic Bragg peak intensities and compare with the actual data. There are several available programs that calculates magnetic intensities (such as GSAS [5] and FullProf [6]) but these programs can only calculate magnetic intensities for *a particular* magnetic structure and is not designed to simulate the intensity of the polycrystal (powder) with applied magnetic field on it. When a magnetic field is applied to a powder sample, as it is in our case, one needs to think of some manipulations to the intensity calculation that should be made. For example, for a zero-field magnetic structure calculation, only one set of Q-reflections associated with one ordering vector **k** is calculated. In our case we need at least two sets of Q-reflections; associated with the **k** = ½½½ and **k** = 000 ordering vectors simultaneously. These manipulations were incorporated in our own program written. Another advantage of our program is that, it can calculate the magnetic intensity with a given spin component perpendicular to **Q** (i.e. $\mathbf{q}_{nj}$), and there is no need to give a specific magnetic structure (i.e. $\mathbf{S}_j$ does not have to be given).

A program was written (in fortran 90) so that it calculates the magnetic intensities from a given set of (i) atom coordinates (x_j, y_j, z_j), (ii) spin orientation of spin j (S_x^j, S_y^j, S_z^j), (iii) spin length of spin j (l_j) and (iv) Q_{hkl}-reflections. All these factors (i)~(iv) are the input variables and hence could be varied separately and/or simultaneously in order to see the effect on the intensity. A *hkl*-list which contained all possible permutations of the Q_{hkl}-reflections that correspond to the **k** = ½½½ and **k** = 000 structure was used (such as $\mathbf{Q}_{\langle 111\rangle}$ = [111], [-111], [-1-11]..., $\mathbf{Q}_{\langle 1/2\ 1/2\ 1/2\rangle}$ = [½ ½ ½], [-½ ½ ½], [-½ -½ ½].....).

8.3.4.1 Backbone of the program

Here we briefly list down the main equations that were used in constructing the program. The magnetic scattering intensity of a particular reflection Q_{hkl} was calculated using

$$I_{mag}(\mathbf{Q}) = K\,L\,W\,\mathbf{F}_{mag}(\mathbf{Q})\,\mathbf{F}_{mag}(\mathbf{Q})^* \qquad (8.3.4\text{-}1)$$

where L is the Lorenz factor = $cos\theta/(sin2\theta)^2$, K is an appropriate scale factor, W is the thermal factor and $\mathbf{F}_{mag}(\mathbf{Q})$ is the magnetic structure factor;

$$\mathbf{F}_{mag}(n,j) = \Sigma_j\, p_{nj}\quad \mathbf{q}_{nj}\, exp\ 2\pi i\ (\mathbf{Q}_n \,.\, \mathbf{r}_j) \qquad (8.3.4\text{-}2)$$

$$\mathbf{q}_{nj} = \frac{\mathbf{Q}_n}{|\mathbf{Q}_n|}\left(\frac{\mathbf{Q}_n}{|\mathbf{Q}_n|}\cdot\frac{\mathbf{S}_j}{|\mathbf{S}_j|}\right) - \frac{\mathbf{S}_j}{|\mathbf{S}_j|} \qquad (8.3.4\text{-}3)$$

where $n = \langle h\,k\,l\rangle$ label and j = magnetic atom.

($\mathbf{q}$ is called the interaction vector which is the perpendicular component of the scatterer spin $\mathbf{S}$ in question to the scattering vector, $\mathbf{Q}$). The followings are some reminder of the common definitions;

$$\mathbf{Q} = \mathbf{k}_i - \mathbf{k}_f \qquad (\mathbf{k}_i/\,\mathbf{k}_i = \text{incident/final neutron wave vector}) \qquad (8.3.4\text{-}4)$$

$$\mathbf{r}_j = (x_j, y_j, z_j) \qquad (\text{position of } j\text{-}th \text{ atom from the origin}) \qquad (8.3.4\text{-}5)$$

$$p_{nj} = (e^2\gamma / m_e c^2)\, g_j J_j\ f_{nj} \qquad (8.3.4\text{-}6)$$

$$g = 1 + \frac{J(J+1) + S(S+1) - L(L+1)}{2J(J+1)} \quad (g = \text{Landé splitting factor}) \qquad (8.3.4\text{-}7)$$

$$f_{nj} = \langle j_0(k_n)\rangle_j + \Sigma_m \langle j_m(k_n)\rangle_j \quad (f_{nj} = \text{magnetic form factor of atom } j) \qquad (8.3.4\text{-}8)$$

$$\langle j_0(k_n)\rangle_j = A_j\, exp(-a_j\, k_n^2) + B_j\, exp(-b_j\, k_n^2) + C_j\, exp(-c_j\, k_n^2) + D_j \qquad (8.3.4\text{-}9)$$

$$\langle j_m(k_n)\rangle_j = A_j(j_m)\, k_n^2\, exp(-a_j(j_m)\, k_n^2) + B_j(j_m)\, k_n^2\, exp(-b_j(j_m)\, k_n^2) + C_j(j_m)\, k_n^2 exp(-c_j(j_m)\, k_n^2) + D_j(j_m)\, k_n^2 \qquad (8.3.4\text{-}10)$$

$$m = 2,4,6,8$$

where $k_n = sin\ \theta_n/\lambda$ and A, a, B, b, C, c and D are tabulated form factor constants determined experimentally [7-10]. The magnetic form factor coefficients $\langle j_0\rangle$ for Gd^{3+} are; A = 0.0186, a = 25.3870, B = 0.2895, b = 11.1420, C = 0.7135, c = 3.7520, D = -0.0217 and e = 0.0488 [7].

8.3.4.2 Multiplicity of reflection $\langle h\ k\ l \rangle$

Once the magnetic intensity for a particular Q_n (i.e. for a particular set of $h\ k\ l$) is calculated, all its permutations should be considered in order to simulate the intensity of a overall magnetic peak. This is

$$\begin{aligned} I_{mag}\langle h\ k\ l\rangle^{\text{overall}} = {} & I_{mag}[h\ k\ l] + I_{mag}[-h\ -k\ -l] + I_{mag}[-h\ k\ l] \\ & + I_{mag}[h\ -k\ -l]\cdots\cdots\text{all permutations.} \\ & = m(\mathbf{Q})\, I_{mag}[h\ k\ l] \end{aligned} \qquad (8.3.4\text{-}11)$$

where $m(\mathbf{Q})$ is the multiplicity of the reflection $\mathbf{Q}$. For example $m(Q_{\langle 111\rangle}) = 8$ as $\langle 111\rangle = [111] + [-1\ 1\ 1] + [1\ -1\ 1] + [1\ 1\ -1] + [-1\ -1\ 1] + [-1\ 1\ -1] + [1\ -1\ -1] + [-1\ -1\ -1]$.

One point that should be noted at this stage is that not all permutations for a particular reflection is allowed when $\mathbf{k} = ½½½$ is employed. This arises as follows; a magnetic Bragg peak appears at the Brillouin zone centre $\mathbf{Q}_{FCC} = \langle h\ k\ l\rangle$ with the restriction h, k, l being all even or odd integers (face-centered cubic selection rule) if $\mathbf{k} = 000$ (see Fig.8.7). When the magnetic structure is described by more than one $\mathbf{k}$, additional peaks occur around the zone centres. In our case, for $\mathbf{k} = ½½½$ therefore, new reflections should be observed at the points $\mathbf{Q}_{FCC} \pm \mathbf{k}$ (i.e. h+½, k+½, l+½, where h, k, and l being integers all even or all odd). For example, the particular reflection with $\mathbf{Q} = [^1/_2\ ^1/_2\ ^3/_2]$ cannot be detected because it is not possible to be derived from the $\mathbf{Q}_{FCC} \pm \mathbf{k}$, whereas $\mathbf{Q} = [^1/_2\ ^1/_2\ -^3/_2]$ can (by $[1\ 1\ -1] - [½,½,½]$).

This condition is important when simulating the intensity for a particular peak and this was always taken into account when calculations of the intensities were done. However, in the rest of this work the signs of the indices are omitted and the possible permutation of $\mathbf{Q} = [^1/_2\ ^1/_2\ -^3/_2]$ is written as $Q = \langle ^1/_2\ ^1/_2\ ^3/_2\rangle$. However, one point to bare in mind is that this condition only takes effect for the intensity calculation of the 1-k structure and hence may differ if the structure is a 4-k structure [4].

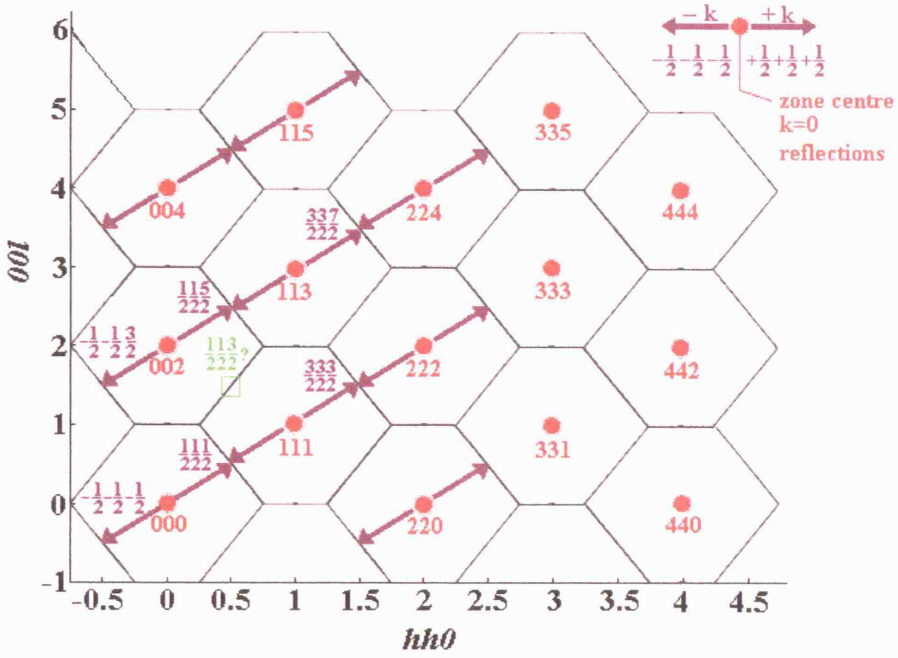

Figure 8.7: A reciprocal lattice in the *hhl* plane for the face-centered cubic (FCC) $Gd_2Ti_2O_7$. The Brillouin zone centres are marked in red circles which in turn corresponds to **k** = 000 Bragg reflections (the lattice is drawn according to the reflection rules for FCC structure). The arrows originating from these zone centres represent the **k** = ½½½ vectors (for the 1-*k* magnetic structure). **Q**(**k**=000) ± **k**(½½½) results in satellite peaks around each zone centre. However, it is shown that the permutation [$-^1/_2$ $-^1/_2$ $^3/_2$] can be represented by this propagation vector addition /subtraction but [$^1/_2$ $^1/_2$ $^3/_2$] cannot. Hence, when calculating the peak intensity for Q = ⟨$^1/_2$ $^1/_2$ $^3/_2$⟩ one should only include contributions from **Q** = [$-^1/_2$ $-^1/_2$ $^3/_2$] and not from **Q** = [$^1/_2$ $^1/_2$ $^3/_2$].

8.3.4.3 Tested magnetic models

Firstly, the magnetic diffraction pattern for $Gd_2Ti_2O_7$ was calculated using two models;

(i) with **k** = ½½½ structure as it is in zero field, and

(ii) with the spins ferromagnetically aligned (**k**=000) for field above saturation field.

These predicted intensities were fitted against the integrated intensities. Good agreement were obtained for the fits of model (i) to the (0.9 K, 0 T) data and of model (ii) to the (1.2 K, 5 T) data. These are plotted in Fig.8.8 (*Top*). This confirms that all the calculation process described above so far is correct and the validity of the program is proved at least for the single magnetic structure cases (either **k** = ½½½ or **k** = 000).

It is seen from the intensity variation plots (Fig.8.3, 8.4 and 8.5) that there are several phase transitions both with the field and with temperature sweeping. After succeeding in fitting the zero field and high field phases, the next task was to fit the intermediate phases ($T < 0.9$ K, $H < 5$ T). For example, investigations into structure factors that kill and leave a particular Q peak intensity were made. These include attempts;

(iii) to find a spin configuration that gives the experimentally determined ratio; $I_{002} \sim 2 \times I_{022}$ (for phase B in $H > 0$; Fig.8.6), and

(iv) to find a spin configuration that gives $I_{1/23/23/2} = 0$, $I_{1/21/25/2} = 0$ and $I_{1/21/23/2} \neq 0$, simultaneously (for phase D; Fig.8.6).

However, despite of a large number of trial with different spin orientations and/or spin lengths (also, attempts were made to vary the interaction vectors, **q**, instead of varying **S**), it was eventually noted that the intermediate phases cannot be modelled using a single field direction with respect to the crystal axis. This is because the phase diagram of a powder sample is a result of a superposition of multiple single crystal phase diagrams with field applied in different directions. This is what lies in the heart of the powder averaging problem. In a powder crystallites can exist in every possible orientation and taking a particular Q peak, its net integrated intensity is an average of

intensities arising from crystallites having field applied to all possible directions perpendicular to **Q**. In other words crystal rotation around **Q** is allowed.

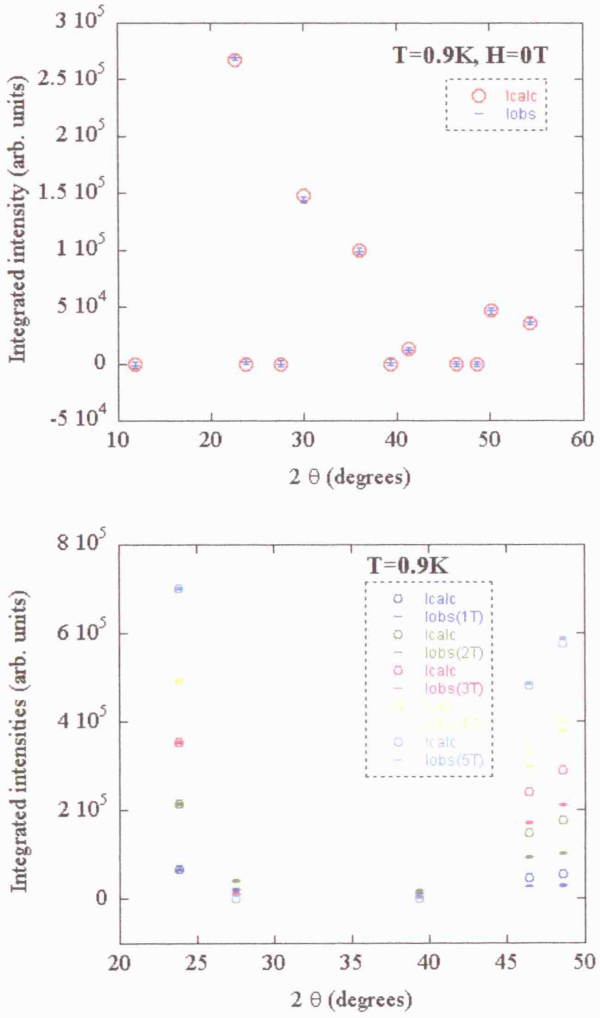

Figure 8.8: Calculated v.s. observed magnetic intensities at 0.9 K (< T_N) in zero field (*Top*) and at in H = 1 to 5 Tesla (*Bottom*). The calculated intensities of the top pattern correspond to the pure **k** = ½½½ ordering and the calculated intensities of the bottom pattern correspond to all spins aligned ferromagnetically (which have their **q**s parallel to the applied field). For the bottom fitting, it is seen that the FM-model works best at low field and high field but deviates significantly for the intermediate fields.

8.3.4.4 Powder averaging problem and its removal

The powder averaging problem is represented as;

$$\langle \langle \langle I(\mathbf{Q}) \rangle_{\text{thermal average}} \rangle_{\text{rotation around } Q} \rangle_{\text{different } Qs}$$

meaning there are mainly three averaging process in the powder diffraction. The powder diffraction pattern consists of; (i) different Q peaks that in turn are individually averaged over (ii) all crystallites rotated around **Q** and (iii) thermally averaged. The outermost bracket, averaging (i), comes from the fact that every crystallites contributing to different Q-reflections have different relative orientation of field with crystal axes. Crystallites associated with $Q = \langle 111 \rangle$ will have the same relative orientation with respect to the field with those associated with $Q = \langle 222 \rangle$ and $\langle 333 \rangle$ but different field orientation relative to those crystallites associated with $Q = \langle 113 \rangle$. Therefore, the problem associated with averaging (i) can in theory be eliminated by decoupling the different Q peaks from the diffraction pattern, treating them in groups; $Q = \langle 111 \rangle$, $\langle 222 \rangle$ and $\langle 333 \rangle$ in one group, $Q = \langle 113 \rangle$ and $\langle 226 \rangle$ in the other group and so on. However, the remaining averaging problems ((ii) and (iii)) are not trivial to solve and this complexity makes the prediction of the overall powder intensity impossible at this stage. The non-systematic variation in peak intensity (Fig.8.3, 8.4 and 8.5) indeed evidence this complex nature of powder averaging. The effect of rotation around **Q** is shown in Fig.8.9.

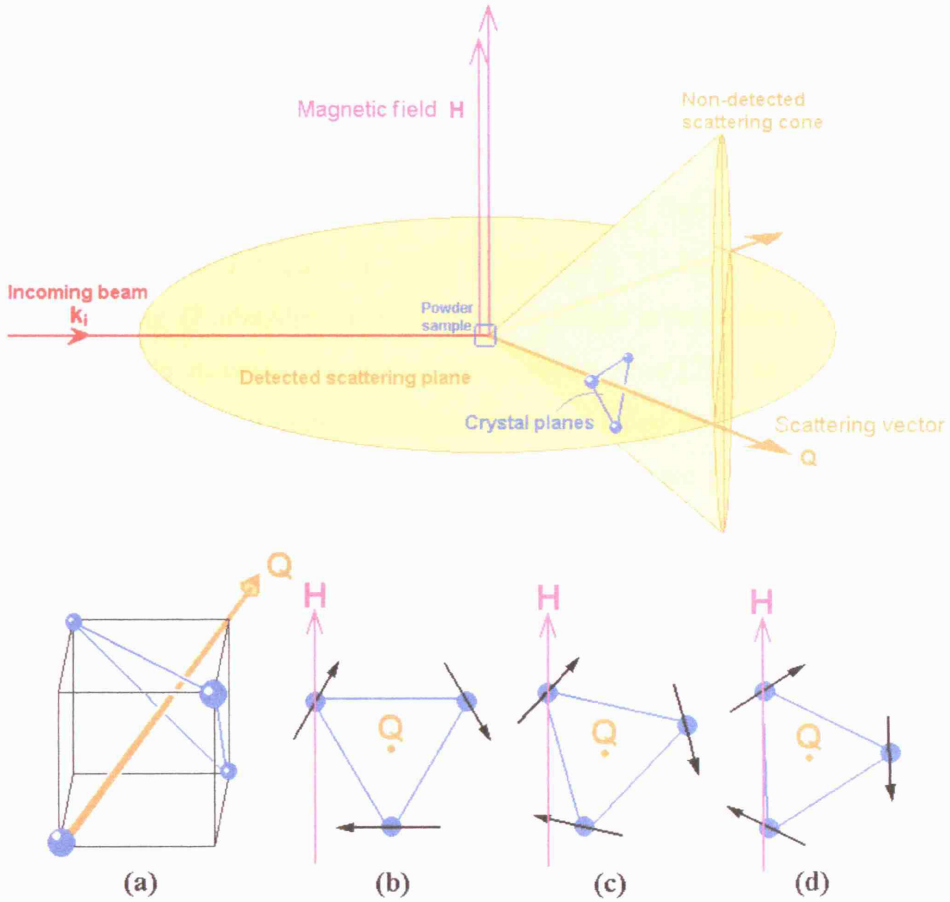

Figure 8.9: A schematic description of the powder averaging problem. In a powder sample, every possible orientation of crystallites is present. This corresponds to the rotations about $\mathbf{k}_i$,(incoming beam) **H** (applied magnetic field) and **Q** (scattering vector), and these give numerous Bragg reflections in all directions. By our experimental set up, the rotation about $\mathbf{k}_i$ (that result in the *scattering cone*) is killed and the **Q**s that lie on the *scattering plane* (the plane defined by the horizontal detector banks) are selected. Then, **H** is always perpendicular to **Q**. However, the rotation around **Q** remains as a problem. Once the crystallites are rotated about **Q** (see (b)~(d)) , the relative orientations of the spins, **S** , and **H** changes. This means that we watch the effect of applying magnetic fields to all 360° directions and the result is an overlap of transitions, i.e. broad transitions.

8.3.5 Comparison of powder neutron diffraction data v.s. single crystal specific heat data

Due to the experiment set up, the crystallites in our sample were experiencing a field always perpendicular to the detected scattering vector **Q**. This means that, the intensity of $\langle {}^1/_2\, {}^1/_2\, {}^3/_2\rangle$ arises from crystallites experiencing field perpendicular to $Q = \langle {}^1/_2\, {}^1/_2\, {}^3/_2\rangle$, for example, H= [2 1-1] ,[1 -1 0] and [-4 1 1]. Having deduced that we have compared our Q intensity variation with the single crystal phase diagrams with corresponding field direction measured by Petrenko *et al.*[2] The observed phase transition points (or range) in both measurements are listed in Table.8.3. In Petrenko *et al.*'s work, measurements using three field directions are presented; H = [111], [110] and [112]. Out of these three field directions, H = [110] and [112] are both perpendicular fields to $Q = \langle {}^1/_2\, {}^1/_2\, {}^3/_2\rangle$, H = [110] is perpendicular to $Q = \langle {}^1/_2\, {}^3/_2\, {}^3/_2\rangle$ and H = [112] is perpendicular to $Q = \langle {}^1/_2\, {}^3/_2\, {}^5/_2\rangle$. Of course there must be other field directions corresponding to each Q reflection. However, here the aim is to verify, by comparison with the neutron data, whether these three field directions chosen by Petrenko *et al.* are indeed 'principal' field directions, enough to represent the whole powder phase diagram just on their own.

At a first glance, the two data sets show similar features. However, the details show slight differences; for example, the transition at low field end at both temperatures (corresponding to transition from phase A to B in Fig.8.6) is not detected in the neutron data and the saturation field/temperature requited to induce the phase transition into paramagnetic state (phase C or D to phase E) varies between the two data sets. A general trend is that there are fewer transitions observed in the neutron diffraction data than the specific heat data with corresponding field direction(s). From this we suspect that several transitions that happen in different applied field directions 'merge' to give a single broader transition in the powder sample. Other field directions, in addition to these three field directions, may be required to reproduce the entire powder phase diagram correctly.

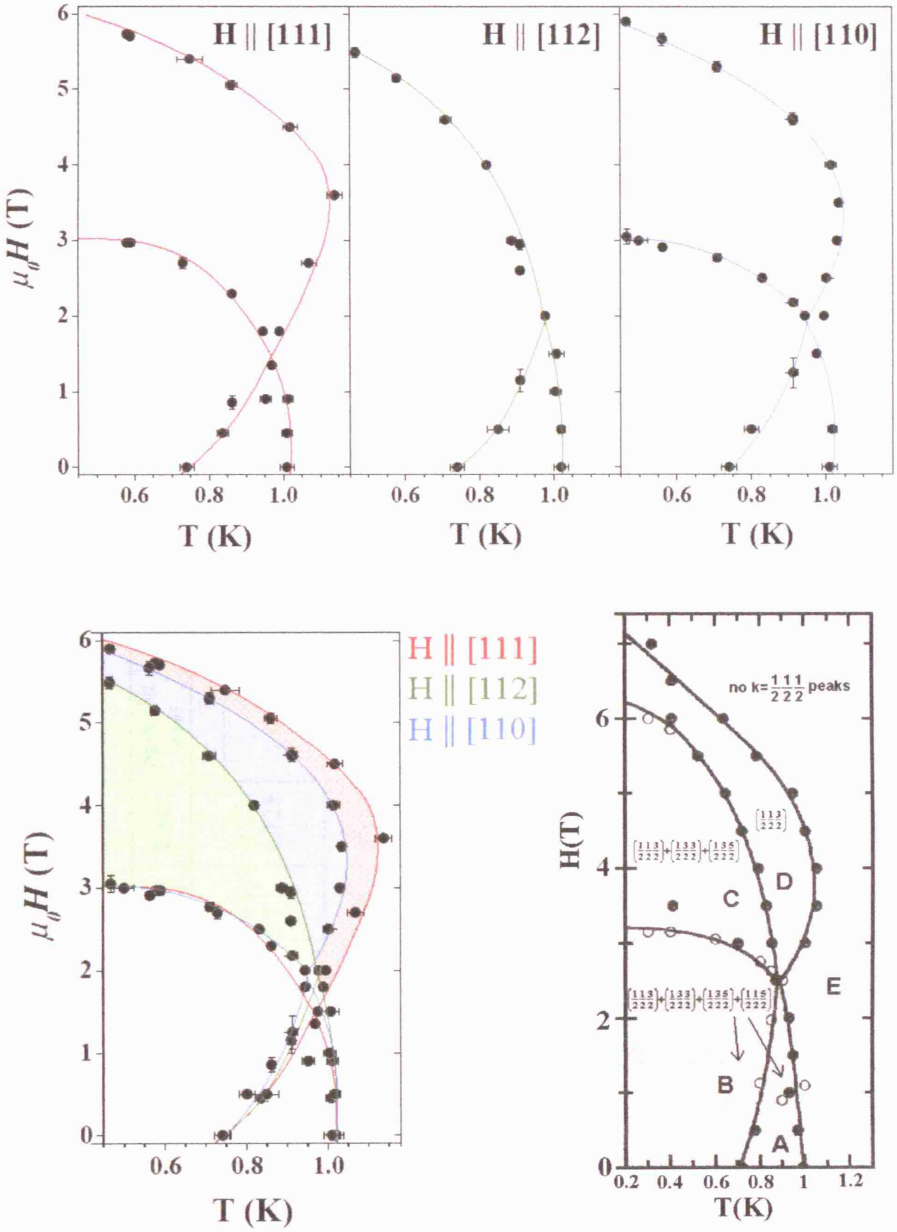

Figure 8.10: Single crystal (*Top* and *Bottom left*) [2] and powder (*Bottom right*) [1] magnetic phase diagrams of $Gd_2Ti_2O_7$. The phase diagrams for three directions of applied magnetic field (**H**‖[111], [112] and [110]) are overlaid (*Bottom left*) for a direct comparison with the powder phase diagram (*Bottom right*). The magnetic **k** = ½½½ Bragg peaks (from our neutron diffraction results) that are present in each phase are also indicated in the powder phase diagram.

		Observed phase transitions											
Scattering vector Q	Corresponding applied field direction	0.9K				0.6K				4T			
		Specific heat	error	Neutron	Error	Specific heat	error	Neutron	Error	Specific heat	error	Neutron	error
$\langle 1/2\ 1/2\ 3/2 \rangle$	[112]	1.0-3 T	0.5	1.75 T 5 T	0.25 0.125	5.1 T	0.1	»5 T? 2.5 T	- 0.25	0.825 K	0.025	1.1 K	0.025
	[110]	1.2 T 2.25 T 4.75 T	0.25 0.1 0.1			2.9 T	0.2			1.025 K	0.025		
$\langle 1/2\ 3/2\ 3/2 \rangle$	[110]	1.2 T 2.25 T 4.75 T	0.25 0.1 0.1	2.5 T	0.125	2.9 T 5.7 T	0.2	3 T 5 T	0.125 0.125	1.025 K	0.025	0.85 K	0.025
$\langle 1/2\ 3/2\ 5/2 \rangle$	[112]	1.0-3 T	0.5	2.75 T 4 T	0.125 0.125	5.1 T	0.1	5 T	0.125-	0.825 K	0.025	1 K	0.05

Table 8.3: Comparison of the observed phase transitions in powder neutron diffraction and in the corresponding single crystal specific heat [2] measured with field direction perpendicular to **Q** (the major differences are highlighted in red).

8.4 Conclusions

In this chapter we have presented the results obtained for the powder neutron diffraction experiment carried out on $Gd_2Ti_2O_7$ with applied magnetic field. As it is generally expected, the behaviour of a polycrystalline sample in field is complex and is not easy to analyze.

$Gd_2Ti_2O_7$ is theoretically the best realizable example of the anisotropy-free pyrochlore Heisenberg antiferromagnet. However, the reality is not as simple as one hopes to be, and recent studies appear to suggest significant degree of single ion anisotropy existing for the Gd^{3+} ion in this compound [2,11-13]. Its behaviour in field is no exception to the example of manifestation of anisotropy. In the work by Petrenko *et al.*, the behaviour of single crystal $Gd_2Ti_2O_7$ in field is described [2]. The phase diagrams produced for three principal crystallographic directions of choice [111], [110] and [112] are reproduced in Fig.8.10 for reference. They point out that the simple mean-field model is not sufficient to explain the double transition that happens when the field is applied along the [111] direction, thus suggesting the need of inclusion of further terms in the Hamiltonian such as the anisotropy [2].

In our powder neutron diffraction experiment in field, we have demonstrated qualitatively that the five phases detected by bulk measurements (on a powder $Gd_2Ti_2O_7$ sample) [1] in the field-temperature phase diagram are consistently reproduced by neutron measurements. It was noticed that all the phases (except the paramagnetic high T – high H phase, phase E in Fig.8.6) contain crystallites that are magnetically ordered with ordering vectors $\mathbf{k}$ = 000 and $\mathbf{k}$ = ½½½. After several attempts to find a solution that can fit the diffraction patterns (corresponding to the two propagation vectors) simultaneously, it was realized that in a powder experiment these two types of crystallites cannot be separated and thus have to be analyzed as a combined data. Also, the problem of powder averaging complicates the solution and it has so far been unsuccessful to decouple the averaging problem.

The possible suggestions that may stand as clues for further data analysis are;

(i) the investigation into the Bragg peaks present or absent in a particular phase. Why is $Q = \langle {}^1/_2\ {}^1/_2\ {}^3/_2 \rangle$ the only reflection surviving in the high T- high H phase (phase D in Fig.8.6)?

(ii) looking into the systematic absence peaks; ⟨200⟩ and ⟨220⟩. Why do they gain in intensity for some ordered phases?

(iii) obtaining a magnetic diffraction pattern with higher Q range. If a powder diffraction pattern with only subsets of Q, ⟨111⟩, ⟨222⟩, ⟨333⟩.... or ⟨113⟩, ⟨226⟩, ⟨339⟩..., can be constructed, then the magnetic structure can be fitted within these subsets of Q (whereas magnetic structure for the crystal giving Q = ⟨111⟩ differs from that of Q = ⟨113⟩).

References for Chapter 8

[1] A.P.Ramirez, B.S.Shastry, A.Hayashi, J.J.Krajewski, D.A.Huse, R.J.Cava, Phys. Rev. Lett. **89**, 067202 (2002).

[2] O.A.Petrenko, M.R.Lees, G.Balakrishnan, and D.McKPaul, Phys. Rev. B **70**, 012402 (2004).

[3] J.D.M.Champion, A.S.Wills, T.Fennell, S.T.Bramwell, J.S.Gardner and M.A.Green, Phys. Rev. B **64,** 140407 (2001).

[4]. J.R.Stewart, G.Ehlers, A.S.Wills, S.T.Bramwell, J.S.Gardner, J.Phys-cond.mat **16** (28), L321-L326 (2004).

[5] A.C.Larsen and R.B.von Dreele, General Structure Analysis System (Lansce,Los Alamos National Laboratory, Los Alamos, 1994).

[6] J.Rodríguez-Carvajal, FULLPROF: *A Program for Rietvelt Refinement and Pattern Matching Analysis*. Abstracts of the Satellite Meeting on Powder Diffraction on the XVth Congress of the International Union of Crystallography. p.127. Toulouse, 1990.

[7] A.J.Wilson and E.Prince, International Tables for Crystallography, vol. C, 2nd ed. (1999); Section 4.4.5.

[8] E.J.Lisher and J.B.Forsyth, Acta Cryst. **A 27**, 545 (1971).

[9] M.Blume, A.J.Freeman and R.F.Watson, J.Chem.Phys. **37**(6), 1245 (1962).

[10] A.J.Freeman and J.P.Desclaux, Int.J.Magnetism **3**, 311 (1972).

[11] A.K.Hassan, L.P.Levy, C.Darie, P.Strobel, Phys. Rev. B **67**, 214432 (2003).

[12] E.Bertin, P.Bonville, J.P.Bouchard, J.A.Hodges, J.P.Sanchez, and P.Vulliet, Eur. Phys. J.B **27**, 347 (2002); P.Bonville, J.A. Hodges, M.Ocio, J.P.Sanchez, P.Vulliet, S.Sosin and D. Braithwaite, J. Phys. Condes. Matter **15**, 7777 (2003).

[13] A.S.Wills, M.E.Zhitomirsky, B.Canals, J.P.Sanchez, P.Bonville, P.Dalmas de Réotier and A.Yaouanc, J. Phys.: Condens. Matter **18**, L37–L42 (2006).

Chapter 9

Discussion and Future Work

In this final chapter of our thesis we summarize the results obtained throughout the thesis, adding possible suggestions to be looked at further as a future work. Chapters 1, 2 and 3 are devoted to review the basic theory and concepts needed to follow the field of frustrated magnetism. The sample synthesis of the series $Er_2Ti_{2-x}Sn_xO_7$ (x = 0 ~2) is discussed in Chapter 4. The experimental results are given in the remaining chapters, Chapter 5 to 8.

9.1 Ordered Magnetic Structure of $Er_2Ti_{2-x}Sn_xO_7$

In Chapter 5, the zero-field magnetically ordered structures of the $Er_2Ti_{2-x}Sn_xO_7$ series with x = 0, 0.5, 1, 1.5, and 2 were investigated by the use of the powder neutron scattering technique. This investigation was inspired by the previous reports showing that $Er_2Ti_2O_7$ shows Néel ordering at T_N~ 1.2 K [1-3] while $Er_2Sn_2O_7$ which has the same crystallographic structure and non-magnetic B-site (Sn^{4+}) does not order down to ~ 150 mK [4]. The first thing we discovered was that actually $Er_2Sn_2O_7$ *does* order – despite being at a rather low temperature of T_N ~ 80 mK. The ordering temperature T_N was plotted as a function of composition x and this showed a linear decrease from T_N ~ 1.2 K of x = 0 down to T_N ~ 0.2 K of x = 1.5 (see Fig.5.6). However, from this T_N plot we suspected the presence of a quantum critical point (QCP) in the composition range $1.5 < x < 2$ and this was further investigated in Chapter 6 by measuring the low temperature magnetization of this narrow range of composition.

Secondly, the ordered magnetic structures of the five members of the $Er_2Ti_{2-x}Sn_xO_7$ series were investigated by the representational analysis method, which is based on a symmetry consideration of the phase transition. From inspection of the diffraction patterns, one can deduce that all members, including $Er_2Sn_2O_7$, orders with an ordering vector $\mathbf{k} = 000$. Another common factor that is shared among the series is that the $\langle 111 \rangle$ Bragg reflection is present; which in turn suggests that all the ordering is happening within the plane perpendicular to the $\langle 111 \rangle$ axes of the tetrahedron. The first four members $x = 2$ to 0.5 orders with the magnetic structure corresponding to the linear combination of basis vectors $a\psi_2 + b\psi_3$ that belongs to the irreducible representation (IR) Γ_5; the Champion model or the combination of State II (ψ_2) and State III (ψ_3). Both these states are solution to the pyrochlore $\langle 111 \rangle$ XY antiferromagnet (AFM) [5]. The IR Γ_5 is two dimensional and for a powder sample, any linear combination $a\psi_2 + b\psi_3$ give identical diffraction patterns that represent arrangements in which the spins are situated in the $\langle 111 \rangle$ planes of the tetrahedron. On the other hand, $Er_2Sn_2O_7$ orders with a distinct structure. Our analysis shows that $Er_2Sn_2O_7$ orders with the Palmar-Chalker (PC) model, that is, with basis vectors ψ_4, ψ_5 or ψ_6 belonging to IR Γ_5. This is a ground state deduced for a pyrochlore Heisenberg AFM with dipolar interactions taken into account [6]. Thus, it should be noted that the ordered ground state shifts from a model with no dipolar interaction in $Er_2Ti_2O_7$ to a model with dipolar interaction in $Er_2Sn_2O_7$. Interestingly, these PC states are also one of the eight solutions of the ground states of the pyrochlore $\langle 111 \rangle$ XY AFM [5].

Once the magnetic structures are deduced for all the members of the $Er_2Ti_{2-x}Sn_xO_7$ series, the ordered moment sizes at the lowest measured temperature (see Table 5.5 for detail) were deduced and were plotted against x. This showed a rather unusual trend; the ordered moments are constant ($\sim 3.5\ \mu_B$) for $x = 0$, 0.5 and 1 and suddenly drops at $x = 1.5$ to $\sim 2\ \mu_B$ and then to a even lower value of $\sim 0.5\ \mu_B$ for $x = 2$. It should be noted that these ordered moments should lie in a plane perpendicular to $\langle 111 \rangle$ and the nature of this sudden disappearance of order is still a mystery at this point. There are two possibilities for the origin; either the shrink in single ion moment in itself (with fully ordered moments), or the disorder of the spins (with constant single ion

moment throughout the series). Together with the verification of the QPC in the range $1.5 < x < 2$, this investigation into the origin of the dramatic drop in order above $x = 1$ became the main interest in our work.

9.2 Low Temperature Magnetization of $Er_2Ti_{2-x}Sn_xO_7$ and the Quantum Critical Point

Following the results in Chapter 5, the first question 'the presence of QCP' was investigated in Chapter 6 by measuring the low temperature magnetization of the $Er_2Ti_{2-x}Sn_xO_7$ in the region of interest $1.5 < x < 2$ in detail. The results were rather complex; starting from the $x = 2$ end ($Er_2Sn_2O_7$), two phase transitions were observed (at $T_N \sim 0.13$ K and the second at $T_C \sim 0.1$ K). However, for compounds with $x < 1.9$, only one transition was observed. The transition gets less and less clear in character and T_N shifts towards zero as $x \rightarrow 1.55$. Thus, although being rather unclear at present, we expect a QCP happening around $x \sim 1.55$, and further investigation is suggested into this composition. The ambiguous points about the measurement are; that the ordering of the compound $x = 1.5$ (SN150) was not carried out with enough accuracy to be compared with the ordering observed in the neutron measurement ($T_N = 0.21(2)$ K; Chapter 5), and also, the absolute magnitude of the measured moments should be determined with better calibration.

The temperature-field phase diagram of $Er_2Sn_2O_7$ was constructed based upon the magnetization measurements, and was compared to the similar phase diagram of $Gd_2Ti_2O_7$. Although similar features (such as the double transitions in zero field) were observed between the two, there are also major differences such as the high field ($H \sim 1.1$ T) broad transition. Although the single ion anisotropy of $Gd_2Ti_2O_7$ is still under discussion (see section 2.5 [7-9]), this should be compared to the anisotropy of $Er_2Sn_2O_7$ (having components of 2.11 μ_B and 4.55 μ_B perpendicular and parallel to $\langle 111 \rangle$-axes; Chapter 7). The origin of the similarities or the differences should then be investigated.

Another important similarity that is shared between the two phase diagrams, and that may stand as a clue to solve the nature of the phases present is that, a transition is happening at a half of saturation field, H_{sat}. Petrenko *et al.* [10] suggest this to be

related to a collinear spin state within the tetrahedra, where three spins aligned and one pointing in the opposite direction with respect to the applied field. (The stabilization of this collinear state in Heisenberg and in kagomé antiferromagnets are predicted to occur at $H = H_{sat}/2$ and $H_{sat}/3$, respectively [11].)

9.3 Crystal Electric Field of $Er_2Ti_{2-x}Sn_xO_7$

In Chapter 7, the crystal electric field (CEF) of the $Er_2Ti_{2-x}Sn_xO_7$ series (x = 0 ~2) was studied by means of inelastic neutron scattering. This revealed that the single ion moment size of Er^{3+} ions defined by the surrounding CEF remains constant (~ 5 μ_B) throughout the series. Thus, the decrease in the detected order (in neutron diffraction experiment; Chapter 5) in compounds with higher Sn substitution is *not* a manifestation of the single ion moment size shrinkage but is likely to be due to the *disorder* of the moments.

The measurements concerning the magnetic properties of the $Er_2Ti_{2-x}Sn_xO_7$ series (x = 0 ~2) are summarized below in Fig.9.1. Although the single ion moment sizes are fixed by CEF to be the same for all x, the actual orderable component, that is the spin component perpendicular to ⟨111⟩ axes, change in size as we examine across the series. Since both Champion states and Palmer-Chalker states are ground state solutions for the pyrochlore ⟨111⟩-XY antiferromagnet (see section 2.3.4.2) it is not straight forward to see what is actually causing the selection between the compounds. The double transition feature in $Er_2Sn_2O_7$ was not observed by the neutron and hence a more careful measurement down to a lower temperature (<< 70mK if possible) will be desirable in order to investigate what change is actually happening during these subsequent transitions.

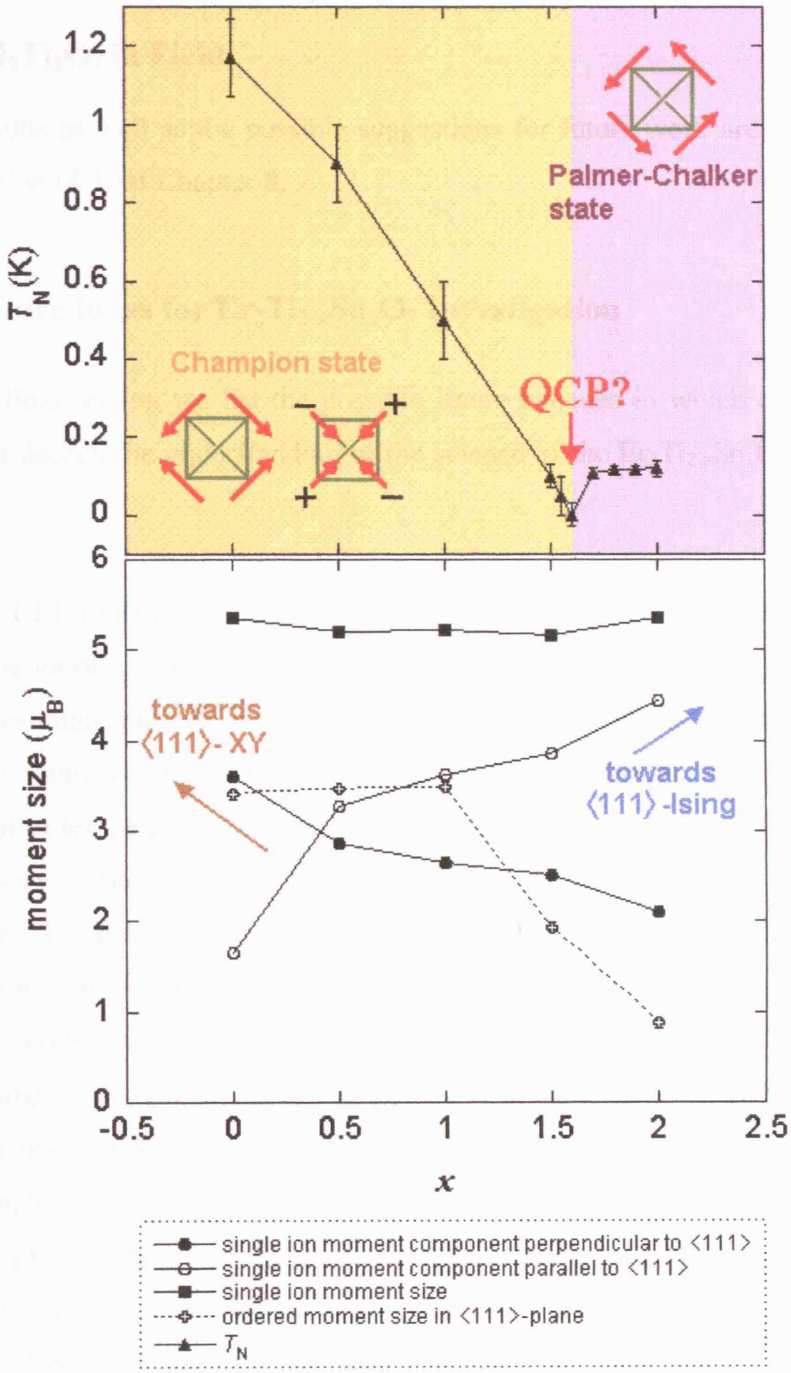

Figure 9.1: A summary of the results obtained for the $Er_2Ti_{2-x}Sn_xO_7$ series ($x = 0 \sim 2$) in this thesis. The ordering temperature is plotted in the top panel together with the verified ordered ground states. The data in solid black line in the lower panel represent the results of the crystal filed measurements (Chapter 7) and the dotted line shows the result of neutron diffraction (Chapter 5).

9.4 $Gd_2Ti_2O_7$ in Field

The results as well as the possible suggestions for future work are summarized in the last section (8.4) of Chapter 8.

9.5 Future Ideas for $Er_2Ti_{2-x}Sn_xO_7$ Investigation

In this final section we list the possible future avenues in which one can go into, in order to deepen the understanding of the science of the $Er_2Ti_{2-x}Sn_xO_7$ discussed in this thesis;

- the CEF analysis should be repeated with a better controlled statistics. Since there were lot of parameters correlated during the refinement of the spectra, it is difficult to estimate the errors associated with the results in our work. It is desirable to simultaneously fit the CEF parameters and the susceptibility (or the magnetization) against temperature, or even better, the neutron scattering data, in order to obtain a more accurate set of CEF parameters.
- The CEF analysis will be ideally done using a magnetically diluted sample. Since our measurements were carried out mostly at a high enough temperature ($T >> J$), the influence from the neighboring magnetic ions (Er^{3+}) is expected to be unimportant. However, to be strictly free from the exchange interaction, the magnetic ions need to be in a environment where they can be treated as proper 'single ions', thus the use of a more diluted compound (such as $Er_{2-y}Y_yTi_{2-x}Sn_xO_7$; $y > 2-y$) is necessary.
- The theoretical developments are also awaited for these erbium titanate/stannate systems. A detailed investigation into the different combinations of second and third neighbor exchange constants, J_2 and J_{31}, that arise to systems with a particular ordering vector was recently made for the gadolinium titanate/stannate system [12]. The different third neighbor exchange pathways, J_{31} and J_{32} are shown in Fig.9.2, together with the instability wavevectors determined for different values of J_2 and J_{31}. Wills *et al.* [12] considered the following Hamiltonian;

$$\hat{H} = \sum_{\langle i,j \rangle} J_{ij} \mathbf{S}_i \cdot \mathbf{S}_j + D \sum_i (\mathbf{n}_i \cdot \mathbf{S}_i)^2 + (g\mu_B)^2 \sum_{\langle i,j \rangle} \left[\frac{\mathbf{S}_i \cdot \mathbf{S}_j}{r_{ij}^3} - \frac{3(\mathbf{S}_i \cdot \mathbf{r}_{ij})(\mathbf{S}_j \cdot \mathbf{r}_{ij})}{r_{ij}^5} \right], \qquad (9.1)$$

where the exchange term J_{ij} is summed up to the third nearest neighbor and the single-ion anisotropy constant D is set to $D > 0$. In Chapter 5, $Er_2Sn_2O_7$ was found to have the ground state of a Heisenberg pyrochlore antiferromagnet with dipolar interaction, the Palmer-Chalker state (PC state), which is also the selected ground state in $Gd_2Sn_2O_7$ [12]. Therefore, a similar attempt to the above will be valid for the erbium case, except, the value for the dipolar interaction should be re-estimated and also the single-ion anisotropy should be varied according to our measurements (note that the Er^{3+} moments in $Er_2Sn_2O_7$ had a stronger Ising-character with respect to the $\langle 111 \rangle$-axes).

- The behavior of $Er_2Ti_{2-x}Sn_xO_7$ in applied magnetic field has only been examined by means of bulk measurements (susceptibility) and not yet by neutron scattering. It will be interesting to look into the anomalous phase diagram of $Er_2Sn_2O_7$ as well as the rest of the series ($x < 2$) by a microscopic probe.
- As a final point, we would like to shed light in the 'disordered' part of the moments, since the 'ordered' components have been dealt fairly thoroughly in this thesis. Now knowing the sizes of the single-ion moments defined by the crystal field, one should approach the diffuse scattering (disordered) of the erbium compounds measured on the D7 polarized neutron spectrometer (ILL, Grenoble) [13]. The amount of disorder should consistently increase as one goes across the $Er_2Ti_{2-x}Sn_xO_7$ series towards higher x (since the moment sizes are fixed in sizes). Once this is confirmed, we can safely conclude that the disappearance in order in the $Er_2Ti_{2-x}Sn_xO_7$ series as we substitute Sn for Ti is a *collective* effect, and not a single-ion effect.

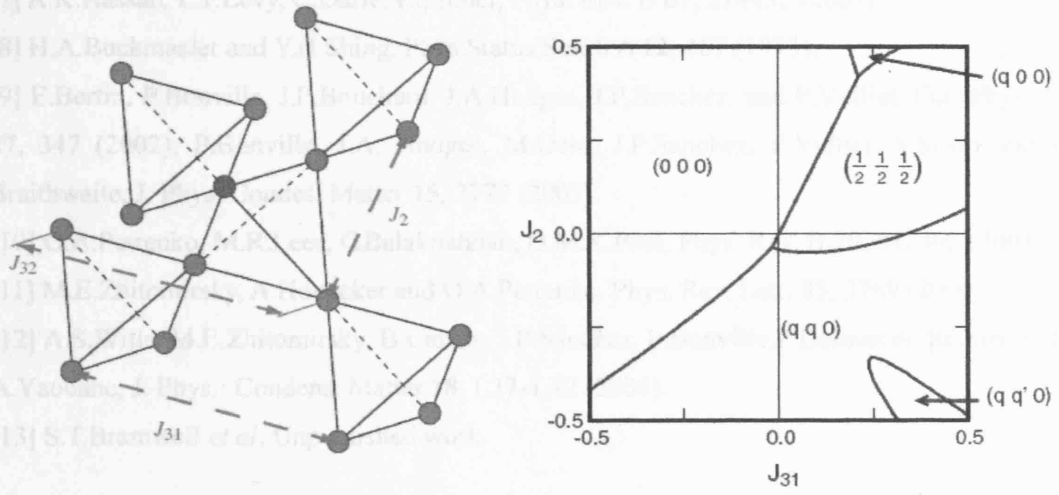

Figure 9.2 [12]: pyrochlore lattice consisting of vertex-sharing tetrahedra of magnetic ions (*Left*). The second nearest neighbor, J_2, and two types of third nearest neighbors, J_{31} and J_{32}, are indicated. J_{31} and J_{32} are mediated by different Ln^{3+}-O^{2-}-O^{2-}-Ln^{3+} brigdes (Ln^{3+} are the magnetic rare earth ions) and as a result, the relations $J_{32} << J_{31}$ and $J_2 < J_{31}$ are suggested [12]. The instability wavevectors for different combinations of J_2 and J_{31} for a Heisenberg pyrochlore antiferromagnet with dipolar interaction [12]. The two commensurate ordering vectors **k** = 000 and **k** = ½½½ together with the three incommensurate wavevectors are predicted.

References for Chapter 9

[1] H.W.J.Blöte, R.F.Weilinga, and H.Huiskamp, Physica **43**, 549 (1969).

[2] J.D.M.Champion, M.J.Harris, P.C.W.Holdsworth, A.S.Wills, G.Balakrishnan, S.T.Bramwell, E.Čižmár, T.Fennell, J.S.Gardner, J.Lago, D.F.McMorrow, M.Orendáč, A.Orendăcová, D.McK. Paul, R.I.Smith, M.T.F.Welling, A.Wildes, Phys. Rev. B **68**, 020401 (2003).

[3] M.J.Harris, S.T.Bramwell, T.Zeiske, D.F.McMorrow, and P.J.C.King, J. Magn. Magn. Mater. **177**, 757 (1998).

[4] K.Matsuhira , Y.Hinatsu, K.Tenya , H.Amitsuka and T.Sakakibara, J. Phys. Soc. Japan **71**, 1576 (2002).

[5] J.D.M.Champion, *Ph.D thesis, University College London* (2002).

[6] S.E.Palmer, J.T.Chalker, Phys. Rev. B **62**, 488 (2000).

[7] A.K.Hassan, L.P.Levy, C.Darie, P.Strobel, Phys. Rev. B **67**, 214432 (2003).

[8] H.A.Buckmaster and Y.H.Shing, Phys.Status Solidi A **12**, 467 (1973).

[9] E.Bertin, P.Bonville, J.P.Bouchard, J.A.Hodges, J.P.Sanchez, and P.Vulliet, Eur. Phys. J.B **27**, 347 (2002); P.Bonville, J.A. Hodges, M.Ocio, J.P.Sanchez, P.Vulliet, S.Sosin and D. Braithwaite, J. Phys. Condes. Matter **15**, 7777 (2003).

[10] O.A.Petrenko, M.R.Lees, G.Balakrishnan, D.M.K.Paul, Phys. Rev. B **70,** 012402 (2004).

[11] M.E.Zhitomirsky, A.Honecker and O.A.Petrenko, Phys. Rev. Lett. 85, 3269 (2000).

[12] A.S.Wills, M.E.Zhitomirsky, B.Canals, J.P.Sanchez, P.Bonville,P.Dalmas de Réotier and A.Yaouanc, J. Phys.: Condens. Matter **18**, L37–L42 (2006).

[13] S.T.Bramwell *et al.* Unpublished work.

Appendix A1

Structural Parameters of Pyrochlores

$R_2Ti_2O_7$				
Cubic, $Fd\bar{3}m$				
	Site	x	y	z
R	16c	0	0	0
Ti	16d	$\frac{1}{2}$	$\frac{1}{2}$	$\frac{1}{2}$
O_1	8a	$\frac{1}{8}$	$\frac{1}{8}$	$\frac{1}{8}$
O_2	48f	x	$\frac{1}{8}$	$\frac{1}{8}$

Table A1-1: The structural parameters for the pyrochlore material with space group $Fd\bar{3}m$; rare earth titanate ($R_2Ti_2O_7$), is shown below. Commonly, the refinable positional parameter x(O_2) ~ 0.42 and the lattice parameter a ~ 10.1 Å.

Appendix A2

Theory of Crystal Electric Field

Here we briefly summarize the basic idea of crystal field theory and its calculation [1-6]. In a free atom/ion of rare earth spherical symmetry exists, and each J level is $(2J+1)$-fold degenerate. When the ion is placed in a crystal, the spherical symmetry is destroyed and each level splits under the influence of the electric field produced by the environment. The degree to which the $(2J+1)$-fold degeneracy is removed will depend on the point symmetry (now lower than spherical) about the rare earth ion. This idea is shown in the schematic diagram below (Fig.A2-1) for crystal fields with different symmetries; axial and non-axial. Watch the mixing of $|J, M_J\rangle$ states.

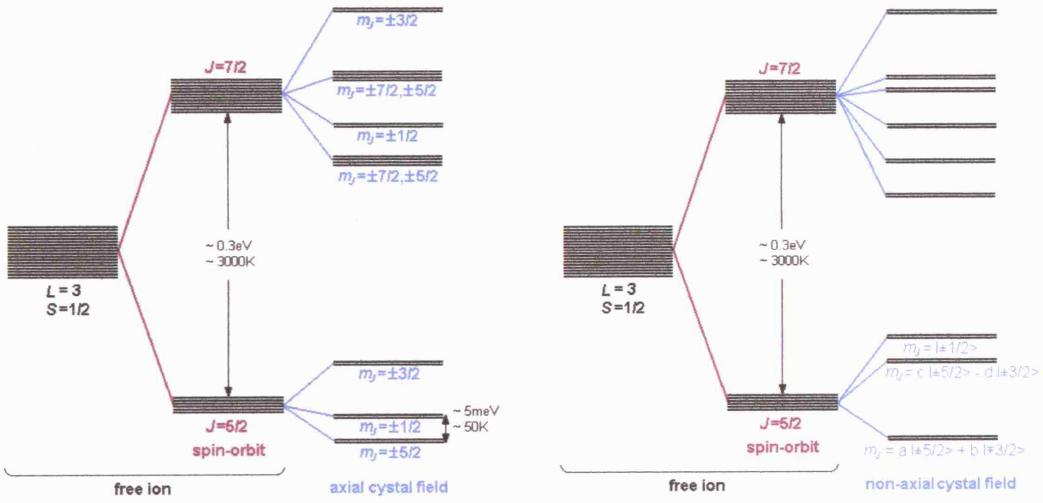

Figure A2-1: Schematic diagram showing effects of different crystal field symmetries (axial and non-axial) on M_J - level splitting.

The Hamiltonian $\hat{H}$ for an ion placed in a crystal field may be written as

$$\hat{H} = \hat{H}_{Free\ ion} + \hat{V}_{CEF} \tag{A2.1}$$

where $\hat{H}_{Free\ ion}$ is the Hamiltonian of the free ion and $\hat{V}_{CEF}$ is the potential provided by the crystal environment about the ion in interest. We suppose that the eigenvalues and eigenfuctions of $\hat{H}_{Free\ ion}$ are known and regard the potential $\hat{V}_{CEF}$ as a perturbation. The unperturbed free ion eigenfuctions will have complete spherical symmetry, and hence we may try to expand $\hat{V}_{CEF}$ in terms of spherical harmonics (or operators that transform like spherical harmonics; tesseral harmonics).

Crystal field potential Hamiltonian $\hat{V}_{CEF}$

Consider a free ion with ground state defined consisting of the degenerate set of quantum states $|J, M_J\rangle$ where $M_J = J, J\text{-}1,...,-J$. We know that for the free ion

$$\langle J, M_J | \hat{J}_z | J, M_J \rangle = M_J \tag{A2.2}$$

and

$$\langle J, M_J | \hat{J}^2 | J, M_J \rangle = J(J+1) \tag{A2.3}$$

(neglecting factors of $\hbar$).

The crystal field perturbs these states, altering their energies and mixing them together. According to perturbation theory, if we know the matrix elements $\langle J, M_J | \hat{V}_{CEF} | J, M'_J \rangle$ then we know the perturbed energies and wavefunctions.

On a basis of a simple point-charge ionic model, the electrostatic potential $V(r, \theta, \phi)$ at a point (r, θ, ϕ) near the origin due to the surrounding charges j is

$$V(r,\theta,\varphi) = \sum_{ion\ j} \frac{q_j}{d(ion-electron)} = \sum_{ion\ j} \frac{q_j}{|(\mathbf{R}_j - \mathbf{r})|} \tag{A2.4}$$

where q_j is the charge at the jth neighboring ion, a distance $|\mathbf{R}_j|$ from the origin and d represents distance. The magnetic electron position with respect to the origin is describ-

-ed by $\mathbf{r}_i = (x_i, y_i, z_i)$ hence $r^2 = x^2 + y^2 + z^2$. If the magnetic ion in question has charge q_i at (r_i, θ_i, ϕ_i), then perturbing crystalline potential energy $\hat{V}_{CEF}$ is the sum of $V_i(r_i, \theta_i, \phi_i)$ over all i magnetic electrons and over all j neighboring ions;

$$\hat{V}_{CEF} = \sum_i q_i V_i = \sum_{electron\ i} \sum_{ion\ j} \frac{q_i q_j}{|(\mathbf{R}_j - \mathbf{r}_i)|}. \tag{A2.5}$$

The crystalline potential $V(r, \theta, \phi)$ and hence $\hat{V}_{CEF}$ can be expressed in terms of Cartesian coordinates, or directly in terms of spherical harmonics. For f electrons, $\hat{V}_{CEF}$ expressed in Cartesian coordinates will be a Taylor series expanded up to 6^{th} degree ($n < 2l!$), a sum of terms in even powers of x, y and z and maybe r:

$$\hat{V}_{CEF} \rightarrow \sum_{electrons} Ax^2 + By^2 + Cz^2 + Dx^4 + \ldots Iz^6 \tag{A2.6}$$

$$\hat{V}_{CEF} = -\sum_{electron\ i} |e|\ V(x_i, y_i, z_i) \tag{A2.7}$$

For example, the potential energy of a single charge q' at (x, y, z) placed in a cubic potential due to sixfold coordination of ligands (each with charge q) is

$$\hat{V}_{CEF} = \frac{6q}{a} + \left(\frac{35qq'}{4a^5}\right)\left[\left(x^4 + y^4 + z^4\right) - \tfrac{3}{5}r^4\right] + \left(\frac{-21q}{2a^7}\right)\left[\left(x^6 + y^6 + z^6\right) + \tfrac{15}{4}\left(x^2y^4 + x^2z^4 + y^2x^4 + y^2z^4 + z^2x^4 + z^2y^4\right) - \tfrac{15}{14}r^6\right] \tag{A2.8}$$

where the six ligands are at the corners of an octahedron; i.e. at $(a,0,0)$, $(-a,0,0)$, $(0,a,0)$, $(0,-a,0)$, $(0,0,a)$ and $(0,0,-a)$.

If the Hamiltonian ($\hat{V}_{CEF}$) is written in spherical harmonics (using the spherical harmonics addition theorem) it takes the form of

$$\hat{V}_{CEF} = \sum_{electron\ i} \sum_n \sum_{m=-n}^{n} r^n\ \gamma'_{nm}\ Y_n^m(\theta, \varphi), \tag{A2.9}$$

where $$\gamma'_{nm} = \sum_j \frac{4\pi}{(2n+1)} \frac{q_j}{R_j^{(n+1)}} (-1)^m Y_n^{-m}(\theta_j, \varphi_j). \quad \text{(A2.10)}$$

Here, $Y_n^m(\theta, \varphi)$ s are the spherical harmonics with indexes n and m. Again, for a single charge q' at (r, θ, ϕ) placed in a cubic potential due to sixfold coordination of ligands (each with charge q) is

$$\hat{V}_{CEF} = \sum_{electron\ i} \frac{12\sqrt{\pi}}{a}\left[Y_0^0(\theta,\varphi)\right] + \left(\frac{7\sqrt{\pi}}{3}\frac{qq'r^4}{a^5}\right)\left\{Y_4^0(\theta,\varphi) + \left(\frac{5}{14}\right)^{\frac{1}{2}}\left[Y_4^4(\theta,\varphi) + Y_4^{-4}(\theta,\varphi)\right]\right\}$$
$$+ \left(\frac{3}{2}\left(\frac{\pi}{13}\right)^{\frac{1}{2}}\frac{qq'r^6}{a^7}\right)\left\{Y_6^0(\theta,\varphi) - \left(\frac{7}{2}\right)^{\frac{1}{2}}\left[Y_6^4(\theta,\varphi) + Y_6^{-4}(\theta,\varphi)\right]\right\} \quad \text{(A2.11)}$$

where the six ligands are at the corners of an octahedron; $(a,0,0)$, $(a,\pi,0)$, $(a,\pi/2,0)$, $(a,\pi/2,\pi)$, $(a,\pi/2,\pi/2)$ and $(a,\pi/2,3\pi/2)$.

Evaluation of the Matrix elements: using Stevens Operator Equivalent method

Now let's see how the matrix element $\langle J, M_J | \hat{V}_{CEF} | J, M'_J \rangle$ can be evaluated. As a fundamental method, this can be found by direct integration:

$$\left\langle J, M_J \middle| \hat{V}_{CEF} \middle| J, M'_J \right\rangle = \iiint \psi^* \hat{V}_{CEF} \psi' \, dxdydz, \quad \text{(A2.12)}$$

where ψ and ψ' are wavefunctions corresponding to $|J, M_J\rangle$ and $|J, M'_J\rangle$. However, as written, this integral is very hard to perform – we would rather have a method of evaluating the matrix elements in terms of the J, M_Js. Instead, we here introduce an elegant approach that facilitates the problem a lot; the Stevens operator equivalent method. Stevens realized that the crystal field Hamiltonian $\hat{V}_{CEF}$, which is the crystalline potential summed over magnetic electrons, has exactly the same matrix elements as simple operator involving only $\hat{J}^2, \hat{J}_x, \hat{J}_y, \hat{J}_z$ and $\hat{J}_\pm$ (where $\hat{J}_\pm = \hat{J}_x \pm i\hat{J}_y$). The rules for determining the operator equivalent to the Cartesian Hamiltonian given by $\hat{V}_{CEF} = -\sum_{electron\ i} |e|\, V(x_i, y_i, z_i)$ stated by Stevens are surprising simple: replace x with

$\hat{J}_x$, y with $\hat{J}_y$, z with $\hat{J}_z$, and replace products (xy etc.) by a sum over all possible combinations of $\hat{J}_x\hat{J}_y$ etc., dividing by the number of such combinations. Then, the resulting expression for the operator equivalent is manipulated further to eliminate $\hat{J}_x$, $\hat{J}_y$ operators in favor of $\hat{J}_z$ and $\hat{J}$. For example:

$$\begin{aligned}
\sum_{electrons\ i}(3z_i^2 - r_i^2) &\equiv \alpha_J < r^2 > \left[3\hat{J}_z^2 - \hat{J}^2\right] \\
&= \alpha_J < r^2 > \left[3J_z^2 - J(J+1)\right] = \alpha_J < r^2 > \boldsymbol{O}_2^0 \\
\sum_{electrons\ i}(x_i^2 - y_i^2) &\equiv \alpha_J < r^2 > \left[J_x^2 - J_y^2\right] \\
&= \alpha_J < r^2 > \left[\hat{J}_+^2 - \hat{J}_-^2\right] = \alpha_J < r^2 > \boldsymbol{O}_2^2 \\
\sum_{electrons\ i} x_i y_i &\equiv \alpha_J < r^2 > \left[(J_x J_y - J_y J_x)/2\right] \\
\sum_{electrons\ i}(x_i^4 - 6x_i^2 y_i^2 + y_i^4) &\equiv \sum_{electrons\ i}\left\{\left[(x_i + iy_i)^4 + (x_i - iy_i)^4\right]/2\right\} \\
&= \beta_J < r^4 > \tfrac{1}{2}\left[\hat{J}_+^4 + \hat{J}_-^4\right] = \beta_J < r^4 > \boldsymbol{O}_4^4
\end{aligned} \tag{A2.13}$$

where the multiplicative factor α_J, β_J and γ_J ,corresponding to second, fourth and sixth-degree terms respectively, are numerical constants depending on l (the orbital quantum number of the electron on the unfilled shell), n' (the number of them) and J. These constants can be determined by returning to the direct integration method [1]. The $\langle r^n \rangle$ terms are radial integral that can be taken as parameters or that can also be calculated [1,7]. This summation of the potential over magnetic electrons is expressed as

$$\begin{aligned}
\hat{V}_{CEF} = -\sum_{electron\ i} |e|\ V(x_i, y_i, z_i) &= \sum_{electron\ i}\sum_{nm} A_n^m f^c{}_{nm}(x_i, y_i, z_i) \\
&= \sum_{nm}\left[A_n^m < r^n > \theta_n\right] \boldsymbol{O}_n^m
\end{aligned} \tag{A2.14}$$

where $f^c{}_{nm}(x_i, y_i, z_i)$ is the function written in the square brackets in the Tesseral harmonics expressions. The quantities $A_n^m \langle r^n \rangle$ are known as the "crystal field paramete-

-rs" and are usually determined by fitting $\hat{V}_{CEF}$ to the experimental data. The operator equivalent Hamiltonian is then written as

$$\hat{V}_{CEF} = \sum_{nm} B_n^m O_n^m \qquad \text{(A2.15)}$$

Where $B_n^m = A_n^m \langle r^n \rangle \theta_n \quad (\theta_2 = \alpha_J,\ \theta_4 = \beta_J,\ \theta_6 = \gamma_J).$ (A2.16)

****

Additional Information

Below we list the equations that define the spherical harmonics and the corresponding Tesseral harmonics.

$$Y_n^m(\theta, \varphi) = (-1)^{(m+|m|)/2} \left[\frac{(2n+1)(n-|m|)!}{2(n+|m|)!} \right]^{\frac{1}{2}} \times \frac{1}{(2\pi)^{\frac{1}{2}}} P_n^{|m|}(\cos\theta) \times \exp(im\varphi)$$

where $P_n^{|m|}(\cos\theta) = (1-\cos^2\theta)^{|m|/2} \ (d^{|m|} / d\cos^{|m|}\theta) \ P_n^0(\cos\theta)$

and $P_n^0(\cos\theta) = (1/2^n n!) \ (d^n / d\cos^n\theta) \ (\cos^2\theta - 1)^n$

are Legendre functions.

In order to avoid imaginary quantities the spherical harmonics are transformed into a real function called the Tesseral harmonics by the relations;

$$Z_{n0} = Y_n^0,$$

$$Z_{nm}^c = \left(\frac{1}{\sqrt{2}} \right) [Y_n^{-m} + (-1)^m Y_n^m] \ , \quad m > 0$$

$$Z_{nm}^s = \left(\frac{i}{\sqrt{2}} \right) [Y_n^{-m} - (-1)^m Y_n^m] \ , \quad m > 0.$$

Some of the common spherical harmonics and equivalent Tesseral harmonics;

$$Y_2^0 = \frac{1}{4}\left(\frac{5}{\pi}\right)^{\frac{1}{2}} (3\cos^2\theta - 1); \quad Z_{20} = \frac{1}{4}\left(\frac{5}{\pi}\right)^{\frac{1}{2}} [(3z^2 - r^2)/r^2]$$

$$Y_2^{\pm 2} = \frac{1}{4}\left(\frac{15}{2\pi}\right)^{\frac{1}{2}} \sin^2\theta \ e^{(\pm 2i\varphi)}; \quad Z_{22}^c = \frac{1}{4}\left(\frac{15}{\pi}\right)^{\frac{1}{2}} [(x^2 - y^2)/r^2]$$

$$Y_4^0 = \frac{3}{16}\left(\frac{1}{\pi}\right)^{\frac{1}{2}}(35\cos^4\theta - 30\cos^2\theta + 3);\ Z_{40} = \frac{3}{16}\left(\frac{1}{\pi}\right)^{\frac{1}{2}}[(35z^4 - 30z^2r^2 + 3r^4)/r^4]$$

$$Y_6^0 = \frac{1}{32}\left(\frac{13}{\pi}\right)^{\frac{1}{2}}(231\cos^6\theta - 315\cos^4\theta + 105\cos^2\theta - 5);\ Z_{60} = \frac{1}{32}\left(\frac{13}{\pi}\right)^{\frac{1}{2}}[(231z^6 - 315z^4r^2 + 105z^2r^4 - 5r^4)/r^6]$$

$$Y_4^{\pm 3} = \mp\frac{3}{8}\left(\frac{35}{\pi}\right)^{\frac{1}{2}}\sin^3\theta\ \cos\theta\ e^{(\pm 3i\phi)};\quad Z_{43}^c = \frac{3}{8}\left(\frac{70}{\pi}\right)^{\frac{1}{2}}[z(x^3 - 3xy^2)/r^4]$$

$$Y_6^{\pm 3} = \mp\frac{1}{64}\left(\frac{2730}{2\pi}\right)^{\frac{1}{2}}\sin^3\theta\,(11\cos^3\theta - 3\cos\theta)\ e^{(\pm 3i\varphi)};\ Z_{63}^c = \frac{1}{32}\left(\frac{2730}{\pi}\right)^{\frac{1}{2}}[(11z^3 - 3zr^2)(x^3 - 3xy^2)/r^6]$$

$$Y_6^{\pm 6} = \frac{231}{64}\left(\frac{13}{231\pi}\right)^{\frac{1}{2}}\sin^6\theta\ e^{(\pm 6i\varphi)};\quad Z_{66}^c = \frac{231}{64}\left(\frac{26}{231\pi}\right)^{\frac{1}{2}}[(x^6 - 15x^4y^2 + 15x^2y^4 - y^6)/r^6]$$

Refernces

[1] M.T.Hutchings, Solid State Phys.**16**, 227 (1964).

[2] B.G.Wybourne, *Spectroscopic Properties of Rare Earths*, Chap. 6, Interscience Publishers, New York (1965).

[3] K.W.Stevens, Proc. Phys. Soc. **A65**, 209 (1952).

[4] R.J.Elliott and K.W.H.Stevens, Proc. Roy. Soc. A **218**, 553 (1953).

[5] R.J.Elliott and K.W.H.Stevens, Proc. Roy. Soc. A **219**, 387 (1953).

[6] B.R.Judd, Proc. Roy. Soc. A **227**, 552 (1955).

[7] A.J.Freeman and R.E.Watson, Phys.Rev.**127**, 2058 (1962).

Appendix A3

Crystal Electric Field data for $Er_2Ti_{2-x}Sn_xO_7$ (x = 0.5, 1, 1.5)

A 3.1 HET Spectra

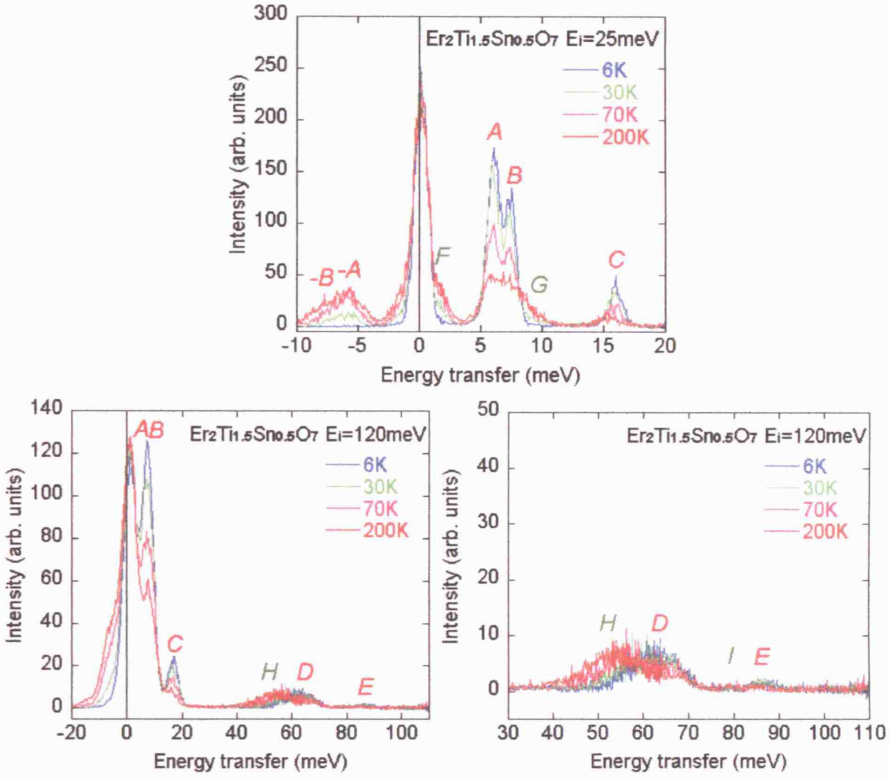

Figure A3-1: Energy spectra for $Er_2Ti_{1.5}Sn_{0.5}O_7$ measured on HET with incident energy E_i = 25 meV (*Top Left*) and E_i =120 meV (*Top Right* and *Bottom*) measured at T = 6, 30, 70 and 200 K. The peaks that grow in intensity with lowering the temperatures are E_i ~ 6.3, 7.6, 16.2, 63.8, 66.3 and 86.5 meV; hence attributed to transition from the ground state. The peaks that grow in intensity with increasing the temperatures are E_i ~ < 2, 8.5 - 10, 45 - 55 meV; hence attributed to transition from the excited states.

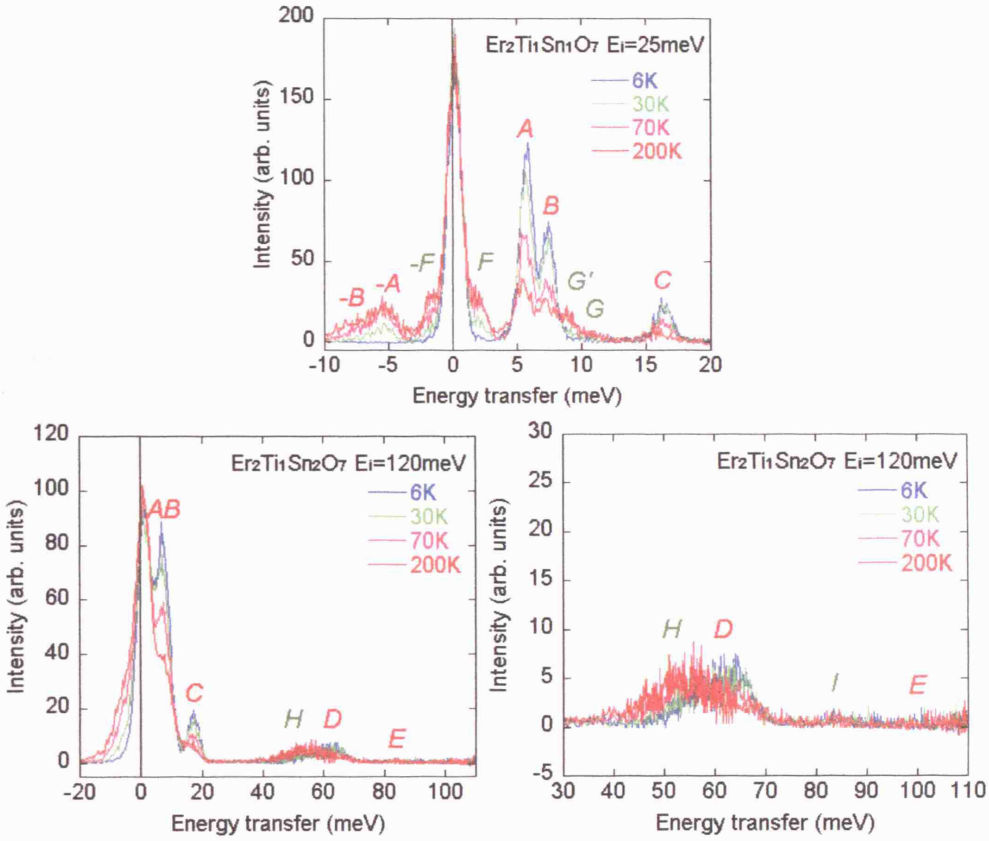

Figure A3-2: Energy spectra for $Er_2Ti_1Sn_1O_7$ measured on HET with incident energy E_i = 25 meV (*Top Left*) and E_i = 120 meV (*Top Right* and *Bottom*) measured at T = 6, 30, 70 and 200 K. The peaks that grow in intensity with lowering the temperatures are $E_i \sim$ 5.7, 7.6, 16.3, 60.5, 65.8 and 86.5 meV; hence attributed to transition from the ground state. The peaks that grow in intensity with increasing the temperatures are $E_i \sim$ < 2, 8.5 - 10, 45 - 55 meV; hence attributed to transition from the excited states.

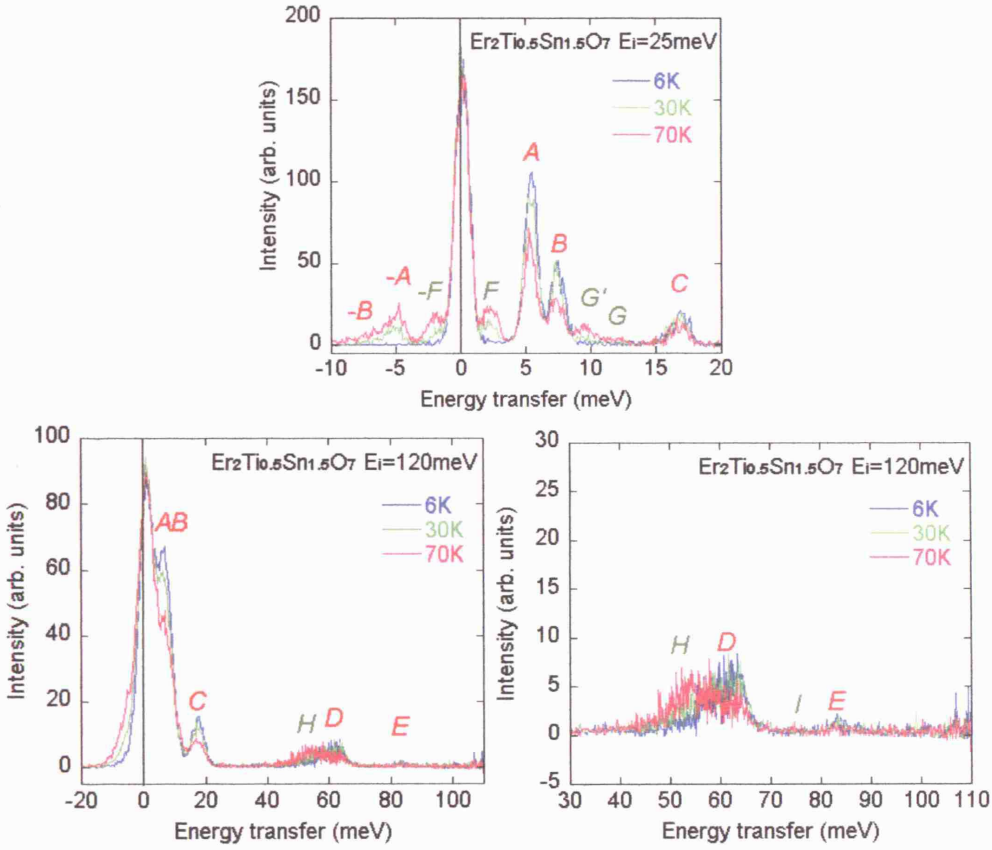

Figure A3-3: Energy spectra for $Er_2Ti_{0.5}Sn_{1.5}O_7$ measured on HET with incident energy E_i = 25 meV (*Top Left*) and E_i =120 meV (*Top Right* and *Bottom*) measured at T = 6, 30, and 70 K. The peaks that grow in intensity with lowering the temperatures are E_i ~ 5.6, 7.8, 16.8, 59.5, 63 and 84.5 meV; hence attributed to transition from the ground state. The peaks that grow in intensity with increasing the temperatures are E_i ~ 2.2, 8.9 - 10, 45 - 55 meV; hence attributed to transition from the excited states.

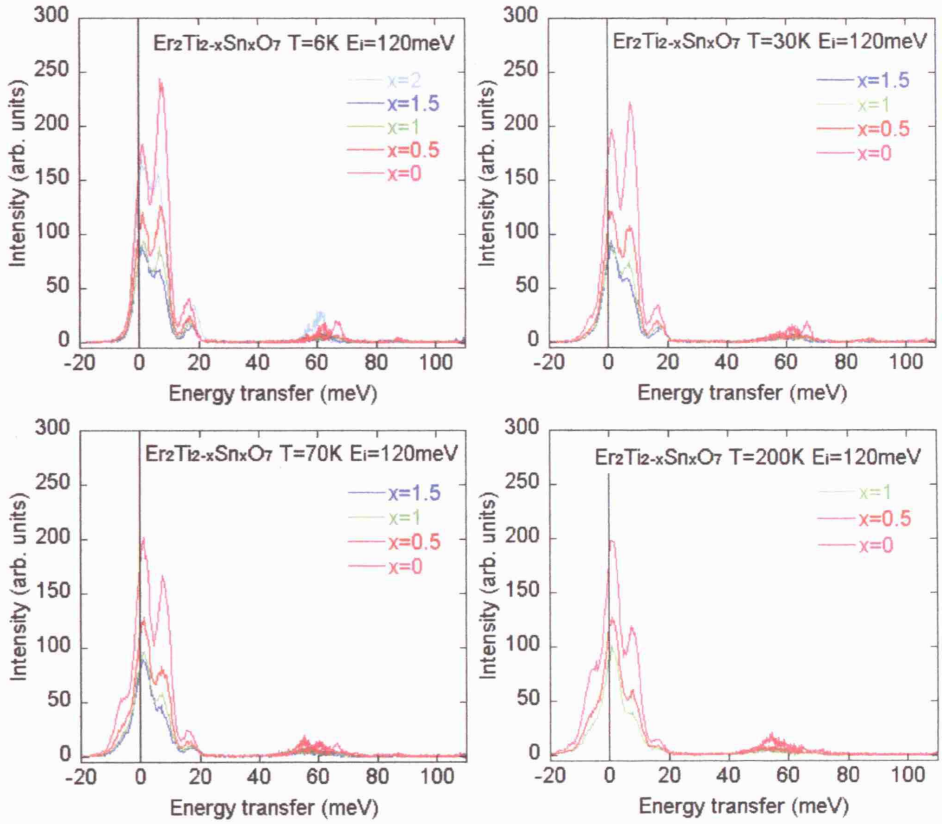

Figure A3-4: Energy spectra for $Er_2Ti_{2-x}Sn_xO_7$ (x = 0, 0.5, 1, 1.5 and 2) measured on HET with incident energy E_i = 120 meV measured at T = 6, 30, 70 and 200 K. They show the gradual variation in peak positions and intensities as one goes across the series. It is also seen that in these high incident energy (E_i = 120 meV) spectra the elastic peak is not at E = 0 but is shifted towards higher energy.

A 3.2 Calculated Wavefunctions of $Ho_2Ti_2O_7$ and $Dy_2Ti_2O_7$

$Ho_2Ti_2O_7$

|1+⟩	=	0.981	|	−8	⟩	|1−⟩	=	0.007	|	−7	⟩
	+	−0.158	|	−5	⟩		+	0.049	|	−4	⟩
	+	0.065	|	−2	⟩		+	0.072	|	−1	⟩
	+	−0.072	|	1	⟩		+	0.065	|	2	⟩
	+	0.049	|	4	⟩		+	0.158	|	5	⟩
	+	−0.007	|	7	⟩		+	0.981	|	8	⟩
|2+⟩	=	0.07	|	−6	⟩						
	+	0.704	|	−3	⟩						
	+	0.704	|	3	⟩						
	+	−0.07	|	6	⟩						
|3+⟩	=	−0.054	|	−8	⟩	|3−⟩	=	−0.039	|	−7	⟩
	+	0.204	|	−5	⟩		+	0.646	|	−4	⟩
	+	0.724	|	−2	⟩		+	0.105	|	−1	⟩
	+	−0.105	|	1	⟩		+	0.724	|	2	⟩
	+	0.646	|	4	⟩		+	−0.204	|	5	⟩
	+	0.039	|	7	⟩		+	−0.055	|	8	⟩
|4+⟩	=	0.131	|	−8	⟩	|4−⟩	=	0.147	|	−7	⟩
	+	0.466	|	−5	⟩		+	0.285	|	−4	⟩
	+	0.238	|	−2	⟩		+	0.774	|	−1	⟩
	+	0.774	|	1	⟩		+	−0.238	|	2	⟩
	+	−0.285	|	4	⟩		+	0.466	|	5	⟩
	+	0.147	|	7	⟩		+	−0.131	|	8	⟩
|5+⟩	=	0.287	|	−6	⟩						
	+	0.306	|	−3	⟩						
	+	0.805	|	0	⟩						
	+	−0.306	|	3	⟩						
	+	0.287	|	6	⟩						
|6+⟩	=	0.847	|	−7	⟩	|6−⟩	=	−0.019	|	−8	⟩
	+	−0.324	|	−4	⟩		+	−0.242	|	−5	⟩
	+	0.182	|	−1	⟩		+	−0.242	|	−2	⟩
	+	0.242	|	2	⟩		+	0.182	|	1	⟩
	+	−0.242	|	5	⟩		+	0.324	|	4	⟩
	+	0.02	|	8	⟩		+	0.847	|	7	⟩
|7+⟩	=	−0.328	|	−6	⟩	|8+⟩	=	−0.703	|	−6	⟩
	+	0.605	|	−3	⟩		+	0.07	|	−3	⟩
	+	−0.226	|	0	⟩		+	0.07	|	3	⟩
	+	−0.605	|	3	⟩		+	−0.072	|	6	⟩
	+	−0.329	|	6	⟩						⟩
|9+⟩	=	0.119	|	−8	⟩	|9−⟩	=	−0.108	|	−7	⟩
	+	0.682	|	−5	⟩		+	−0.421	|	−4	⟩
	+	−0.565	|	−2	⟩		+	−0.082	|	−1	⟩
	+	−0.082	|	1	⟩		+	0.565	|	2	⟩
	+	0.421	|	4	⟩		+	0.682	|	5	⟩
	+	−0.108	|	7	⟩		+	−0.119	|	8	⟩
|10+⟩	=	−0.476	|	−7	⟩	|10−⟩	=	−0.04	|	−8	⟩
	+	−0.46	|	−4	⟩		+	−0.432	|	−5	⟩
	+	0.583	|	−1	⟩		+	−0.181	|	−2	⟩
	+	0.181	|	2	⟩		+	0.583	|	1	⟩
	+	−0.432	|	5	⟩		+	0.46	|	4	⟩
	+	0.041	|	8	⟩		+	−0.477	|	7	⟩
|11+⟩	=	0.556	|	−6	⟩						
	+	0.199	|	−3	⟩						
	+	−0.549	|	0	⟩						
	+	−0.199	|	3	⟩						
	+	0.556	|	6	⟩						

Table A3-1: Calculated wavefunctions for $Ho_2Ti_2O_7$ using the program FOCUS and CEF parameters (B_k^q) given in Rosenkrantz's work [see section 7.3.2 and Ref.13 of Chapter 7]. The groundstate wavefunctions (|1+⟩ and |1−⟩) are the Kramers doublet.

$Dy_2Ti_2O_7$

|1+⟩	=	0.986	| -15 /2 ⟩	|1−⟩	=	0	| -15 /2 ⟩
	+	0.156	| -9 /2 ⟩		+	0.007	| -9 /2 ⟩
	+	-0.041	| -3 /2 ⟩		+	0.036	| -3 /2 ⟩
	+	-0.036	| 3 /2 ⟩		+	-0.041	| 3 /2 ⟩
	+	0.007	| 9 /2 ⟩		+	-0.156	| 9 /2 ⟩
	+	0	| 15 /2 ⟩		+	0.986	| 15 /2 ⟩
|2+⟩	=	-0.076	| -13 /2 ⟩	|2−⟩	=	-0.599	| -13 /2 ⟩
	+	-0.176	| -11 /2 ⟩		+	0.023	| -11 /2 ⟩
	+	-0.022	| -7 /2 ⟩		+	-0.172	| -7 /2 ⟩
	+	-0.111	| -5 /2 ⟩		+	0.014	| -5 /2 ⟩
	+	0.095	| -1 /2 ⟩		+	0.742	| -1 /2 ⟩
	+	0.742	| 1 /2 ⟩		+	-0.095	| 1 /2 ⟩
	+	0.014	| 5 /2 ⟩		+	0.111	| 5 /2 ⟩
	+	0.172	| 7 /2 ⟩		+	-0.022	| 7 /2 ⟩
	+	-0.023	| 11 /2 ⟩		+	-0.176	| 11 /2 ⟩
	+	-0.6	| 13 /2 ⟩		+	0.077	| 13 /2 ⟩
|3+⟩	=	0.642	| -13 /2 ⟩	|3−⟩	=	0.282	| -13 /2 ⟩
	+	0.053	| -11 /2 ⟩		+	-0.121	| -11 /2 ⟩
	+	0.281	| -7 /2 ⟩		+	0.123	| -7 /2 ⟩
	+	-0.042	| -5 /2 ⟩		+	0.096	| -5 /2 ⟩
	+	0.569	| -1 /2 ⟩		+	0.25	| -1 /2 ⟩
	+	-0.25	| 1 /2 ⟩		+	0.569	| 1 /2 ⟩
	+	-0.096	| 5 /2 ⟩		+	-0.042	| 5 /2 ⟩
	+	0.123	| 7 /2 ⟩		+	-0.281	| 7 /2 ⟩
	+	-0.121	| 11 /2 ⟩		+	-0.053	| 11 /2 ⟩
	+	-0.282	| 13 /2 ⟩		+	0.642	| 13 /2 ⟩
|4+⟩	=	0.076	| -15 /2 ⟩	|4−⟩	=	-0.001	| -15 /2 ⟩
	+	-0.181	| -9 /2 ⟩		+	0.192	| -9 /2 ⟩
	+	0.297	| -3 /2 ⟩		+	0.915	| -3 /2 ⟩
	+	0.915	| 3 /2 ⟩		+	-0.297	| 3 /2 ⟩
	+	-0.192	| 9 /2 ⟩		+	-0.181	| 9 /2 ⟩
	+	-0.002	| 15 /2 ⟩		+	-0.076	| 15 /2 ⟩
|5+⟩	=	-0.051	| -13 /2 ⟩	|5−⟩	=	0.238	| -13 /2 ⟩
	+	0.411	| -11 /2 ⟩		+	0.09	| -11 /2 ⟩
	+	0.059	| -7 /2 ⟩		+	-0.268	| -7 /2 ⟩
	+	0.806	| -5 /2 ⟩		+	0.176	| -5 /2 ⟩
	+	0.019	| -1 /2 ⟩		+	-0.088	| -1 /2 ⟩
	+	0.088	| 1 /2 ⟩		+	0.019	| 1 /2 ⟩
	+	-0.176	| 5 /2 ⟩		+	0.806	| 5 /2 ⟩
	+	-0.268	| 7 /2 ⟩		+	-0.059	| 7 /2 ⟩
	+	0.09	| 11 /2 ⟩		+	-0.411	| 11 /2 ⟩
	+	-0.238	| 13 /2 ⟩		+	-0.052	| 13 /2 ⟩
	+	-0.268	| 7 /2 ⟩		+	-0.059	| 7 /2 ⟩
	+	0.09	| 11 /2 ⟩		+	-0.411	| 11 /2 ⟩
	+	-0.238	| 13 /2 ⟩		+	-0.052	| 13 /2 ⟩
|6+⟩	=	-0.008	| -13 /2 ⟩	|6−⟩	=	0.174	| -13 /2 ⟩
	+	0.841	| -11 /2 ⟩		+	0.042	| -11 /2 ⟩
	+	0.018	| -7 /2 ⟩		+	-0.371	| -7 /2 ⟩
	+	-0.277	| -5 /2 ⟩		+	-0.014	| -5 /2 ⟩
	+	-0.011	| -1 /2 ⟩		+	0.213	| -1 /2 ⟩
	+	0.213	| 1 /2 ⟩		+	0.011	| 1 /2 ⟩
	+	-0.014	| 5 /2 ⟩		+	0.277	| 5 /2 ⟩
	+	0.371	| 7 /2 ⟩		+	0.018	| 7 /2 ⟩
	+	-0.042	| 11 /2 ⟩		+	0.841	| 11 /2 ⟩
	+	0.174	| 13 /2 ⟩		+	0.009	| 13 /2 ⟩
|7+⟩	=	-0.147	| -15 /2 ⟩	|7−⟩	=	0	| -15 /2 ⟩
	+	0.951	| -9 /2 ⟩		+	0.047	| -9 /2 ⟩
	+	-0.133	| -3 /2 ⟩		+	0.234	| -3 /2 ⟩
	+	0.234	| 3 /2 ⟩		+	0.133	| 3 /2 ⟩
	+	-0.047	| 9 /2 ⟩		+	0.951	| 9 /2 ⟩
	+	0	| 15 /2 ⟩		+	0.148	| 15 /2 ⟩
|8+⟩	=	-0.21	| -13 /2 ⟩	|8−⟩	=	0.096	| -13 /2 ⟩
	+	-0.105	| -11 /2 ⟩		+	-0.231	| -11 /2 ⟩
	+	0.741	| -7 /2 ⟩		+	-0.336	| -7 /2 ⟩
	+	0.193	| -5 /2 ⟩		+	0.426	| -5 /2 ⟩
	+	-0.007	| -1 /2 ⟩		+	0.003	| -1 /2 ⟩
	+	0.003	| 1 /2 ⟩		+	0.007	| 1 /2 ⟩
	+	0.426	| 5 /2 ⟩		+	-0.193	| 5 /2 ⟩
	+	0.336	| 7 /2 ⟩		+	0.741	| 7 /2 ⟩
	+	0.231	| 11 /2 ⟩		+	-0.105	| 11 /2 ⟩
	+	0.096	| 13 /2 ⟩		+	0.211	| 13 /2 ⟩

Table A3-2: Calculated wavefunctions for $Dy_2Ti_2O_7$ using the program FOCUS and CEF parameters given in Table 7.4 [section 7.3.2 of Chapter 7]. The groundstate wavefunctions (|1+⟩ and |1−⟩) are the Kramers doublet.

$Er_2Ti_2O_7$

|1+⟩	=	−0.189	|−6.5⟩	|1−⟩	=	0.2	|−6.5⟩
	+	0.51	|−5.5⟩		+	0.482	|−5.5⟩
	+	0.25	|−3.5⟩		+	−0.264	|−3.5⟩
	+	−0.388	|−2.5⟩		+	−0.367	|−2.5⟩
	+	−0.081	|−0.5⟩		+	0.086	|−0.5⟩
	+	0.086	|0.5⟩		+	0.081	|0.5⟩
	+	−0.367	|2.5⟩		+	0.388	|2.5⟩
	+	0.264	|3.5⟩		+	0.25	|3.5⟩
	+	−0.482	|5.5⟩		+	0.51	|5.5⟩
	+	0.2	|6.5⟩		+	0.19	|6.5⟩
|2+⟩	=	−0.041	|−7.5⟩	|2−⟩	=	0	|−7.5⟩
	+	0.707	|−4.5⟩		+	0.265	|−4.5⟩
	+	−0.415	|−1.5⟩		+	−0.506	|−1.5⟩
	+	−0.506	|1.5⟩		+	0.415	|1.5⟩
	+	−0.265	|4.5⟩		+	0.707	|4.5⟩
	+	−0.001	|7.5⟩		+	0.042	|7.5⟩
|3+⟩	=	−0.052	|−6.5⟩	|3−⟩	=	−0.382	|−6.5⟩
	+	0.544	|−5.5⟩		+	−0.075	|−5.5⟩
	+	0.07	|−3.5⟩		+	0.509	|−3.5⟩
	+	0.053	|−2.5⟩		+	−0.007	|−2.5⟩
	+	−0.073	|−0.5⟩		+	−0.527	|−0.5⟩
	+	−0.527	|0.5⟩		+	0.073	|0.5⟩
	+	−0.007	|2.5⟩		+	−0.053	|2.5⟩
	+	−0.509	|3.5⟩		+	0.07	|3.5⟩
	+	0.075	|5.5⟩		+	0.544	|5.5⟩
	+	−0.383	|6.5⟩		+	0.053	|6.5⟩
|4+⟩	=	0.116	|−6.5⟩	|4−⟩	=	0.808	|−6.5⟩
	+	−0.008	|−5.5⟩		+	0.001	|−5.5⟩
	+	0.009	|−3.5⟩		+	0.063	|−3.5⟩
	+	0.25	|−2.5⟩		+	−0.036	|−2.5⟩
	+	−0.073	|−0.5⟩		+	−0.51	|−0.5⟩
	+	−0.51	|0.5⟩		+	0.073	|0.5⟩
	+	−0.036	|2.5⟩		+	−0.25	|2.5⟩
	+	−0.063	|3.5⟩		+	0.009	|3.5⟩
	+	−0.001	|5.5⟩		+	−0.008	|5.5⟩
	+	0.808	|6.5⟩		+	−0.116	|6.5⟩
|5+⟩	=	−0.247	|−7.5⟩	|5−⟩	=	−0.022	|−7.5⟩
	+	0.601	|−4.5⟩		+	0.182	|−4.5⟩
	+	0.716	|−1.5⟩		+	−0.178	|−1.5⟩
	+	0.178	|1.5⟩		+	0.716	|1.5⟩
	+	0.182	|4.5⟩		+	−0.601	|4.5⟩
	+	0.023	|7.5⟩		+	−0.248	|7.5⟩
|6+⟩	=	0.095	|−6.5⟩	|6−⟩	=	−0.112	|−6.5⟩
	+	0.332	|−5.5⟩		+	0.281	|−5.5⟩
	+	0.109	|−3.5⟩		+	−0.129	|−3.5⟩
	+	0.503	|−2.5⟩		+	0.426	|−2.5⟩
	+	0.369	|−0.5⟩		+	−0.436	|−0.5⟩
	+	0.436	|0.5⟩		+	0.369	|0.5⟩
	+	−0.426	|2.5⟩		+	0.503	|2.5⟩
	+	−0.129	|3.5⟩		+	−0.109	|3.5⟩
	+	0.281	|5.5⟩		+	−0.332	|5.5⟩
	+	0.113	|6.5⟩		+	0.095	|6.5⟩
|7+⟩	=	−0.093	|−6.5⟩	|7−⟩	=	0.278	|−6.5⟩
	+	0.124	|−5.5⟩		+	0.042	|−5.5⟩
	+	−0.243	|−3.5⟩		+	0.716	|−3.5⟩
	+	0.438	|−2.5⟩		+	0.149	|−2.5⟩
	+	−0.108	|−0.5⟩		+	0.316	|−0.5⟩
	+	−0.316	|0.5⟩		+	−0.108	|0.5⟩
	+	−0.149	|2.5⟩		+	0.438	|2.5⟩
	+	0.716	|3.5⟩		+	0.243	|3.5⟩
	+	0.042	|5.5⟩		+	−0.124	|5.5⟩
	+	−0.278	|6.5⟩		+	−0.094	|6.5⟩
|8+⟩	=	0	|−7.5⟩	|8−⟩	=	0.967	|−7.5⟩
	+	0.021	|−4.5⟩		+	0.189	|−4.5⟩
	+	−0.041	|−1.5⟩		+	0.161	|−1.5⟩
	+	0.161	|1.5⟩		+	0.041	|1.5⟩
	+	−0.189	|4.5⟩		+	0.021	|4.5⟩
	+	0.967	|7.5⟩		+	0	|7.5⟩

$Er_2Ti_{1.5}Sn_{0.5}O_7$

|1+⟩	=	−0.015	|−6.5⟩	|1−⟩	=	0.248	|−6.5⟩
	+	0.72	|−5.5⟩		+	0.047	|−5.5⟩
	+	0.023	|−3.5⟩		+	−0.351	|−3.5⟩
	+	−0.532	|−2.5⟩		+	−0.035	|−2.5⟩
	+	−0.007	|−0.5⟩		+	0.1	|−0.5⟩
	+	0.1	|0.5⟩		+	0.007	|0.5⟩
	+	−0.035	|2.5⟩		+	0.532	|2.5⟩
	+	0.351	|3.5⟩		+	0.023	|3.5⟩
	+	−0.047	|5.5⟩		+	0.72	|5.5⟩
	+	0.248	|6.5⟩		+	0.016	|6.5⟩
|2+⟩	=	−0.037	|−7.5⟩	|2−⟩	=	−0.003	|−7.5⟩
	+	0.673	|−4.5⟩		+	0.355	|−4.5⟩
	+	−0.337	|−1.5⟩		+	−0.553	|−1.5⟩
	+	−0.553	|1.5⟩		+	0.337	|1.5⟩
	+	−0.355	|4.5⟩		+	0.673	|4.5⟩
	+	−0.004	|7.5⟩		+	0.038	|7.5⟩
|3+⟩	=	0.266	|−6.5⟩	|3−⟩	=	0.218	|−6.5⟩
	+	0.333	|−5.5⟩		+	−0.407	|−5.5⟩
	+	−0.413	|−3.5⟩		+	−0.339	|−3.5⟩
	+	0.06	|−2.5⟩		+	−0.073	|−2.5⟩
	+	0.431	|−0.5⟩		+	0.354	|−0.5⟩
	+	−0.354	|0.5⟩		+	0.431	|0.5⟩
	+	0.073	|2.5⟩		+	0.06	|2.5⟩
	+	−0.339	|3.5⟩		+	0.413	|3.5⟩
	+	−0.407	|5.5⟩		+	−0.333	|5.5⟩
	+	−0.218	|6.5⟩		+	0.266	|6.5⟩
|4+⟩	=	−0.021	|−6.5⟩	|4−⟩	=	0.842	|−6.5⟩
	+	−0.03	|−5.5⟩		+	−0.001	|−5.5⟩
	+	−0.001	|−3.5⟩		+	0.028	|−3.5⟩
	+	0.243	|−2.5⟩		+	0.006	|−2.5⟩
	+	0.013	|−0.5⟩		+	−0.479	|−0.5⟩
	+	−0.479	|0.5⟩		+	−0.013	|0.5⟩
	+	0.006	|2.5⟩		+	−0.243	|2.5⟩
	+	−0.028	|3.5⟩		+	−0.001	|3.5⟩
	+	0.001	|5.5⟩		+	−0.03	|5.5⟩
	+	0.842	|6.5⟩		+	0.022	|6.5⟩
|5+⟩	=	0.017	|−7.5⟩	|5−⟩	=	−0.21	|−7.5⟩
	+	0.083	|−4.5⟩		+	0.623	|−4.5⟩
	+	−0.302	|−1.5⟩		+	0.685	|−1.5⟩
	+	0.685	|1.5⟩		+	0.302	|1.5⟩
	+	−0.623	|4.5⟩		+	0.083	|4.5⟩
	+	−0.211	|7.5⟩		+	−0.017	|7.5⟩
|6+⟩	=	−0.072	|−6.5⟩	|6−⟩	=	−0.127	|−6.5⟩
	+	0.376	|−5.5⟩		+	−0.215	|−5.5⟩
	+	−0.076	|−3.5⟩		+	−0.132	|−3.5⟩
	+	0.574	|−2.5⟩		+	−0.328	|−2.5⟩
	+	−0.285	|−0.5⟩		+	−0.499	|−0.5⟩
	+	0.499	|0.5⟩		+	−0.285	|0.5⟩
	+	0.328	|2.5⟩		+	0.574	|2.5⟩
	+	−0.132	|3.5⟩		+	0.076	|3.5⟩
	+	−0.215	|5.5⟩		+	−0.376	|5.5⟩
	+	0.128	|6.5⟩		+	−0.073	|6.5⟩
|7+⟩	=	0.298	|−6.5⟩	|7−⟩	=	−0.017	|−6.5⟩
	+	0.007	|−5.5⟩		+	0.123	|−5.5⟩
	+	0.752	|−3.5⟩		+	−0.044	|−3.5⟩
	+	0.027	|−2.5⟩		+	0.458	|−2.5⟩
	+	0.343	|−0.5⟩		+	−0.02	|−0.5⟩
	+	−0.02	|0.5⟩		+	−0.343	|0.5⟩
	+	0.458	|2.5⟩		+	−0.027	|2.5⟩
	+	0.044	|3.5⟩		+	0.752	|3.5⟩
	+	−0.123	|5.5⟩		+	0.007	|5.5⟩
	+	−0.018	|6.5⟩		+	−0.298	|6.5⟩
|8+⟩	=	0	|−7.5⟩	|8−⟩	=	0.977	|−7.5⟩
	+	0.018	|−4.5⟩		+	0.161	|−4.5⟩
	+	−0.033	|−1.5⟩		+	0.138	|−1.5⟩
	+	0.138	|1.5⟩		+	0.033	|1.5⟩
	+	−0.161	|4.5⟩		+	0.018	|4.5⟩
	+	0.977	|7.5⟩		+	0	|7.5⟩

Table A3-3: Calculated wavefunctions for $Er_2Ti_2O_7$ and $Er_2Ti_{1.5}Sn_{0.5}O_7$ using the program FOCUS and the refined CEF parameters [Table 7.7 of Chapter 7]. The ground state wavefunctions ($|1+\rangle$ and $|1-\rangle$) are the Kramers doublet.

$Er_2Ti_1Sn_1O_7$

|1+⟩	=	0.22	|-6.5⟩	|1-⟩	=	-0.038	|-6.5⟩
	+	0.131	|-5.5⟩		+	0.733	|-5.5⟩
	+	-0.329	|-3.5⟩		+	0.059	|-3.5⟩
	+	-0.093	|-2.5⟩		+	-0.52	|-2.5⟩
	+	0.076	|-0.5⟩		+	-0.014	|-0.5⟩
	+	0.014	|0.5⟩		+	0.076	|0.5⟩
	+	0.52	|2.5⟩		+	-0.093	|2.5⟩
	+	0.059	|3.5⟩		+	0.329	|3.5⟩
	+	0.733	|5.5⟩		+	-0.131	|5.5⟩
	+	0.039	|6.5⟩		+	0.22	|6.5⟩
|2+⟩	=	-0.033	|-7.5⟩	|2-⟩	=	0	|-7.5⟩
	+	0.696	|-4.5⟩		+	0.33	|-4.5⟩
	+	-0.349	|-1.5⟩		+	-0.532	|-1.5⟩
	+	-0.532	|1.5⟩		+	0.349	|1.5⟩
	+	-0.33	|4.5⟩		+	0.696	|4.5⟩
	+	-0.001	|7.5⟩		+	0.034	|7.5⟩
|3+⟩	=	-0.039	|-6.5⟩	|3-⟩	=	0.322	|-6.5⟩
	+	-0.495	|-5.5⟩		+	-0.062	|-5.5⟩
	+	0.069	|-3.5⟩		+	-0.552	|-3.5⟩
	+	-0.13	|-2.5⟩		+	-0.016	|-2.5⟩
	+	-0.07	|-0.5⟩		+	0.56	|-0.5⟩
	+	0.56	|0.5⟩		+	0.07	|0.5⟩
	+	-0.016	|2.5⟩		+	0.13	|2.5⟩
	+	0.552	|3.5⟩		+	0.069	|3.5⟩
	+	0.062	|5.5⟩		+	-0.495	|5.5⟩
	+	0.322	|6.5⟩		+	0.04	|6.5⟩
|4+⟩	=	0.857	|-6.5⟩	|4-⟩	=	0.003	|-6.5⟩
	+	0	|-5.5⟩		+	-0.037	|-5.5⟩
	+	0.013	|-3.5⟩		+	0	|-3.5⟩
	+	-0.001	|-2.5⟩		+	0.236	|-2.5⟩
	+	-0.458	|-0.5⟩		+	-0.001	|-0.5⟩
	+	0.001	|0.5⟩		+	-0.458	|0.5⟩
	+	-0.236	|2.5⟩		+	-0.001	|2.5⟩
	+	0	|3.5⟩		+	-0.013	|3.5⟩
	+	-0.037	|5.5⟩		+	0	|5.5⟩
	+	-0.003	|6.5⟩		+	0.857	|6.5⟩
|5+⟩	=	0.004	|-7.5⟩	|5-⟩	=	-0.184	|-7.5⟩
	+	0.128	|-4.5⟩		+	0.609	|-4.5⟩
	+	-0.26	|-1.5⟩		+	0.715	|-1.5⟩
	+	0.715	|1.5⟩		+	0.26	|1.5⟩
	+	-0.609	|4.5⟩		+	0.128	|4.5⟩
	+	-0.185	|7.5⟩		+	-0.004	|7.5⟩
|6+⟩	=	0.07	|-6.5⟩	|6-⟩	=	-0.104	|-6.5⟩
	+	0.36	|-5.5⟩		+	0.241	|-5.5⟩
	+	0.051	|-3.5⟩		+	-0.076	|-3.5⟩
	+	0.572	|-2.5⟩		+	0.383	|-2.5⟩
	+	0.312	|-0.5⟩		+	-0.466	|-0.5⟩
	+	0.466	|0.5⟩		+	0.312	|0.5⟩
	+	-0.383	|2.5⟩		+	0.572	|2.5⟩
	+	-0.076	|3.5⟩		+	-0.051	|3.5⟩
	+	0.241	|5.5⟩		+	-0.36	|5.5⟩
	+	0.105	|6.5⟩		+	0.07	|6.5⟩
|7+⟩	=	-0.001	|-6.5⟩	|7-⟩	=	0.308	|-6.5⟩
	+	0.091	|-5.5⟩		+	0.001	|-5.5⟩
	+	-0.004	|-3.5⟩		+	0.755	|-3.5⟩
	+	0.418	|-2.5⟩		+	0.002	|-2.5⟩
	+	-0.002	|-0.5⟩		+	0.39	|-0.5⟩
	+	-0.39	|0.5⟩		+	-0.002	|0.5⟩
	+	-0.002	|2.5⟩		+	0.418	|2.5⟩
	+	0.755	|3.5⟩		+	0.004	|3.5⟩
	+	0.001	|5.5⟩		+	-0.091	|5.5⟩
	+	-0.308	|6.5⟩		+	-0.002	|6.5⟩
|8+⟩	=	0.982	|-7.5⟩	|8-⟩	=	0	|-7.5⟩
	+	0.139	|-4.5⟩		+	0.016	|-4.5⟩
	+	0.123	|-1.5⟩		+	-0.028	|-1.5⟩
	+	0.028	|1.5⟩		+	0.123	|1.5⟩
	+	0.016	|4.5⟩		+	-0.139	|4.5⟩
	+	0	|7.5⟩		+	0.982	|7.5⟩

$Er_2Ti_{0.5}Sn_{1.5}O_7$

|1+⟩	=	0.206	|-6.5⟩	|1-⟩	=	0.01	|-6.5⟩
	+	-0.035	|-5.5⟩		+	0.758	|-5.5⟩
	+	-0.323	|-3.5⟩		+	-0.015	|-3.5⟩
	+	0.024	|-2.5⟩		+	-0.522	|-2.5⟩
	+	0.061	|-0.5⟩		+	0.003	|-0.5⟩
	+	-0.003	|0.5⟩		+	0.061	|0.5⟩
	+	0.522	|2.5⟩		+	0.024	|2.5⟩
	+	-0.015	|3.5⟩		+	0.323	|3.5⟩
	+	0.758	|5.5⟩		+	0.035	|5.5⟩
	+	-0.01	|6.5⟩		+	0.206	|6.5⟩
|2+⟩	=	-0.03	|-7.5⟩	|2-⟩	=	0.005	|-7.5⟩
	+	0.748	|-4.5⟩		+	0.217	|-4.5⟩
	+	-0.419	|-1.5⟩		+	-0.465	|-1.5⟩
	+	-0.465	|1.5⟩		+	0.419	|1.5⟩
	+	-0.217	|4.5⟩		+	0.748	|4.5⟩
	+	0.005	|7.5⟩		+	0.031	|7.5⟩
|3+⟩	=	-0.278	|-6.5⟩	|3-⟩	=	0.133	|-6.5⟩
	+	-0.207	|-5.5⟩		+	-0.435	|-5.5⟩
	+	0.518	|-3.5⟩		+	-0.246	|-3.5⟩
	+	-0.067	|-2.5⟩		+	-0.142	|-2.5⟩
	+	-0.51	|-0.5⟩		+	0.243	|-0.5⟩
	+	0.243	|0.5⟩		+	0.51	|0.5⟩
	+	-0.142	|2.5⟩		+	0.067	|2.5⟩
	+	0.246	|3.5⟩		+	0.518	|3.5⟩
	+	0.435	|5.5⟩		+	-0.207	|5.5⟩
	+	0.133	|6.5⟩		+	0.279	|6.5⟩
|4+⟩	=	-0.353	|-6.5⟩	|4-⟩	=	0.791	|-6.5⟩
	+	-0.036	|-5.5⟩		+	-0.016	|-5.5⟩
	+	-0.001	|-3.5⟩		+	0.002	|-3.5⟩
	+	0.21	|-2.5⟩		+	0.094	|-2.5⟩
	+	0.18	|-0.5⟩		+	-0.402	|-0.5⟩
	+	-0.402	|0.5⟩		+	-0.18	|0.5⟩
	+	0.094	|2.5⟩		+	-0.21	|2.5⟩
	+	-0.002	|3.5⟩		+	-0.001	|3.5⟩
	+	0.016	|5.5⟩		+	-0.036	|5.5⟩
	+	0.791	|6.5⟩		+	0.354	|6.5⟩
|5+⟩	=	-0.167	|-7.5⟩	|5-⟩	=	0.017	|-7.5⟩
	+	0.608	|-4.5⟩		+	0.088	|-4.5⟩
	+	0.704	|-1.5⟩		+	-0.314	|-1.5⟩
	+	0.314	|1.5⟩		+	0.704	|1.5⟩
	+	0.088	|4.5⟩		+	-0.608	|4.5⟩
	+	-0.017	|7.5⟩		+	-0.168	|7.5⟩
|6+⟩	=	0.062	|-6.5⟩	|6-⟩	=	-0.071	|-6.5⟩
	+	0.33	|-5.5⟩		+	0.282	|-5.5⟩
	+	0.005	|-3.5⟩		+	-0.006	|-3.5⟩
	+	0.551	|-2.5⟩		+	0.47	|-2.5⟩
	+	0.342	|-0.5⟩		+	-0.401	|-0.5⟩
	+	0.401	|0.5⟩		+	0.342	|0.5⟩
	+	-0.47	|2.5⟩		+	0.551	|2.5⟩
	+	-0.006	|3.5⟩		+	-0.005	|3.5⟩
	+	0.282	|5.5⟩		+	-0.33	|5.5⟩
	+	0.072	|6.5⟩		+	0.062	|6.5⟩
|7+⟩	=	0.141	|-6.5⟩	|7-⟩	=	0.287	|-6.5⟩
	+	0.041	|-5.5⟩		+	-0.02	|-5.5⟩
	+	0.333	|-3.5⟩		+	0.675	|-3.5⟩
	+	0.315	|-2.5⟩		+	-0.156	|-2.5⟩
	+	0.201	|-0.5⟩		+	0.406	|-0.5⟩
	+	-0.406	|0.5⟩		+	0.201	|0.5⟩
	+	0.156	|2.5⟩		+	0.315	|2.5⟩
	+	0.675	|3.5⟩		+	-0.333	|3.5⟩
	+	-0.02	|5.5⟩		+	-0.041	|5.5⟩
	+	-0.287	|6.5⟩		+	0.141	|6.5⟩
|8+⟩	=	0	|-7.5⟩	|8-⟩	=	0.985	|-7.5⟩
	+	0.015	|-4.5⟩		+	0.125	|-4.5⟩
	+	-0.024	|-1.5⟩		+	0.114	|-1.5⟩
	+	0.114	|1.5⟩		+	0.024	|1.5⟩
	+	-0.125	|4.5⟩		+	0.015	|4.5⟩
	+	0.985	|7.5⟩		+	0	|7.5⟩

Table A3-4: Calculated wavefunctions for $Er_2Ti_1Sn_1O_7$ and $Er_2Ti_{0.5}Sn_{1.5}O_7$ using the program FOCUS and the refined CEF parameters [Table 7.7 of Chapter 7]. The groundstate wavefunctions (|1+⟩ and |1−⟩) are the Kramers doublet.

$Er_2Sn_2O_7$

|1+>	=	-0.089	|-6.5>	|1->	=	0.145	|-6.5>
	+	0.682	|-5.5>		+	0.424	|-5.5>
	+	0.147	|-3.5>		+	-0.237	|-3.5>
	+	-0.423	|-2.5>		+	-0.263	|-2.5>
	+	-0.006	|-0.5>		+	0.009	|-0.5>
	+	0.009	|0.5>		+	0.006	|0.5>
	+	-0.263	|2.5>		+	0.423	|2.5>
	+	0.237	|3.5>		+	0.147	|3.5>
	+	-0.424	|5.5>		+	0.682	|5.5>
	+	0.145	|6.5>		+	0.09	|6.5>
|2+>	=	-0.023	|-7.5>	|2->	=	0	|-7.5>
	+	0.685	|-4.5>		+	0.399	|-4.5>
	+	-0.273	|-1.5>		+	-0.544	|-1.5>
	+	-0.544	|1.5>		+	0.273	|1.5>
	+	-0.399	|4.5>		+	0.685	|4.5>
	+	0	|7.5>		+	0.024	|7.5>
|3+>	=	-0.271	|-6.5>	|3->	=	0.004	|-6.5>
	+	-0.006	|-5.5>		+	-0.419	|-5.5>
	+	0.608	|-3.5>		+	-0.008	|-3.5>
	+	-0.003	|-2.5>		+	-0.229	|-2.5>
	+	-0.573	|-0.5>		+	0.008	|-0.5>
	+	0.008	|0.5>		+	0.573	|0.5>
	+	-0.229	|2.5>		+	0.003	|2.5>
	+	0.008	|3.5>		+	0.608	|3.5>
	+	0.419	|5.5>		+	-0.006	|5.5>
	+	0.004	|6.5>		+	0.272	|6.5>
|4+>	=	0.238	|-6.5>	|4->	=	0.855	|-6.5>
	+	-0.056	|-5.5>		+	0.016	|-5.5>
	+	-0.006	|-3.5>		+	-0.022	|-3.5>
	+	0.207	|-2.5>		+	-0.058	|-2.5>
	+	-0.108	|-0.5>		+	-0.387	|-0.5>
	+	-0.387	|0.5>		+	0.108	|0.5>
	+	-0.058	|2.5>		+	-0.207	|2.5>
	+	0.022	|3.5>		+	-0.006	|3.5>
	+	-0.016	|5.5>		+	-0.056	|5.5>
	+	0.855	|6.5>		+	-0.238	|6.5>
|5+>	=	0	|-7.5>	|5->	=	-0.129	|-7.5>
	+	0.169	|-4.5>		+	0.578	|-4.5>
	+	-0.231	|-1.5>		+	0.753	|-1.5>
	+	0.753	|1.5>		+	0.231	|1.5>
	+	-0.578	|4.5>		+	0.169	|4.5>
	+	-0.13	|7.5>		+	0	|7.5>
|6+>	=	0.017	|-6.5>	|6->	=	-0.066	|-6.5>
	+	0.407	|-5.5>		+	0.104	|-5.5>
	+	-0.018	|-3.5>		+	0.07	|-3.5>
	+	0.729	|-2.5>		+	0.186	|-2.5>
	+	0.123	|-0.5>		+	-0.482	|-0.5>
	+	0.482	|0.5>		+	0.123	|0.5>
	+	-0.186	|2.5>		+	0.729	|2.5>
	+	0.07	|3.5>		+	0.018	|3.5>
	+	0.104	|5.5>		+	-0.407	|5.5>
	+	0.067	|6.5>		+	0.017	|6.5>
|7+>	=	0.322	|-6.5>	|7->	=	0.001	|-6.5>
	+	0	|-5.5>		+	0.001	|-5.5>
	+	0.74	|-3.5>		+	0.002	|-3.5>
	+	-0.001	|-2.5>		+	0.296	|-2.5>
	+	0.512	|-0.5>		+	0.001	|-0.5>
	+	0.001	|0.5>		+	-0.512	|0.5>
	+	0.296	|2.5>		+	0.001	|2.5>
	+	-0.002	|3.5>		+	0.74	|3.5>
	+	-0.001	|5.5>		+	0	|5.5>
	+	0.001	|6.5>		+	-0.322	|6.5>
|8+>	=	0	|-7.5>	|8->	=	0.991	|-7.5>
	+	0.012	|-4.5>		+	0.092	|-4.5>
	+	-0.017	|-1.5>		+	0.092	|-1.5>
	+	0.092	|1.5>		+	0.017	|1.5>
	+	-0.092	|4.5>		+	0.012	|4.5>
	+	0.991	|7.5>		+	0	|7.5>

Table A3-5: Calculated wavefunctions for $Er_2Sn_2O_7$ using the program FOCUS and the refined CEF parameters [Table 7.7 of Chapter 7]. The groundstate wavefunctions ($|1+\rangle$ and $|1-\rangle$) are the Kramers doublet.